Dynamic adhesion breaking in laminated glass – effect of interfaces and polymer's rheology

Paul Fourton

PSL UNIVERSITÉ PARIS

THÈSE DE DOCTORAT

DE L'UNIVERSITÉ PSL

Préparée à l'ESPCI Paris

Mécanismes de résistance à l'impact des vitrages feuilletés : effet de l'interface et de la rhéologie du polymère

Adhesion rupture in laminated glass: effect of the interface and the rheology of the polymer

Soutenue par

Paul FOURTON

Le 7 novembre 2019

École doctorale n°397

Physique et Chimie des Matériaux

Spécialité

Physico-chimie

Composition du jury :

Dominique LEGUILLON Directeur de Recherche émérite, Sorbonne Université – CNRS	*Président*
Muriel BRACCINI Chargée de Recherche HDR, Grenoble INP – CNRS	*Rapportrice*
Gregory B. McKENNA Professor, TexasTech University	*Rapporteur*
Julien JUMEL Professeur, ENSTA Bretagne	*Examinateur*
Véronique LAZARUS Professeure, ENSTA ParisTech – Université Paris-Saclay	*Examinatrice*
Matteo CICCOTTI Professeur, ESPCI Paris	*Co-directeur de thèse*
Etienne BARTHEL Directeur de Recherche, ESPCI Paris – CNRS	*Directeur de thèse*

ESPCI PARIS | PSL

Remerciements

Ce travail de doctorat a été possible grâce à un contrat CIFRE avec Saint-Gobain Research Paris. Je tiens en particulier à remercier François Creuzet, directeur scientifique, et Boris Jaffrenou, directeur du département PCRS, de m'avoir recruté en octobre 2016 et avoir participé à tous les points de suivi organisés à SGR Paris, au cours de ces trois années.

Au-delà du département PCRS, je remercie également tous les ingénieurs et techniciens avec lesquels j'ai pu interagir de manière riche pendant ces trois années.

Au sein de SGR Paris, j'ai fait partie du groupe Physico-chimie des Interfaces et des Liquides. Parmi tous les ingénieurs ou techniciens de recherche aux grandes qualités du groupe, je tiens en particulier à adresser mes remerciements :

- à Nicolas Taccoen, mon encadrant industriel, pour ta bienveillance, ta curiosité, tes conseils au-delà des sciences. S'il est dommage que tu n'aies pu assister au sprint final et à la soutenance officielle, travailler et échanger avec toi pendant deux ans et demi a été plaisant et enrichissant.
- à Keyvan Piroird, pour ton implication continue, voire intense dans la période de rédaction, pour ta rigueur scientifique et tes questions toujours pertinentes. Enfin, merci à toi d'avoir représenté SGR Paris dans mon jury de thèse, en tant qu'invité.
- à Nathalie Dideron et Diamante Macé, pour le temps consacré à me former et à m'initier aux arcanes du verre feuilleté. Votre disponibilité sans faille et votre expérience pratique m'ont été précieuses du début jusqu'à la fin de ma thèse.

- à Marie Lamblet, cheffe de groupe, pour m'avoir si bien accueilli dans le groupe PIL, m'avoir fait prendre part à la vie du groupe, et m'avoir proposé de rester dans le groupe en tant qu'ingénieur de recherche, le jour même de la fin de mon contrat de thèse.

Au sein de mon laboratoire de thèse, Science et Ingénierie de la Matière Molle, je souhaite tout d'abord remercier Etienne Barthel et Matteo Ciccotti, mes directeurs de thèse :

- à Etienne, merci pour ta positivité et ton humour à toute épreuve, pour ta disponibilité quasi-illimitée tant au long cours que dans l'urgence des dernières corrections, pour la qualité de nos échanges, même si nous nous sommes parfois perdus dans les méandres de la viscoélasticité en grandes déformations, et enfin pour tous tes conseils à propos de mécanique de la fracture, de rédaction de manuscrit, de présentation orale, ou de chocolat.
- à Matteo, merci pour ta vision de la mécanique physique, nos discussions de plusieurs heures à ton bureau, ta patience pour se triturer l'esprit autour d'une feuille de papier et d'un café.

Pour ces trois années riches de nouvelles connaissances scientifiques et humains, mes sincères mercis à tout le laboratoire SIMM :

- à l'équipe Soft Polymer Networks : Alba, Yvette, Dominique, Tetsu, Bruno et Costantino.
- à l'escalier H : Freddy, Mayu, Fabienne, Emilie, Laurence, Artem, Antoine, Christian et Hélène.
- à l'escalier C : Mohamed, Armand, Nadège, Cécile, François, Jean-Baptiste, Patrick, Nicolas et Guylaine.
- à l'atelier de mécanique : Alex et Ludo, les deux artistes de la CAO et de la fraiseuse numérique.

Ces trois années au SIMM n'auraient pas été aussi plaisantes si je n'avais été entouré de doctorants et post-doctorants formidables. Je tente ici de tous les citer, avec l'assurance d'en oublier :

- pour l'escalier H : Miléna, Giorgia, Pascal, Aude, Raphaëlle, Xavier, Cécile M, Cécile C, Gabo, Victoria, Heiva, Nassim, Franz, Clotilde, Gaétan, Gaëlle, Guillaume, Valentine.

- pour l'escalier C : Julien, Claire, Charles, Tom, Sandrine, Clément, Christophe, Wilbert, Yuan-Yuan.

Parmi tous ces non-permanents, quelques-uns méritent de faire couler un peu plus d'encre : Julie, ma "bibi de PC", avec qui nous aurons grandi de jeune élève-ingénieur à docteur, toujours aux cotés l'un de l'autre ; Pierre et Louis, les deux autres compères du bureau E005 à l'humour décapant ; Ludo et Juliette, acolytes de conférences en terre de crocodiles et de pauses thé salvatrices ; et enfin Mélanie, meilleure découverte de ma thèse.

Je garde de précieux souvenirs de week-ends labo, de conférences, de dégustations de bière et de vin, de parties de pétanque aux Arènes de Lutèce, de pots de thèse ... avec chacun d'entre vous.

Cette thèse de doctorat vient également conclure le chapitre ESPCI, après sept années passées à arpenter les bâtiments du 10 rue Vauquelin depuis l'intégration de la promotion 131. J'ai rencontré à l'Ecole Supérieure de Physique et de Chimie Industrielles de la Ville de Paris de véritables amis : J-Luc, Florent, Gaëtan, Alice T, Alex, Alice B.

Au cours de cette thèse, j'ai également dédié de mon temps à l'Ecole Doctorale 397 et à l'organisation de ses fameuses JED, avec Karol et Agathe, le froid mordant de décembre et la chaleur brûlante des champignons chauffants du campus des Cordeliers.

Comme le dit le diction, *anima sana in corpore sano* : cette thèse n'aurait pas été la même sans le sport : virtuel sur MonPetitGazon (ou l'art de gérer 6 ligues de *fantasy football* en parallèle), réel sur les terrains de l'Urban d'Ivry (avec les grands sportifs du SIMM ou du LCMCP, parfois les deux) ou les cours de tennis de la ville de Paris au petit matin.

Enfin, *last but not least*, merci à ma famille. J'ai une pensée émue pour mes grand-mères Jeanne et Josette, parties avant de m'avoir vu docteur, et pour mon grand père Julien venu assister à ma soutenance, lui le gardien des tomates du jardin et des parties de pétanque à Limoges, de ces moments qui font les souvenirs d'enfance.

Merci à mes parents, Richard et Corine, à l'amour inaltérable et au soutien indéfectible. Enfin, merci à Anne, docteur Fourton première du nom, pour être la meilleure des sœurs qu'on puisse imaginer.

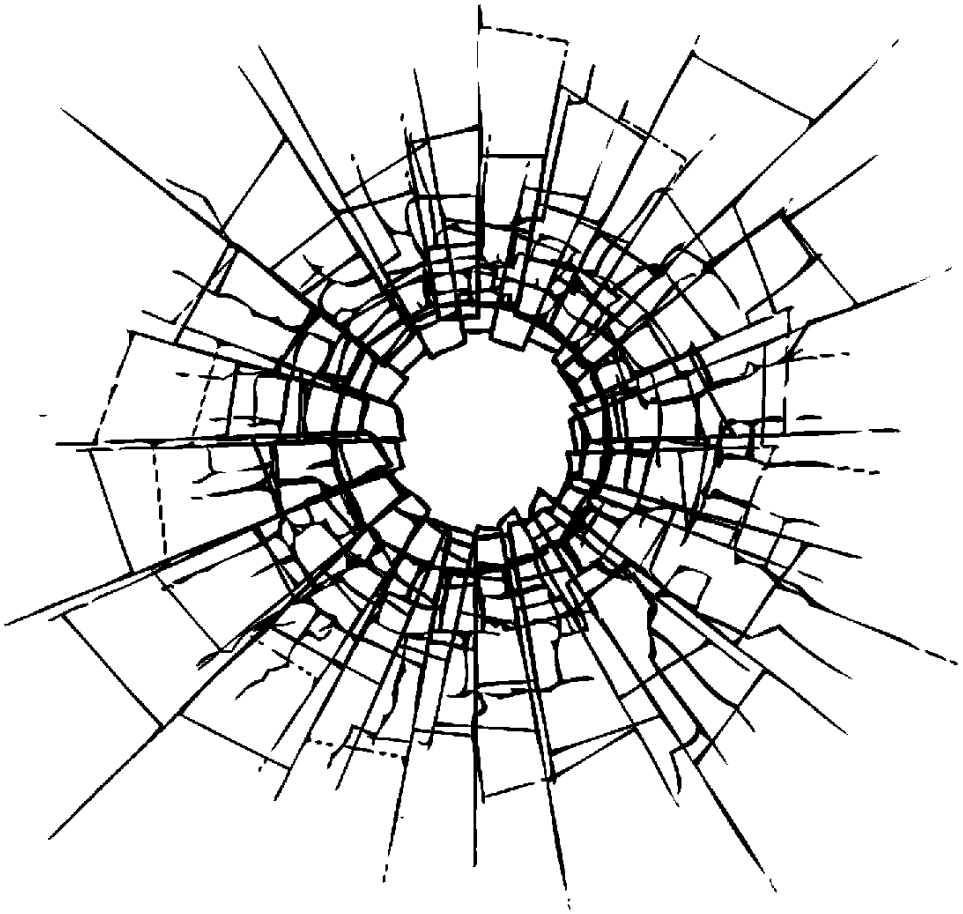

Résumé en français

Introduction

Le verre feuilleté est un produit industriel centenaire destiné à des applications de sécurité. Il est composé d'un feuillet de polymère placé entre deux plateaux de verre, comme illustré sur . Au cours du procédé de fabrication, cet assemblage est transformé en un produit transparent par application de température et de pression.

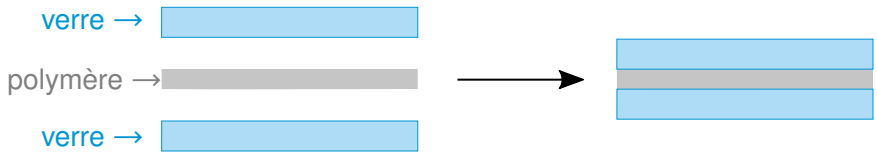

Figure 1 Le verre feuilleté

L'intercalaire polymère assure un double rôle lorsque le vitrage est brisé par un impact : il assure la rétention des éclats de verre, par ses propriétés d'adhésion, et assume une grande partie de la dissipation d'énergie, par ses propriétés mécaniques. Ainsi, l'intercalaire évite qu'un objet ne traverse le vitrage et ne projette des éclats de verre tranchants.

Dans l'industrie automobile ou du bâtiment, des normes régissent les performances du verre feuilleté. Elles consistent typiquement à lacher un impacteur avec une énergie contrôlée, que ce soit un pendule de 50 kg (norme EN12600) ou une bille en métal de 4 kg (norme EN356). Comme l'illustre la figure 2, au cours d'un test de chute à la bille, le polymère agit comme un ligament reliant des fragments de verre brisés entre eux.

Dans le chapitre I, nous présentons un état de l'art dans l'étude du verre feuilleté sous impact. En particulier, nous nous appuyons sur le *Through Crack Tensile Test* comme test mécanique de choix pour étudier le comportement du ligament de

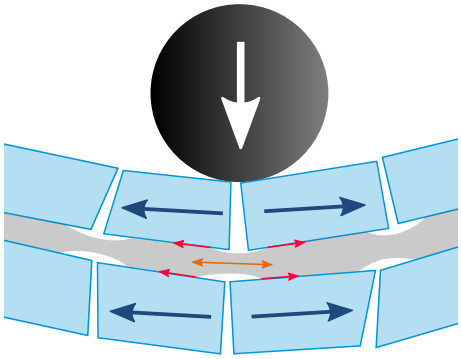

Figure 2 Schéma d'un verre feuilleté sous impact : tension entre fragments (← →), élongation (↔) et délamination (→) de l'intercalaire.

polymère dans un échantillon de verre feuilleté. Un exemple de *TCTT* est présenté sur la figure 3 : l'expérience consiste en une traction uniaxiale sur un échantillon de verre feuilleté, au milieu duquel on a déjà fissuré les morceaux de verre de manière contrôlée. On observe alors la déformation et la délamination simultanées du ligament de polymère qui relie les deux fragments. Dans le *TCTT*, nous pouvons définir une grandeur énergétique pertinente, le travail macroscopique de délamination G_{m}, égal au travail extérieur injecté et dissipé par ces deux mécanismes.

Les concepts de mécanique de la fracture utiles sont également rappelés : avec les polymères dissipatifs utilisés dans le verre feuilleté, nous nous appuyons sur les théories de propagation de fissure dans des matériaux viscoélastiques[1] et plastiques[2,3].

En particulier, à partir des travaux de *Elzière*[4,5] sur l'intercalaire PVB, le travail macroscopique de délamination peut être décrit comme la contribution d'un terme d'interface Γ_{crack}, qui contient la dissipation proche du front de délamination, et d'un terme volumique Π_{bulk} qui caractérise l'énergie dissipée par la grande déformation du ligament viscoélastique. Pour une épaisseur h d'intercalaire, l'énergie dissipée dans le *TCTT* peut s'écrire :

$$G_{\mathrm{m}} = 2\,\Gamma_{\mathrm{crack}} + h \cdot \Pi_{\mathrm{bulk}} \tag{1}$$

La sollicitation de l'intercalaire dans le verre feuilleté sous impact met donc en jeu un couplage entre l'interface et le volume, entre l'adhésion et le comportement mécanique. Avec comme idée directrice la compréhension de ce couplage, ce manuscrit traite de deux questions :

- Quel est l'effet d'une modification d'adhésion sur les mécanismes de dissipation d'énergie ?
- Quel est l'effet d'un changement de comportement mécanique de l'intercalaire sur ces phénomènes de déformation et délamination ?

Matériels et méthods

Dans le chapitre II, les deux matériaux polymères rencontrés dans ce manuscrit sont d'abord présentés :

- Le PVB, poly(butyral de vinyle), intercalaire le plus répandu dans les applications industrielles, constitué de 70% de résine et 30% de plastifiant.
- L'EVA, poly(éthylène - acétate de vinyle), un copolymère statistique contenant 75% de monomères ethylène et 25% acétate de vinyle, ainsi que des agents réticulants et des promoteurs d'adhésion.

Par la suite, nous décrivons la modification de surface, avec les chimies de silanes utilisées et la méthode de chiffonnage, puis les méthodes de caractérisation de la structure des polymères – DSC, SAXS-WAXS – et de leurs propriétés mécaniques – DMTA, traction uniaxiale. Enfin, nous développons ensuite les tests de caractérisation de l'adhésion : le test de pelage et, surtout, le test *TCTT* (figure 3).

Modification d'adhésion

La question du contrôle de l'adhésion du PVB sur le verre est abordée ici par la modification de la chimie de surface du verre.

Chimie sol-gel TEOS–MTES

Dans le chapitre III, nous avons développé une méthode de modification d'adhésion entre le PVB et le verre. Nous utilisons la chimie des silanes, avec un mélange de TEOS (orthosilicate de tétraethyle) et MTES (méthyl-triéthoxysilane), dans l'idée de contrôler la quantité de groupes hydroxyles présents à la surface du verre.

Avec cette chimie de surface, nous montrons que l'adhérence du PVB sur le verre peut être modulée entre 0.2 $kJ \cdot m^{-2}$ et 2.5 $kJ \cdot m^{-2}$, lorsque la fraction volumique en TEOS augmente entre 0 et 100% (figure 4a).

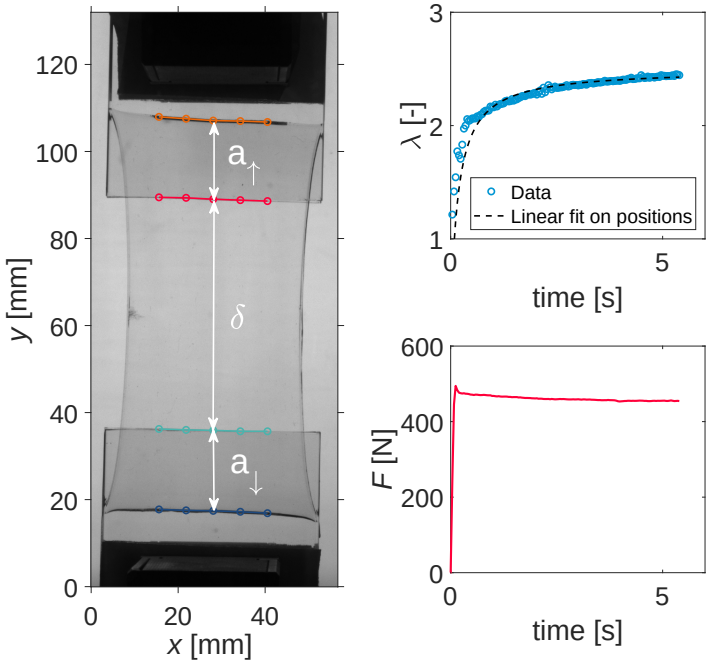

Figure 3 Exemple de test *TCTT* : après une traction δ à la vitesse $\dot{\delta} = 10\,\mathrm{mm}\cdot\mathrm{s}^{-1}$, l'intercalaire s'est décollé d'une longueur $2a$. L'élongation est $\lambda = 1 + \delta/2a$.

Effet sur la dissipation à l'interface

Afin d'évaluer l'effet de la modification de surface sur les mécanismes de dissipation, nous faisons varier l'épaisseur de l'intercalaire de PVB, de 0.38 mm à 1.52 mm, afin de pouvoir estimer les contributions interfaciale Γ_{crack} et volumique Π_{bulk} selon l'équation (1).

Les résultats expérimentaux de *TCTT*, présentés sur la figure 4b, ont montré que, quand l'affinité du PVB pour la surface augmente, seule la contribution interfaciale Γ_{crack} varie significativement, et qu'elle augmente proportionnellement à l'adhérence mesurée en pelage.

L'apparente indépendance de la dissipation volumique Π_{bulk} est expliquée qualitativement par un effet de compétition entre valeur de l'élongation et taux de déformation dans le PVB. En effet, dans le *TCTT* à vitesse de chargement imposée, une augmentation de la déformation macroscopique de l'intercalaire, à cause de la plus forte adhésion, induit une diminution de la vitesse de délamination, et donc une diminution du taux de déformation. Ainsi, comme le PVB se déforme davantage mais plus lentement, l'énergie dissipée sur le chemin de chargement ne varie pas

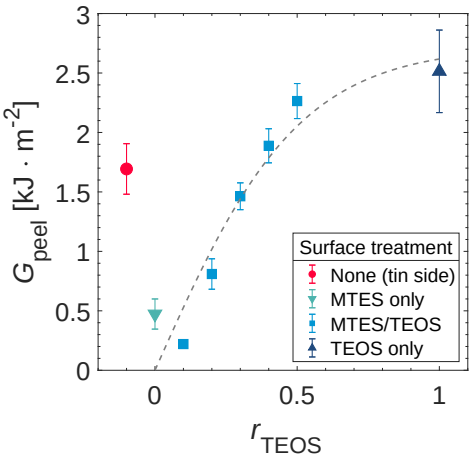

(a) Pelage : adhérence du PVB sur un verre traité TEOS–MTES.

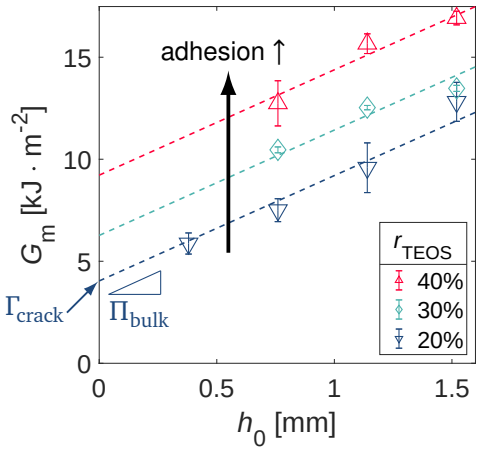

(b) *TCTT* : augmentation de l'énergie macroscopique de fracture avec l'épaisseur de PVB et la concentration en TEOS du traitement de surface.

Figure 4 Modification d'adhésion dans le verre feuilleté avec du PVB.

sensiblement *in fine*.

Un intercalaire semi-cristallin élasto-plastique : l'EVA

Une grande partie de la littérature scientifique sur le verre feuilleté traite du PVB comme intercalaire, car c'est le polymère majoritairement utilisé dans les applications industrielles. Afin d'étudier l'effet du comportement mécanique du polymère sur la délamination, nous avons choisi de changer radicalement de matériau. Pour cela, nous avons sélectionné l'EVA, poly(éthylène - acétate de vinyle). Dans le chapitre IV, nous effectuons une caractérisation physico-chimique et mécanique de cet intercalaire original.

Réticulation

L'intercalaire commercial utilisé ici contient des peroxydes : au cours du traitement thermique du procédé feuilleté, le polymère réticule par des réactions radicalaires. Nous avons montré que la cinétique de réticulation, caractérisée par des courbes de cuisson en rhéologie plan-plan, peut être modélisée par une cinétique du premier ordre de la concentration en peroxyde. Dans ce modèle cinétique, la durée de la

réaction de réticulation suit une loi de type Arrhénius en fonction de la température, pour laquelle l'énergie d'activation est donnée par la décomposition du peroxyde.

Structure semi-cristalline

Du fait de la composition de la résine d'EVA, avec 75% de monomères éthylène, l'intercalaire est semi-cristallin, ce que nous avons confirmé par analyses DSC et diffusion de rayons X. Nous avons ainsi pu estimer que 10% environ du matériau est composé de domaine cristallins, d'une taille typique de 4–5 nm.

Réponse mécanique élasto-plastique

Les mesures rhéologiques en DMA (figure 5a) montrent une transition vitreuse vers -20°C, et une zone de fusion/recristallisation vers 50°C. Par conséquent, le comportement mécanique de ce matériau autour à 20°C est élasto-plastique. Sur les courbes contrainte-déformation en traction uniaxiale (figure 5b), l'EVA présente une comportement indépendant du taux de déformation. On observe une contrainte seuil, de l'ordre de 3 MPa à 20°C, ainsi qu'une hystérèse à la décharge et une déformation résiduelle, preuves du caractère plastique de la réponse mécanique.

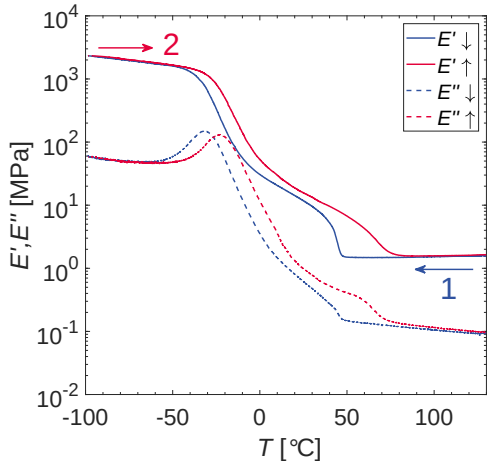

(a) DMTA en petites déformations : module de stockage E' et module de perte E'' of EVA en fonction de la teméprature ($\varepsilon = 0.1\%$, f =1 Hz, β = 1°C·min^{-1})

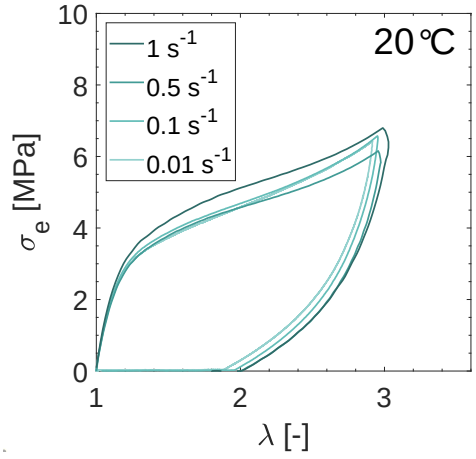

(b) Traction uniaxiale en grande déformations : contrainte–déformation à 20°C

Figure 5 Comportement mécanique de l'EVA, (a) en petites déformations et (b) en grandes déformations.

Délamination dans un verre feuilleté avec intercalaire EVA

Nous nous intéressons donc au comportement d'un verre feuilleté avec un intercalaire EVA, à l'aide du *TCTT*.

Nécessité de modifier l'adhésion pour délaminer

Le premier constat expérimental est la nécessité de modifier l'adhésion entre EVA et verre afin de permettre la délamination de cet intercalaire. En effet, à cause de l'adhérence trop grande, l'intercalaire subit une rupture cohésive avant de pouvoir se décoller du verre. Nous avons donc à nouveau utilisé la chimie des silanes pour maitriser les interactions à l'interface. Les résultats de pelage (figure 6a) montrent que l'adhérence de l'EVA peut être contrôlée sur deux ordres de grandeur. Nous avons sélectionné la surface méthylée (MTES) pour pouvoir observer une délamination stable.

Pas d'effet de vitesse et d'épaisseur à l'ambiante

Nous avons fait varier l'épaisseur h_0 de l'intercalaire EVA (figure 6b) et la vitesse de chargement $\dot{\delta}$. Expérimentalement, on observe une faible augmentation de G_{m} avec l'épaisseur et la vitesse, mais non significative comme c'était le cas avec le PVB viscoélastique.

La propagation de fissure adhésive est donc le mécanisme dissipatif dominant dans l'intercalaire EVA. Ainsi, nous écrivons le travail macroscopique de délamination dans ce matériau élasto-plastique comme :

$$G_{\mathrm{m}} \approx 2\,\Gamma_{\mathrm{crack}}$$

Retour de la va viscoélasticité à basse température

A l'instar du PVB proche de sa T_g, l'EVA se révèle être un excellent matériau dissipatif à -20°C, comme le montrent les courbes contrainte–déformation (figure). A cette basse température, nous retrouvons sur la figure 7b l'augmentation claire de G_{m} avec l'épaisseur d'intercalaire, signe de la dissipation en volume.

Ainsi, les effets de vitesse de chargement et de dissipation dans le volume de l'intercalaire sont retrouvés à basse température, lorsqu'on se rapproche de la tem-

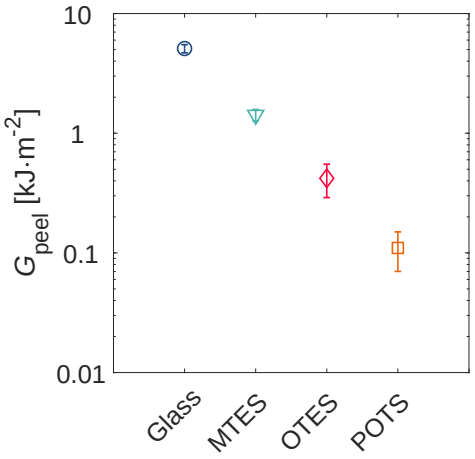

(a) Pelage : adhérence de l'EVA pour 4 chimies de surface différentes.

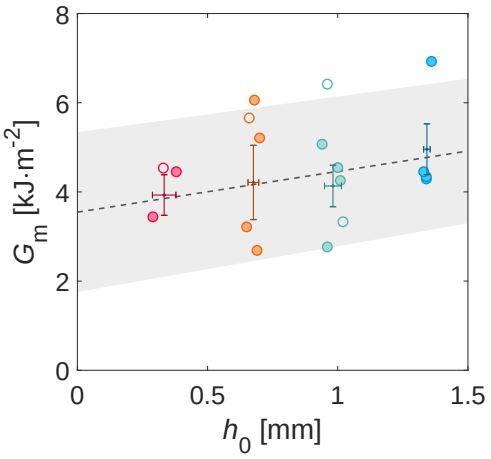

(b) Travail macroscopique de délamination G_m dans un feuilleté EVA, à 20°C

Figure 6 Délamination de l'EVA : (a) contrôle de l'adhésion par la chimie de surface, (b) énergie de délamination dans le *TCTT*.

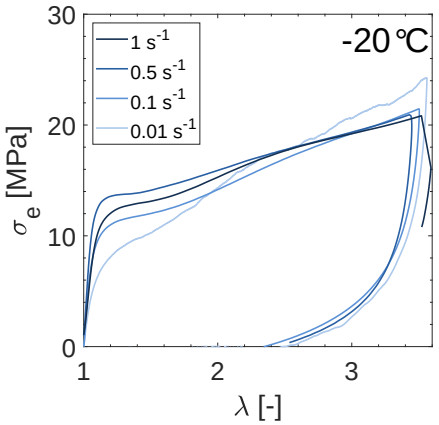

(a) Relation contrainte–déformation en traction uniaxiale à -20°C

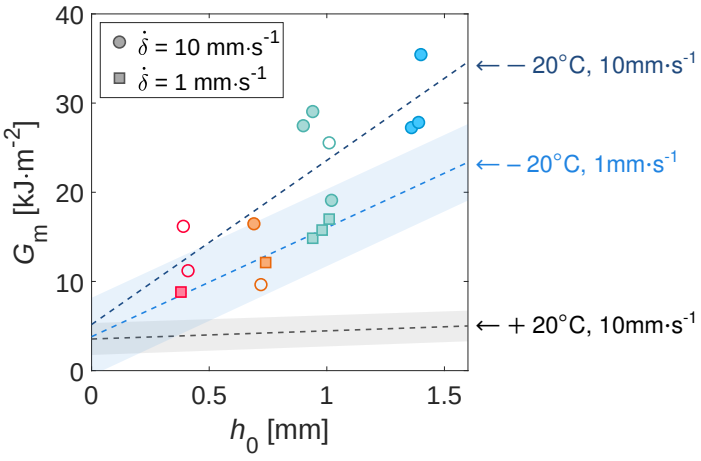

(b) Travail macroscopique de délamination G_m dans un verre feuilleté EVA à -20°C : dissipation volumique et effet de vitesse.

Figure 7 Intercalaire EVA à sa T_g : (a) comportement mécanique dissipatif et (b) *TCTT*.

pérature de transition vitreuse du matériau. Ce résultat expérimental suggère donc que la viscoélasticité, proche de la T_g, est un mécanisme indispensable pour dissiper l'énergie dans un verre feuilleté.

Simulation numérique d'une propagation de fissure en régime stationnaire

Dans le chapitre VI, nous présentons une méthode de simulation numérique par éléments finis (*FEM*) pour le problème de propagation d'une fissure adhésive. L'originalité de la méthode réside dans l'utilisation d'une approche dite "régime stationnaire", qui permet de transformer l'histoire temporelle du matériau en gradient spatial, comme illustré sur la figure 8. De fait, les contributions dépendant du temps sont obtenues en intégrant le long des lignes de courant.

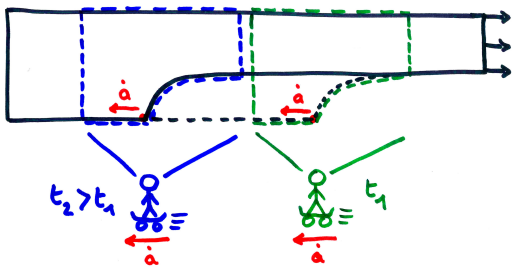

Figure 8 Principe de l'approche en régime stationnaire : l'observateur suit l'avancée du front de fissure à la vitesse $\dot{a}$.

Schéma numérique

Nous avons développé cette méthode avec un logiciel FEM commercial, ABAQUS[6], couplé à un logiciel de calcul numérique (MATLAB). En résumé, la résolution suit le schéma suivant :

- Le code FEM résout le problème élastique de propagation de fissure : on obtient une solution d'équilibre respectant les conditions aux limites imposées.
- Le calcul numérique évalue une contribution inélastique à la déformation, dans le champ de contraintes déterminé par le code FEM. Dans le cas de la plasticité en petite déformations, la déformation plastique s'ajoute simplement à la déformation élastique.
- Cette déformation résiduelle est injectée dans le code FEM comme état initial, et un nouvel état d'équilibre est calculé.

Ce schéma numérique a été développé dans un cadre de petites déformations, et validé sur des exemples de la littérature, dans le cas d'un matériau viscoplastique. On utilise une décomposition additive du taux de déformation, en deux composantes élastique et plastique. La plasticité est donnée par la théorie J_2 pour la plasticité, avec l'équation constitutive de *Landis et al.*[3] pour la loi d'écoulement :

$$\dot{\varepsilon}^p_{ij} = \dot{\overline{\varepsilon}}^{\mathrm{p}} \frac{3}{2} \frac{\sigma'_{ij}}{\overline{\sigma}} \qquad \text{avec} \qquad \frac{\dot{\overline{\varepsilon}}^{\mathrm{p}}}{\dot{\varepsilon}_0} + 1 = \left(\frac{\overline{\sigma}}{\sigma_Y} \right)^m$$

Validation sur une fissure en mode I

Le schéma numérique a été validé sur les cas traités par *Landis et al.*[3]. Après optimisation, le code par éléments finis a une vitesse en $\mathcal{O}(N)$ où N est le nombre d'éléments dans le modèle FEM, typiquement de l'ordre de 10^3 à 10^4. L'étape limitante est la réinjection de contraintes résiduelles dans ABAQUS.

Les résultats numériques en Mode I, présentés figure 9a, montrent l'évolution de l'énergie de fracture en régime stationnaire, G_{ss}, normalisée par l'énergie cohésive G_0, en fonction du rapport entre contrainte cohésive $\hat{\sigma}$ et contrainte seuil de plasticité σ_Y. On constate que G_{ss} augmente fortement quand la contrainte cohésive augmente, ou que le seuil de plasticité diminue. Cette augmentation est d'autant plus précoce que la vitesse de propagation du front est lente, ce qui signifie que le matériau dispose d'assez de temps pour se déformer plastiquement.

Application au mode II : *TCTT*

Dans le cas du *TCTT*, le ligament est initialement sollicité en mode II. Sur la figure 9b, nous constatons que l'augmentation de G_{ss} est plus violente et précoce, dans le sens où elle se manifeste pour des valeur plus faibles de $\hat{\sigma}/\sigma_Y$ qu'en mode I. Si l'effet de mixité modale a été étudié par *Tvergaard*[7] dans un matériau plastique, nous ajoutons ici l'effet de dépendance à la vitesse.

Grâce à la visualisation des champs de déformation, cette augmentation extrêmement rapide a été attribuée au passage d'un cas de plasticité confinée (ou *small-scale yielding*) à une plasticité développée sur toute la longueur de l'intercalaire.

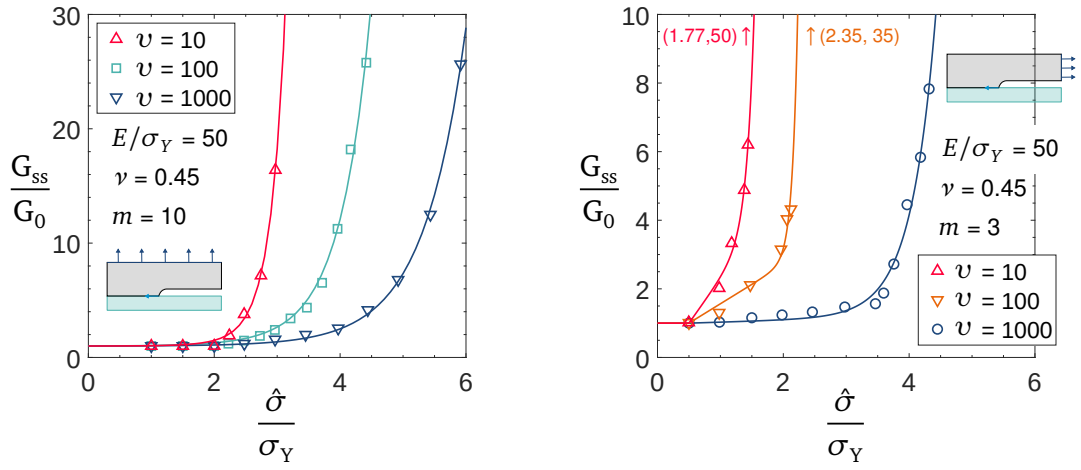

(a) Mode I **(b)** Mode II (*TCTT* en petites déformations).

Figure 9 Énergie de fracture en régime stationnaire *vs.* contrainte cohésive, dans un matériau visco-plastique : effet de la vitesse de propagation υ.

Conclusions

Dans le chapitre VII, nous résumons les résultats principaux présentés dans ce manuscrit, accompagnés de quelques pistes de réflexion pour la suite.

- La modification de chimie de surface, présentée au chapitre III, a montré que l'adhésion entre PVB et verre affecte surtout les mécanismes de dissipation à l'interface. Du fait de la compétition entre élongation totale et taux de déformation, la dissipation dans le volume de PVB varie peu avec l'adhésion.
- Avec un intercalaire élasto-plastique tel que l'EVA à température ambiante, nous avons montré dans le chapitre V que les effets de vitesse et d'épaisseur sur l'énergie macroscopique de délamination disparaissent. La plasticité au niveau du front de fissure est alors le seul mécanisme de dissipation d'énergie. En revanche, si l'EVA est sollicité à une température basse, proche de sa transition vitreuse, l'exaltation de l'énergie dissipée par la viscoélasticité est retrouvée et domine l'effet de la plasticité.

Les simulations numériques en régime stationnaire du chapitre VI, développées sur le code éléments finis ABAQUS, ont été validées sur des cas de la littérature et appliquées au cas du *TCTT* en petites déformations. Cette méthode numérique ne demande qu'à être développée plus avant, par l'ajout de lois de comportements visco-élastiques, et surtout le passage aux grandes déformations.

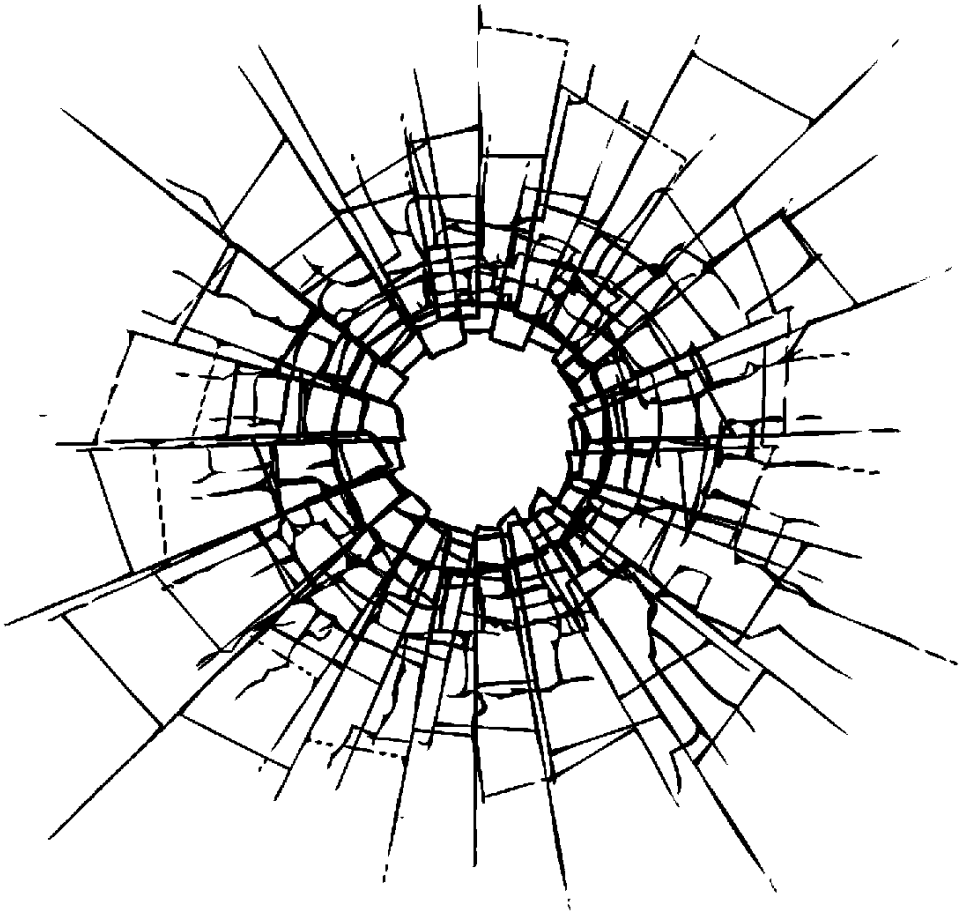

Contents

Résumé en français vii

Introduction 1

I Laminated glass under impact 5

I.1 Introduction to laminated glass: an industrial product for safety applications . . . 6

I.2 Laminated glass under impact: from standard tests to lab-scale experiments . . . 7

I.2.1 Impact tests . . . 7

I.2.2 Proceedings of a dynamic impact on laminated glass . . . 9

I.2.3 Interlayer's key role for energy dissipation . . . 11

I.3 State of the art on glass breakage: from quasi-static flexion to blast loading . . . 13

I.4 Post-breakage behavior: investigating adhesion, stretching and delamination of the interlayer . . . 15

I.4.1 Debonding characterization: the peel test . . . 15

I.4.2 State-of-the art of the TCTT . . . 17

I.5 Fracture mechanics concepts . . . 22

I.5.1 Fracture energy: the basics . . . 22

I.5.2 Modeling crack propagation with a cohesive zone model . . . 22

I.5.3 Cracks in viscoelastic media . . . 23

I.5.4 Cracks in plastic media . . . 25

I.5.5 Mode mixity: the influence of loading conditions . . . 27

I.6 Our Holy Grail: understanding the coupling between energy dissipation at the interface and in the volume of the interlayer . . . 28

II Experimental methods 31

II.1 Polymers used as interlayers in laminated glass 32
II.1.1 Poly(vinyl butyral) 32
II.1.2 Poly(ethylene - vinyl acetate) 34
II.2 Surface modification with silane chemistry 35
II.2.1 Surface characterization: contact angle measurement with a sessile drop 38
II.3 Thermal and structural analyses: DSC and X-ray diffusion 38
II.3.1 Differential Scanning Calorimetry 38
II.3.2 Wide and Small Angle X-ray Scattering 39
II.4 Mechanical testing 41
II.4.1 Small strain mechanical analysis 41
II.4.2 Large strain tensile testing 42
II.5 Adhesion characterization 43
II.5.1 The peel test 43
II.5.2 The Through Crack Tensile Test 44

III Adhesion modification with PVB 51

III.1 Surface treatment protocol with silane mixes 52
III.2 Control of PVB/glass adhesion by the TEOS content 53
III.3 Through Crack Tensile Tests with adhesion-modified laminates 56
III.3.1 The steady-state regime and its limits 56
III.3.2 Lateral crack initiation at high adhesion for thin interlayers 57
III.3.3 Loss of symmetry at low adhesion for thick interlayers 59
III.3.4 Higher work of fracture at higher adhesion: a stretch effect 62
III.3.5 Adhesion modification affects mostly the interface dissipation 64
III.4 Comparison with previous experiments: effect of the relative humidity 65
III.5 A hand-waving model for the coupling between adhesion and macroscopic work of fracture 68

IV EVA: elasto-plastic interlayer 71

IV.1 Thermal transitions of EVA: crosslinking, crystallization, glass transition 72
IV.1.1 Thermal treatment during lamination 72
IV.1.2 Effect of temperature on the structure 72
IV.2 Structural characterization: semi-crystalline nature 73
IV.2.1 Crystalline content and crystallite size from DSC 73
IV.2.2 Characterization of the crystallinity by X-ray diffraction 75
IV.3 Crosslinking upon thermal treatment 76
IV.3.1 Characterization of the curing kinetics: cure law 77
IV.3.2 Kinetics model 78

IV.4 Mechanical behavior of cured EVA: elasto-plasticity 80
IV.4.1 Small strain behavior of EVA 80
IV.4.2 Large strain behavior of EVA 82

V Delamination in EVA laminates 89

V.1 Adhesion between EVA and glass: surface chemistry strikes back 90
V.1.1 EVA on bare glass: immediate rupture in the TCTT 90
V.1.2 Modification of the adhesion between EVA and glass: return of the silanes 92
V.1.3 Surface chemistry and TCTT—from rupture to unstable regimes, and recovery of stable delamination 93
V.2 Adhesion rupture in the TCTT with EVA at ambient temperature 95
V.2.1 (No?) effect of interlayer thickness 96
V.2.2 (No?) effect of velocity 99
V.3 Recovery of high fracture energy at the glass transition of EVA 100
V.3.1 Thickness effect at the glass transition: high dissipation in the bulk . . 100
V.3.2 A strong rate effect at the glass transition 102
V.3.3 Plastic at the crack tip, viscoelastic in the bulk? 105

VI Numerical modeling: steady-state crack 107

VI.1 Modeling the TCTT: dissipative interlayer and cohesive zone model? . 109
VI.2 Constitutive behaviors in small deformations 111
VI.2.1 Plasticity in the linear regime: additive decomposition of the strain . . 111
VI.2.2 Non-linear viscoelasticity in small strains: creep formulation 114
VI.3 Steady-state scheme 115
VI.3.1 Principle of the method: “integrate along streamlines” 115
VI.3.2 Technical implementation: post-processing of elastic solutions 117
VI.3.3 Energy release rate and total work of fracture 119
VI.4 Validation of the model: plane-strain opening crack in a rate-dependent plastic material 121
VI.4.1 Material properties and plastic zone size 121
VI.4.2 Stress-based crack propagation criterion 122
VI.4.3 Effects of plasticity and loading rate 123
VI.5 Application to steady-state TCTT, with rate-dependent plasticity 126
VI.5.1 Mixed-mode propagation criterion 126
VI.5.2 Steady-state fracture energy with a viscoplastic material 126
VI.5.3 From small-scale yielding to a fully-plastifying interlayer 127
VI.6 Conclusions and perspectives 129

VI.6.1 Successful implementation of a steady-state crack with a commercial FEA code . . . 129
VI.6.2 Perspectives and improvements . . . 132

VII Conclusion(s) & perspectives 135

VII.1 Adjusting adhesion for optimal energy dissipation . . . 136
VII.1.1 Surface chemistry: a toolbox for a quantitative approach to adhesion modification . . . 136
VII.1.2 Interlayer strength as the limit to delamination . . . 137
VII.2 A large dissipating volume is needed for optimal performance . . . 139
VII.2.1 Elasto-plastic interlayer above the glass transition: localized dissipation? 139
VII.2.2 Dissipation dominated by viscoelasticity at the glass transition . . . 140
VII.3 Numerical modeling of a steady-state crack . . . 141
VII.3.1 Steady-state modeling, long story short . . . 141
VII.3.2 Lower limit in the TCTT phase diagram: bridging viscoelasticity and plasticity . . . 142
VII.3.3 Perspectives: finite deformations and rate-dependent materials . . . 143

Appendices 145

A Implementation with Abaqus 147

A.1 Using residual stresses to input additional deformation . . . 147
A.2 Data post-processing . . . 148
A.3 Definition of the model: geometry and boundary conditions . . . 149
A.3.1 Mesh . . . 149
A.4 Numerical integration . . . 149
A.4.1 Quadrature scheme in matrix form . . . 151
A.4.2 1D integration . . . 151
A.4.3 Special case of line integration: steady-state . . . 152
A.4.4 Integration of non-linear viscoelastic behavior . . . 153
A.5 Fracture energy computation . . . 153
A.5.1 Elastic energy release . . . 154
A.5.2 Plastic contribution . . . 154
A.5.3 Steady-state work of fracture for the elasto-plastic model . . . 155
A.6 Summary of the steady-state numerical scheme . . . 155
A.6.1 Determination of the additional strain and stress fields . . . 155
A.6.2 Slowing down convergence . . . 155
A.6.3 Global convergence iterations for delamination . . . 156

A.7 Perspective: towards complete “integration” in ABAQUS 158

B Perspectives on numerical modeling: finite deformations 161

B.1 Multiplicative decomposition of the deformation gradient 162

B.1.1 The deformation gradient 162

B.1.2 Decomposition into elastic and inelastic deformation gradients 162

B.2 Constitutive equation for plastic flow 163

B.3 Mapping back to the initial configuration 164

Bibliography 167

Introduction

The present work focuses on the debonding of a polymer material from a glass substrate, upon large deformation of the polymer. Practically, this broad subject is related to the impact resistance of laminated glass, an industrial product made of a polymer foil—the interlayer—sandwiched between two glass plies, as depicted in figure 10.

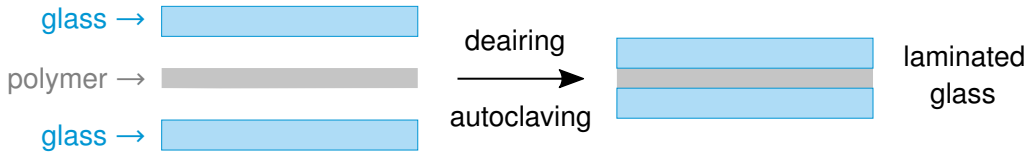

Figure 10 How laminated glass is made

The interlayer has two roles: it should increase the resistance of the glazing to perforating impacts, and it also should retain the glass splinters in case of glass breakage.

Laminated glass has a centennial history of development and improvement in the glass-manufacturing industry, since the invention by the French chemist *Edouard Benedictus* in 1903 and the first patent in 1909. Still, the mechanisms which couple the behavior of the polymer, the properties of the interface and the amount of energy dissipated by the system are yet to be fully understood—despite the incremental enhancements of laminated products over the years.

From the industrial point of view, unveiling the fundamental mechanisms for impact performance would allow better product quality assessment, and also help to create and develop new products. At the dawn of changing climate and increased stress on resources, the design of more sustainable building products seems necessary. Innovation goes along with the basic understanding of the physical or chemical processes involved: if we grasp and characterize what phenomena drive impact resistance, then the transition to safer, lighter, and greener products should be facilitated.

Interfacial crack propagation is the fundamental problem here. Indeed, as reviewed in chapter I, impact performance has been shown for the past thirty years to be somehow strongly linked to the debonding of the interlayer from the interface, and to the concomitant stretching of the interlayer membrane up to large deformations, as schematized in figure 11. Obviously, crack propagation and material properties are strongly coupled: polymer physical-chemistry and rheology are consequently needed to characterize how stress, deformation, de-adhesion and energy dissipation are related.

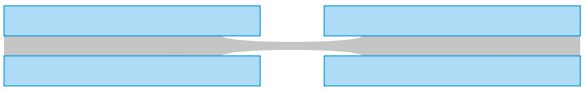

Figure 11 How the interlayer is stretched and debonded from the glass under impact

The experimental transposition of this "debonding and stetching" situation is the Through Crack Tensile Test, or TCTT. The geometry of the test corresponds exactly to the schematic in figure 11. At first, the glass plies of a laminated-glass specimen are pre-cracked in their middles, so that we obtain two laminated pieces bridged only by the polymer ligament. Then, a tensile traction is applied on the glass plies: the polymer ligament deforms and—if adhesion allows it—delaminates from the glass. Relying on the experimental tool of the TCTT, the present work addresses two problems:

- What is the effect of a controlled modification of the interface on interlayer delamination and stretching?
- What is the effect of a different mechanical behavior of the polymer on interlayer delamination and stretching?

On the "interface" side, we propose an original method to finely tune the adhesion between glass and interlayer in chapter III. In this endeavor, we choose plasticized poly(vinyl butyral)—PVB—as interlayer material. PVB is the standard interlayer in the industry and has concentrated most of the research work in the laminated-glass area. PVB is tailored to exhibit a glass transition close to ambient temperature: thus, it presents a highly viscoelastic mechanical behavior. The surface of the glass is modified with sol-gel chemistry using two silane species. Despite a non-standard deposition

method and coatings thicker than a perfect molecular layer, we demonstrate that adhesion of PVB can be tuned *via* surface chemistry. Adhesion is related to the exposure of hydroxyl groups at the surface. Afterwards, we present results of TCTT with PVB laminates with three levels of adhesion. We demonstrate that the total work of fracture increases along with adhesion, and that this increase arises from a stretch effect.

On the "polymer" side, we decided to change completely the nature of the interlayer, switching from PVB to poly(ethylene – vinyl acetate), or EVA. This polymer has received less attention for impact resistance due to poorer performance in standard tests. However, as we will demonstrate in chapter IV, EVA is stretchy and also dissipative at ambient temperature—due to a plastic behavior originating in the crystalline content. Thus, EVA will provide an interesting contrast with the behavior of PVB, and help understand the mechanisms at stake in the delamination process in chapter V. In the first place, we investigated whether delamination between the EVA interlayer and glass could be obtained. We show that, contrary to the industrially-optimized PVB system, the interactions between EVA and glass should be tuned to obtain a delamination regime. Then, our TCTT results show that the work of fracture does not change much with loading rate and interlayer thickness with this plastic interlayer. We attribute this feature to a localized dissipation occurring only in the vicinity of the crack fronts. Furthermore, we prove that bulk dissipation is recovered close to the glass transition of the polymer, when viscoelastic processes predominate.

Last but not least, to try and make a connection between interfaces, polymer rheology and delamination properties in laminated glass, we present a numerical simulation of the crack propagation problem with a steady-state approach in chapter VI. Since the steady-state crack scheme is not implemented in commercial finite-element codes, we propose a strategy coupling FEA and numerical computing softwares. Decomposition of the deformation into elastic and inelastic parts is the funding principle of the numerical scheme. The FEA code provides elastic solutions, while the time-dependent inelastic mechanical behavior is computed in post-processing. The corresponding inelastic contribution is re-injected in the FEA code as the initial state. We discuss some preliminary results for an opening crack and for the TCTT problem, with a viscoplastic constitutive law.

This manuscript winds up with a general conclusion and some thoughts for further studies.

I

Laminated glass under impact: from ball drop tests to fracture mechanics

After a brief introduction to laminated glass in section I.1, we review the experimental methods for impact-resistance testing in section I.2, from standard tests to lab-scale setups.

Then, we enter in the details of the literature on laminated glass under impact. First, the problem of glass breakage is addressed in section I.3. However, even if glass breakage matters for impact resistance, we will see that the role of the interlayer is critical for energy dissipation and that most of the energy dissipation occurs in the post-breakage behavior. That is why we present in section I.4 the methods to characterize debonding and stetching of the interlayer between glass fragments, the peel test and the Through Crack Tensile Test.

Finally, some notions of fracture mechanics are developed in section I.5. In particular, we insist on the enhancement of the fracture energy by dissipation mechanisms in the materials, which will be the underlying principle all along this work. We discuss the crack propagation problem in viscoelastic and plastic media, and also the influence of mode-mixity on the fracture resistance of materials.

I.1 Introduction to laminated glass: an industrial product for safety applications

Safety is a major—if not the most important—issue in every industrial application. Brittleness of glass limits its use in structural applications: nobody would want a transparent flooring or a windshield to break into pieces like a basic annealed soda-lime glass window would do, as depicted in figure I.1. The aftermath of glass breakage is the main issue: glass shards are extremely sharp and can potentially induce severe wounds. In order to answer the market demand for elegant, transparent but also safe materials, glass needs to be strengthened and toughened.

Glass strength can be improved with tempering, by thermal or chemical methods. Tempering results in compressive stresses at the surface of the glass which prevent the propagation of small cracks. Tempered glass is easily recognizable: it breaks into thousands of tiny pieces (figure I.1). Tempered glass is used for lateral windows in cars, glazings for bus stops, and screens for smartphones.

Toughness and resistance to impacts is enhanced with laminated glass. Lamination consists in inserting a polymer interlayer between two glass plies. The interlayer has two roles: holding the shards together when the glass breaks, and dissipating the kinetic energy of the impactor. Laminated glass is easily recognizable: the window breaks in a radial pattern but retains its structural integrity (*cf* figure I.1). Windshields, glass floorings and balustrades, building facades and store windows are made of laminated glass.

Another advantage of laminated glass resides in the post-breakage behavior. With the interlayer, the structure of the glazing is preserved even if the glass plies are cracked. It prevents foreign objects from going through the glazing, such as debris carried by strong winds.

Chemical composition of the polymer was originally celluloid or derivatives[8]. Since the second half of the 20th century, plasticized poly(vinyl butyral)—PVB—has been used in most laminated products. A more detailed description of the interlayers will be provided later in II.1.

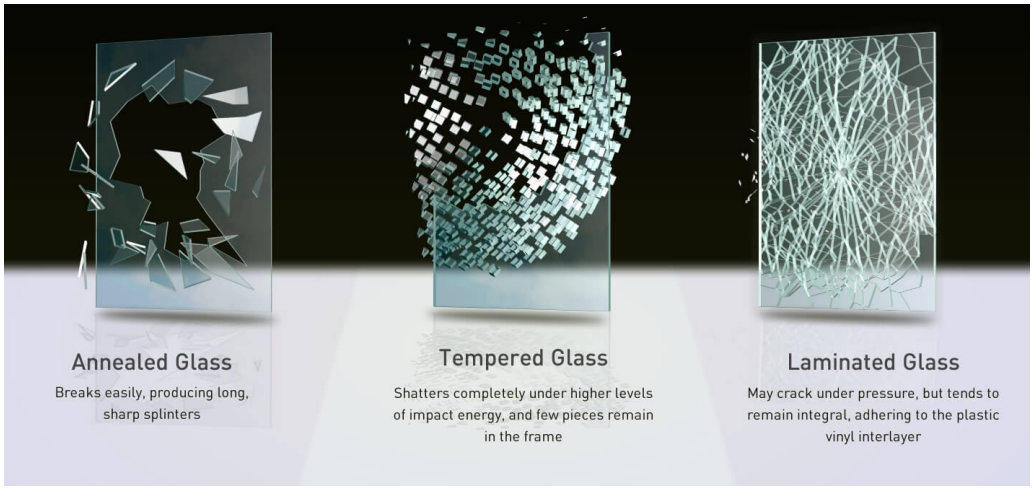

Figure I.1 Illustration of the differences between standard (annealed) glass, toughened glass and laminated glass upon breakage.
Source: "Laminated Glass: Assured Protection", *Pioneer Glass* (online).

Manufacturing process

Laminates are assembled in the controlled environment of a cleanroom. After piling up one glass ply, the polymer interlayer and another glass ply, air is removed by the use of a calender ("nip-rolling" process) or a vacuum bag. The de-airing step is crucial to avoid the formation of bubbles at the interfaces. Later, the laminate is heated under pressure in an autoclave. During the thermal treatment, the polymer flows and achieves initimate contact with the glass surface: in other words, the interlayer is adhered to the glass. The laminate is then cut to the adequate dimensions, and ready for use.

I.2 Laminated glass under impact: from standard tests to lab-scale experiments

I.2.1 Impact tests

Resistance of laminated glass to impacts is assessed and classified by several norms that depend on the application.

Ball drop test

The ball drop test is defined by the European standard EN356 for buildings applications and ECE R43 for automotive applications. This test consists in letting a steel ball fall on a glazing, and merely assess if the ball has gone through the glazing completely.

In EN356, the steel ball (radius 10 cm, weight 4 kg) impacts a 1 m^2 specimen 3 times in a row, in a 20-cm wide triangle approximately located at the center of the panel. The temperature of the specimen should be around 23°C. The drop height is 1.5 m for the minimum safety level P1A, and increases up to 9 m—and 9 repeated impacts—for the highest level P5A. The laminate passes the test if the steel ball never goes through the panel entirely. In building applications like EN356, impacts are in the dynamic range with strain rates between 10 and 100 s^{-1} [4].

For the automotive version ECE R43, the principle is the same with a smaller and lighter impactor, smaller glass specimens ($30 \times 30\,cm^2$), and various temperatures.

Pendulum test

The pendulum test is defined by the European standard EN12600 and mimics the impact of a human body—affectionately known as the "stepmother test" for the cognoscenti. The test temperature is also 23°C. The pendulum is actually a 50 kg weight, decorated with two rubber tires. This impactor is then pulled up to a certain angle, or equivalent drop height, and then released to let it impact the glass specimen. The glazing has to resist one single impact from this heavy mass to be certified.

More original impactors: axe, pummel, birds and bullets

More original testing methods are used to assess impact performance. For instance, EN356 also defines the "axe" test, designed to determine the resistance to manual attack. The level of protection is defined according to the number of axe strikes required to hack out an opening in the glazing—typically between 30 and 90.

The "pummel" test is similar and evaluates adherence between glass and interlayer. In this peculiar adhesion test, the laminate is pummeled with a hammer and the mass of glass lost in the process defines a grade: the lower the amount of glass detached, the higher the pummel grade.

Transport applications are worth mentioning for the wide variety of impactors encountered in impact tests, among which birds—of different sizes, shapes and weights—

for plane windshields or stone gravels for windshields of road vehicles. Nonetheless, such complex impactors are irrelevant for the present work—we only evoke them for the curious reader.

Finally, a noteworthy field of application is ballistic protection. For instance, STANAG 4569 defines four types of bullets, depending on their velocity and hardness. Ballistic glass is then evaluated by shooting a few bullets and assess whether the projectile went through, and also whether glass splinters were projected. However, ballistic impacts are out of the scope of this work, as perforation by a bullet is a peculiar phenomenon that involves pulverization of the glass and heating effects.

I.2.2 Proceedings of a dynamic impact on laminated glass

In all these impacts tests, in particular for building applications, we notice a similar course of events. Indeed, we observe that the breakage of a laminated glass piece can be decomposed into 4 critical stages (figure I.2):

1. "Bending" step: the impactor reaches the glass panel, which first bends. For dynamic impacts, elastic waves propagate within the laminate and participate to the shattering of glass plies. The bending properties are the focus for structural applications, for which the deflection under constant or quasi-static loading should be as small as possible.

2. "Shattering" step: the glass plies break into several pieces maintained together by interlayer ligaments. As developed in section I.3, the crack pattern depends on the glass properties, on the thickness of the interlayer and on the velocity of the impactor.

3. "Stretching" step: once the glass plies are broken into pieces, the interlayer undergoes a membrane deformation due to the remaining kinetic energy of the impactor. This step actually concentrates most of the energy dissipation, as explained in section I.4.

4. "Tearing" step: in the case of high energy impacts, the interlayer is torn by the impactor and/or the glass shards. As a result, the impactor perforates the interlayer and goes through the laminate. Sharp glass shatters induce cracks within the interlayer, which results in the tearing of the polymer membrane. This last perforation

stage is the focus of the standard tests such as EN356 and EN12600, and a major point of concern for the manufacturing industry.

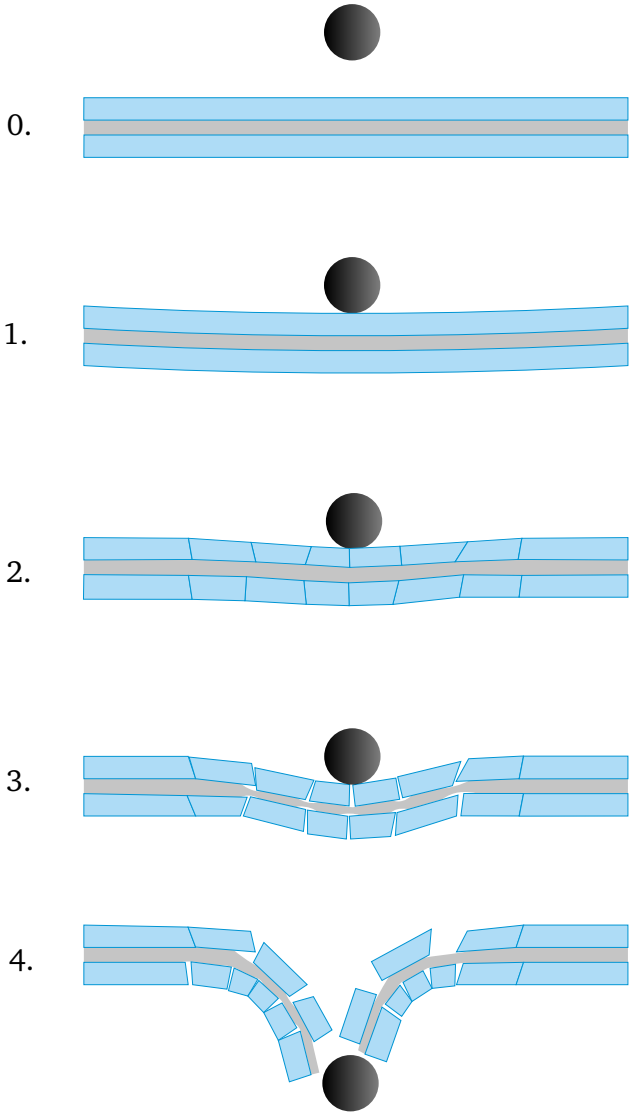

Figure I.2 Schematic of laminated glass during impact:
1. bending, 2. shattering, 3. stretching, 4. tearing and perforation.

From the industrial point of view, performance upon impact has usually been assessed considering only the outcome of the last "tearing" step. Nevertheless, perforation of the laminate critically depends on the previous stages of the impact. Indeed, the "shattering" process dictates how many glass fragments are formed, conversely generating a given number of interfaces for adhesive rupture. Then, the "stretching" stage is crucial for energy dissipation:

I.2.3 Interlayer's key role for energy dissipation

Energy dissipation occurs in the interlayer

A noteworthy experimental setup is the "cannon" setup, developed at *Saint-Gobain Research Compiègne* in the early 2000s by *Nourry*[9,10] and then *Decourcelle*[11]. Inspired from the split Hopkinson bar dynamic test, this setup is meant to mimic the ball drop test on $30\times30\,\mathrm{cm}^2$ specimens. The position of the impactor head was measured in real time, allowing access to the velocity and therefore to the evolution of the kinetic energy over time (figure I.3).

The characteristic value obtained with this setup was the critical energy for perforation, defined as the initial kinetic energy of the impactor required for complete perforation. As shown by figure I.3, 100% of the initial kinetic energy is dissipated in the case of a non-perforating impact.

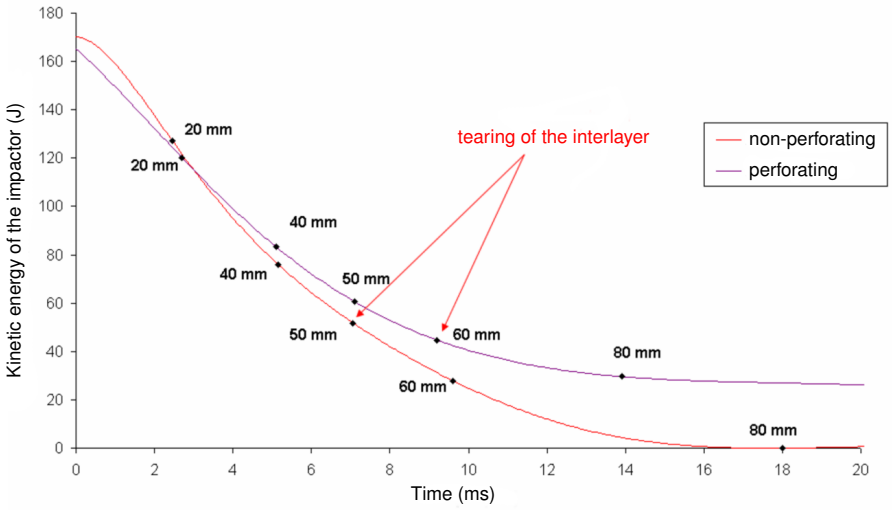

Figure I.3 Impactor kinetic energy decrease over time during a ball-drop-like impact, from *Nourry*'s PhD thesis[9]. The initial impactor energy is close to the critical energy for perforation. Lengths in mm correspond to the arrest distance of the impactor in the incremental procedure.

Using an incremental procedure, energy dissipation could be decomposed into the contributions of glass breakage and polymer stretching. One of the major conclusion of *Nourry*'s work is that the breakage of the glass is negligible compared to the energy spent to delaminate and stretch the interlayer bridges between glass shards. Once the glass plies are broken, the interlayer dissipates 70% to 90% of the impactor kinetic energy.

Impact performance depends on the interlayer

The key role of the interlayer appears even more clearly in the experimental results of *Novotny & Poot*[12] (figure I.4). They investigated the effect of temperature on impact performance for 5 different interlayers with the mean break height (MBH) strategy, a quantitative variation around the "ball drop" test. The MBH procedure consists in dropping a 2-kg steel ball on 30 cm×30 cm glass panes from a variable height. The drop height is increased when the laminate retains the steel ball ("OK" case), and decreased when the impactor perforates through the glass ("NOK" case). After a few trials, the test sequence oscillated between "OK" and "NOK" cases around the so-called mean break heigh. In figure I.4, the MBH value varied from 1 m at the lowest impact resistance up to 8 m at the optimum of performance. These results quantify

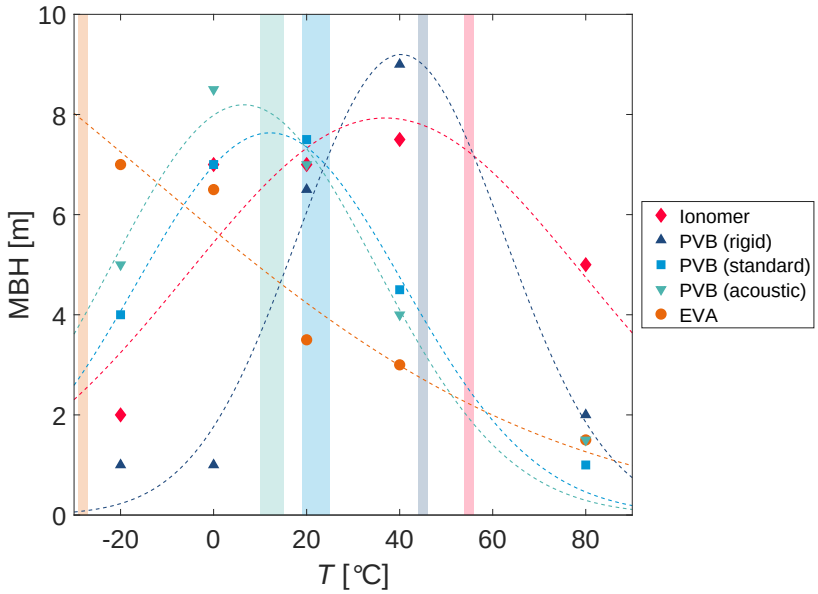

Figure I.4 Mean Break Height of laminates made of different interlayers, measured at temperatures from -20°C to 80°C. Dashed lines are gaussian fits made to highlight the optimum of performance. Shaded bars indicate the glass transition temperature of each polymer. Data from *Novotny & Poot (2016)*[12]

the strong dependance of impact performance upon the nature of the polymer. In fact, a performance optimum was observed for a temperature correlated to the glass transition temperature T_g, indicated as a range by colored bars in figure I.4.

For instance, the EVA—poly(ethylene – vinyl acetate)—interlayer shows poor impact resistance around 20°C—the usual temperature for standard tests in building

applications—but outperforms all other interlayers at -20°C. Such significant difference upon temperature will guide our choice of a different interlayer later in this work: EVA appears as a good candidate for a complete change is mechanical response compared to standard PVB.

I.3 State of the art on glass breakage: from quasi-static flexion to blast loading

Getting into more details of the four stages of laminated-glass breakage (*cf* section I.2.2), we will now describe the state-of-the art on glass fracture in section I.3, and then focus on the "stretching" problem in section I.4. In this section, we present significant results from the literature, from the late 1990s to contemporary publications, about laminated glass fracture—what we called "shattering" step. We rely on the recent review by *Vedrtnam & Pawar*[13] on plate theories and numerical simulations developed for both quasi-static and impact testing of laminated glass.

Number of cracks?

The shape of radial cracks was rationalized by *Vandenberghe et al.*[14,15], providing a scaling law for the number of cracks which depends on elastic modulus E, thickness h, density (*via* the speed of sound waves c) and fracture energy Γ of the material, and the impact velocity V:

$$n \sim \left(\frac{E\,h}{\Gamma}\right)^{1/3} \left(\frac{V}{c}\right)^{1/2}$$

High-rate laminated glass fracture was investigated by *Chen et al.*, with experiments[16] and numerical simulations[17,18]: they showed that the number of radial and ortho-radial cracks increased at higher impact rates—as derived by *Vandenberghe* for glass alone—and also when the thickness of the PVB interlayer decreased.

Locus of failure?

Strength of laminated glass was assessed experimentally by *Bennison et al.*[19], with a three-point flexion test. They focused on the influence of the impactor velocity on the failure of the glass plies, using time-temperature superposition to access fast and slow regimes. When the loading rate increased, they predicted a transition from monolithic

to layered response of the laminate. “Monolithic” referred to the behavior of single glass specimen with doubled thickness, “layered” to the behavior of two glass plies stacked upon each other. Such transition implied a change of the preferred locus of failure from the upper glass ply to the lower glass ply (figure I.5). Their predictions were in agreement with earlier numerical simulations of slow-rate impacts by *Flocker & Dharani*[20,21].

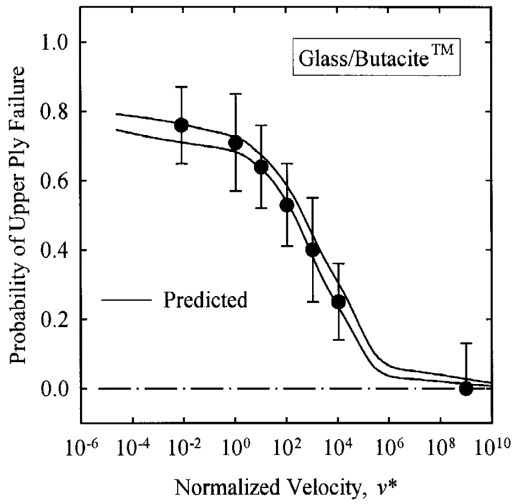

Figure I.5 Probability of upper glass ply failure vs velocity in biaxial flexure, from Bennison et al.[19]

Analytical models were derived by *Galuppi & Royer-Carfagni*, for laminated glass flexion[22,23] and post-breakage behavior[24,25].

Towards the coupling between cracking and delamination

Seshadri et al.[26] investigated laminated glass cracking upon flexion with a major difference compared to *Bennison et al.*[19]: their samples were laminated with only one glass ply, placed on the opposite side from the indenter. The key point was that the polymer interlayer could debond and stretch without no risk of tearing by glass shards.

The number of glass fragments was controlled by an intentional defect. They showed that the force acting on the ligament increased with the displacement rate, according to a power-law model, and also highlighted the role of friction in the debonding process. This work introduces the idea that stretching and de-adhesion of the polymer membrane is, in fact, the dominant process for energy dissipation.

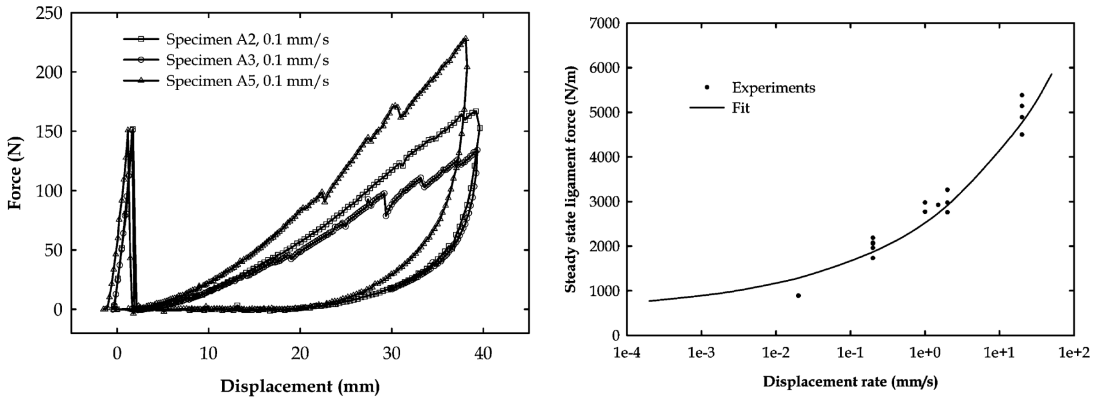

(a) Force *vs* displacement curves: the first peak corresponds to glass breakage, the following cycle to loading and unloading of the interlayer ligaments bridging the glass fragments.

(b) Force *vs* displacement rate: experimental data were fitted with a power-law model $F(v) = F_0\left[1 + \left(\frac{v}{v^*}\right)\right]$

Figure I.6 Flexural and indentation test on laminated glass, from *Seshadri et al.*[26]

I.4 Post-breakage behavior: investigating adhesion, stretching and delamination of the interlayer

After the "shattering" step, glass shards are still bound to each other by the polymer interlayer, and the impactor velocity is most likely still significant. The interlayer accommodates the remnant impactor energy through deformation between glass fragments, and also through debonding from the glass surface. In this section, we review the major literature results relevant to polymer de-adhesion and stretching.

I.4.1 Debonding characterization: the peel test

The peel test consists in debonding a thin strip of material from a surface (*cf* section II.5.1): it is widely used to characterize the adherence of a material on a substrate, such as pressure sensitive adhesives[27].

90-degree peel test

90°-peel is widely used because the evaluation of an adhesion—or strictly-speaking adherence—energy is merely the measurement of a force divided by the thickness of the peeled strip, following Kendall's elastic analysis[28]. The kinematics of the test is

also simple: the pull velocity of the adhered strip is equal to the translation velocity of the glass substrate. Simplicity of both aspects—implementation and interpretation—makes the peel test convenient for routine characterization.

In his PhD work, *Klock*[29] synthetized PVB foils with controlled composition and additives. Using the peel test, he studied the effect of the hydroxyl content and the water content on adhesion (figure I.7). In figure I.7a, the peel force increases with the hydroxyl content of the PVB interlayer. On the contrary, in figure I.7b, the peel force decreases when the water content in the PVB interlayer increases.

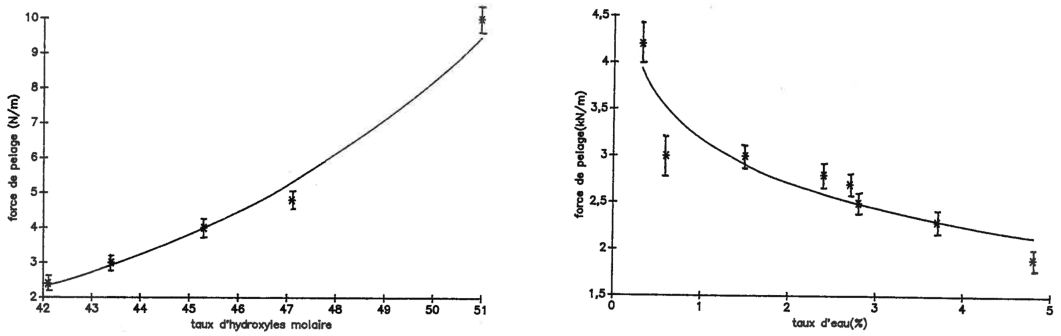

(a) Peel energy *vs.* hydroxyl content ($v = 10\ mm{\cdot}min^{-1}$, [plast.] = 26.5%)

(b) Peel energy *vs.* water content ($v = 10\ mm{\cdot}min^{-1}$, [OH] = 43.4%, [plast.] = 26.5%)

Figure I.7 Effects of the hydroxyl content [OH] and the water content on the adhesion of plasticized PVB, with a plasticizer content [plast.] = 26.5%, from *Klock*'s PhD thesis[29]

The effect of water content had already been observed by *Huntsberger*, who related adhesion to a nanometric aqueous layer at the interface between PVB and glass[30]. Surprisingly, such effect of humidity has been sparsely investigated further—at least in published literature.

Still, *Tupy et al.* investigated the effect of humidity and "adhesion modifier" additives on commercial PVB grades, however with the pummel test.

Butchart & Overend[31] explored the effect of liquid water on PVB de-adhesion, also with the peel test. Liquid water is deposited at the peel front during the test, which triggers an almost immediate decrease of more than 50% of the peel force. The decrease in adhesion was observed as long as water was available at the peel front.

The peel test is also adapted to numerical simulations, due to its simple geometry and kinematics. For instance, *Pelfrene et al.*[32] evaluated the adhesive properties of a PVB interlayer to glass with a numerical model of the 90°-peel test. PVB was

considered as viscoelastic, with a generalized Maxwell model. A zone of maximum strain rates, where viscoelastic dissipation is concentrated, was evidenced at the peel front. The cohesive stress, *i.e.* the critical stress required for interface separation (*cf* section I.5), was estimated around $5-15$ MPa.

Zero-degree peel test

The zero-degree peel of soft materials has recently received some experimental attention. Using a PDMS rubber adhered onto glass, *Ponce et al.*[33] investigated the effect of sliding at the interface: they observed a steady-state peeling front which was attributed to shear stresses.

Hui et al.[34] studied a common office tape in zero-degree peel: they show that the strain-hardening behavior of the pressure-sensitive adhesive must be considered to estimate accurately the peel force at large deformations. They highlight the link between non-linear rheology and the rise of lateral stresses and hydrostatic pressure at the peel front.

I.4.2 State-of-the art of the TCTT

Huntsberger described the stress state between glass shards as constrained biaxial extension[30], which is not straightforward to implement in an instrumented test. The stress state was simplified to uniaxial extension between two glass fragments, as pictured in figure I.8. Such tensile test between two glass pieces bridged by a polymer ligament has been reported in the literature as the Through Crack Tensile Test—the TCTT—since the late 1990s [19,26,35,36]. Since it will be our preferred tool in the following, we review here in detail the main results from the literature.

In the TCTT, the laminate specimen is pre-cracked on both glass plies. The tensile deformation is applied by pulling one of the laminate pieces with a tensile testing machine. The TCTT differs from the zero-degree peel in two aspects. On the pulling side, the interlayer is bonded to the glass on both faces whereas, in the peel test, one face of the adhesive is either free or attached to a thin backing. Moreover, the interlayer is allowed to delaminate on both sides so that four crack fronts are able to propagate, instead of one in the peel test. Practical considerations of the test are described in section II.5.

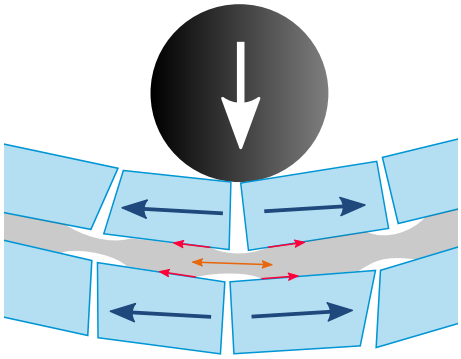

Figure I.8 Schematic of a cracked laminate in the “stretching” phase: displacement between two glass shards is approximated as a tensile deformation (← →). The interlayer ligament undergoes both stretching (↔) and delamination (→) from the interface.

The TCTT was at the center of *Paul Elzière*'s PhD[4,5]. Recent work by *Samieian et al.*[37] also considered a "random crack" version of the TCTT, in an effort to rationalize the resistance of laminated glass to blast loading.

Macroscopic work of fracture in the TCTT

In the TCTT, it is not straightforward to derive an energetic balance and compute an energy release rate, due to the highly dissipative nature of the polymer materials, which induce a coupling between debonding and deformation. However, in the case of steady-state delamination, a well-defined quantity is the total external work injected in the system, which we designate as G_{m}, the macroscopic work of fracture. As detailed in section II.5.2, the work of fracture is derived from the steady-state force F_{ss}, steady-state stretch λ_{ss}, and the width b_0 of the TCTT sample:

$$G_{\mathrm{m}} = \frac{F_{ss}}{b_0}(\lambda_{ss} - 1)$$

G_{m} represents the energy dissipated in the laminate, somehow by interlayer deformation and adhesive crack propagation. The whole point of our work is to understand how these deformation and deadhesion processes are coupled, and how they relate to the properties of the interface and the polymer interlayer.

Velocity effect: three regimes in the TCTT

Elzière has shown that steady-state delamination regime is restricted to a range of tensile velocities, range which also depends on the temperature (figure I.9).

Recent work by *Del Linz et al.* focuses on the delamination behavior at high strain rates using a high-speed hydraulic testing machine[38,39]. In their data, the stretch does not reach a steady value: it increases until rupture of the interlayer, so that we cannot define a consistent G_m value. We chose to compare the "adherence energy"—*i.e.* force at the plateau F_{ss} normalized by the sample width b_0—in order to combine their data with those of *Elzière* in figure I.9.

At low velocities, undulation of the crack fronts leads—though not systematically—to an arrest of the delamination. The stretch increases continuously, until rupture of the interlayer. The empirical "unstable limit" is indicated by the black straight line in figure I.8.

The adherence energy increases with the tensile velocity $\dot{\delta}$: naively, one could think that the higher the velocity, the better the impact performance since more energy can be dissipated. However, the interlayer also bears a higher stress, limited by the strength and toughness of the polymer: the work of fracture is limited by the rupture of the interlayer at high velocities. In the TCTT, the transition from the steady-state regime to the "rupture" regime occurred around $100\,\mathrm{mm}\cdot\mathrm{s}^{-1}$ at 20°C.

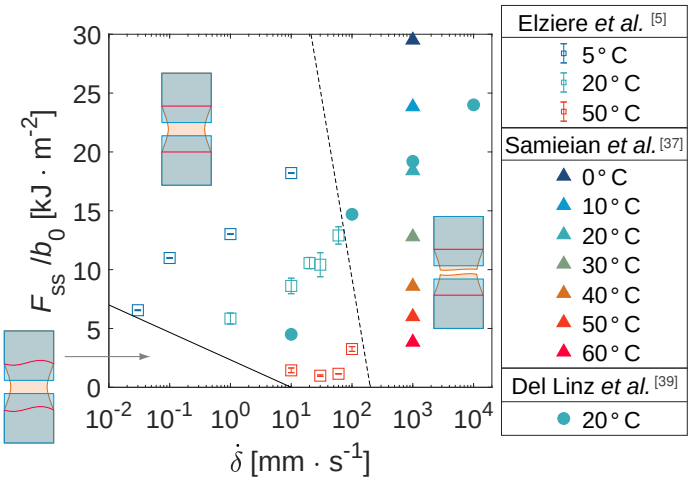

Figure I.9 Influence of traction velocity and temperature on the delamination force measured with the TCT-Test (PVB thickness = 0.76 mm) Solid line: empirical limit between unstable and steady delamination behaviors. Dashed line: empirical limit from steady behavior to rupture of the interlayer.[5,37,39]

Over the traction velocity range, from 1 to $10^4\,\mathrm{mm}\cdot\mathrm{s}^{-1}$, the adhesive force increases from 5 to $25\,\mathrm{kJ}\cdot\mathrm{m}^{-2}$. Such increase is attributed to viscoelastic dissipation by the PVB interlayer. Indeed, the fracture energy is expected to increase with $\dot{\delta}$ according to viscoelastic crack theories (*cf* section I.5.3).

Interlayer thickness effect

Elzière also demonstrated that a higher interlayer thickness h_0 increases the delamination force and conversely reduces the average stretch of the interlayer[5]. Overall, the total macroscopic work of fracture increases with h_0.

At a given temperature and loading rate, this increase of the work of fracture is affine with the thickness of the interlayer: The total work of fracture can be decomposed into a constant term (ordinate at origin) plus a contribution proportional to the thickness h_0:

$$G_\mathrm{m} = \Gamma_\mathrm{crack} + h \cdot \Pi_\mathrm{bulk} \tag{I.1}$$

This relation is reminiscent of usual fracture mechanics theories presented in section I.5. Equation (I.1) conveys the principle that the effective fracture energy is greatly enhanced by the dissipative behavior: the slope Π_bulk is related to viscoelastic dissipation in the volume of the stretched interlayer, and the ordinate at origin Γ_crack represents the energy required for de-adhesion. Of the order of a few $\mathrm{kJ}\cdot\mathrm{m}^{-2}$, the Γ_crack term itself involves dissipative processes at the crack tip.

Temperature effect

As presented in the introduction, in particular with figure I.4, impact performance strongly varies with the temperature.

Recently, *Samieian et al.*[37,40] performed systematic Through Crack Tensile Tests on PVB laminates from 0 to 60°C, at the testing rate of $1\,\mathrm{m}\cdot\mathrm{s}^{-1}$. Their data is reported on figure I.9, and confirm the increase in adhesive force at lower temperatures as the PVB interlayer stiffens.

However, we need to keep in mind that the “rupture” limit is also shifted towards lower solicitation rates when temperature decreases, which explains why the impact performance actually decreases at low temperatures in *Novotny & Poot*'s impact results(*cf* figure I.4).

Samieian et al. interpreted the effect of temperature based on the stiffness of the interlayer. A stiffer interlayer, at low temperatures, undergoes a lower deformation which affects the local peel angle at the debonding front. Their argument refers to the mode mixity at the crack tip: the energetically costly mode II contribution increases when the local peel angle decreases.

Polymer/glass adhesion

As established by *Klock*[29] (*cf* section I.4.1), adhesion between PVB and glass can be tuned by adjusting the hydroxyl content in the PVB, the amount of plasticizer, the amount of "adhesion modifiying" metallic salts, or a combination of these three factors.

The effect of the adhesion between glass and PVB in the TCTT was briefly addressed in the seminal work of Sha *et al.*[35]. Three PVB grades were formulated, without further information on their compositions. Adhesion was roughly estimated by the pummel test. In figure I.10, the TCTT force-displacement curves show that the load increases along with adhesion. However, their data is limited to a displacement length of 1 mm, and they do not reach a steady-state regime—whereas they predict steady-state by numerical simulations.

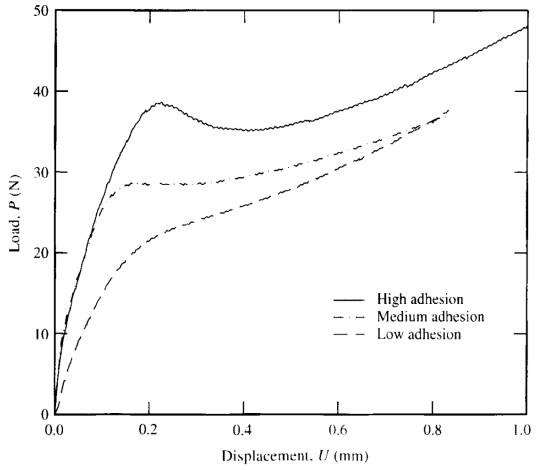

Figure I.10 TCTT force-displacement curves for high, medium and low adhesion PVB laminates at low strain rate ($\dot{\delta} = 8.5 \cdot 10^{-6} \mathrm{m} \cdot \mathrm{s}^{-1}$) [35]

To our knowledge, in spite of the critical relevance of the adhesion parameter for industrial applications, a systematic study of a changing adhesion with the TCTT has not been reported in the literature.

I.5 Fracture mechanics concepts

I.5.1 Fracture energy: the basics

In a usual fracture test, a controlled-size defect—a crack—is induced in a specimen. That specimen is then loaded mechanically, until crack propagation occurs, either in a controlled or in a catastrophic manner. The energy input is characterized by the energy release rate G, which depends on the type of loading and on the geometry of the sample.

Griffith's criterion[41] states that crack propagation occurs when the energy release rate reaches a critical value G_c equal to Γ, the fracture energy, which is a material property.

The fundamental fracture energy—or fundamental work of separation—Γ_0 is related to surface energy. In order to separate a solid into two smaller solids, a given area $2A$ is created: the energy cost of this operation is $2A\gamma$, where γ is the surface energy of the material. The value of the thermodynamic work of separation $\Gamma_0 = 2\gamma$ reaches typically $10^{-2} - 10^{-1}\,\mathrm{J\cdot m^{-2}}$.

However, in real-life materials and applications, the observed critical energy release rate G_c—hence the fracture energy Γ—is actually much larger than Γ_0. Consider an office adhesive tape on a desk: the actual energy to peel off the tape reaches around 10^2—$10^3\,\mathrm{J\cdot m^{-2}}$, at least a thousand times higher than Γ_0. In the TCTT with laminated glass, the work of fracture was measured around $10^3 - 10^4\,\mathrm{J\cdot m^{-2}}$.

The discrepancy arises when the adhesive material exhibits an inelastic dissipative behavior. In this case, Γ contains the work of separation Γ_0 and also all the energy spent into deforming the dissipative material. The details of this latter contribution depend upon the type of inelastic behavior and dissipative processes: in the fracture mechanics literature, a distinction exists between viscoelastic (section I.5.3) and plastic materials (section I.5.4).

I.5.2 Modeling crack propagation with a cohesive zone model

For modeling purposes, we need a method to prescribe the debonding behavior between two interfaces. The cohesive zone model—such as developed by *Needleman*[42,43]—appears as the preferred candidate in numerical models. In a cohesive zone model (CZM), the interface behaves elastically up to a critical point dictated by a cohesive

stress $\hat{\sigma}$. Above this threshold, the stiffness of the interface decreases until complete separation: during this process, the amount of energy dissipated is Γ_0 (*cf* figure I.13). The corresponding crack opening displacement is given by $\delta_{op} \sim \Gamma_0/\hat{\sigma}$.

The cohesive zone model is then characterized by the prescription of a traction-separation law. A simple and common example is the bilinear law in figure I.11, for which $\Gamma_0 = \hat{\sigma}\delta_{op}/2$. The shape of the damaged part varies in the literature: linear, exponential, or constant before decreasing.

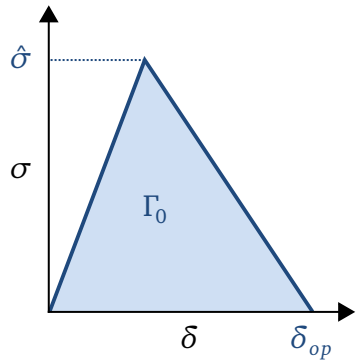

Figure I.11 Unidimensional bilinear traction-separation law for a cohesive zone model, characterized by a cohesive stress $\hat{\sigma}$ and a separation energy Γ_0.

Altogether, a crack model should relate the effective fracture energy Γ to interface characteristics—typically $\hat{\sigma}$ and Γ_0—and to material properties, which depend on the type of dissipative processes we intend to model.

I.5.3 Cracks in viscoelastic media

Viscoelasticity is a prominent characteristic of polymer systems above their glass transition. In a few words, viscoelasticity means that the mechanical response of a polymer above T_g combines an immediate reversible elastic response and a delayed response originating in irreversible viscous flow. The viscous response is dictated (in a simplistic vision) by a characteristic time τ: viscoelastic effects arise at finite strain rates, when $\dot{\varepsilon} \sim \tau^{-1}$.

Enhancement of the fracture energy by viscous dissipation has received significant attention for the applications in the rubber industry, since the seminal paper of *Rivlin & Thomas*[44] or *Gent & Petrich*[45]. A significant scientific literature emerged in the 1990s, with experimental data from *Gent et al.*[46] and the "viscoelastic trumpet"

model of *P. G. de Gennes*[47,48]. Viscoelastic crack theories were reviewed by *Bradley et al.*[49] and later *Persson et al.*[50].

The original "trumpet" model addressed the increase in adhesion energy for slow cracks, considering three zones in the material depending on the local loading rate (figure I.12). The material is considered as a soft solid, characterized by the long-time modulus, except in the vicinity of the crack tip. Close to the crack, the material goes through a "liquid region", which means the glass transition. Even close to the crack tip, a "hard region" is in the glassy state. *Saulnier et al.* enhanced the "trumpet" model to account for the decrease of the fracture energy at high rates[51], for which the material is entirely in the "hard solid" region.

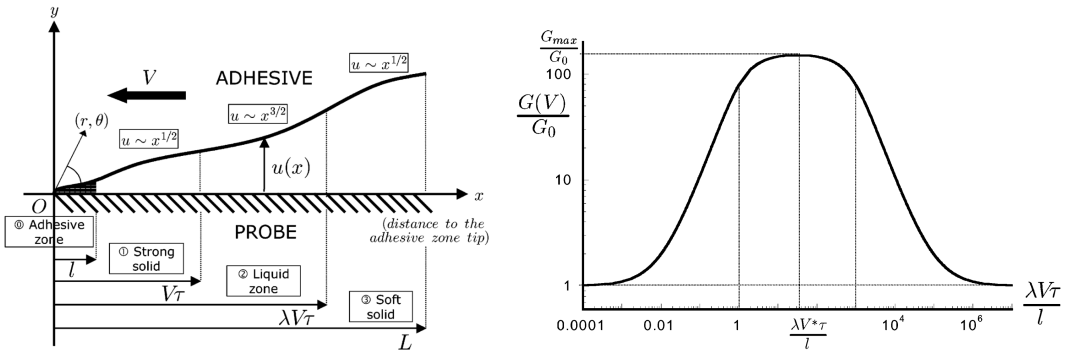

(a) Crack profile **(b)** Fracture energy *vs* crack velocity

Figure I.12 *De Genne*'s "viscoelastic trumpet" model: the maximum value of G/G_0 is given by $\lambda = \mu_0/\mu_\infty$, the ratio of instantaneous modulus over relaxed modulus. From *Saulnier et al.*[51]

Barthel & Fretigny [52] expressed the enhancement in relation with the creep function $\phi(t)$ of the material. They evaluated the so-called effective creep compliance for an opening crack $\phi_{op}(t)$. They defined a "dwell time" t_r, time required for the crack to advance over the cohesive zone length. The central message is that t_r itself depends self-consistently upon material response and interface properties, such as the cohesive stress. The effective adhesion energy is then evaluated from the effective creep compliance at t_r:

$$\frac{G}{G_0} = \frac{\phi_{op}(\infty)}{\phi_{op}(t_r)}$$

The effective creep compliance can be evaluated analytically on the example of a three-element model.

However, most real-life application go beyond the scope of linear theories, as outlined by *Creton & Ciccotti*[53]. Non-linear behavior and finite deformations participate to high energy dissipation at a crack tip.

I.5.4 Cracks in plastic media

Plasticity corresponds to irreversible flow under shear, encountered in polymers below T_g or in semi-crystalline polymers below their melting point. Contrary to viscous processes, plastic flow occurs only above a certain threshold, the yield stress σ_Y. Below the yield stress, the material exhibits an elastic reversible response. Above the yield stress, irreversible deformation occurs.

A plastic crack model aims at establishing the link between Γ, $\hat{\sigma}$ and plastic properties such as the yield stress σ_Y. The total fracture energy is decomposed in the separation energy and the energy dissipated by plastic deformation:

$$\Gamma = \Gamma_0 + \Gamma_{\text{diss}} \qquad \Leftrightarrow \qquad \frac{\Gamma}{\Gamma_0} = 1 + \mathfrak{F}(\sigma_Y, \hat{\sigma})$$

Usually, the material behaves elastically except in the vicinity of the crack tip, where the yield stress σ_Y is reached. An "active plastic zone" develops around the crack tip, where energy dissipation is concentrated.

The minimum plastic zone size, for a bi-material interface, was calculated by *Tvegaard & Hutchinson*[54]. In our case, since the elastic modulus of the glass substrate is much greater than the modulus of the interlayer, the plastic zone size only depends on the properties of the interlayer. We can also neglect elastic-mismatch terms for a polymeric interlayer. Thus, the minimum plastic zone size is given by:

$$R_p \approx \frac{2}{3\pi} \frac{E}{1-\nu^2} \frac{\Gamma_0}{\sigma_Y^2} \tag{I.2}$$

The seminal work of *Dean & Hutchinson*[2] established in 1980 the fundamental principles of the steady-state approach for crack propagation. *Wei & Hutchinson*[55] reviewed two approaches for the elasto-plastic crack problem: the embedded process zone (EPZ)[54,56] and plasticity-free strip (SSV)[57] models. They also presented a unifying model, which includes a saturation of the steady-state work of fracture at high cohesive stresses. We will focus on the EPZ scheme (figure I.13), as it makes

use of a cohesive zone model for the prescription of the separation energy Γ_0 and the behavior of the interface.

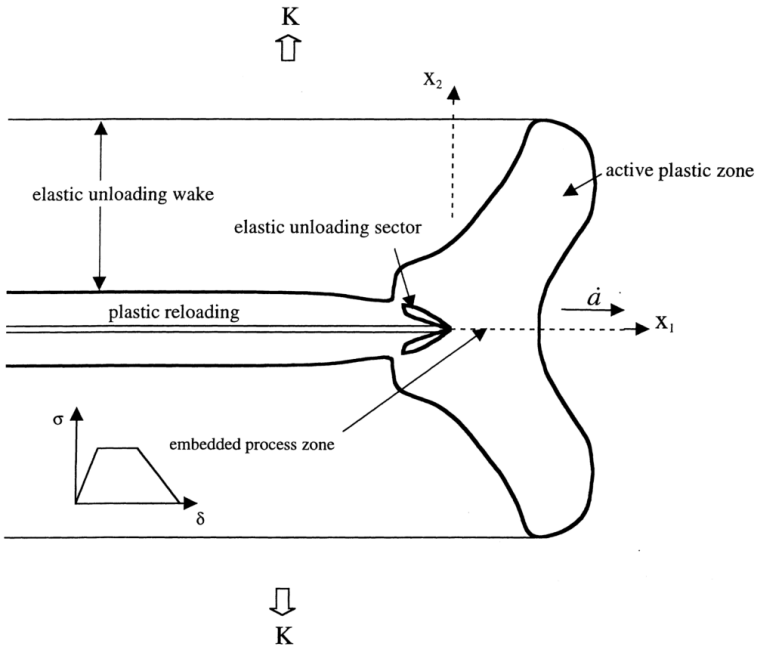

Figure I.13 Crack propagation in mode I in an elasto-plastic material, from *Wei & Hutchinson*[55]

In figure I.14a, the steady-state work of fracture is shown to increase sharply when the cohesive stress $\hat{\sigma}$ is larger than 2 to 4 times the yield stress σ_Y. The steady-state fracture toughness Γ_{ss} skyrockets when the active plastic zone size scales as the size of the specimen, *i.e.* when the entire material is undergoing plastic deformation. Indeed, the actual size of the plastic zone R_{ss} is given by replacing Γ_0 by Γ_{ss} in equation (I.2). In this situation, all the energy input from external forces is dissipated by plasticity, so that releasable energy at the crack tip does not attain Γ_0 anymore.

Landis, Pardoen & Hucthinson[3] later developed a viscoplastic formulation of the steady-state crack problem. The plastic behavior was described in a rate-dependent formulation through the prescription of the plastic strain rate according to J_2-flow theory. In the case of a rate-independent process zone model, their results also showed a dramatic increase of the fracture energy when the cohesive stress was 3 –5 times higher than the yield stress.

Pardoen et al.[58,59] applied the same methodology to the analysis of the wedge-peel test and the fixed-arm 90° peel test.

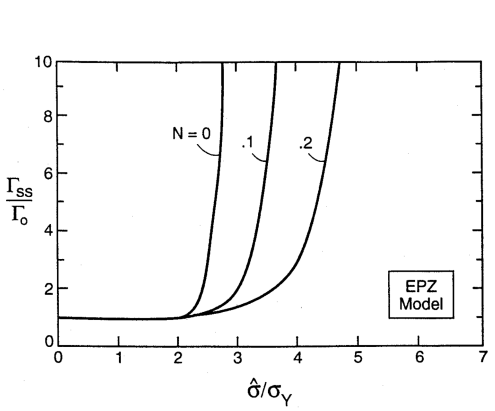

(a) Rate-independent plastic material with power-law hardening behavior [55]

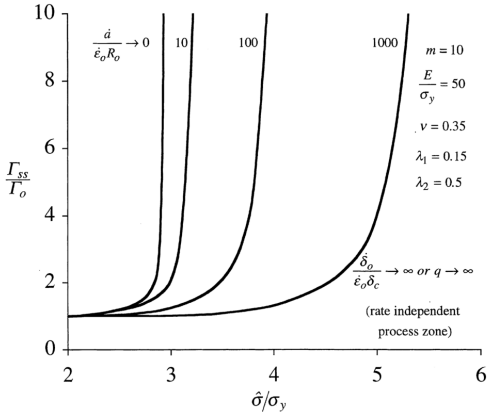

(b) Rate-dependent viscoplastic material [3]

Figure I.14 Ratio between steady-state fracture energy and cohesive energy, as a function of the ratio between cohesive stress and yield stress. **(a)** Rate-independent plastic material, **(b)** rate-dependent viscoplastic material.

I.5.5 Mode mixity: the influence of loading conditions

Fracture modes are defined respectively to the nature of the stresses acting on the crack tip: tensile stresses, perpendicular to crack propagation, contribute to mode I ("opening mode"), in-plane shear stresses contribute to mode II, out-of-plane shear stresses contribute to mode III.

Effect of mode mixity was reviewed extensively by *Hutchinson & Suo*[60], for a wide variety of cracks in layered systems. The general equation for the energy release rate can be simplified in the case of a polymer adhered onto a rigid substrate: the effective modulus reduces to the modulus of the polymer E, and the elastic mismatch parameter can be neglected for an almost incompressible material ($\nu \approx 0.5$). The energy release rate in plain strain is given by:

$$G = \frac{1}{2}\left(\frac{1-\nu^2}{E}\right)\left(K_I^2 + K_{II}^2\right) = G_I + G_{II}$$

Mode mixity is defined as the ratio of stress intensity factors in mode II versus mode I, which can be translated through the release rates $G_i = K_i^2/E^*$. The mode-mixity angle ψ is defined by:

$$\psi = \tan^{-1}\left(\pm\sqrt{\frac{G_{II}}{G_I}}\right)$$

Pure mode I corresponds to $\psi = 0°$.

Numerical simulations in plain strain by *Tvergaard & Hutchinson*[56] in mode I paved the way for the study of mode-mixity effects[54]. Mode-mixity affects both the shape of the plastic zone (figure I.15a) and the shape of the steady-state toughness curve (figure I.15b). In particular, the onset for toughness enhancement is shifted towards higher values of $\hat{\sigma}/\sigma_Y$ for a mode-mixity angle $\psi > 0°$, and lower values for $\psi < 0°$.

Mode-mixity with out-of-plane contribution G_{III} was addressed numerically by *Tvergaard*[7,61]. Using a rate-independent plastic material, he computed that mode mixity affected the onset of fracture energy increase, which shift towards lower values of $\hat{\sigma}/\sigma_Y$ when modes II and III are at play.

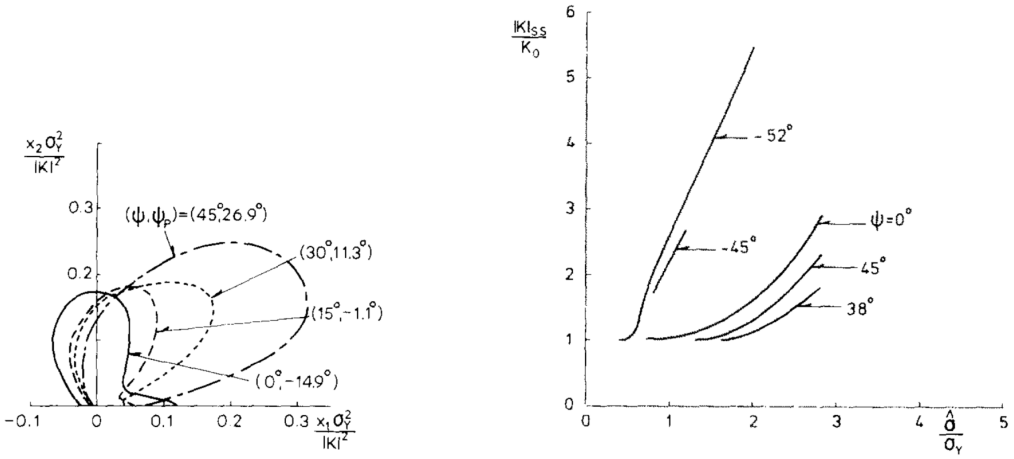

(a) Plastic zone size **(b)** Steady state toughness

Figure I.15 Effect of mode mixity on the fracture toughness in a plastic material, from *Tvergaard & Hutchinson*[54]

.

I.6 Our Holy Grail: understanding the coupling between energy dissipation at the interface and in the volume of the interlayer

The present work aims at investigating the coupling between adhesion, finite-strain deformations, crack propagation and energy dissipation in a polymer material sand-

wiched between two glass plies. With the TCTT as the principal experimental method, we focus on two main aspects: the effect of the interface—chapter III—and the effect of the interlayer's mechanical behavior—chapter V—on the macroscopic work of fracture. Chapter II presents the materials and methods used in this work: surface silanization, polymer characterization, mechanical tests.

In chapter III, we present an original surface treatment protocol based on sol-gel chemistry, which enables to tune the adhesion between a PVB interlayer and glass with a finer control compared to previously reported work. Then, the effect of a changing adhesion—between PVB and glass—is investigated with the TCTT. We explore the dependency of steady-state regime limits on the surface chemistry, and the relation between interfacial adherence and macroscopic work of fracture.

On the polymer side, the mechanics of the interlayer is changed completely in chapters IV and V, switching from PVB to EVA.

The polymer material was characterized, in terms of structural and mechanical properties, in chapter IV. While PVB was highly viscoelastic at room temperature, EVA exhibits an elasto-plastic behavior, due to its semi-crystalline nature.

The stretching and delamination behavior of this elasto-plastic EVA interlayer is investigated with the TCTT in chapter V. With this different polymer material, we emphasize that the steady-state regime requires some effort to be attained. Here again, surface chemistry is used to adjust the adhesion and allow controlled delamination of the EVA interlayer in the TCTT. Once a steady-state regime is recovered, we show that the plastic behavior of EVA dissipates less energy compared to viscoelasticity in PVB, mostly because of localized dissipation at the crack tip. The crucial role of bulk dissipation by viscoelasticity is underlined by TCTT with EVA laminates at the glass transition temperature of the interlayer, as greater work of fracture values and rate-dependency are recovered closer to the glass transition.

The geometry of this crack propagation problem mixes mode I and mode II with finite strains and complex material behaviors. A realistic analytical derivation of the mechanical fields seems out of reach: analytical crack-tip fields are already a complex problem in non-linear elasticity[62], the task would be even greater with a the time-dependent mechanical history.

Still, geometry and constitutive behavior difficulties can be overcome with numerical simulations by finite-element analysis. In chapter VI, a steady-state crack

numerical model is presented. Using the commercial FEA software ABAQUS coupled to a numerical computing environment, we developed and implemented a steady-state approach to model adhesive rupture in a rate-dependent material. First results with a visco-plastic model are presented here. We assess the legitimacy of the method by comparing our results to the literature. Then, we apply the numerical scheme to the modelization of the TCTT.

II

Experimental methods

In this chapter, we describe the materials studied in this work, along with the experimental techniques for their characterization.

The two interlayers encountered in this work – PVB and EVA – are first described shortly in section II.1, in terms of chemical composition. Structural and mechanical properties of PVB were already described and discussed by *Elzière*[4,63]. An extensive characterization of EVA is provided in chapter IV.

The surface modification protocol by sol-gel chemistry is described in section II.2, along with the robust implementation with the "wiping" technique, suitable for a repeatable coating of several glass samples at a time.

Thermal, structural and mechanical characterization techniques are described in section II.4, applied to polymer materials.

Finally, adhesion characterization tests are described in section II.5. Emphasis was put on the Through Crack Tensile Test, which will be the core of the experimental investigations in the following chapters.

II.1 Polymers used as interlayers in laminated glass

PVB – poly(vinyl butyral) is the standard in laminated glass industry and has been extensively studied in the literature. It is widely used because it is cheap and performs well in terms of impact resistance.

However, a few other polymer materials are used for specialized laminated glass applications. EVA, poly(ethylene vinyl acetate), known in solar panels applications, is used for colored and interior glazings.

Ionomer materials based on polyethylene, such as SentryGlas® by Kuraray™ (former DuPont™). This ionomer is glassy at room temperature which provides the high stiffness required in structural applications. However, the higher bending and tearing resistance does not mean the impact resistance is much higher than with PVB laminates (figure I.4).

Polyurethanes are used when impact resistance at low temperatures is required, for instance in transport applications. These specialty polymers are costly, and therefore used only for high added-value products, in the aeronautics industry for example.

Polycarbonates are also found in transport and balistic applications.

II.1.1 Poly(vinyl butyral)

Chemical formulation

What is called PVB in the laminated glass industry is actually a copolymer of vinyl butyral, vinyl alcohol and vinyl acetate (figure II.1). In the synthesis process, poly(vinyl acetate) is first hydrolyzed to yield poly(vinyl alcohol), with around 98% hydroxyl functions. Butanal is then added to perform acetalisation, to obtain vinyl butyral moieties[64]. The final hydroxyl content varies typically between 10 to 20%.

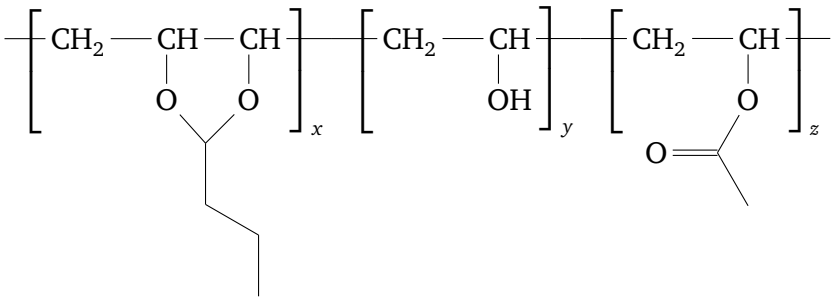

Figure II.1 PVB chemical formula ($x \approx 0.80$, $y \approx 0.18$, $z \approx 0.02$)

A significant amount of plasticizer is also added into the formulation, typically around 30%, in order to shift the glass transition from 75-80°C for pure PVB to room temperature. Common plasticizers are linear diesters, such as dibutyl sebacate, dihexyl adipate or TEG-EH (tri(ethylene glycol) bis(2-ethylhexanoate))[64]. Other additives, such as anti-oxidants and UV stabilizers, are present in the formulation in negligible amounts: we just consider they have no effect on mechanics or adhesion. Finally, metallic salts (typically divalent cations like Mg^{+}) are incorporated in the formulation: they act as "adhesion modifiers" as they form metal-ligand interaction between hydroxyl groups of PVB and the glass surface[29,65].

Macromolecular structure

Such a high amount of plasticizer has a strong effect on the molecular structure of PVB. A structuration at the molecular level has been suggested in the literature[4,66,67]. This macromolecular structure arises from the presence of hydroxyl groups which tend to segregate in OH-rich domains, while the plasticizer molecules are expelled from these domains. As a result, hard and soft domains coexist within the material, between the glass transition around 20°C up to around 70°C.

Mechanical properties

The large deformation behavior of PVB is presented in figure II.2.

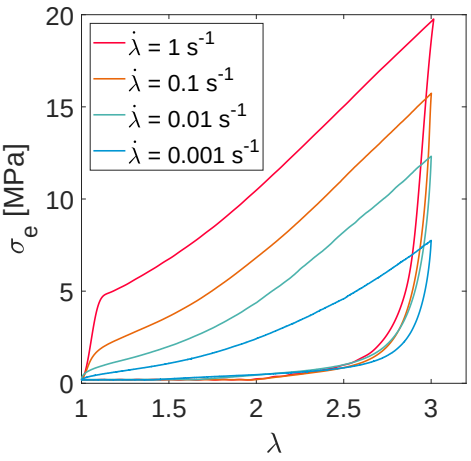

Figure II.2 Uniaxial tensile test on PVB: engineering stress vs stretch.

Though it might resemble non-linear elastic behavior on the loading part, the unloading shows that a large fraction of the strain energy is dissipated. A "pseudo-yield stress" arises at high strain rates, typically above $1\,s^{-1}$ [68].

Elzière et al. recently proposed a relationship between macromolecular architecture and mechanical behavior[63].

II.1.2 Poly(ethylene - vinyl acetate)

EVA is a statistical copolymer of ethylene and vinyl acetate (figure II.3).

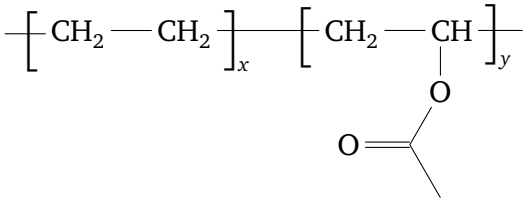

Figure II.3 EVA chemical formula ($x \approx 0.75$, $y \approx 0.25$)

The structural and mechanical properties of the copolymer strongly depend on the vinyl acetate (VA) content (y in figure II.3). Based on figure II.4, a distinction can be made between low VA contents (*i.e.* below 30%wt.VA) when EVA is semi-crystalline, and high VA content (*i.e.* above 50%wt.VA) when EVA behaves like a rubber.

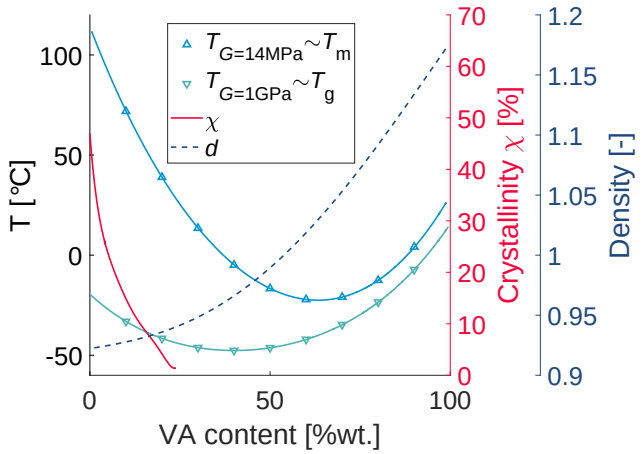

Figure II.4 EVA properties depending on the vinyl acetate (VA) weight content ($\bar{M}_n \sim 30{,}000\,g{\cdot}mol^{-1}$): melting temperature T_m, glass transition temperature T_g, crystalline content χ and density d. Data were taken from *Salyer & Kemyon*[69] and re-plotted.

We used a formulated EVA interlayer containing about 25 %wt.VA, with a molecular mass around 150,000 $g{\cdot}mol^{-1}$. Even though the molar mass is higher compared to figure II.4, we suppose this EVA to have a semi-crystalline nature.

For laminated glass applications, EVA interlayers are compounded with a crosslinker, often a peroxide[70]. The addition of crosslinks modifies the mechanical properties of the interlayer.

"Adhesion promoters" are also incorporated in the EVA formulation: they typically are vinyl-functionalized silanes which can bind both to the glass surface and to the polymer chains[71], as depicted in figure II.5.

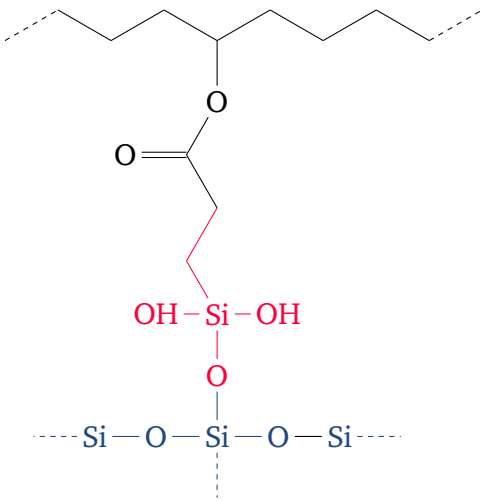

Figure II.5 Vinyltriethoxysilane binding the glass substrate and the EVA interlayer.

Chapter IV is dedicated to a detailed experimental characterization of the structural and mechanical properties of the EVA interlayer.

II.2 Surface modification with silane chemistry

In this section, we describe a surface modification protocol based on silane chemistry. Before going into details, we must emphasize that the coating technique presented below may not seem standard for the well-versed chemist. Our goal was not to obtain a perfect monolayer of silane molecules on an ideal substrate, but rather obtain reproducible coatings on a large number of glass samples.

Silane chemistry

Triethoxysilanes $R-Si-(OEt)_3$ allow efficient and versatile functionalization of glass surfaces. The reaction follows the hydrolysis-condensation mechanism[72]:

1. Ethoxy moities are hydrolyzed in the presence of water:
   $Si-O-Et + H_2O \rightarrow Si-OH + EtOH$
2. Silanols undergo condensation to yield prepolymers:
   $Si-OH + OH-Si \rightarrow Si-O-Si + H_2O$
3. Silanol groups react with free silanols at the surface of the glass, according to the condensation reaction. The silane layer is grafted onto the surface.

Several chemistries are available for the functional group *R*. Alkyl chains make the surface hydrophobic, and the hydrophobicity increase with the carbon content[73].

Silane	Chemical formula	Functionality
TEOS	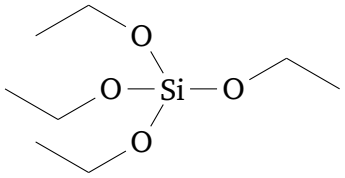	Silica precursor Hydrophilic
MTES	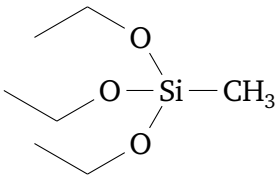	Hydrophobic
OTES	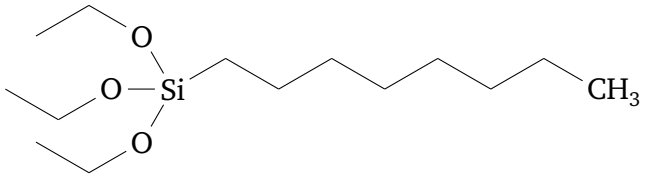	Hydrophobic
POTS	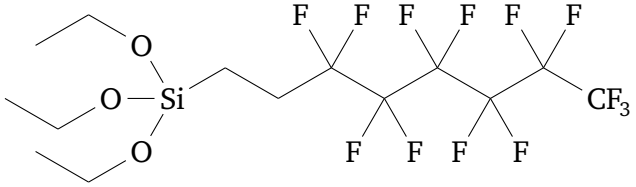	Hydrophobic

Table II.1 Triethoxysilanes used in this work: tetraethylorthosilicate, methyltriethoxysilane, octytriethoxysilane, perfluorooctyltriethoxysilane

The modification of the glass surface with triethoxysilanes was performed by a "wiping technique" as reported in the work of Elzière[4]. This method has the advantage of being simple, robust and applicable to several glass pieces at a time.

Sol formulation

The sols were prepared in a mix with 90wt% isopropanol (propan-2-ol or IPA) and 10% hydrochloric acid solution at pH = 1 ($HCl_{(aq)}$ $0.1 mol \cdot L^{-1}$). Silanes were added to the solvent in a concentration between 1wt% and 3wt%, which corresponds to molar concentrations between 10^{-5} and $10^{-4} mol \cdot L^{-1}$.

Surface preparation and coating

The glass surface was cleaned first with a non-foaming alkaline soap and then with an abrasive cerium oxide solution. A solution of TEOS (tetraethylorthosilicate) at 0.3wt% in IPA:HCl (0.1M) was then applied by wiping. The TEOS sol was left to hydrolyze 30min prior to application. This base coating of TEOS was applied for both cleaning and activation of the surface, in order to provide a large density of hydroxyl groups at the surface[72]. The surface was rinsed with IPA after 10min and dried with nitrogen.

The functional silane solution was also hydrolyzed for 30min before application onto the glass. A cleanroom wipe was impregnated with the sol and applied on the glass sample according to the wiping pattern in figure II.6. The surface was left to dry under the hood for 10 minutes prior to a gentle rinsing. The sample was then heated to 100°C for 30min to complete the condensation reaction. Finally, the surface was thoroughly rinsed with IPA to remove any remaining excess of ungrafted silane: 3 times by wiping as in figure II.6 and one last time with a flow of solvent, eventually dried with nitrogen.

The coatings obtained may be considered as “thin films”, although they are not monolayers of silanes. Thickness measurements were not performed, however we estimate the thickness of the coating to range between 10 nm and 100 nm.

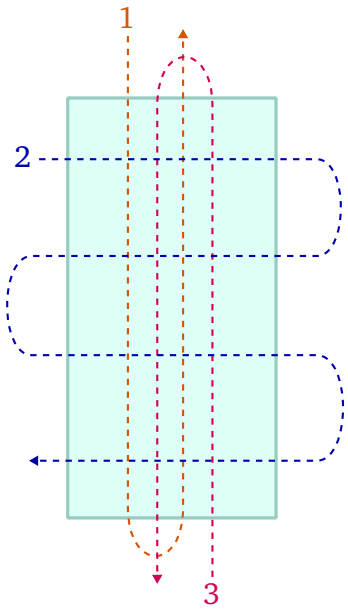

Figure II.6 Wiping pattern in the silanisation protocol

II.2.1 Surface characterization: contact angle measurement with a sessile drop

The efficiency of the surface modification was assessed by wetting experiments in the sessile drop configuration (Drop Shape Analyzer DSA100, Kruss). Sessile drop experiments consist in depositing a droplet of controlled volume and measuring the resulting contact angle. The testing liquid was deionized water. The droplet was inflated and deflated to achieve a dynamic measurement, in order to get both advancing θ_a and receding θ_r contact angles. Contact angle results are shown in sections III.2 and V.1.

II.3 Thermal and structural analyses: DSC and X-ray diffusion

II.3.1 Differential Scanning Calorimetry

Differential Scanning Calorimetry consists in measuring the heat capacity of the material over a range of temperature, in order to unveil endothermal (*e.g.* melting, glass transition) and exothermal (*e.g.* crystallization) processes.

DSC experiments were performed in closed aluminum pans, with samples between 5 mg and 15 mg in weight, with a DSC Q200 (TA Instruments) device. Cooling was ensured with liquid nitrogen, and an helium flow was maintained at 25 mL·min^{-1}. Heating was performed at 20°C·min^{-1} and cooling at -10°C·min^{-1}, except when specified otherwise.

II.3.2 Wide and Small Angle X-ray Scattering

Scattering techniques probe the structure of materials: it consists in illuminating a material sample with a photon—or particle—beam, and analyze the pattern obtained when the photons are diffracted by the structure. As the characteristic lengthscale is inversely proportional to the energy of the photons, atomic and molecular scales are accessible with X-rays. "Wide angle" X-ray scattering typically gives information about organisation at the nanometer scale ($10^{-10}-10^{-9}$ m). Molecular and macromolecular structure is accessible with "small angle" experiments which probes lengthscales up to 100 nm.

X-ray scattering experiments were conducted at the *LLB* (*Laboratoire Léon Brillouin*, CEA Saclay) in collaboration with *Dr. Alexis Chennevière*. The "SWAXS" setup is a versatile tool that allows the collection of data from wide to small angles by changing the sample-to-detector distance D.

WAXS and SAXS configurations

A copper source provides the X-ray beam at the wavelength $\lambda_{CuK\alpha} = 1.5406$Å. The 2D detector (Pilatus^{TM}1M) is composed of 10 bidimensional detectors arranged in a 5×2 array (figure II.7). The raw data is a photon count over a plane $N(x, y)$, which

Configuration	D [m]	Acquisition time	q range [Å^{-1}]
WAXS	0.4	5 min	$0.1-3$
SAXS	2.1	2h	$0.01-0.2$

Table II.2 Parameters for X-ray scattering experiments

has to be converted into an absolute intensity curve *vs.* scattering vector. The photon count is analyzed in polar coordinates: $N(r, \phi)$. Radial distances are related to the characteristic length scales in the material while the azimut angle ϕ gives information about the local (an)isotropy of the specimen.

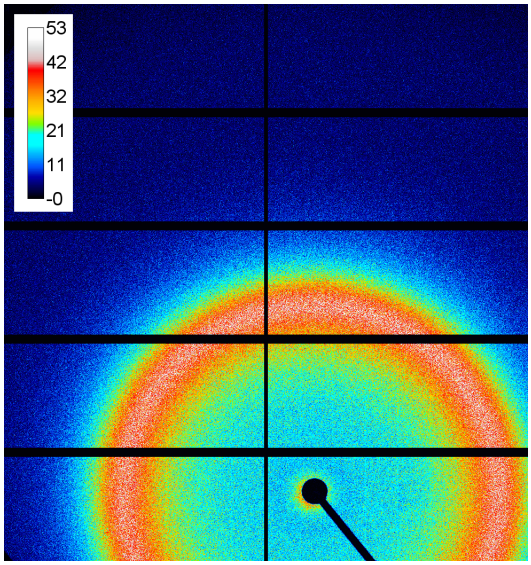

Figure II.7 Wide angle X-ray scattering of PVB. Color bar = photon count N.

Data analysis

A "mask" image is first applied to remove the beamstop, the blanks between detector areas and outlier pixels from the analysis. The total photon count N is then integrated in the polar plane (r, ϕ) centered on the direct beam:

$$I_{\text{raw}}(r) = \int_{\phi_1}^{\phi_2} N(r, \phi)\, \mathrm{d}\phi$$

The integral is evaluated on the entire angular range for isotropic samples ($\phi_1 = 0°, \phi_2 = 360°$). For anisotropic samples, an angular range of 30° is defined for a given direction ϕ using the mask ($\phi_1 = \phi - 15°,\ \phi_2 = \phi + 15°$).

The radial distances r are calibrated using the scattering pattern of silver behenate[74] and converted from pixels to millimeters. As the sample-detector distance D is known, the scattering angle 2θ is given by the geometrical relation:

$$\tan 2\theta = \frac{r}{D}$$

Reciprocal distances are obtained with the scattering equation:

$$q = \frac{4\pi}{\lambda_{CuK\alpha}} \sin\theta$$

The raw scattering spectrum $I_{raw}(q)$ is then corrected by subtracting the background noise ("dark") and the photons from the direct beam ("empty beam"). After normalization by the transmission and thickness of the sample, the absolute intensity $I(q)$ is obtained in cm^{-1}. Adequate subtraction and normalization procedures allow to combine scattering data from several configurations. Still, a vertical shift factor (typically between 0.5 and 2) was applied to ensure superposition of the data between SAXS and WAXS configurations.

II.4 Mechanical testing

The mechanical response of polymers depends on the temperature and the loading rate. We characterized the materials in small strains, by dynamic mechanical analysis, and in large strains by tensile testing.

II.4.1 Small strain mechanical analysis

Dynamical mechanical analysis was performed in two geometries: film tension on a Dynamic Mechanical Analyzer (DMA Q800, TA Instruments) and plate-plate shear with a strain-controlled rheometer (MCR501, AntonPaar).

Sample preparation

The samples were cut with a 5 mm-wide rectangular die and the length was measured between the clamps. The sample was tightened using a dynamometric screwdriver.

For shear measurements, several disks of interlayer were cut with a die of diameter 25 mm and stacked under the plate-plate geometry. A normal force between 0.1 and 1 N was applied to ensure good contact and de-airing between polymer layers. The stack was eventually heated up to a temperature at which the interlayers could melt and form a homogeneous sample.

Strain sweep: determination of the linear regime

The linear domain of the material is determined with a strain-sweep experiment. The applied oscillatory strain is logarithmically increased from 0.01% to a few %. The linear regime is characterized by a constant modulus, which means the response

is independent from the applied strain. The modulus decreases when non-linearity arises and the material softens.

Temperature sweep: determination of thermal transitions

The variation of mechanical properties with temperature is obtained with a temperature sweep at fixed frequency and amplitude.

The heating (or cooling) rate β affects the observed temperature of properties transitions due to a dynamic thermal lag, also observed in DSC experiments[75]. In fact, the temperature is measured by a thermocouple next to the sample within the chamber. The polymer sample needs time to reach thermal equilibrium with the convected surrounding gas. Consequently, The measured T_g upon heating was higher than the measured T_g upon cooling. An average glass transition temperature[75] was calculated from symmetrical heating and cooling ramps:

$$\overline{T}_g = \tfrac{1}{2}\big(T_g(\beta) + T_g(-\beta)\big)$$

II.4.2 Large strain tensile testing

Mechanical properties in large deformations were characterized with an Instron® 5965 tensile testing device. Polymer foils were cut in dogbone-shaped samples with a thickness $b_0 = 4$mm in the central part (figure II.8).

The dogbone samples were held by pneumatic clamps. Gripping was ensured by sand paper adhered onto the clamps.

The test was controlled in displacement δ at a constant tensile velocity $\dot{\delta}$.

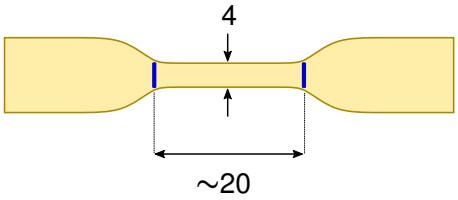

Figure II.8 Schematic of a tensile specimen. Paint marks are applied for video extensometry measurements. Dimensions are in mm.

Deformation $\varepsilon^{\text{extenso}}$ was measured with an Instron® *SVE2* video extensometer. Two paint marks were drawn on the sample surface at the edges of the central part of the dogbone (figure II.8). The initial distance between paint marks was $\ell_0 \approx 20$ mm.

Image acquisition by the video extensometer was limited to a framerate of 50 Hz. As a consequence, the detection of the paint marks could fail for the highest traction velocities, typically $25\,\mathrm{mm}\cdot\mathrm{s}^{-1}$. When the extensometer encoutered an error during the test, the clamp displacement $\varepsilon^{\mathrm{clamp}} = \delta/\ell_0$ was later used to determine the deformation. The relationship between video and clamp deformation was fitted with a 2nd-degree polynomial: $\varepsilon^{\mathrm{extenso}} = P(\varepsilon^{\mathrm{clamp}})$, and extrapolated over the entire displacement range. The stretch was then calculated as:

$$\lambda = 1 + \varepsilon^{\mathrm{extenso}}$$

The engineering stress was calculated as the force divided by the initial area:

$$\sigma_e = \frac{F}{A_0} = \frac{F}{b_0 \cdot h_0}$$

II.5 Adhesion characterization

II.5.1 The peel test

As stressed out in the introduction (section I.4), the peel test is a convenient method to characterize the adhesive bonding between the interlayer and the glass substrate.

The glass samples dimensions were 150 mm × 45 mm, the polymer strip was 200 mm long × 20 mm wide (see figure II.9). The nominal thickness of the polymer strip was 0.76 mm. A cotton fabric was placed on top of the interlayer to prevent the polymer from stretching. The fabric did not deform along the traction direction and presented a low bending stiffness.

The peel energy—or adherence—is estimated from the balance between the total work applied, the deformation of the strip under pulling, the elastic bending energy of the backing, and the energy required to propagate the peel front. The cotton backing is rigid enough to allows us to neglect the contribution of bending and the deformation of the delaminated strip. According to Kendall's elastic analysis[28], the adherence energy is given by:

$$G_{\mathrm{peel}} = \frac{F}{b_0}(1 - \cos\theta)$$

In the actual test, the polymer strip was attached to a bottom clamp. The glass was maintained horizontal on two rolling cylinders. The glass was pulled up while being

free to translate horizontally on the cylinders. This setup ensures that the vertical displacement in traction is converted into an equal horizontal displacement of the glass, as depicted in figure II.9. Therefore, the peel angle θ is maintained equal to 90° throughout the experiment.

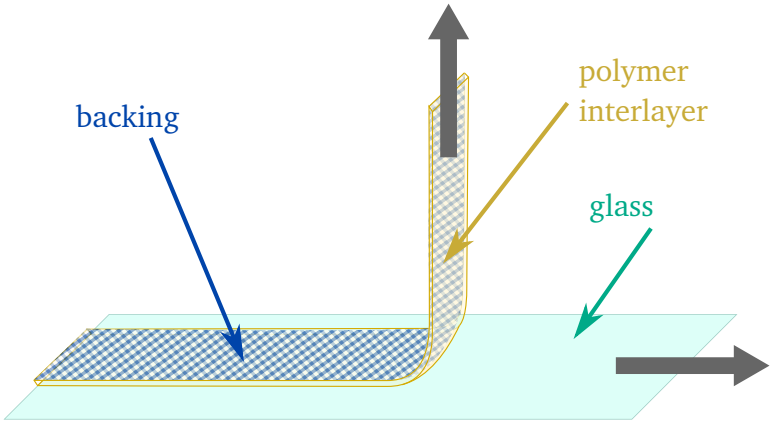

Figure II.9 Schematic of the peel sample and peel test geometry

In the end, the 90°-peel energy reduces to the peel force divided by the strip width:

$$G_{\text{peel}} = \frac{F}{b_0}$$

II.5.2 The Through Crack Tensile Test

The TCTT is the lab-scale adaptation of the stretching and delamination solicitation observed in laminates under impact. We describe here the experimental setup and the image analysis procedure.

Servo-hydraulic traction device

Through Crack Tensile Tests (TCTT) were performed on a servo-hydraulic testing machine (Amsler HC25, Zwick/Roell) equipped with a 10kN force cell. The traction speed allowed by the hydraulic jack ranged from 0.1 to 100 mm $\cdot$ s^{-1}, over a maximal distance of 95mm.

The sample was held with pneumatic clamps (Zwick/Roell). The alignment of the clamps was ensured with a custom H-shaped piece, in order to enforce the alignement

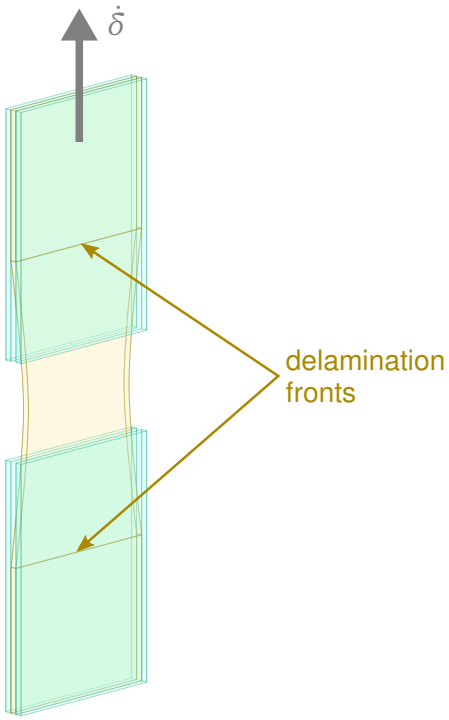

Figure II.10 Schematic of a Through Crack Tensile Test specimen during the test.

along the vertical traction axis, and also in the plane of the sample in order to avoid rotation and torsion in the tensile direction.

Aluminum corners were adhered to the glass with double-sided tape to prevent slippage between the clamps.

The temperature of the sample was controlled by a thermal chamber between −20°C and 100°C. Cooling was achieved with liquid nitrogen. The temperature was monitored with an external data logger close to the sample, with an accuracy of ±1°C.

A backlight (Effilux) was mounted at the back of the thermal chamber to provide contrast for image acquisition.

Video Acquisition

Video acquisition was performed with a Baumer VCXU-32M camera. Image data was acquired with the *Image Acquisition Toolbox* of MATLAB®, using the *GenICam GenTL* hardware package. The custom GUI *GIGEACQ*, previously developped by P. Elzière[4], was adapted for the USB3 camera.

A macro objective (Kowa LZ69M) was mounted on the camera. The working distance was approximately 1m, the field of view about 20cm. With 2000 pixels, the resolution of the images was around 100µm.

Image correction was performed using the *Calibrate Camera* application provided with MATLAB®, in order to account for image distortion by the macro lens. 3 to 5 images of a reference checkerboard were acquired with the clamps in full-open position to calibrate the entire field of view. The checkerboard was slightly tilted in the sample plane between each calibration image.

Image post-processing: measure of the interlayer stretch

Image post-processing was also performed with MATLAB with a custom code based on edge detection. Each image was divided into 2 regions of interest: the lower regions where the glass is fixed and the upper region where the glass moves with the clamp. The boundaries of the upper regions change for every image to follow the displacement of the upper glass ply.

The short version of the image analysis code is the following:

1. Edges detection with the `edge` function.
2. Extraction of a vertical profile: average over a given width (5 to 15 pixels) and convolution with a Gaussian to smooth out non-significant edges.
3. Positions of the glass edges and delamination fronts recovered with the `findpeaks` function.
4. Update ROIs boundaries and go to the next frame.

The positions of the delamination fronts and glass edges are detected on 5 points along the width of the sample, which helps rejecting outliers (from an error in the automatic edge detection) and average the values when the delamination fronts became unstable and wavy.

Relative displacements are then computed from the differences between absolute positions, as illustrated in figure II.12: delaminated lengths $a_\uparrow$ and $a_\downarrow$ and imposed displacement δ. The initial length of the interlayer corresponds to the total delaminated length $a_\uparrow + a_\downarrow = 2a$. The average stretch of the interlayer is defined by equation (II.1)

$$\lambda = \frac{\delta + 2a}{2a} = \frac{\delta}{2a} + 1 \tag{II.1}$$

The very first images are not suitable for automatic edge detection, as the delamination fronts are not clearly separated from the glass edges. Manual input was requested when the automatic routine could not find the 4 distinct edges. The first values of the stretch therefore lack accuracy and shouldn't be considered meaningful.

Shape of the stretch increase with time

The positions of the delamination fronts were linearly increasing with time when steady-state propagation occured (figure II.11a).

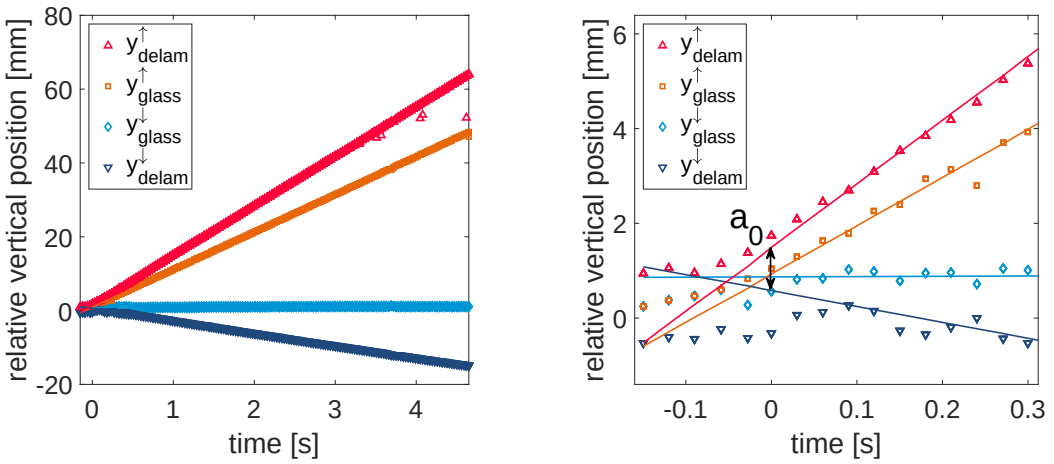

(a) Linear evolution of the crack front positions. For each position, 5 points are measured along the sample width.

(b) Transitory regime at the initiation of delamination. Affine models of the positions do not intercept at the exact same initial position.

Figure II.11 Positions of delamination fronts and glass cracks over time in the TCTT.

The average delaminated length could be written $a(t) = \dot{a}t + a_0$. The constant term a_0 arises from the non-linearity of crack front position in the early moments of the experiment: a_0 can be interpreted as the shortest debonded length for which the steady-state regime was reached (figure II.11b).

The displacement δ is linear with time as the traction velocity is imposed. Then the stretch can be expressed as:

$$\lambda(t) = 1 + \frac{\dot{\delta}t}{2(\dot{a}t + a_0)}$$

The a_0 value accounts for the evolution of the stretch with time as shown in figure II.12: the increase of λ from 1 to the steady-state value $\lambda_{ss} = 1 + \dot{\delta}/2\dot{a}$ is not immediate. Such shape of $\lambda(t)$ was also observed in the literature[37,39].

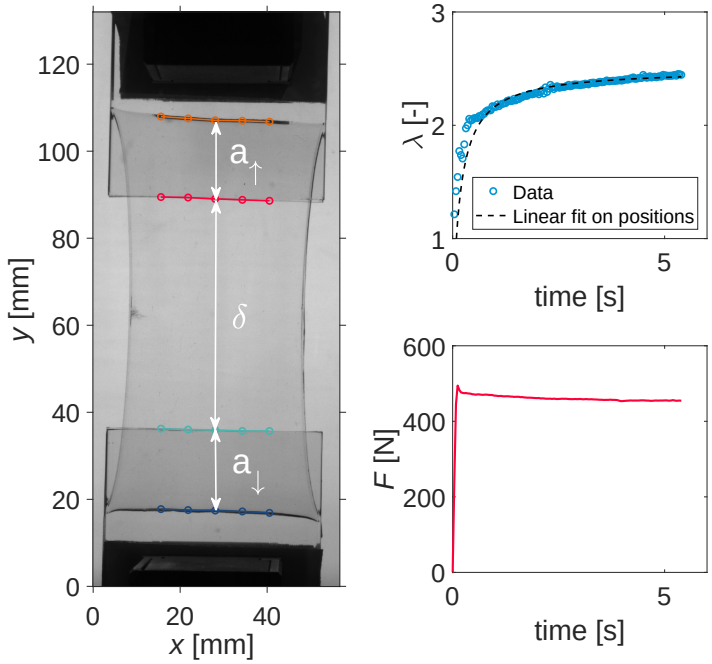

Figure II.12 Through Crack Tensile Test data analysis: measurement of the stretch by image analysis. Steady-state regime is reached when both force and stretch are constant with time.
(PVB laminate, $\dot{\delta}$ = 10 mm·s^{-1} , T = 20°C, h_0 = 0.76 mm)

Macroscopic work of fracture

The mechanical work injected in the laminated system for an increment of displacement $\mathrm{d}\delta$ in stead-state regime is:

$$\mathrm{d}W_{\mathrm{ext}} = F_{\mathrm{ss}}\,\mathrm{d}\delta$$

This mechanical work is dissipated within the laminated system by the interlayer and by crack propagation. The macroscopic work of fracture is defined as the total energy dissipated per crack area created:

$$G_{\mathrm{m}} = \frac{\mathrm{d}W_{\mathrm{ext}}}{\mathrm{d}A} = \frac{1}{b_0}\frac{F_{\mathrm{ss}}\,\mathrm{d}\delta}{2\,\mathrm{d}a}$$

Recalling the definition of the stretch $\lambda = 1 + \delta/2a$, the displacement increments are related by the stretch: $\mathrm{d}\delta = (\lambda_{ss} - 1)\,2\,\mathrm{d}a$ in steady-state regime. Hence, the macroscopic work of fracture is defined by equation (II.2):

$$G_m = \frac{1}{b_0} F_{ss} (\lambda_{ss} - 1) \tag{II.2}$$

III

Modification and control of adhesion in PVB-laminated glass

In the previous work by P. Elziere and R. Kulis [4], adhesion was tuned via chemical modification of the glass surface.

An aminosilane such as APTES increases the adhesion to PVB through acid-base interaction between amino and hydroxyl groups. With APTES, the adhesion increase was so high that only the immediate rupture of the interlayer was observed.

A long-chain alkylsilane, such as OTES, exposes densely packed alkyl chains which makes the surface hydrophobic and prevents adhesion with PVB. With OTES, the delamination of the interlayer was unstable. A partial steady-state could be recovered at lower temperatures and faster velocities. As the behavior of the interlayer was changing at lower temperature, the effect of the interface modification alone could not be investigated.

Their preliminary results proved that the interface interactions should be tuned carefully in order to preserve the delamination behavior. Silane chemistry offers a large toolset and the same approach was continued here. The goal was to obtain a change in adhesion fine enough to observe a delamination behavior at a given temperature and traction velocity.

In this chapter, a surface coating of a specific mixture of tetraethylorthosilicate (TEOS) and methyltriethoxysilane (MTES) was developed to control the adhesion between a poly(vinyl butyral) interlayer and float glass. The adhesion of PVB was assessed by the 90° peel test, and shown to increase with the TEOS content in the sol-gel coating. Three compositions, resulting in adhesion energies from 1 to 2 $kJ \cdot m^{-2}$, were applied to TCTT samples with various interlayer thicknesses.

III.1 Surface treatment protocol with silane mixes

PVB adhesion is related to the presence of silanol groups at the surface of the glass. The hydroxyl content in the PVB as well as the presence of metallic salts - known as "adhesion modifiers" - affect the strength of interactions between PVB and the surface.

The MTES-TEOS system was reported in the literature—particularly in the 1990s—for coating applications[76,77]. Co-condensation of the hydrolyzed silanes was evidenced by ^{29}Si NMR[78–80]. Co-condensation leads to the formation of a statistical pre-polymer, without phase-separation of the two chemical species.

The fine adjustment of the hydroxyl concentration at the glass surface was assumed possible with the MTES-TEOS system. Our main assumption was that a higher TEOS content results in a higher OH density at the surface, which would provide a higher adhesion.

Formulation of the silane solutions

Sols were prepared as detailed in section II.2, with a total 1 %wt. silane concentration in a solvent isopropanol/HCl (pH=1) . The molar ratio between TEOS and MTES was varied:

$$r_{TEOS} = \frac{n_{\mathrm{TEOS}}}{n_{\mathrm{TEOS}} + n_{\mathrm{MTES}}}$$

The silane solutions were deposited by the wiping technique, also described in section II.2. Control surfaces with 100% MTES and 100% TEOS were obtained by the same wiping process. The 100%-TEOS surface corresponded to the “undercoat” surface treatment only, with a silane concentration of 0.3wt.% in the sol. The detail of the sol formulations is given in table III.1.

r_{TEOS}	V_{TEOS} [µL]	V_{MTES} [µL]	c_{total} [mol · L^{-1}]
0	–	106	$5.9{\cdot}10^{-5}$
0.1	16	90	$5.6{\cdot}10^{-5}$
0.2	30	77	$5.3{\cdot}10^{-5}$
0.3	43	64	$5.1{\cdot}10^{-5}$
0.4	54	53	$4.9{\cdot}10^{-5}$
0.5	65	42	$4.7{\cdot}10^{-5}$
1	32	–	$1.2{\cdot}10^{-5}$

Table III.1 Sol formulations for MTES-TEOS treatments. Silanes were added to an isopropanol (90wt%) / hydrochloric acid 0.1M (10wt%) solution.

As underlined in section II.2, we do not obtain perfect silane monolayers with this coating technique. Still, adherence characterization in section III.2 shows that the method is robust and repeatable despite the coarse appearance.

Wetting experiments

Contact angle measurements (figure III.1) confirmed that the surface was succesfully modified: the contact angle was measured around 80° for an advancing water droplet on methylated surfaces. As a reference, the contact angles on clean glass were around 35° ($\theta_a = 38°$, $\theta_r = 29°$). The TEOS-only surface was hydrophilic as the water droplet reached a complete wetting state, to the extent that a reliable contact angle value could not be obtained: the contact angle value was estimated to be less than 5°.

Little variation of the contact angle was observed for a TEOS content between 10 and 40 %mol., which was consistent with data from the literature[77].

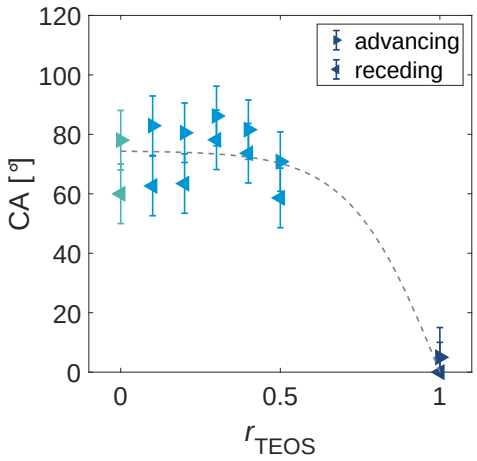

Figure III.1 Contact angle between water and the glass substrate *vs.* TEOS content of the surface treatment. The grey dashed line is a guide for the eye.

III.2 Control of PVB/glass adhesion by the TEOS content

Higher adherence at higher TEOS content...

Peel tests were performed according to the protocol described in section II.5. Samples were conditioned in the testing room at 22°C and a controlled 50 %RH for 24h before peel experiments. A reference value of the peel energy was obtained with PVB

adhered onto an untreated float glass substrate. A plateau of force was reached for all samples, and the corresponding adherence energy was calculated as $G_{\text{peel}} = F/b_0$ with $b_0 = 20\,\text{mm}$.

The adherence energy of PVB on glass ranged between 0.2 and 2.5 $\text{kJ} \cdot \text{m}^{-2}$ with the MTES-TEOS system, as shown in figure III.2. The 90°-peel energy is roughly proportional to the TEOS molar ratio in the range $10\% - 50\%$.

... due to a higher hydroxyl content at the surface?

We attribute the increase in adherence to the higher amount of hydroxyl groups available at the surface when the TEOS content increases in the coating. Upon condensation, at least one of the OH groups of hydrolyzed TEOS remains unreacted at the surface. As the coating is heated only to 100°C, these surface silanols do not undergo further condensation and are available for the bonding with PVB. This interpretation could be confirmed by specific surface analysis techniques, such as XPS, to quantifiy the amount of free silanols at the surface.

The data point with a TEOS-only surface shows that $2.5\,\text{kJ} \cdot \text{m}^{-2}$ is the upper adherence value achieved with these two silanes. The adherence plateau was attributed to a saturation in OH bonds formed between the interlayer and the substrate. Saturation occurs when the number of OH groups available for bonding within the PVB interlayer limits the adhesion.

This hypothesis of saturation in the number of OH bonds could also be checked with a different PVB formulation with another hydroxyl content, as in *Klock*'s work[29]. If the OH content of the PVB decreased, we would expect the saturation to occur for a lower amount of TEOS in the coating. However, changing the hydroxyl content in PVB also affects the miscibility of the plasticizer and the effect of "adhesion promoting" metallic salts. Understanding the relationship the formulation, the structure and the adhesive properties of PVB still is a work-in-progress.

Uncertainty at very low adherence

Surprisingly, we observe that adherence decreases when a little TEOS is added to MTES, from 0.4 to $0.2\,\text{kJ} \cdot \text{m}^{-2}$.

The higher value of peel energy for the MTES-only surface was attributed to a change in the local peel angle. In fact, the PVB strip debonded quickly from the glass

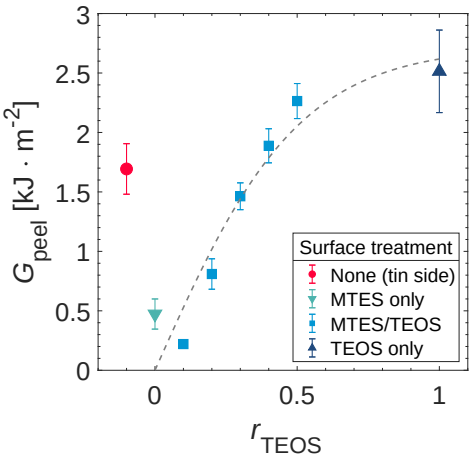

Figure III.2 Adhesive peel energy *vs.* TEOS content of the surface treatment. Peel tests at 50 mm·min^{-1}, 22°C, 50 %RH. The grey dashed line is a guide for the eye.

surface at the beginning of the tests. Steady-state peeling was achieved with a large radius of curvature of the backing. As a result, the peel angle was lower at the front which induced an increase in the adherence energy, either from mode-mixity—the local peel angle is different from 90°—or sliding friction effects (*cf* section I.4).

Also, the hypothesis of chemical inhomogeneity of the methylated surface cannot be excluded: some uncondensed free hydroxyl groups could still be present at the interface, providing a significant bonding energy.

Conclusion: a method to control the interface

It is worth noticing that the adherence between PVB and glass did not exhibit a straightforward relationship with the water contact angle. Indeed, adhesion between PVB and glass relies on more than polar interaction at the interface. In particular, the "adhesion modifying" metallic salts enhance the bond strength via metal-ligand interactions. Thus, wetting cannot predict PVB–glass adhesion, that is why peel tests are inevitable in order to obtain a meaningful adhesion characterization.

Altogether, for our application to mechanical testing, the peel results prove that the adherence between PVB and glass can be controlled and—even better—tuned *via* the surface chemistry. Although non-standard, such approach appears to be robust considering the good repeatability of adherence values in the peel test.

Furthermore, the adherence appeared to be linear with r_{TEOS} in the range 10%–50%. As described in the introduction (*cf* I.5.3), the adherence contains a viscoelastic

dissipation contribution. Still, we can fairly assume—at least according to viscoelastic crack theories—that the peel adherence scales linearly with the separation energy.

$$G_{\text{peel}} \sim r_{\text{TEOS}} \quad \& \quad G_{\text{peel}} \sim \Gamma_0 \quad \Rightarrow \quad \Gamma_0 \sim r_{\text{TEOS}}$$

III.3 Through Crack Tensile Tests with adhesion-modified laminates

Experimental conditions: surface composition, temperature, loading rate

Through Crack tensile Tests were performed with glass coated with the MTES-TEOS mix. All the experiments were performed at 20°C and the traction velocity was set at $\dot{\delta} = 10\,\text{mm}\cdot\text{s}^{-1}$. In these conditions we expect a steady-state delamination with standard TCTT samples at ambient RH.

The samples were placed in the temperature-controlled cabinet of the traction machine 30 min before testing (see II.5 for details). Our samples were conditioned in a 23%RH cabinet at room temperature at least 24h before the experiments. The effect of this relative humidity difference is discussed in section III.4.

The TEOS ratios were 20%, 30% and 40%, which means the adhesive energy varied between *ca.* 1 to $2\,\text{kJ}\cdot\text{m}^{-2}$. The goal of this work was to investigate the variation of the "crack" and "bulk" components of the macroscopic work of fracture in the TCTT, according to equation (I.1), when adhesion between PVB and glass varied with a changing surface chemistry. In these experiments, the PVB thickness was varied between 1 and 4 nominal thicknesses, *i.e.* between 0.38 and 1.52 mm. Three samples were tested for each initial thickness and each surface treatment.

III.3.1 The steady-state regime and its limits

Delamination of the interlayer is observed in the TCTT for every sample tested, for all interlayer thicknesses and surface treatments.

The best case is for an interlayer thickness *i.e.* $h_0 = 1.14\,\text{mm}$, for which we obtain steady-state delamination in all cases. In figure III.3, the delamination fronts form a straight horizontal line, and the debonded area—darker grey in the pictures—has the same length on both sides of the cracked laminate. For the same displacement

$\delta = 20\,\text{mm}$, the debonded length decreased when adhesion increased from "low" (figure III.3a) to "high" (figure III.3c) values: this increase in deformation is detailed and discussed in III.3.4.

However, a steady-state regime was not systematically obtained, in particular in the two following cases:

- at high adhesion and low thicknesses: rupture of the interlayer occurred after partial delamination (*cf* III.3.2);
- at low adhesion and high thicknesses: delamination was asymmetric (*cf* III.3.3).

(a) r_{TEOS} = 20% **(b)** r_{TEOS} = 30% **(c)** r_{TEOS} = 40%

Figure III.3 TCTT: delamination of the PVB interlayer at $\delta = 20\,\text{mm}$ (h_0 = 1.14 mm, $\dot{\delta}$ = 10 mm·s^{-1}, T = 20°C).

III.3.2 Lateral crack initiation at high adhesion for thin interlayers

The limit between steady-state delamination and "rupture" behavior was reached with the highest adhesion ($r_{\text{TEOS}} = 40\%$) for the two smaller thicknesses. In fact, only one out of three samples at $h_0 = 0.76\text{mm}$ exhibited a steady-state behavior, while the two others ended up with a crack initiating and propagating from the edges of the interlayer during the test.

Figure III.4 presents an example of rupture behavior for the thinnest PVB. The interlayer remained attached to the left edge of the sample, preventing the delamination there, whereas the crack fronts were straight and horizontal in the central part of the laminate. The stretch increased to $\lambda = 2.3$ before a lateral crack started

to propagate through the interlayer, from the left edge (figure III.4a). Consequently, the force decreased when this lateral crack propagated until complete tearing of the interlayer (figure III.4b).

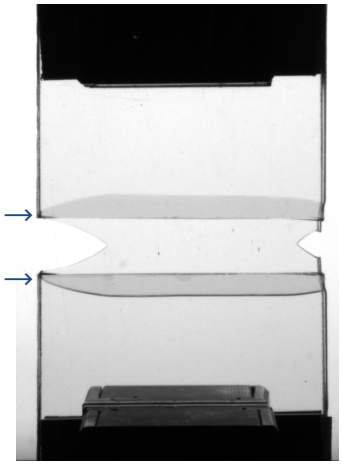

(a) Lateral crack propagation in the TCTT at δ = 9 mm. The interlayer did not delaminate on the left edge of the cracked laminate.

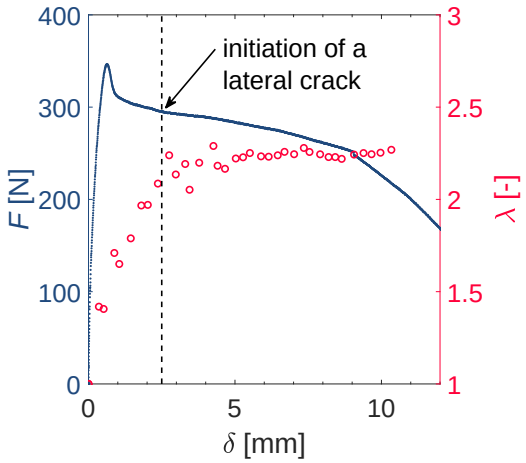

(b) Force and stretch *vs.* displacement: the lateral crack initiates at $\delta \approx$ 2.5mm and the force decreases at constant stretch.

Figure III.4 Lateral crack initiation and propagation in the TCTT for the thinnest interlayer (h_0 = 0.38 mm).

Consequently, the values of stretch for those failed samples – hollow symbols in figure III.9b – were lower than the steady-state value $\lambda_{ss} = 2.4$. At the smallest thickness $h_0 = 0.38$ mm, TCTT for both intermediate ($r_{\text{TEOS}} = 30\%$) and high adhesion ($r_{\text{TEOS}} = 40\%$) resulted in the rupture of the interlayer after a partial delamination.

Rupture of the interlayer could have happened because of an extrinsic defect, such as a small crack created in the interlayer during glass pre-cracking. Another possible source of extrinsic defects is the pinning of the interlayer on the sides of the glass plies (figure III.5). Indeed, PVB flows during the lamination process and tends to form a "bulge" on the sides on the samples (figure III.5b), which does not affect the result of the TCTT most of the time. However, in the worst-case scenario, the interlayer can get "pinned" on the lateral sides of the glass plies (figure III.5c). Stress concentration can then occur at the pinning location and provoke unexpected crack initiation.

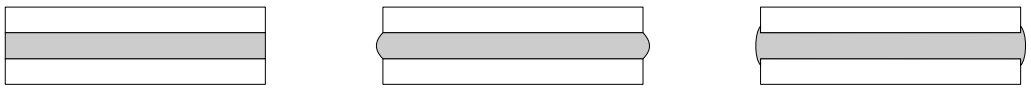

(a) Ideal TCTT specimen

(b) Actual TCTT specimen: interlayer flow induces a bulge on the sides.

(c) Worst-case TCTT specimen: the interlayer sticks to the lateral sides of the glass.

Figure III.5 Schematics of a TCTT specimen, view through the width. Lamination conditions (heat, pressure, sealing) may induce the formation of a bulge at the edges of the sample.

III.3.3 Loss of symmetry at low adhesion for thick interlayers

The delamination behavior departed from a steady-state regime for low adhesion ($r_{\mathrm{TEOS}} = 20\%$) and thick interlayers ($h_0 \geq 1\,\mathrm{mm}$). Crack propagation was asymmetrical (figure III.7), either from the beginning of the experiment or after crack arrest during the test.

Asymmetric crack initiation

In “asymmetric initiation”, the delamination fronts did not initiate at the same initial speed between the two sides of the cracked laminate. A “fast” front detached from only one side of the glass from the very beginning of the experiment (figure III.6a). This asymmetric situation could correspond to two cases, “shear” mode (figure III.7b) or “side selection” (figure III.7c).

Shear initiation could occur because of a misalignment of the glass cracks: if the cracks are not at the exact same vertical position, mode mixity shifts from pure tension to a mix between uniaxial tension and shear, which is reminiscent of the single-lap shear test. Moreover, a slight misalignment of the clamps could also favor asymmetry.

The side-selection mode could be favored by a chemical inhomogeneity between the two glass plies: the standard deviation of the adhesive energy being $0.2\,\mathrm{kJ \cdot m^{-2}}$ (see figure III.2), it could suffice to induce a preferred debonding on one side. Here again, misalignment of the clamps could account for the asymmetry by inducing a bending mode, which would favor propagation on the glass side undergoing more tension than the other.

Relying only on image contrast does not allow to asses which scenario actually occurred in the experiments.

In all cases, a second front propagated with a delay on the opposite glass ply (figure III.6b), and eventually caught up with the first front, so that the steady-state configuration (figure III.7a) was retrieved.

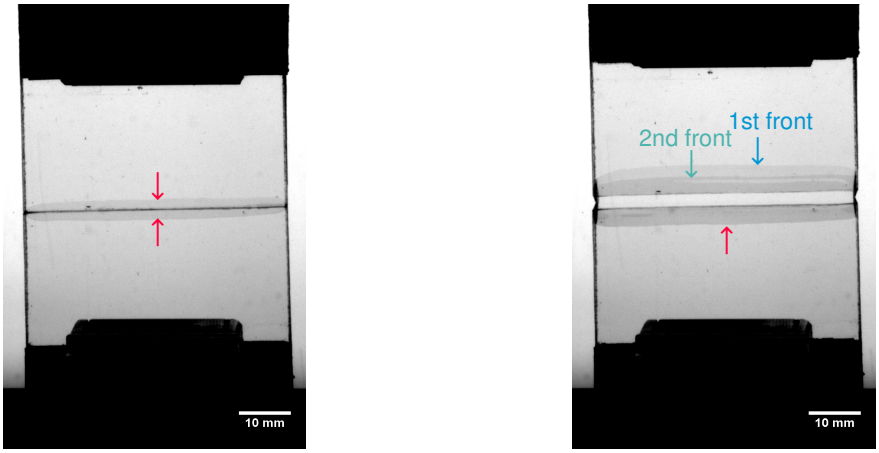

(a) δ = 0.3 mm: the delamination fronts initiate only on one of the two glass faces.

(b) δ = 3.6 mm: a second front propagates

Figure III.6 Asymmetric crack initiation (r_{TEOS} = 20%, h_0 = 1.52 mm).

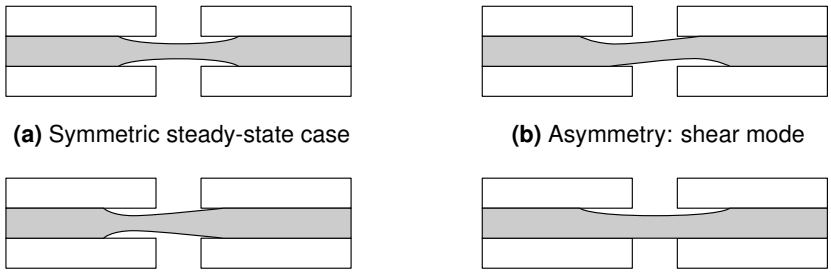

(a) Symmetric steady-state case

(b) Asymmetry: shear mode

(c) Asymmetry: side selection

(d) Asymmetry: face selection

Figure III.7 Interfacial delamination behaviors: scenarii of divergence from steady state at low adhesion

This asymmetric behavior is remminiscent of *Elzière*'s results with OTES. The difference of delamination length between "fast" and "slow" fronts was even more pronounced in his experiments, as the adhesion between PVB and OTES-treated glass was lower than $0.5\,\mathrm{kJ}\cdot\mathrm{m}^{-2}$.

Crack arrest: bifurcation phenomenon

Asymmetry was also observed between the two parts of the cracked sample. For the sample in figure III.8a, steady-state crack propagation (zone 1 in figure III.8b) was

observed until $\delta \approx 21\,\text{mm}$ when the front stopped advancing at the bottom side. After crack arrest, delamination went on at the top side and both force and stretch increased (zone 2).

As the propagation occurred between the clamps, the stretch measurement could not be performed further. Delamination restarted at the bottom front when the top front reached the extremity of the sample, resulting in a second plateau of force (zone 3). After complete delamination on both ends, the force increased as the interlayer was stretched between the pneumatic clamps (zone 4).

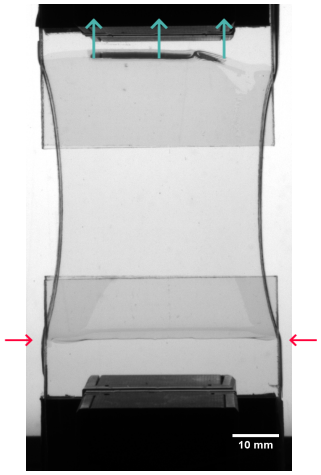

(a) Asymmetric front propagation (δ = 30mm). The bottom-side crack front stopped propagating while the top-side

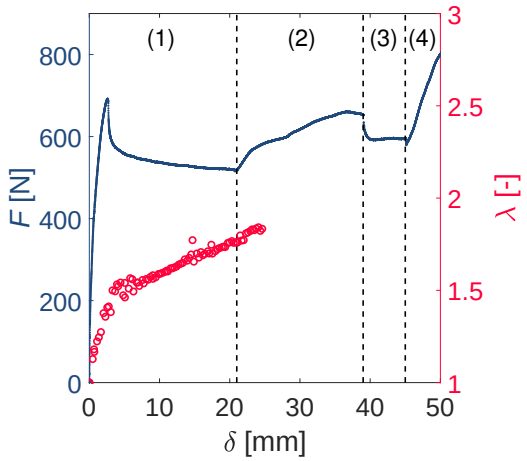

(b) Force and stretch *vs.* displacement curves. (1) Steady-state delamination; (2) bottom front arrest; (3) top front fully debonded, bottom front delamination restarts; (4) both fronts fully debonded.

Figure III.8 Crack arrest phenomenon and asymmetric propagation at low adhesion and thick interlayer (r_{TEOS} = 20%, h_0 = 1.14 mm).

Mode-mixity could be a hand-waving explanation for this “side-selection” phenomenon. At low adhesion, the local peel angle is close to zero, so that delamination occurs mostly in mode II. With the loading rate $\dot{\delta} = 10\,\text{mm} \cdot \text{s}^{-1}$, the crack velocity is too low to ensure stable propagation. Instead of four crack fronts propagating, Thus, the upper fronts propagate at a doubled velocity compared to the steady-state case: locally, the higher crack velocity induces a higher peel angle, so that these cracks can propagate.

III.3.4 Higher work of fracture at higher adhesion: a stretch effect

As detailed in the introduction to section III.3, we investigate here the evolution of $G_m$with the polymer thickness h_0 for three values of TEOS content in the surface coating, which means three values of PVB/glass adhesion. Before further examination, our results confirmed that the force—normalized by the initial width b_0—increased (figure III.9a) and the stretch decreased (figure III.9b) when h_0 increased, which was consistent with the literature about the TCTT[5].

Higher adhesion: same steady-state force, but more interlayer deformation

An increased amount of TEOS at the surface induced a higher deformation of the interlayer, while the delamination force remained the same. Indeed, the values of force were not significantly different for the three coatings (figure III.9a) while the average stretch of the interlayer increased when r_{TEOS} increased (figure III.9b).

Even if the force was fairly constant, the true stress increased with r_{TEOS} (figure III.9c). The stress σ was defined with respect to the current thickness h of the interlayer, assuming incompressibility:

$$\sigma = \frac{F}{bh} = \lambda \frac{F}{b_0 h_0}$$

The thinner interlayer supported the most tensile stress, around 30–35 MPa, whereas the thickest interlayer was submitted to 20 MPa.

Higher adhesion: higher macroscopic work of fracture

The macroscopic work of fracture increases with r_{TEOS} for a given thickness (figure III.10). For $h_0 = 0.76\,\text{mm}$, G_m increases from 7 to 10 to $12\,\text{kJ}\cdot\text{m}^{-2}$ when the TEOS content increased from 20 to 30 to 40% respectively. For a given coating, the trend of $G_m(h_0)$ appears to be linear considering only the steady-state experiments. Interpretation of this linear relationship, according to equation (I.1), is detailed in III.3.5.

Limit of the work of fracture for thin interlayers

In fact, the macroscopic work of fracture appears to be bounded around $6.5 - 7\,\text{kJ}\cdot\text{m}^{-2}$ for $h_0 = 0.38\,\text{mm}$, as interlayer rupture occurred for all three samples at $r_{TEOS} =$

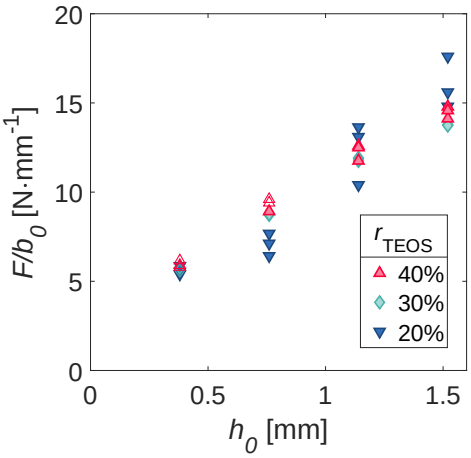

(a) Adhesive energy: force F at the plateau, normalized by the initial width b_0.

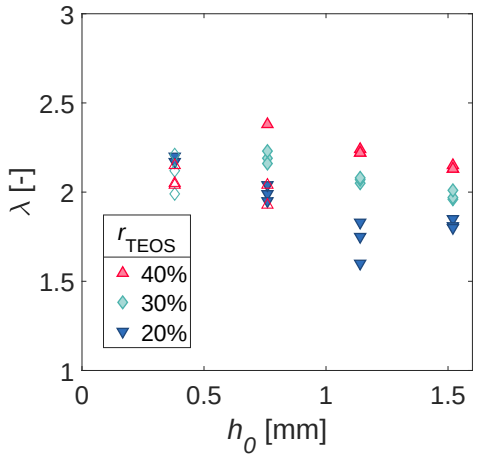

(b) Macroscopic stretch λ.

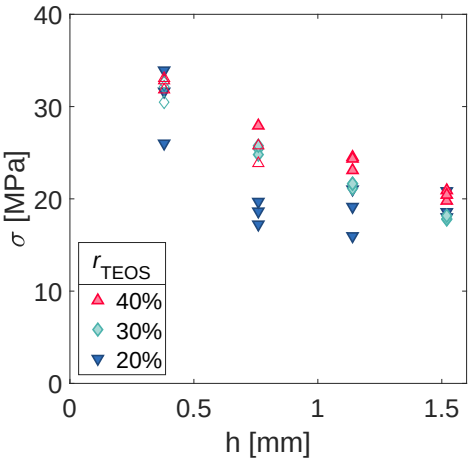

(c) Average true stress in the interlayer: $\sigma = \lambda F/(b_0 h_0)$.

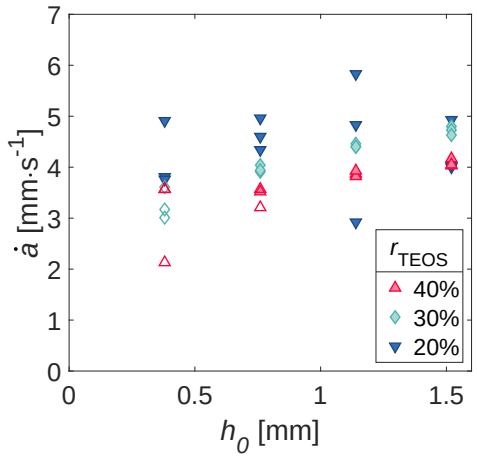

(d) Average crack velocity $\dot{a}$

Figure III.9 Through Crack Tensile tests with varying PVB/glass adhesion.
Filled symbols = steady-state delamination values.
Open symbols = values before propagation arrest (interlayer rupture or asymmetric cracks)

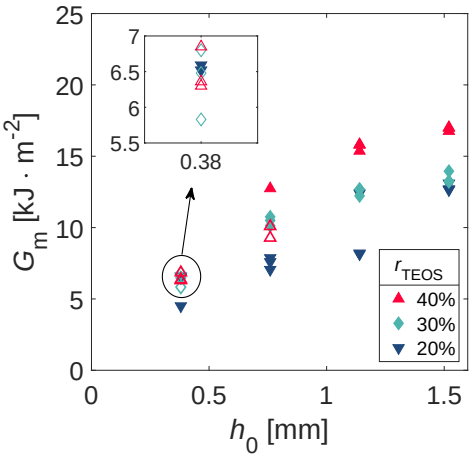

Figure III.10 Experimental macroscopic work of fracture. Filled symbols: steady-state delamination. Hollow symbols: interlayer rupture after partial delamination.

30% and 40%. In practice, a crack is more likely to initiate and propagate within PVB at lower thicknesses. Indeed, the stress borne by the interlayer increases from 20 MPa to 35 MPa (figure III.9c) when h_0 diminishes, while the thinner interlayer is also intrinsically less resistant to rupture—there is less material to break. We discuss this "rupture limit" in chapter VII. Over all, small lateral cracks or side-pinning defects are more likely to provoke a catastrophic tearing of the interlayer at lower thicknesses, despite all the experimental precautions we take.

III.3.5 Adhesion modification affects mostly the interface dissipation

A constant bulk dissipation...

The total macroscopic work of fracture was decomposed into an interfacial "crack" energy and into a bulk dissipation contribution according to equation (I.1) with a linear regression (figure III.11a). The ordinate at the origin $2\Gamma_{crack}$ increased with r_{TEOS} (figure III.11d) while the slope Π_{bulk}did not exhibit a significant trend (figure III.11b).

The mean value $\overline{\Pi}_{bulk} = 5.2\text{MJ} \cdot \text{m}^{-3}$ was fixed to perform the linear regression $G_m(h_0)$ again (figure III.11c). Indeed, the value of Π_{bulk} for the intermediate series was lower mostly due to the last point, at $h_0 = 1.52$ mm: the value of G_m was $13\,\text{kJ} \cdot \text{m}^{-2}$ while a value of $15\,\text{kJ} \cdot \text{m}^{-2}$ would be expected. The hypothesis of a constant slope

seemed reasonable, as confirmed by the good agreement of the linear fits with experimental data in figure III.11c.

...and an increased crack contribution

The crack contributions Γ_{crack} were reported in figure III.11d, for both models—Π_{bulk} unconstrained in filled symbols and constant $\overline{\Pi}_{\text{bulk}}$ in grey hollow symbols. The values of Γ_{crack} are comparable between the two fit methods and show a linear trend with respect to the TEOS content in the coating.

Here we remember that the adherence measured in peel was also increasing linearly with r_{TEOS} in the range 10% to 50% (figure III.2). However, the values in peel are about twice lower than the Γ_{crack}, which is consistent with a mode mixity effect. Mode mixity is lower in the peel test compared to the TCTT, therefore we expect a lower adhesion (*cf* section I.5.5)

All in all, we conclude that the interfacial crack contribution scales at the first order with the work of separation, while the bulk contribution does not:

$$\Gamma_{\text{crack}} \sim (\Gamma_0)^1 \qquad \Pi_{\text{bulk}} \sim (\Gamma_0)^0$$

III.4 Comparison with previous experiments: effect of the relative humidity

We compared our TCTT experimental data with *Elzière*'s for non-treated glass.

The PVB foils were same grade from the same supplier (Solutia® RB11 and RB41), but not from the same roll nor produced the same year. Nonetheless, we considered that the PVB composition did not change significantly between the two experimental series, and also assumed that both chemical composition and mechanical behavior were unchanged.

From a lower adherence at the same RH...

The peel tests were all performed at a relative humidity of *ca.* 50%RH, in a controlled environment. The peel adhesive energy was higher for the *Elzière* samples: $2.1\,\text{kJ}\cdot\text{m}^{-2}$ *vs.* $1.6\,\text{kJ}\cdot\text{m}^{-2}$ for our PVB-peel series. The standard error in our peel

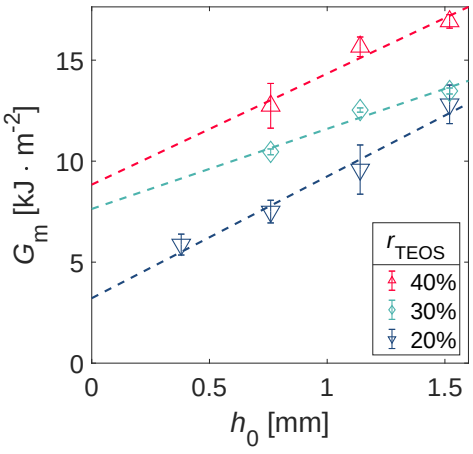

(a) Additive decomposition of the work of fracture: $G_m = 2\,\Gamma_{\text{crack}} + \Pi_{\text{bulk}} \cdot h$

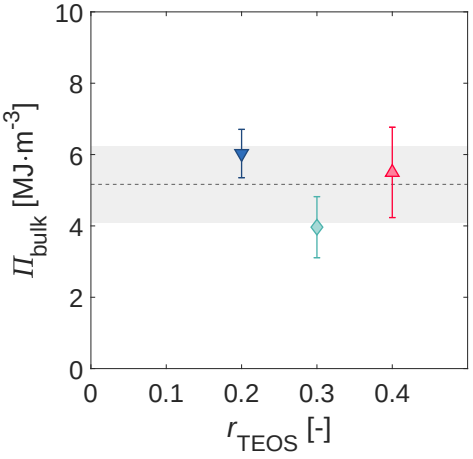

(b) Bulk contribution Π_{bulk}
Dashed line: average $\overline{\Pi}_{\text{bulk}}$ = 5.2 (1.1) MJ·m^{-3}

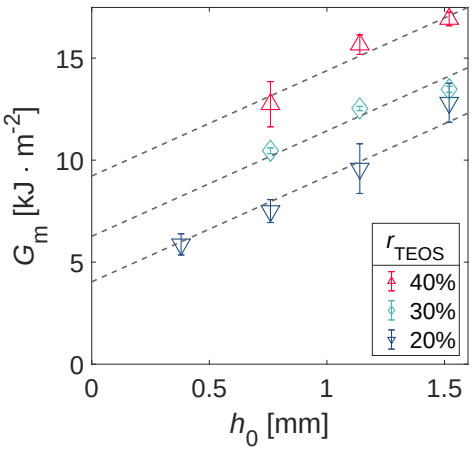

(c) Additive decomposition of G_m with a constant bulk term $\overline{\Pi}_{\text{bulk}}$ = 5.2 MJ·m^{-3}.

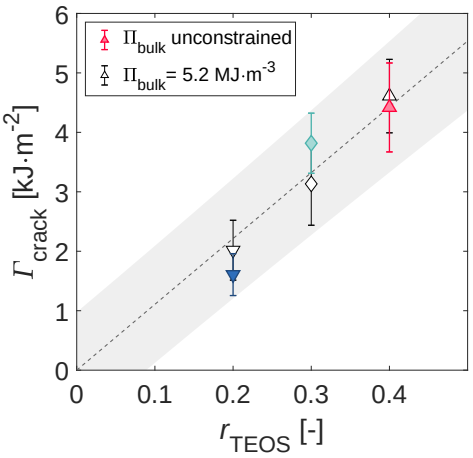

(d) Interface contribution Γ_{crack}.
Shaded area: 95% prediction bounds of the linear regression.

Figure III.11 Macroscopic work of fracture *vs.* initial interlayer thickness, for three surface treatments. The adhesion energy increased from 20% to 40% of TEOS in the surface coating.

experiments usually is $0.2\,\mathrm{kJ\cdot m^{-2}}$, which means the difference observed in the peel test can be considered as significant. The origin of this difference may arise from the surface state of the glass.

...to a higher crack contribution when RH decreases

In previous TCTT experiments, the relative humidity during storage and testing of the specimens was not controlled. For the present work, the interlayer was conditioned at 23–25 %RH prior to assembly. The laminate samples were also conditioned at 23 %RH after lamination, until the TCTT. As we know since section I.4.1, the water content influence drastically the adherence of PVB to glass, but it also affects its mechanical properties[81].

The macroscopic work of fracture was compared to the data of *Elziere*, who assembled a PVB interlayer stored at ambient relative humidity, and tested laminate samples stored also at ambient humidity, around 50 to 60 %RH.

Our series of samples conditioned at 23 %RH exhibited a higher macroscopic work of fracture in the TCTT: we attribute this increase to an increased adhesion, originating in the lower water content within the PVB interlayer (*cf* section I.4.1).

The additive decomposition of G_m resulted in a comparable value of Π_bulk: even though the water content also modifies the rheology of the PVB, our results did not show a significant difference in the bulk dissipation term. This conclusion obviously needs to be confirmed by more systematic experiments.

Thus higher probability of fracture for the lowest thickness in section III.3 could be explained by the increase of the adhesion energy, consequence of the lower relative humidity.

	Previous work	This work
G_peel $[\mathrm{kJ\cdot m^{-2}}]$	2.1	1.6
%RH in the TCTT	uncontrolled	23
$2\,\Gamma_\mathrm{crack}$ (s.d) $[\mathrm{kJ\cdot m^{-2}}]$	4.1 (1.0)	9.5 (3.9)
Π_bulk (s.d.) $[\mathrm{MJ\cdot m^{-3}}]$	7.9 (0.9)	8.3 (3.0)

Table III.2 Comparison of TCTT results with previous experiments (T = 20°C, $\dot{\delta}$ = 10mm/s)

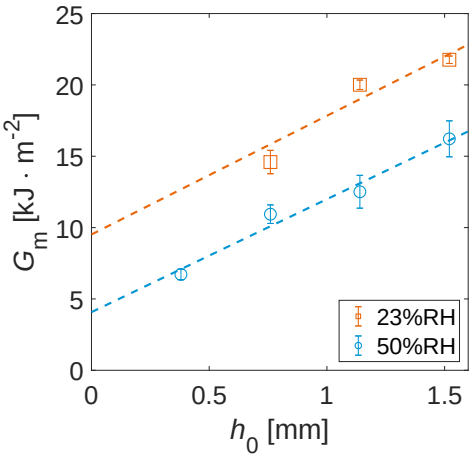

Figure III.12 Macroscopic work of fracture f or two relative humidities. Data at 50%RH were from *Elzière*[4].

III.5 A hand-waving model for the coupling between adhesion and macroscopic work of fracture

The effect of interfacial adhesion on the crack term is intuitive: a higher adhesion Γ_0 leads to a higher crack dissipation term Γ_{crack}. However, the apparent independence of the bulk contribution and of the steady-state force upon interface properties is surprising. We attempt here to explain this experimental observation.

Imposed loading rate: lower stretch at higher crack velocities

In the TCTT experiments, the crack velocity $\dot{\delta}$ is imposed. Recalling the definition of the stretch in section II.5.2, crack velocitiy $\dot{a}$ and macroscopic stretch λ are linked in steady-state: $\dot{\delta} = 2\,\dot{a}(\lambda - 1)$. Thus, crack velocity and stretch go opposite ways: under the same macroscopic loading rate $\dot{\delta}$, a faster crack—due to a different interface—leads to a smaller macroscopic stretch.

Competition between stretch and strain rate in the TCTT

In order to make the crack propagate, the polymer ligament must provide enough recoverable strain energy to the crack tip. The available energy density can be evaluated as the area under the unloading curve in the traction response of PVB (figure III.13). Intuitively, this recoverable energy increases when the polymer stretch increases (fig-

ure III.13a). In addition, rate-dependency and strain-hardening properties of PVB (*cf* figure II.2) imply the recoverable energy increases with the strain rate, for an imposed deformation (figure III.13b).

In the TCTT, the strain rate changes along the loading path: $\dot{\lambda}$ first peaks at the crack tip and reaches finite values in the fast stretching zone. These finite strain rates account for the viscoelastic bulk dissipation term Π_{bulk}. Far away from the crack tip, deformation of the polymer ligament is constant and the strain rate reaches zero. In figure III.13c, we have represented the loading path for the low and high adhesion cases:

- At low adhesion, crack velocity and strain rates are higher, but a lower stretch value is required to provide the crack tip with enough energy to propagate.
- At higher adhesion, crack velocity and strain rates are lower: the interlayer needs to deform further to provide a higher releasable energy to the crack tip.

All in all, compensation between the two effects—strain rate *vs.* stretch—may result in an essentially constant bulk contribution.

Clearly, the complexity of the problem calls for a more precise analysis. In this endeavor, we propose a numerical procedure in chapter VI.

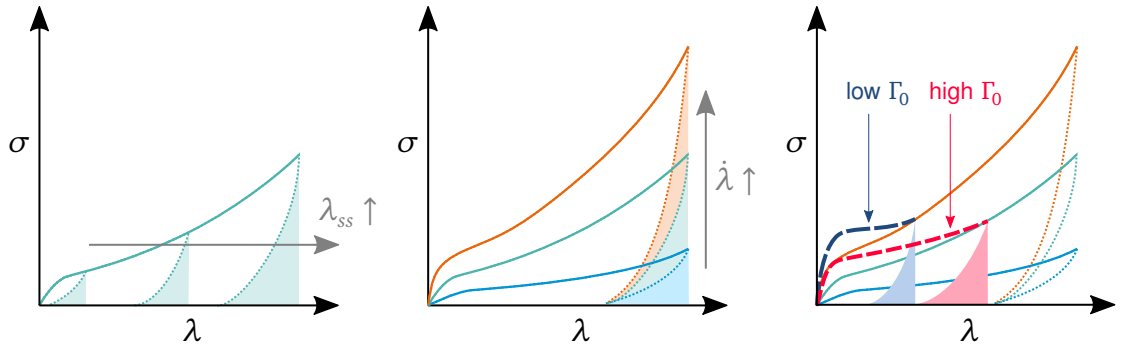

(a) Increase in recoverable energy at higher steady-state stretch, at constant rate.

(b) Increase in recoverable energy at higher strain rate, at constant stretch.

(c) Concurrent stretch and strain rate effects on recoverable energy. Dashed lines: loading path of the interlayer in the TCTT.

Figure III.13 Schematic of the evolution of the elastic recoverable energy in PVB.

Take-home messages of chapter III

- A methodology based on silane sol-gel chemistry was developed to modify the adherence between PVB and glass. The mix of MTES and TEOS, deposited by a wiping technique, allowed the control of PVB adherence to glass, *via* the control of the amount of hydroxyl groups exposed at the surface.

- The effect of adhesion on the delamination behavior was assessed with the TCTT with three MTES–TEOS coatings. Destabilization of the crack fronts was observed for lower adhesion, whereas rupture of the interlayer occurred at higher adhesion. Still, a common steady-state regime was observed for a PVB thickness of 1.1 mm.

- In steady-state TCTT, the force surprisingly did not vary much, while the stretch increased at higher adherence, resulting in a higher work of fracture. The linear evolution of G_m with interlayer thickness was decomposed into "crack" and "bulk" dissipation terms:

$$\Gamma_{crack} \sim (\Gamma_0)^1 \qquad \Pi_{bulk} \sim (\Gamma_0)^0$$

  The apparent independence of bulk dissipation upon interface adhesion has been attributed at the compensation of strain rate and stretch effects. At imposed loading rate, the adhesive crack propagates faster at lower adhesion: a higher crack velocity implies that the interlayer needs to deform less to ensure crack propagation.

IV

EVA: a semi-crystalline elasto-plastic interlayer

In this chapter, we provide a characterization of the EVA interlayer material, and more specifically its properties after the thermal treatment during the lamination process. First, we look at the evolution of EVA properties with temperature, and evidence three features: glass transition, fusion–crystallization and reticulation. We propose a thorough analysis of the reticulation process, and a kinetic model for the crosslinking reaction. The structure of the EVA interlayer is shown to be semi-crystalline, which is responsible for irreversible processes upon deformation. Finally, the mechanical properties are investigated in small strains with dynamic mechanical analysis, and in large strain by tensile testing. EVA is shown to be elasto-plastic at ambient temperature, plastic and viscoelastic at lower temperatures, and brittle at high temperatures.

Several brands and grades are available for industrial applications. A single reference was selected reference, namely Bridgestone™ EvaSafe, because it is actually used for laminated glass manufacturing. The interlayer consisted in a single foil of nominal thickness 0.38 mm: we can thus assume that the properties of the pristine material are consistent throughout all the experiments.

IV.1 Thermal transitions of EVA: crosslinking, crystallization, glass transition

IV.1.1 Thermal treatment during lamination

According to industrial specifications, the EVA interlayer is laminated in vacuum bags without additional pressure. The thermal treatment is performed in an autoclave to control both heating and cooling rates. Laminates are heated to 115°C for 1h and then at 135°C for 15min. Cooling from 135°C to room temperature is achieved in 30min, at a rate of $3°C \cdot min^{-1}$ approximately (figure IV.1).

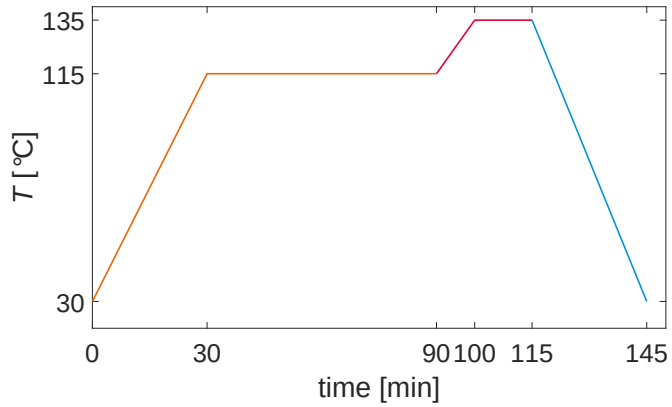

Figure IV.1 Thermal cycle for EVA lamination

The consequences of this thermal treatment on the final structure and mechanical properties of the interlayer are detailed in this chapter.

IV.1.2 Effect of temperature on the structure

Differential scanning calorimetry was performed as described in II.3.1. A heat-cool-heat run was carried out on the pristine EVA polymer. The results—solid lines in figure IV.2—show three main features, based on the first heat-cool cycle:

- A broad decrease of the heat capacity around −20°C typical of the glass transition region;
- A reversible feature, observed in both heating and cooling runs between 40°C and 80°C, which can be associated with a fusion–crystallization process.

- An exothermal peak above 130°C which is the signature of a bond forming chemical reaction.

In the second heating run, the shape of the fusion peak around 60°C was different compared to the first cycle. Moreover, the exothermal peak at high temperature was not observed in the second heat cycle.

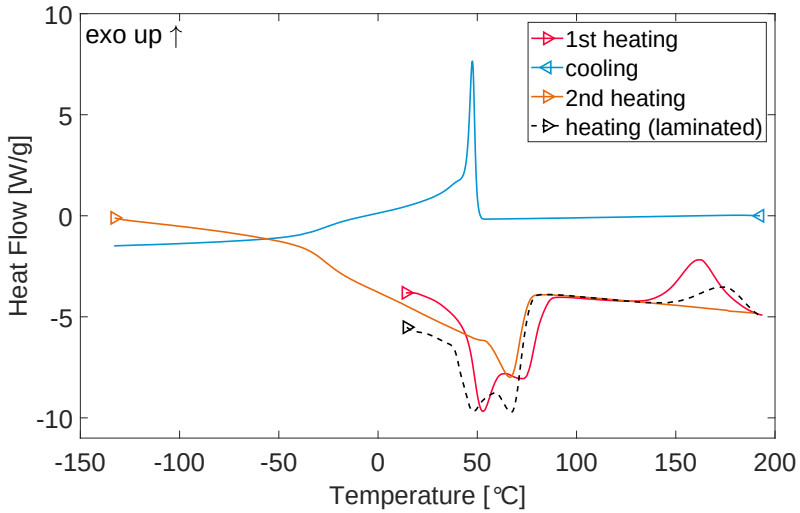

Figure IV.2 DSC of the EVA interlayer. Solid lines: pristine EVA in a heat-cool-heat cycle (heating rate = 20°C·min^{-1}, cooling rate = 10°C·min^{-1}). Dashed line: EVA after lamination between glass plies.

The EVA interlayer was also recovered after lamination, and analyzed in DSC with a single heat run (dashed line in figure IV.2). The fusion feature around 40–80°C is also observed, while the exothermal signal above 120°C is not retrieved. In the following, these DSC results and complemented with other experimental techniques to provide a characterization of the EVA structure, of the crosslinking process and of final mechanical properties of the interlayer.

IV.2 Structural characterization: semi-crystalline nature

IV.2.1 Crystalline content and crystallite size from DSC

The semi-crystalline nature of EVA is evidenced by the sharp and intense exothermal peak around 50°C upon cooling. Upon heating, the corresponding fusion signals

exhibits significant differences depending on the thermal history of the sample. For the pristine EVA sample, the fusion signal in the first heat run is composed of two peaks, around 50°C and 70°C. Then, after the fast cooling at -10°C/min in the DSC, we distinguish a unique peak around 65°C in the second heating cycle. For the EVA sample recovered from a laminated assembly (dashed line in figure IV.2), we also observe a double fusion signal around 50°C and 65°C.

The crystalline content is estimated by integrating the enthalpy of fusion upon heating. Crystallinity was determined as the ratio of the measured enthalpy over the reference enthalpy of 100% crystalline polyethylene[82]:

$$\chi = \frac{\Delta H_f}{\Delta H_f^*}$$

The reference enthalpy ΔH_f^* is reported in the range 277–293 $\mathrm{J \cdot g^{-1}}$ [82–84], rounded at 285 $\mathrm{J \cdot g^{-1}}$ here.

The approximate size of crystallites L can be estimated from the melting temperature T_m through the Gibbs-Thomson equation[83]:

$$T_m = T_m^0 \left(1 - \frac{2\,\sigma_e}{L\,\Delta H_f^*} \right)$$

The Gibbs-Thomson equation states that the reduction of the melting temperature from T_m^0—the thermodynamic value for an infinite crystal—to T_m is a surface-driven phenomenon: smaller crystallites melt earlier than large ones because the fusion enthalpy is lowered by surface energy of the crystallite. Therefore, two melting temperatures mean that two characteristic sizes of crystallites coexist within the material. However, in order to get an estimate of the crystallite size, we average the fusion temperature to 65°C, which corresponds to nanometric crystallites (table IV.1).

T_m [°C]	ΔH_f [$\mathrm{J \cdot g^{-1}}$]	T_m^0 [°C]	ΔH_f^* [$\mathrm{J \cdot g^{-1}}$]	σ_e [$\mathrm{mJ \cdot m^{-2}}$]	χ [%]	L [nm]
65	20.8	145.5	285	90	7.2	4

Table IV.1 Experimental values from DSC, reference thermodynamic values[82,83], calculated crystalline content and crystallite size

IV.2.2 Characterization of the crystallinity by X-ray diffraction

X-ray scattering experiments were performed at room temperature (21°C), before and after stretching.

Stretched samples were deformed to 200% strain ($\lambda = 3$) in a tensile testing machine prior to the SWAXS experiments (*cf* section II.4), and exhibited a permanent deformation. A sample of 3 mm×3 mm was cut from the central part of the dogbone specimen for SWAXS experiments.

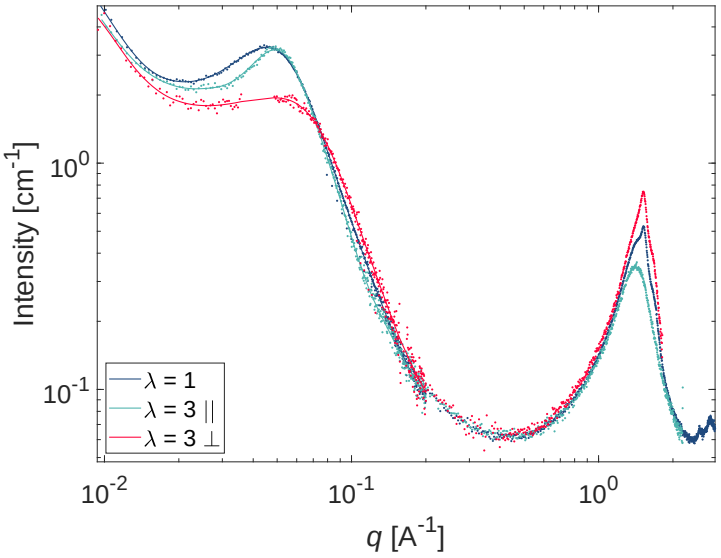

Figure IV.3 X-ray diffusion spectrum of EVA (combined SAXS and WAXS data). Isotropic integration for λ=1. λ = 3: azimutal integration over a 30° angle parallel and perpendicular to the traction direction.

On the diffraction signal of the unstretched sample, the wide peak around $1.4\,\text{Å}^{-1}$ is attributed to the amorphous phase. In addition, we notice a sharp peak at $q = 1.53\,\text{Å}^{-1}$: this distance matches the $(110)_o$ orthorombic planes of polyethylene crystallites, reported at $2\theta = 21.4°$ [85,86]. The bump at $q = 1.7\,\text{Å}^{-1}$ is the trace of the $(200)_o$ peak, reported at $2\theta = 24°$. More diffraction peaks from polyethylene can be distinguished above $2\,\text{Å}^{-1}$, although at the limit of detection.

In deformed EVA specimens, the WAXS crystalline signal increases perpendicular to traction and decreased along the tensile direction. This feature is attributed to the alignment of the ethylene chains aligned along the tensile direction within the crystallites[87]. Our WAXS observations are consistent with the literature on strain-

induced phase transitions in pure polyethylene, such as the orthorombic to monoclinic phase transition[86].

The SAXS signal evolves the opposite way: the peak around $q = 7 \cdot 10^{-2}\,\text{Å}^{-1}$ diminishes in intensity perpendicular to the traction direction, while this peak shifts slightly to higher q values along the tensile direction. In the literature, this long-spacing feature is attributed to the inter-lamellae distance. This evolution of the long spacing is related to a slip of the crystalline lamellae[87]: while the crystallized ethylene chains align towards the tensile direction (*cf* WAXS signal), the lamellar plane tilts perpendicular to the tensile direction. Melting–recrystallization processes triggered by shear[88] are also evoked in the literature.

IV.3 Crosslinking upon thermal treatment

As we have seen in the previous section, EVA undergoes a crosslinking reaction during the lamination process. Indeed, the formulation of the interlayer contains one or several types of peroxide curing agents.

Degree of crosslinking

The exothermic signal above 130°C indicated that a crosslinking reaction occurred. This peak was observed only for the first heating run: the sample was completely crosslinked upon heating to 200°C. The total enthalpy of reaction was measured by integration of the exothermal peak: $\Delta H_r^0 = 20.5\,\text{J} \cdot \text{g}^{-1}$.

This exothermal signal was also detected on the EVA sample after lamination: the EVA interlayer was not completely crosslinked between glass plies. The associated reaction enthalpy was $\Delta H_r = 7.1\,\text{J} \cdot \text{g}^{-1}$. The degree of crosslinking x was calculated with the ratio of the reaction enthalpies between the laminated sample and the pristine sample.

$$x = 1 - \frac{\Delta H_r}{\Delta H_r^0}$$

The degree of crosslinking was $x = 0.66$ from the DSC measurements. To our knowledge, under-curing EVA is advised by interlayer suppliers, and the crosslinking degree of 66% estimated here is consistent with their recommendations.

IV.3.1 Characterization of the curing kinetics: cure law

The kinetics of the curing reaction was investigated with rheology measurements in oscillatory mode[89]. The material was heated up to a cure temperature and the evolution of the complex modulus was monitored. The crosslinking reaction induces an increase in the total modulus along with a decrease in the loss factor. Indeed, the storage modulus increases more compared to the loss modulus.

This increase in storage (elastic) modulus is represented in figure IV.4: G' increases from around 30 kPa up to 0.5–1 MPa. The rate of the crosslinking reaction depends on the curing temperature: the higher the temperature, the faster the completion of the reaction (figure IV.4a).

For temperatures lower than 125°C, the actual duration of the measurement was longer than 3h in order to reach a plateau of modulus. Experiment duration was extended up to 12h for the 105°C sample. Characteristic times are defined in terms

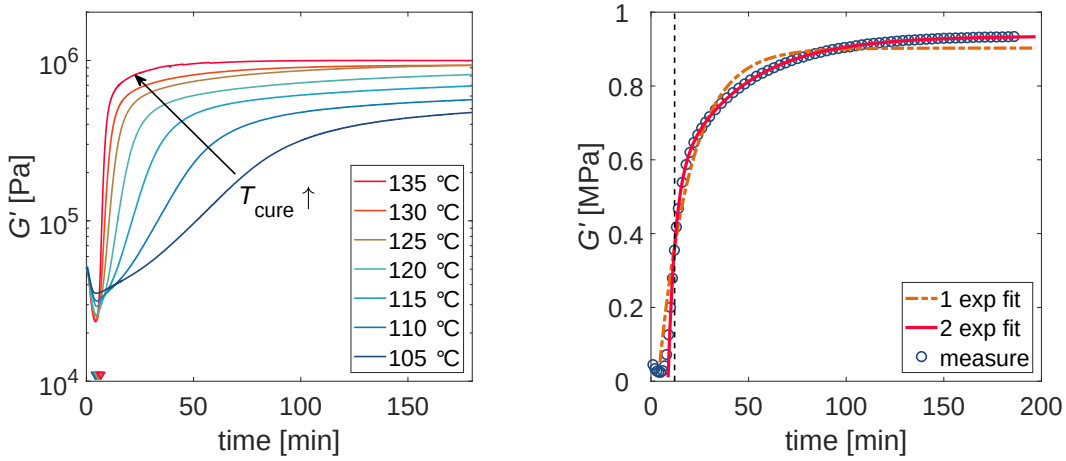

(a) Experimental cure laws *G'(t)* at various temperatures. The initial drop of *G'* is due to the heating from T_{init} = 90°C to T_{cure}. Triangular markers indicate the time when $T = T_{cure}$.

(b) Fit of the cure law with 1st-order exponential models, T_{cure} = 130°C. The dashed line indicates the time corresponding to the peak of *G"*, above which the material is considered as an elastic solid.

Figure IV.4 Curing behavior of EVA: time evolution of the storage shear modulus *G'* increases at constant temperature T_{cure}.

of the degree of completion x of the reaction:

$$G'(t_x) = \frac{x}{100}\left(G'_{\max} - G'_{init}\right)$$

For instance, the "optimal time of cure" is usually defined as t_{90} in the rubber industry. We chose the half time of reaction t_{50} as a characteristic time to develop a kinetic model. The values of the experimental t_{50} for different cure temperatures are reported in figure IV.5.

IV.3.2 Kinetics model

Peroxide degradation as the limiting step

The crosslinking reaction starts when a peroxide X is activated: the scission of the $O-O$ bond yields two radicals $R^\bullet$. These unstable radicals extract a hydrogen atom from surrounding polymer chains. In the case of EVA, the terminal methyl group of the vinyl acetate monomer is the preferred site of attack for the radical. The crosslink is formed when two activated monomers $P^\bullet$ encounter. In the end, one peroxide molecule ends up into one crosslink:

$$1X \rightarrow 2R^\bullet \overset{+2P}{\rightarrow} 2P^\bullet + 2R \overset{-2R}{\rightarrow} P-P \tag{IV.1}$$

According to the literature, we consider that the first step is the kinetically limiting one. A first-order kinetics is considered for peroxide degradation[90]

$$\frac{\partial [X]}{\partial t} = -k[X] \Rightarrow [X](t) = [X]_0 \, \mathrm{e}^{-kt}$$

The volume density of crosslinks ν is related to the number of reacted peroxide molecules, in a 1:1 ratio according to equation (IV.1).

$$\nu(t) = [X]_0 - [X](t)$$

The maximum crosslink density is equal to the initial peroxide concentration at 100% conversion: $[X]_0 = \nu_{\max}$.

$$\nu(t) = \nu_{\max}\left(1 - \mathrm{e}^{-kt}\right)$$

The increase in elastic modulus of the material is attributed to the addition of crosslinks according to classical rubber elasticity theory:

$$\Delta G'(t) \sim \nu(t)\,\mathrm{k_B}T = \nu_{\max}\mathrm{k_B}T(1-\mathrm{e}^{-kt})$$

Arrhenius equation

The Arhhenius equation states that the evolution of the reaction rate is exponentially activated by the temperature:

$$k = A \exp\left(-\frac{E_a}{RT}\right)$$

The gas constant R, product of the Avogadro and Boltzmann constants, is equal to $8.314\,\mathrm{J \cdot mol^{-1} \cdot K^{-1}}$. Assuming the first-order kinetics model, the half-time of curing was directly related to the activation energy with the Arrhenius equation:

$$t_{50} = \frac{\ln 2}{k} = \frac{\ln 2}{A} \exp\left(\frac{E_a}{RT}\right) \Rightarrow \ln(t_{50}) = A' + \frac{E_a}{RT}$$

The observed curing time is faster than the half-time reported for usual peroxides, and the experimental cure laws are not well fitted with a single exponential model.

In fact, polyethylene and EVA formulations can contain a "cure booster", such as a triallyl isocyanurate (also called triallyl-triazine-trione) in addition to peroxides[70]. The "cure booster" is a smaller molecule compared to long entangled polymer chains, therefore it diffuses faster within the polymer network. We assume that the "cure booster" accelerates the transfer of the radical towards surrounding available vinyl acetate groups. The activation energy of the reaction is not affected: the limiting step is still the decomposition of the peroxide. The cure booster only affects the value of the frequency factor in the Arrhenius equation by increasing the frequency of crosslink formation.

Assuming the presence of a cure booster, the kinetics model was enhanced with addition of another term:

$$\Delta G'(t) = b_1 \exp(-k_1 t) + b_2 \exp(-k_2 t) \tag{IV.2}$$

$$k_i = A_i \exp\left(-\frac{E_a}{RT}\right) \qquad\qquad b_1 + b_2 = G'_1 - G'_0$$

Isothermal curves were fitted with the two-exponential model (IV.2) (figure IV.4b). Corresponding half-cure times were calculated as $t_{1/2}^{\mathrm{fit,i}} = \ln 2 / k_i$ and plotted in the Arrhenius form (figure IV.5). The activation energy is identical for the two characteristic times (table IV.2) which confirms our assumption of a unique activation energy

for the reaction.

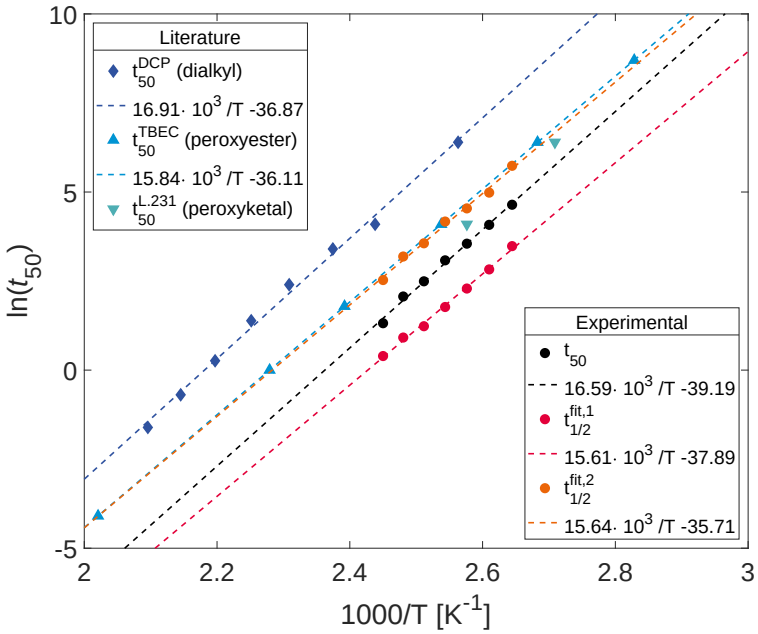

Figure IV.5 Arrhenius plots for the curing of the EVA interlayer. Literature data are taken from peroxides' technical information[89,91,92]

	Experimental	Fit, 1st term	Fit, 2nd term	Average (± s.d.)
E_a [kJ · mol^{-1}]	137.9	129.8	130.0	132.6 (± 4.6)

Table IV.2 Activation energy of the crosslinking reaction.

The activation energy of 132.6 kJ · mol^{-1} was consistent with the literature[93] as a typical value of activation energy for peroxide degradation activation.

IV.4 Mechanical behavior of cured EVA: elasto-plasticity

IV.4.1 Small strain behavior of EVA

Small-strain response of EVA has been analyzed by DMA (*cf* section II.4). Temperature-sweep experiments were performed at 1Hz and 0.1% strain, in the linear domain (figure IV.6). The storage G' and loss G'' moduli were measured upon heating and cooling at 1°C/min.

In figure IV.6a, G' decreases and G'' reaches a maximum around -20°C, which is characteristic of the glass transition. The temperature shift between heating and cooling curves is attributed to the dynamic thermal lag detailed in II.4.1. The glass transition temperature— temperature corresponding to the maximum of $\tan\delta = G''/G'$—is reported in figure IV.6b. The thermal lag of the measurement can affect significantly the observed T_g. Averaging between heating and cooling experiments (*cf* section II.4) allows to determine a T_g between -20 and -18°C.

Below T_g, the glassy modulus G'_0 is equal to $2-3$ GPa, a typical value for glassy polymers. Above the glass transition, the storage modulus decreases to $10-30$ MPa at room temperature. These values are one order of magnitude above the modulus of a standard elastomer in the rubbery state. This modulus increase is due to the semi-crystalline nature of EVA, characterized in IV.2. Upon heating, both G' and G'' decrease from 60°C to 80°C, which is attributed to the fusion of the crystalline domains. Above 80°C, the storage modulus reaches a plateau $G'_\infty \approx 1$ MPa, typical for a crosslinked polymer network.

Overall, the small strain behavior of EVA exhibits the features of a semi-crystalline polymer.

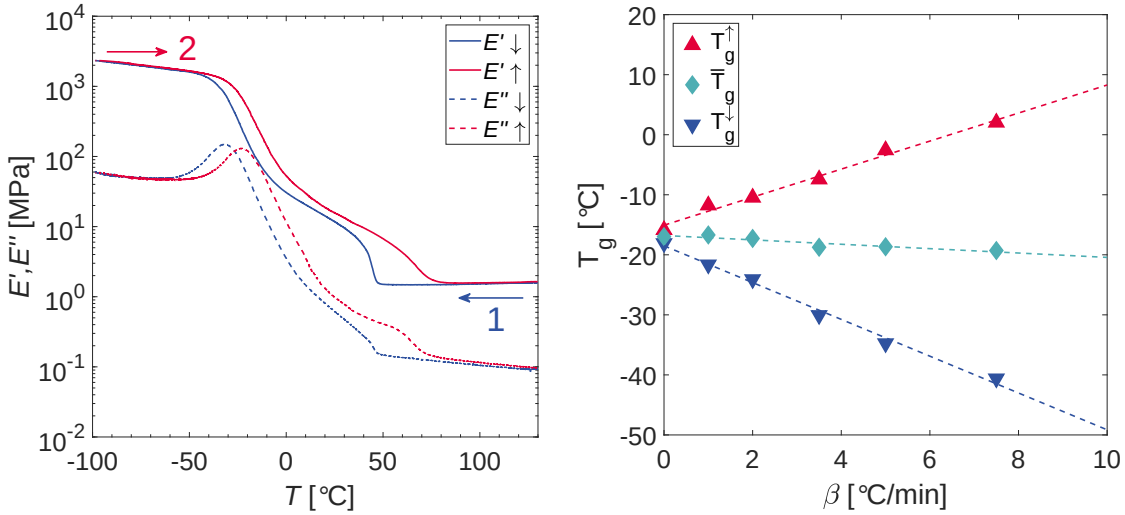

(a) Storage modulus E' and loss modulus E'' of EVA *vs.* temperature, 0.1% deformation, 1Hz. (heating/cooling rate β = 1°C·min^{-1})

(b) Glass transition temperature of EVA *vs.* heating or cooling rate in DMA. $T_g^{\uparrow}$ = heating, $T_g^{\downarrow}$ = cooling, $\overline{T}_g$ = average.

Figure IV.6 DMTA of EVA. Glass transition occurs around -20°C and crystallization/fusion around 50°C to 80°C (frequency = 1Hz, deformation = 0.1%).

IV.4.2 Large strain behavior of EVA

Tensile testing has been performed as described in section II.4.2. EVA specimens were stretched up to around 200% deformation ($\lambda = 3$) at imposed displacement rate, and then unloaded until return to the initial clamp position.

Dissipative behavior in a wide range of temperature

Tensile properties at various temperatures are presented in figure IV.7. The temperature was varied between -20°C, around the glass transition, up to 40°C, below the melting temperature. First, we notice that the initial stiffness of EVA increases at lower temperatures, over one order of magnitude (table IV.3).

We observe a pronounced strain-softening around $\lambda = 1.2$–1.3 for all temperatures between -20°C and 40°C. This strain-softening is accompanied by a large hysteresis and a remnant deformation upon unloading. The critical value for stress softening also increases at lower temperature (table IV.3).

Elasto-plastic behavior at ambient temperature

Tensile tests have also been performed at various loading rates (figure IV.8).

At 20°C and 40°C, tensile properties of EVA were mostly independent from the strain rate (figures IV.8b and IV.8a). The residual deformation upon unloading is never recovered, even if we wait several minutes. The combination of a rate-independent dissipative behavior, a yield stress and a permanent deformation is the signature of a plastic behavior.

T [°C]	E_0 [MPa]	σ_Y [MPa]
-20	172	14
0	42	5
20	21	3
40	11	2

Table IV.3 Young's modulus at 5% strain E_0, engineering yield stress σ_Y of EVA. (strain rate = 0.5 s^{-1})

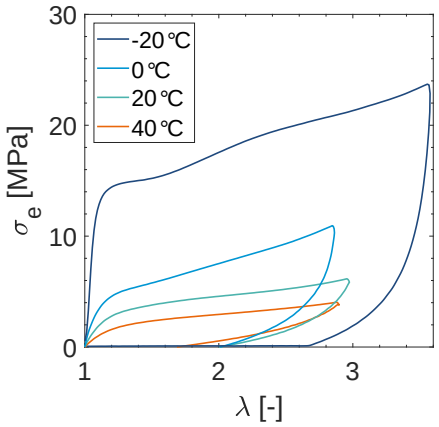

Figure IV.7 Engineering stress *vs.* stretch curves of EVA at the strain rate $\dot{\lambda}$ = 0.5s^{-1}. Both Young's modulus and yield stress increased towards the glass transition ($T_g = -18$°C).

Loading-rate effects at lower temperatures

The tensile response begins to exhibit a strain-rate dependency at 0°C. Both initial modulus and yield stress increase at higher strain rates, at 0°C and even more at -20°C (table IV.3). Around the glass transition temperature, the yield stress increases from 10 to 14 MPa when the strain rate is raised by two orders of magnitude.

We rationalize higher stiffness and yield stress at lower temperature as the manifestation of the glass transition in the amorphous content of EVA. Indeed, the apparition of a pseudo-yield stress close to the glass transition was also observed with PVB (*cf* figure II.2). Close to the glass transition, polymer chain dynamics is slowed down, hence the higher stiffness. Rearrangement events are activated by the strain energy, hence the apparent yielding behavior. We infer identical processes to occur here in the amorphous phase of EVA, which represents around 90% of the material. Still, truly plastic deformation in the crystalline domains may still occur, but it would be lumped in a single yield phenomenon.

Experimentally, the samples recover most of their initial shape when taken out of the -20°C chamber and left sitting at room temperature. Therefore, we attribute the large hysteresis mostly to viscoelastic processes close to the glass transition. This interpretation could be consolidated by a stress relaxation test, or a zero-stress creep experiment after unloading.

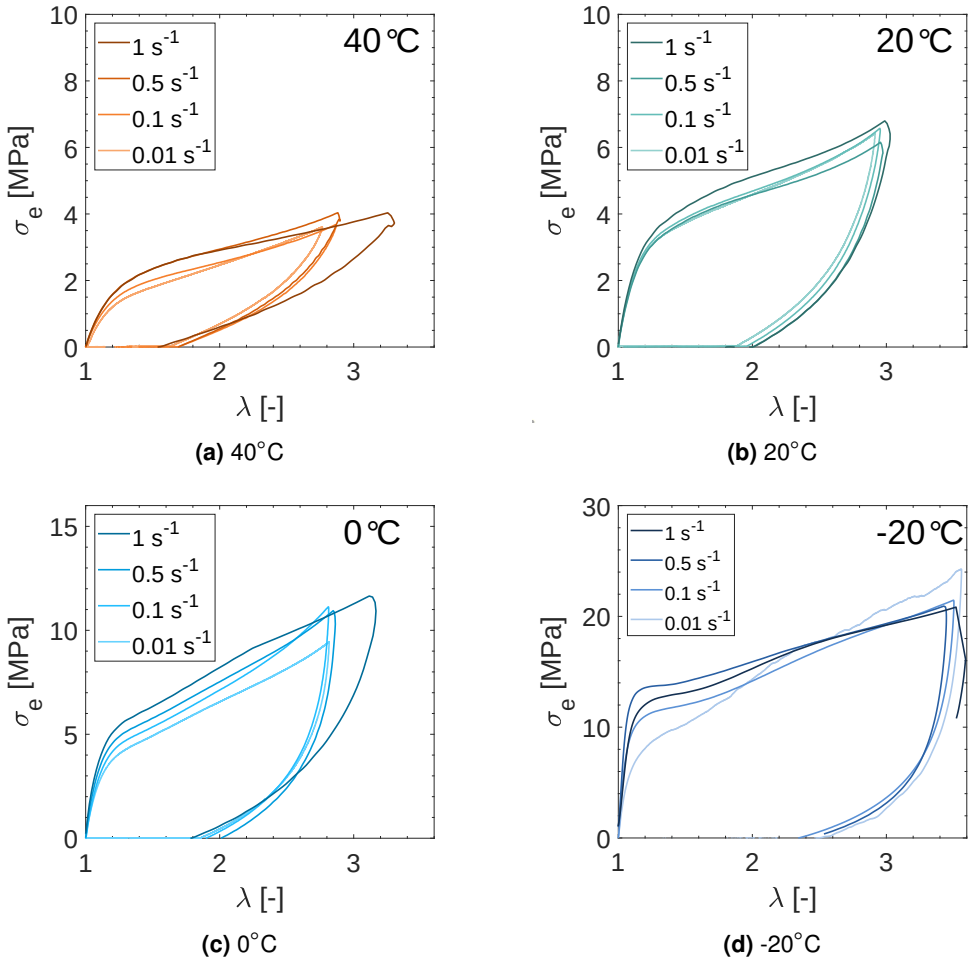

(a) 40°C **(b)** 20°C

(c) 0°C **(d)** -20°C

Figure IV.8 Engineering stress *vs.* stretch curves of EVA until 200% deformation at strain rates from $0.01 s^{-1}$ to $1 s^{-1}$ (maximal displacement = 50 mm).

A fragile rubber at high temperatures

The initial modulus decreased to 2.4 MPa above the melting temperature, at 80°C. This modulus value was consistent with DMA measurements (IV.6a) and in the typical MPa range for an elastomer in the rubbery state. The material followed a non-linear elastic behavior: neither viscoelastic nor plastic features were observed in the tensile tests. Stretchiness was strongly decreased at 80°C: the maximal extensibility decreased to around 100% ($\lambda = 2$) compared to $250-300$% at 20°C.

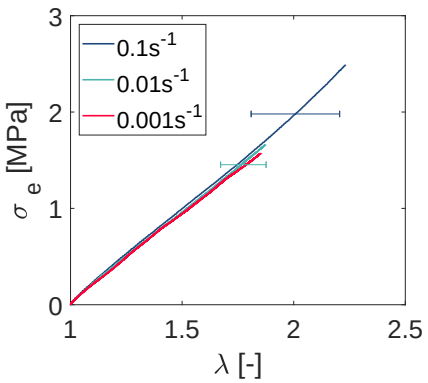

Figure IV.9 Tensile test to rupture for EVA at 80°C. The errorbars indicate the standard deviation of the strain at break (3 samples).

Cyclic experiments: dissipated energy

Cyclic tensile experiments have been performed at 20°C. Beforehand, we have noticed that the shape of the unloading curve—at a given stretch—is not affected by repeated cycles, even if the reloading curve follows a softer path. Upon reloading, we recover the stress value obtained at the maximum stretch in the previous cycle, as expected of a plastic material. Therefore, loading-unloading cycles are repeated on the same sample at an increasing maximum stretch (figure IV.10a).

Strain energies are estimated as suggested in section III.5. The total strain energy $W_t(\lambda)$ is computed by integrating the loading stress-strain curve, the recoverable strain energy $W_r(\lambda)$ with the unloading curves. The true stress σ is deduced from the engineering strain σ_e assuming incompressibility: $\sigma = \lambda\,\sigma_e$.

$$W_t(\lambda) = \int_1^{\lambda} \sigma_{\text{load}}\,\mathrm{d}\lambda \qquad W_r(\lambda) = -\int_{\lambda}^{1} \sigma_{\text{unload}}\,\mathrm{d}\lambda \qquad W_d = W_t - W_r$$

Total and recoverable strain energies coincide up to $\lambda = 1.3$, when plastic deformation starts to arise. The dissipated energy ratio W_d/W_t increases with the deformation, until saturation for $\lambda \geq 3$. Despite the small fraction of crystalline domains in the material, around 10%, EVA can dissipate up to 70% of the total strain energy at large deformations.

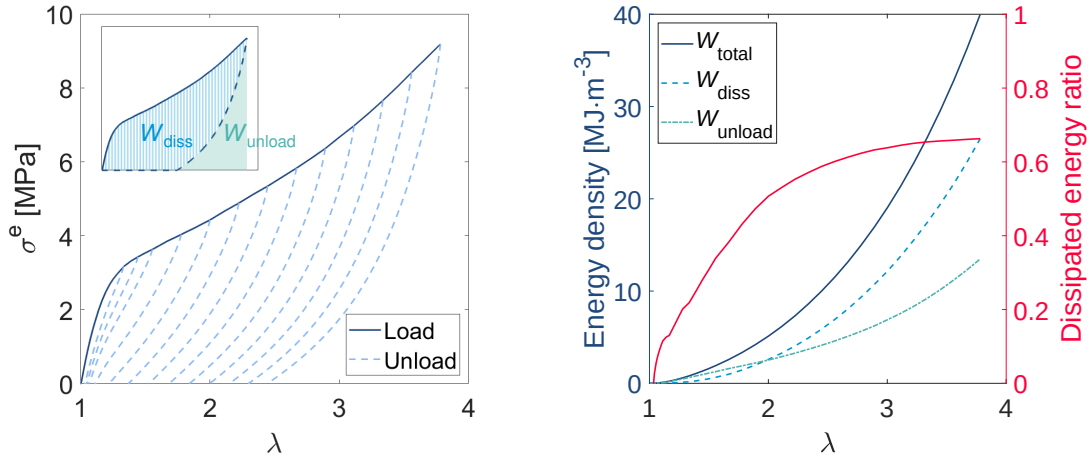

(a) Cyclic engineering stress *vs.* stretch curves. Intermediate re-loading curves are not shown.

(b) Energy densities from tensile curves. Dissipated energy ratio = W_{diss} / W_{total}.

Figure IV.10 Cyclic tensile tests on EVA at 20°C.

Take-home messages of chapter IV

- The EVA interlayer used in this works exhibits a glass-transition around −20°C, fusion–crystallization features between 50 and 70°C, and a crosslinking reaction above 120°C.

- The rate of the crosslinking reaction, characterized by rheology, follows a first-order kinetics limited by the decomposition of the peroxide crosslinker. The presence of a "cure booster" in the formulation induced a process with two characteristic times, however with the same activation energy estimated around 130 $kJ \cdot mol^{-1}$.

- The mechanical properties of EVA are elasto-plastic at ambient temperature, up to the melting temperature. The plastic behavior is characterized by a yield stress, around 3 MPa at 20°C, above which strain-softening and permanent deformation are observed. The plastic behavior is attributed to the semi-crystalline content, around 10% in volume. X-ray scattering experiment confirm the presence of crystallized ethylene domains, which deform irreversibly upon deformation.

  Below 0°C degrees and below towards the glass transition, viscoelastic features arise and EVA become stiffer and more dissipative at lower temperatures.

  Above the melting temperature, EVA behaves as a crosslinked elastomer which breaks around 100% deformation.

V

Delamination between EVA and glass: recovery of a steady-state

After the characterization of the polymer in the previous chapter, EVA is studied here as interlayer in laminated glass. We do not have control over the formulation of the EVA foil, in particular in terms of additives (*cf* section II.1). Even worse, EVA is designed to stick as much as possible to its substrate, as shown in V.1.1. Nonetheless, we know that delamination and stretching of the interlayer would enable significant energy dissipation. Thus, we address the following questions:

- Is it possible to obtain a stable delamination behavior with this plastic interlayer?
- How does the work of fracture relate to the plastic properties of EVA?

We first demonstrate that modifying the chemistry of the glass surface is a successful tweak that allows stable delamination between EVA and glass, in particular with a coating of methyltriethoxysilane (section V.1). Then, EVA laminates with a methylated glass surface are subjected to the TCTT, in order to probe the effects of interlayer thickness and loading rate at ambient temperature, well above the glass transition (section V.2). Finally, the major role of viscoelasticity in energy dissipation is underlined with TCTT at lower temperature (section V.3). Rate-dependency and volume dissipation are recovered close to the glass transition of the EVA interlayer. Interestingly, when the interlayers are tested at their respective glass transitions, EVA exhibits a higher energy dissipation compared to PVB.

V.1 Adhesion between EVA and glass: surface chemistry strikes back

V.1.1 EVA on bare glass: immediate rupture in the TCTT

After glass is laminated with EVA without any additional surface treatment than washing with an alkaline soap, no delamination occurs in the TCTT: the EVA ligament fails almost immediately (figure V.1).

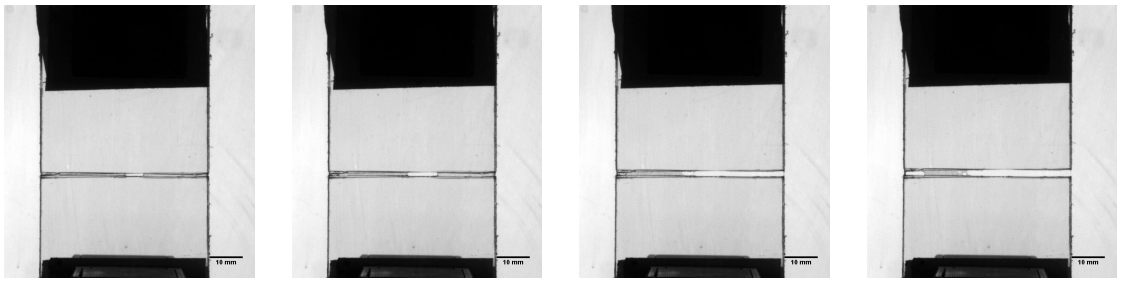

(a) $\delta = 0.5\,\text{mm}$ **(b)** $\delta = 1.0\,\text{mm}$ **(c)** $\delta = 1.5\,\text{mm}$ **(d)** $\delta = 2.0\,\text{mm}$

Figure V.1 Through Crack Tensile Test of an EVA laminate: immediate rupture

At the origins of EVA–glass adhesion

In order to understand why the interlayer cannot debond from the glass, we review shortly the interactions responsible for adhesion between EVA and glass. We have identified three main origins to EVA adhesion:

- Van der Waals interactions, always present between polymer chains and a surface, account for the thermodynamic work of adhesion in the order of 10–100 $\text{mJ}\cdot\text{m}^{-2}$. However, we will see that we can neglect the dispersive Van der Waals forces compared to other contributions.
- Surface crystallization, in semi-crystalline polymers, has been demonstrated to affect adherence—see the work of *Cho et al.*[94] for instance. The surface energy of the substrate influences the local arrangement of crystallizable segments in the vicinity of the surface.

  High-energy surfaces promote nucleation of crystallites at the surface, referred to as trans-crystallization: it increases the strength of the interface and results in a

higher adhesion. Low-energy surface favor crystallite nucleation in the bulk of the material, without enhancing the adhesion. Surface crystallization induces up to a thousand-fold increase between thermodynamic work of separation and interface strength, as shown by *Cho et al.* on highly crystallizable polypropylene.

Even though the crystalline content of the EVA studied here is low, around 10% (*cf* section IV.2), surface crystallization could still occur and increase the adherence.

- Functional silanes incorporated in the polymer formulation, such as vinyltriethoxysilane[71,95], form covalent bonds to the glass surface via hydrolysis-condensation and to the polymer chains via radical activation of the C=C bond during the curing process (*cf* section IV.3).

Covalent bonds at the interface: the dark side of adhesion

Covalent bonding induced by the silane additive is supposed to be the critical contribution to the adhesion energy. We suggest to estimate the work of separation as $\Gamma_0 = a_b \cdot W_b$, with a_b the area density of "bridging strands" and W_b the energy required to break them. The "bridging strand" in our system is the vinylsilane. We consider the dissociation energy of a C–C bond E_D, equal to 370 kJ/mol[96], as the energy required to break the vinylsilane bridge. Our argument is reminiscent of the *Lake & Thomas* model for polymers[97]. In the *L&T* model however, the bond energy is lower than the dissociation energy but an enhancement effect arises from the stretching of long polymer chains[98]. Here, we simply consider that the vinylsilane is the weakest link and breaks upon deadhesion.

Under the hypothesis that all available surface silanols are linked to the interlayer, a_b is assimiliated to the area density of hydroxyl groups at the surface of the glass, estimated around $a_{OH} \approx 2\,\mathrm{OH/nm^2}$[99]. All in all, we evaluate the separation energy as:

$$\Gamma_0 = a_{OH} \frac{E_D}{N_A} \approx 1\,\mathrm{J \cdot m^{-2}}$$

This value of Γ_0 is already one to two orders of magnitude larger than the usual value for the work of separation, around $10 - 100\,\mathrm{mJ \cdot m^{-2}}$.

The actual interface strength being several orders of magnitude greater than Γ_0 in polymer systems, we understand that adhesion of the commercial EVA interlayer onto bare glass is merely too high for delamination to occur. Thus, it appears necessary to reduce the strength of the interactions between the glass surface and the interlayer.

V.1.2 Modification of the adhesion between EVA and glass: return of the silanes

Now, we need to adjust adhesion of EVA to make delamination—and therefore TCTT experiments—possible. Chemical modification of the glass surface proved itself to be an adequate method for adhesion control in chapter III, so we followed a similar strategy with EVA. Hydrophobic silanes are selected to reduce adhesion, specifically triethoxysilanes with an alkyl or a fluorinated moiety (*cf* section II.2). The goal of surface modification is to prevent "adhesion promoters" from bonding with the glass surface. The effect of the chemistries on adherence are assessed with peel tests (figure V.2a).

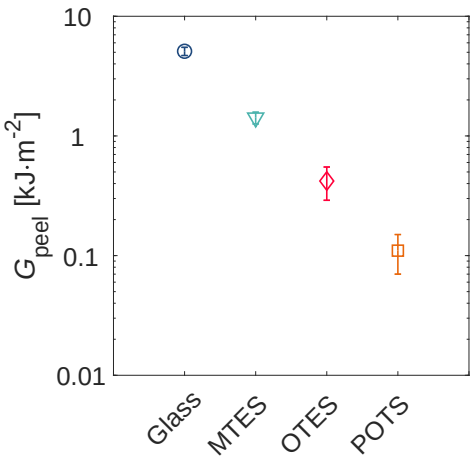

(a) Adherence energies of the EVA interlayer *vs.* surface chemistry of the glass substrate.

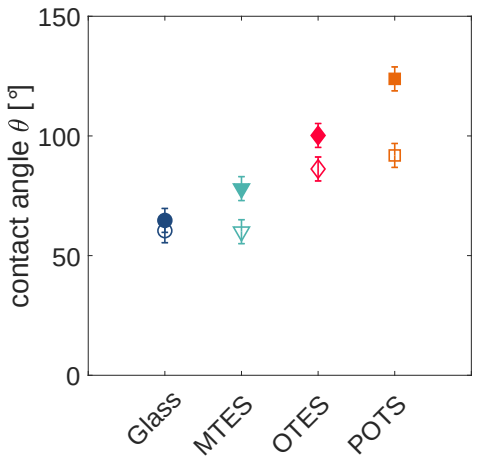

(b) Contact angle (sessile drop method) *vs.* surface chemistry of the glass substrate. Filled symbols = advancing drop. Hollow symbols = receding drop.

Figure V.2 Controlling adhesion of EVA via surface chemistry: peel adherence and contact angle.

Note the logarithmic scale in figure V.2a: the adherence decreases from $5\,\mathrm{kJ}\cdot\mathrm{m}^{-2}$ on bare glass to 1.5, 0.5 and $0.1\,\mathrm{kJ}\cdot\mathrm{m}^{-2}$ with MTES, OTES and POTS respectively. Furthermore, the value on bare glass is surely underestimated, as the EVA interlayer debonded from the backing instead of the substrate after an initial steady-state peel regime. The variation of the adherence with surface chemistry follows the same trend—but with a widely different magnitude—than the surface energy characterized by wetting experiments (figure V.2b). Hydrophobicity of the surface

increased continuously from pristine glass to MTES, OTES and POTS-treated glass, which means that the surface energy decreased. The trans-crystallization effect—described in V.1.1—appears as a a consistent explanation for the order of magnitude difference in adherence between fluorinated, octylated and methylated surfaces, as it exalts the differences in surface energies.

However, the control of adhesion is still coarse. As mixing two silanes was successful with PVB (chapter III), the same approach has been investigated for EVA, with a silane mix of MTES and OTES. Following a comparable protocol as in section III.1, the molar ratio of MTES and OTES was varied in surface coatings. The peel-test results are presented in figure V.3.

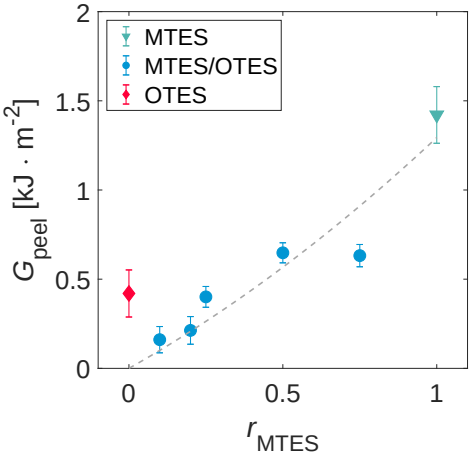

Figure V.3 Peel adherence of EVA vs. MTES content in MTES–OTES coatings. The grey dashed line only a guide for the eye.

Adherence of EVA onto glass could be varied between 0.2 and 1.5 kJ · m^{-2} with the MTES–OTES coatings, but it did not follow a clear and consistent trend with the MTES content. In particular, no significant difference was observed between 50% and 75% of MTES in the coating. We suspect phase segregation between silanes to occur, which prevents us from controlling the surface chemistry well.

V.1.3 Surface chemistry and TCTT—from rupture to unstable regimes, and recovery of stable delamination

Snapshots of TCTTs with these surface coatings are presented in figure V.4. Varying surface chemistry, we evidence the transitions between a “rupture” regime at high

adhesion, a stable delamination regime for intermediate adherence values, and "unstable" regime at low adhesion. In the next paragraphs, we describe qualitatively the effect of the surface chemistry on the debonding mechanisms.

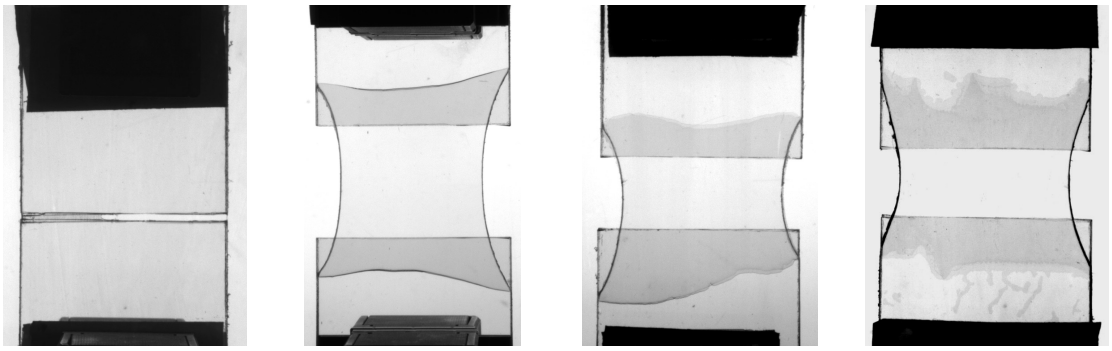

(a) Untreated glass **(b)** MTES **(c)** OTES **(d)** POTS

Figure V.4 Through Crack Tensile Test of EVA for various surface chemistries. ($T = 20°C$, $\dot{\delta} = 10\,mm{\cdot}s^{-1}$)

POTS and OTES: unstable and catastrophic delamination

Adhesion is reduced drastically using a fluorosilane such as POTS. The fluorosilane is assumed to prevent the chemical bonding of adhesion promoters and penalize surface crystallization, due to the lower surface energy. As a result, delamination of the interlayer was obtained in the TCTT but the fronts were not straight and symmetrical (figure V.4d). In fact, the fronts propagated with an intermittent and irregular behavior (figure V.5). Even worse, the interlayer ends up completely debonded from the glass at the end of the experiment.

The debonding behavior of EVA on the POTS surface is reminiscent of "kissing bonds"[100] even though it appeared well bonded, the interface is actually weak.

Still, a delamination force is measured in the TCTT, around 3 N/mm for an interlayer thickness of 0.76 mm. Resistance to debonding may originate from two phenomena, the first being friction of the polymer against the interface, as the interlayer is pressed between the glass plies by pneumatic clamps. The second reason could be mode mixity: despite a low adherence value (figure V.2a) in mode-I dominated peel test, the energy required to propagate the adhesive crack in mode II could still be significant in the TCTT.

Analogous results are obtained with OTES-treated glass. Delamination occurs with features typical of an "unstable" regime: the crack fronts are irregular and

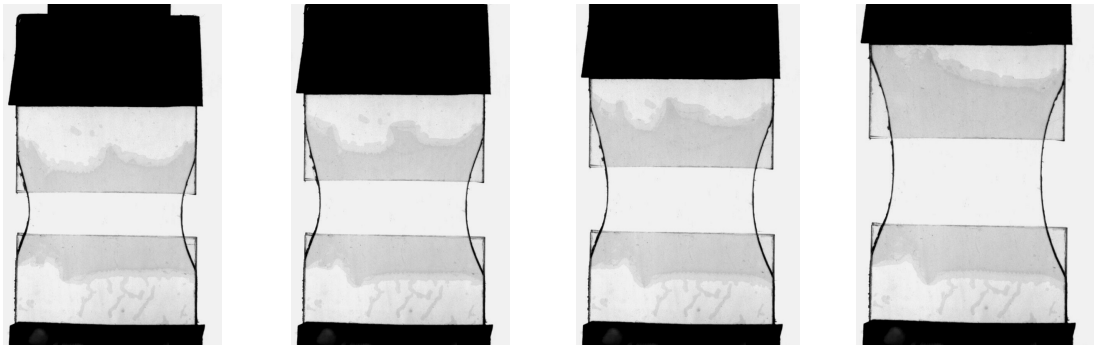

Figure V.5 Intermittent delamination behavior of the EVA interlayer in the TCTT with a fluorinated glass surface.
($T = 20°C$, $\dot{\delta} = 10\,mm{\cdot}s^{-1}$)

undulating (figure V.4c), and propagation is sometimes intermittent. A delamination force around 3.5 N/mm is obtained for a 0.76 mm interlayer thickness.

The chosen one: MTES

The closest to a steady-state regime was obtained with MTES (figure V.4b). Even so, the shape of the delamination front was not as regular and perfectly linear as in TCTT with PVB. Such behavior is suspected to be linked to the plastic properties of the interlayer, which are not as prone to "regularize" the crack front compared to viscoelasticity. We discuss the role of plastic dissipation further in section V.2.

All in all, the surface treatment by MTES is the best solution to go on with the TCTT. For this reason, all experiments are conducted with glass coated with MTES in the following.

V.2 Adhesion rupture in the TCTT with EVA at ambient temperature

Using MTES-treated glass, laminate specimens are now tested in the TCTT (*cf* section II.5). The experiments are first conducted at a controlled temperature of 20°C, for comparison with PVB laminates and also for consistency with standard tests. Even though this temperature is 40°C above the glass transition, the behavior of EVA is strongly dissipative due to plastic deformations, as described in section IV.4. In this

section, we investigate the effect of interlayer thickness and traction velocity on the macroscopic work of fracture G_m.

V.2.1 (No?) effect of interlayer thickness

The thickness of EVA was varied by stacking from 1 to 4 layers, with a nominal thickness of 0.38 mm. In fact, the actual thickness of polymer in the laminated assembly was lower because the interlayer flowed during the lamination process. The measured EVA thicknesses are reported in table V.1. The polymer "bulge" on the sides (*cf* section III.3.2) was cut with a razor blade and polished with sand paper, in order to avoid extrinsic edge defects and crack initiation during the TCTT.

Number of foils	1	2	3	4
h_0 (s.d.) [mm]	0.33 (0.05)	0.68 (0.02)	0.99 (0.03)	1.34 (0.01)

Table V.1 Initial thicknesses of EVA interlayer after lamination

TCTT have been performed at the loading rate $\dot{\delta} = 10\,\text{mm}\cdot\text{s}^{-1}$, and the temperature was controlled at 20°C. The results, for the four EVA thicknesses, are presented in figure V.6. Steady-state delamination is observed at all thicknesses though not systematically: for some specimens, represented with open symbols in figure V.6, rupture of interlayer spuriously occurs after an initial delamination regime.

The effect of an increased interlayer thickness is a higher steady-state force (figure V.6a) and a lower deformation (figure V.6b) of the polymer ligament. In steady-state cases, the force plateau is repeatable, while the stretch values display a larger scattering. The normalized force increases from $2\,\text{N}\cdot\text{mm}^{-1}$ to $5\,\text{N}\cdot\text{mm}^{-1}$, in a linear trend with respect to h_0. The stretch decreases from 3 to 2, *i.e.* from 200% to 100% deformation.

The engineering tensile stress was estimated by dividing the force by the initial cross-section of the interlayer: $\sigma_0 = F/(b_0 h_0)$. The estimated stretch-stress values coincide well with the uniaxial tensile curves (figure IV.8b). For the thickest case, a 4 MPa stress induces around 100% deformation ($\lambda = 2$) of the EVA foil. For the thinnest interlayer, the stress reaches 6 MPa, which corresponds to 200% deformation ($\lambda = 3$). In all cases, the yield stress—estimated at 3 MPa at 20°C—is overcome in the interlayer in the steady state regime: the interlayer deforms plastically in the TCTT.

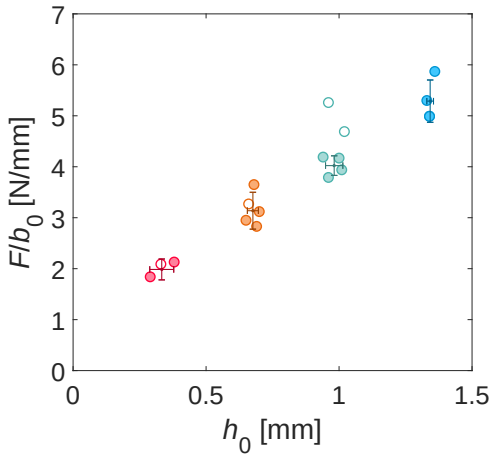

(a) Steady-state force normalized by the initial sample width b_0.

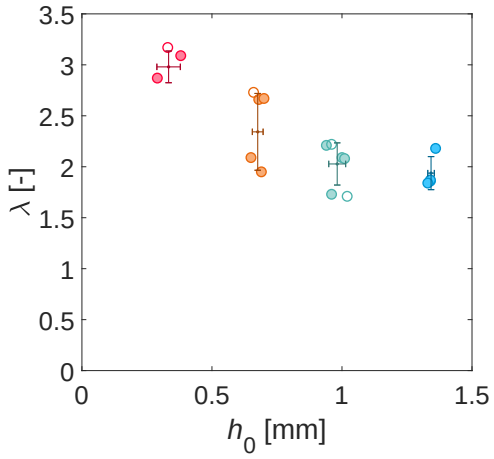

(b) Average stretch of the interlayer.

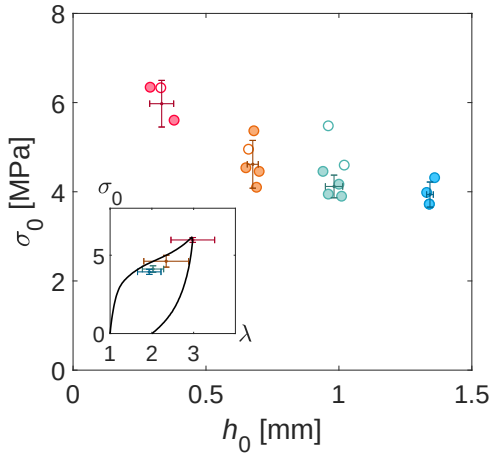

(c) Engineering tensile stress in the interlayer $\sigma_0 = F/(b_0 h_0)$. Insert: comparison of TCTT stretch-stress value with uniaxial tensile response.

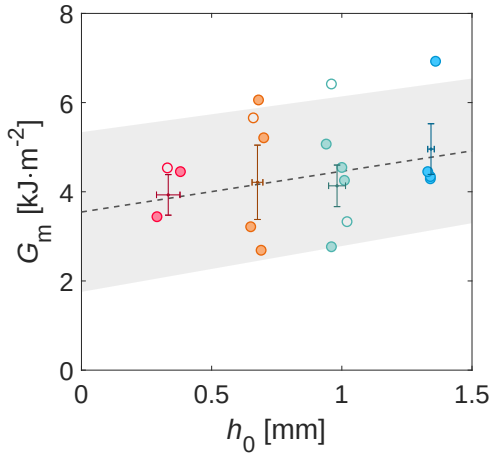

(d) Macroscopic work of fracture G_{m}. Shaded area: 95% prediction bounds from the linear regression on average values.

Figure V.6 Through Crack Tensile Test with varying interlayer thickness of EVA, at T = 20°C and $\dot{\delta}$ = 10mm·s^{-1}. • = steady-state, ∘ = delamination followed by rupture of the interlayer. Averages and s.d. were computed on steady-state samples only.

Almost no dissipation in the volume

Here, we define again the macroscopic work of fracture G_{m} as in section II.5.2:

$$G_{\mathrm{m}} = \frac{F}{b_0}(\lambda - 1)$$

In EVA laminates at 20°C, G_{m} varied between 4 to 5 $\mathrm{kJ \cdot m^{-2}}$ when the interlayer thickness increased by a factor of 4 (figure V.6d). In comparison with PVB (see section III.4), G_{m} was roughly three times lower with EVA laminates for $h_0 = 0.76\,\mathrm{mm}$.

The trend of G_{m} with the thickness h_0 appears to be linear, and the decomposition of the work of fracture into interfacial and volume contributions, according to equation (I.1), seems reasonably correct. With a linear model, we obtain the values $\Gamma_{\mathrm{crack}} = 1.8\,\mathrm{kJ \cdot m^{-2}}$ and $\Pi_{\mathrm{bulk}} = 0.9\,\mathrm{MJ \cdot m^{-3}}$. The value of the crack contribution is strikingly similar to the peel adherence, measured at $1.5\,\mathrm{kJ \cdot m^{-2}}$ (*cf* figure V.2). However, the bulk dissipation term is one order of magnitude smaller compared to PVB at the same temperature of 20°C.

Localized plastic dissipation?

We have seen that, despite the dissipative behavior, the increase in thickness did not provide a significant enhancement of the macroscopic work of fracture. We now interpret this result based on fracture mechanics of plastic materials, presented in section I.5.4.

In an elasto-plastic material, the dissipative processes manifest at the vicinity of the crack tip in an active plastic zone. The size of this active plastic zone can be estimated from the fracture energy Γ according to equation (I.2) (*cf* section I.5.4):

$$R_p \sim \frac{2}{3\pi}\frac{E^*\Gamma}{\sigma_Y^2}$$

Considering the elasto-plastic properties of EVA* and adherence from the peel test to be $\Gamma = 1.5\ \mathrm{kJ \cdot m^{-2}}$, the size of the active plastic zone was estimated at $R_p \sim 1\,\mathrm{mm}$ which is the order of magnitude of interlayer thickness h_0. The active plastic zone therefore develops over the entire thickness of the interlayer, as schematized in figure

*$E = 30\,\mathrm{MPa}$, $\nu = 0.45$, $E^* = E/(1-\nu^2) = 35\,\mathrm{Mpa}$, $\sigma_Y = 3\,\mathrm{MPa}$

V.7b. Note that, according to this scaling, plastic dissipation also occurs over the entire thickness in the peel test, with $h_0 = 0.76\,\text{mm}$.

Over all, the macroscopic work of fracture in EVA appears to be only due to interface crack propagation and the associated plastic processes. The increase in G_m with h_0 is attributed to the extension of the plastic zone at the crack tip.

$$G_\text{m} \approx 2\Gamma_\text{crack}$$

This effect of the plastic zone size is also discussed in the numerical simulations of chapter VI. The simulations with a plastic material show a dramatic increase of the fracture energy when the plastic zone develops over the entire interlayer (*cf* section VI.5). However, the effect in the experiments is not that pronounced since EVA is still made of 90% of amorphous polymer that is able to transmit stress to the crack tip. A complete plastic blunting effect might occur in materials with a much higher crystalline content.

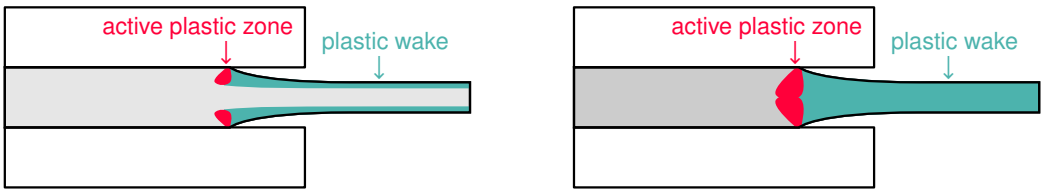

(a) $R_p \ll h_0$: small-scale yielding and localized plastic dissipation at the crack tip.

(b) $R_p \sim h_0$: full plastification of the interlayer

Figure V.7 Scenarii of plastic dissipation in the TCTT: (a) small-scale yielding *vs.* (b) development of the active plastic zone over the entire thickness of the interlayer.

V.2.2 (No?) effect of velocity

The effect of traction velocity is investigated with TCTT specimens with $h_0 = 1.0\,\text{mm}$: we chose a larger thickness to avoid spurious rupture of the interlayer. The traction velocity is varied from 1 to 100 $\text{mm}\cdot\text{s}^{-1}$. Experimental results are shown in figure V.8. The steady-state force increases with $\dot{\delta}$, but only from 4 to 5 $\text{N}\cdot\text{mm}^{-1}$ over two decades of velocities (figure V.8a). The stretch also increases from 2 to 2.5 (figure V.8b). Overall, the macroscopic work of fracture increases from 4 to 6 $\text{kJ}\cdot\text{m}^{-2}$ (figure V.8d).

Delamination occurred at a slower rate—relatively to the imposed traction velocity $\dot{\delta}$—when the stretch increased (figure V.8c), according to the scaling $\dot{a} = \dot{\delta}/2(\lambda - 1)$ (*cf* section II.5.2).

A frictional effect?

Such shallow evolution in the work of fracture does not have an unequivocal explanation. We have ruled out viscoelastic effects in EVA at 20°C, although they could still play a role, as the loss modulus is still in the order of 1 MPa. This increase in work of fracture could also be due to friction at the interface. From the work of *Newby & Chaudhury*[101] and *Amouroux et al.*[102] for instance, we know that slippage at the interface and concomitant friction processes induce an increase of the adhesion at higher loading rates. In our case in the TCTT, friction at the interface is probable due to the strong mode II loading. Experimental confirmation and observation would require DIC at the interface for instance.

V.3 Recovery of high fracture energy at the glass transition of EVA

In the previous section, with EVA at room temperature, the macroscopic work of fracture was twice to three times lower compared to PVB, and G_{m} did not evolve much with interlayer thickness and loading rate. Thus, the plastic interlayer seems less worthy of interest in terms of impact performance.

However, as stressed out in previous works on PVB, it is the viscoelastic behavior of the interlayer which provides most of the energy dissipation. As shown by the mechanical characterization in section IV.4, viscoelastic properties can be recovered in EVA at negative temperatures. In this section, the laminate system EVA–methylated-glass was tested at -20°C, *i.e.* at the glass transition temperature of the interlayer.

V.3.1 Thickness effect at the glass transition: high dissipation in the bulk

TCTT with variable interlayer thickness is conducted as in section V.2.1, results are presented in figure V.9. The choice of a loading rate of $10\,\mathrm{mm}\cdot\mathrm{s}^{-1}$ resulted in a

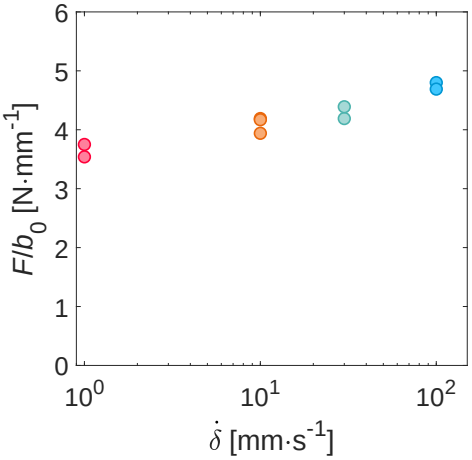

(a) Steady-state force normalized by the sample width b_0.

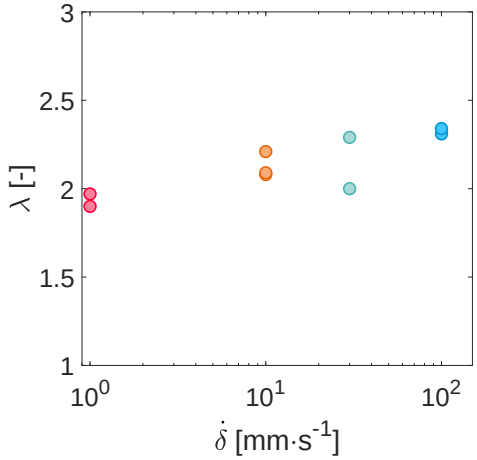

(b) Average stretch of the interlayer.

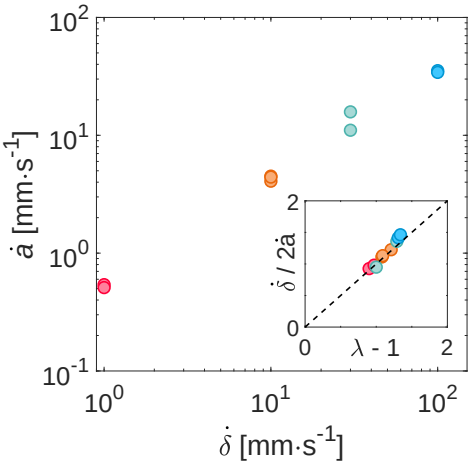

(c) Crack velocity *vs.* traction velocity. Insert: velocity ratio *vs.* deformation.

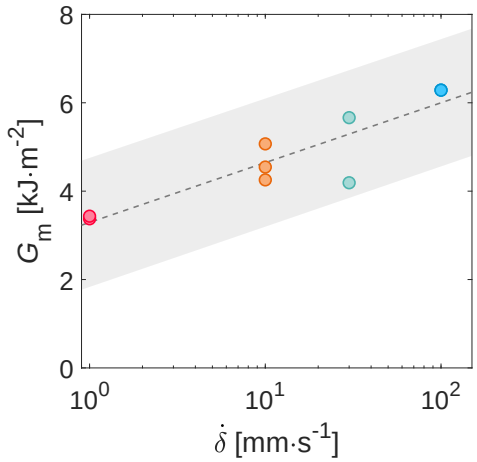

(d) Macroscopic work of fracture.

Figure V.8 Through Crack Tensile Test at varying traction velocities with EVA-laminates. T = 20°C, initial interlayer thickness h_0 = 1mm.

rupture of the interlayer for interlayers thinner than 1 mm. Failure happened after initial delamination, but this still prevents us from evaluating significant steady-state values. Consequently, the linear model of $G_{\mathrm{m}}(h_0)$ suffers from a large uncertainty at -20°C and $\dot{\delta} = 10\mathrm{mm} \cdot \mathrm{s}^{-1}$, due to the scattering of data points and the small number of steady-state values.

Traction velocity was decreased to $1\,\mathrm{mm} \cdot \mathrm{s}^{-1}$in order to diminish the probability of interlayer failure during the test (square symbols in figure V.9). at $1\,\mathrm{mm} \cdot \mathrm{s}^{-1}$, steady-state delamination was observed for all samples, with lower stretch and debonding force compared to higher loading rate.

All in all, the laminate system composed of MTES-coated glass and EVA dissipated more energy at the T_g of the polymer compared to the PVB-glass system when tested close to their respective T_g. Reminding the results of *Novotny & Poot* in section I.2, we now understand why EVA performs better in an actual impact test compared to other interlayers at -20°C. Moreover, our results on adhesion modification suggest that the impact performance could be even higher, providing the adherence of EVA is decreased in the range $1\text{–}2\,\mathrm{kJ} \cdot \mathrm{m}^{-2}$.

T [°C]	$\dot{\delta}$ [$\mathrm{mm} \cdot \mathrm{s}^{-1}$]	Γ_{crack} [$\mathrm{kJ} \cdot \mathrm{m}^{-2}$]	Π_{bulk} [$\mathrm{MJ} \cdot \mathrm{m}^{-3}$]
20	10	1.78 (0.16)	0.88 (0.36)
-20	1	1.9 (0.6)	12.2 (1.4)
-20	10	2.58 (2.23)	18.4 (4.5)

Table V.2 Decomposition of the macroscopic work of fracture into interfacial and bulk contributions for EVA laminates.

V.3.2 A strong rate effect at the glass transition

TCTT specimens with an EVA thickness $h_0 = 1$ mm have been tested at -20°C at tensile velocities $\dot{\delta}$ from 1 to $100\mathrm{mm} \cdot \mathrm{s}^{-1}$. The results are presented in figure V.10. Steady-state delamination was obtained for 1 and $10\,\mathrm{mm} \cdot \mathrm{s}^{-1}$, while EVA failure occurred at $100\ \mathrm{mm} \cdot \mathrm{s}^{-1}$. The velocity limit between steady-state and "rupture" regimes appeared to lie around $\dot{\delta} = 30\,\mathrm{mm} \cdot \mathrm{s}^{-1}$, when one of the two tested specimens failed. A larger number of experiments would be required to improve the statistics and define a more precise boundary.

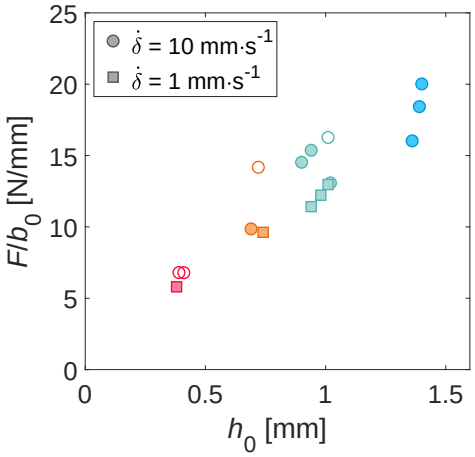

(a) Normalized delamination force.

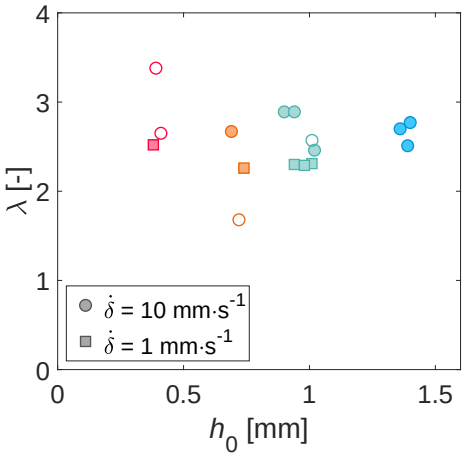

(b) Average interlayer stretch

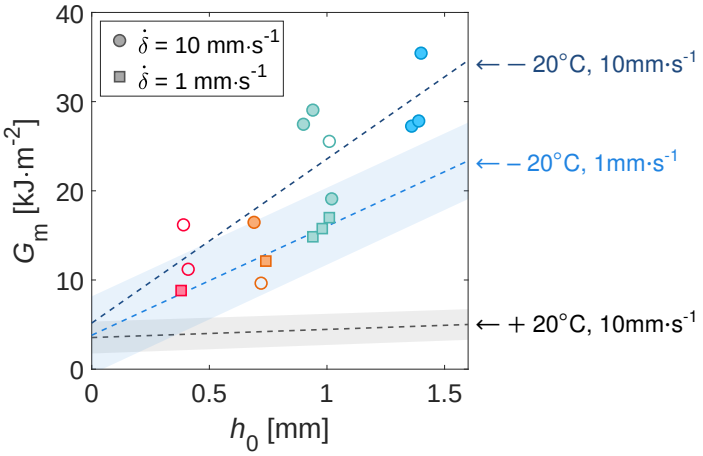

(c) Macroscopic work of fracture G_m *vs.* interlayer thickness. Shaded areas: 95% prediction bounds for the linear models. Prediction bounds are not drawn for the (-20°C,10mm·s^{-1}) case.

Figure V.9 TCTT values for 4 interlayer thicknesses, with MTES-tretaed glass, at – 20°C. Filled symbols: steady-state delamination. Open symbols: rupture of the interlayer.

Both the debonding force and stretch increased when the traction velocity increased, resulting in a higher work of fracture (figure V.10). The slope of the $G_m(\dot{\delta})$ curves was significantly larger compared to the ambient temperature case. At -20°C, we recover the features of a PVB-like system, with the principle of viscoelastic dissipation in the volume. Thus, at higher loading rate, a higher amount of energy is dissipating upon stretching according to the rate-dependent tensile response of EVA (figure IV.8b).

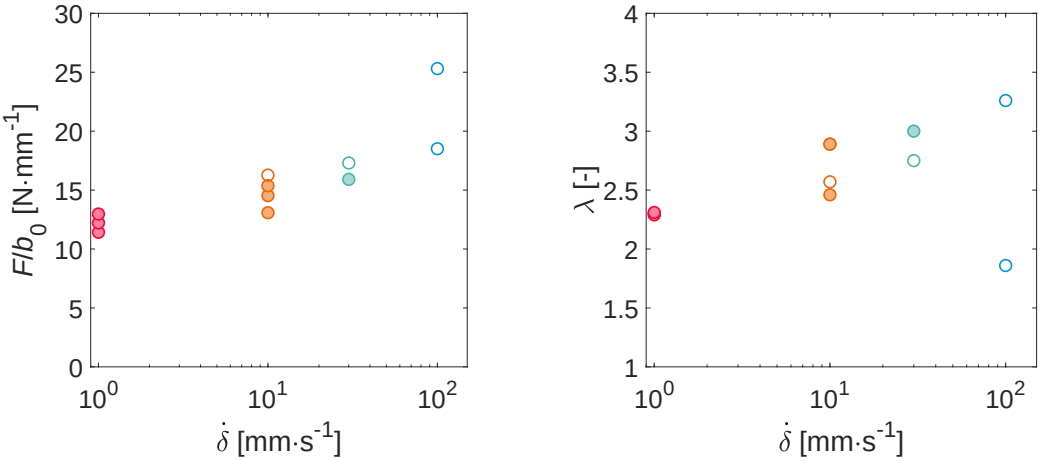

(a) Normalized delamination force.

(b) Average interlayer stretch

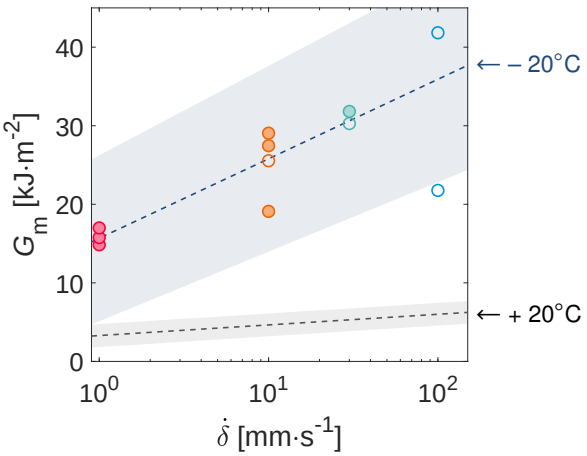

(c) Macroscopic work of fracture G_m *vs.* traction velocity $\dot{\delta}$.
Shaded areas: 95% prediction bounds of the linear models.

Figure V.10 TCTT values for increased MTES-tretaed glass, at – 20°C. Filled symbols: steady-state delamination. Open symbols: rupture of the interlayer.

V.3.3 Plastic at the crack tip, viscoelastic in the bulk?

The macroscopic work of fracture evolution with the thickness (figure V.9c) was interpreted with equation (I.1). The interfacial contribution Γ_{crack} was estimated to 1.8 – 2.0 $\text{kJ} \cdot \text{m}^{-2}$ (table V.2), the same value as in experiments at ambient temperature (*cf* section V.2.1). In fact, at -20°C, the size R_p of the active plastic zone is still of the order of 1 mm—considering E = 172 MPa, $\sigma_Y = 14\,\text{MPa}$ and $\Gamma = 1.5\,\text{kJ} \cdot \text{m}^{-2}$: the higher stiffness is compensated by the concomitant higher yield stress. The contribution at the crack tip appears to be still dominated by plastic processes, even close to the glass transition.

However, the slope of the linear decomposition does increase from 20°C to -20°C: Π_{bulk} was evaluated at $12\text{MJ} \cdot \text{m}^{-3}$ around the glass transition (*cf* table V.2). Such enhancement does not scale directly with the stiffness of the interlayer: while the Young's modulus increases by a factor 8 (table IV.3), the bulk dissipation energy increases 12 to 18 times between room temperature and T_g (*cf* table V.2). An argument of *Samieian et al.* [37] to explain the temperature effect—in PVB laminates—is the increased stiffness of the interlayer at lower temperatures. However, this factor alone seems insufficient to account for the increase in bulk dissipation observed in our experiments with EVA laminates.

Dissipation mechanisms in viscoelastic EVA are depicted in figure V.11. The semi-crystalline nature of the polymer still provides dissipation from plastic deformations, while viscoelasticity comes into play and provides most of the energy dissipation. Following the interpretation of Elzière [5], viscous dissipation is thought to occur in a region localized behind the crack tip, where deformation goes from zero to a significant fraction of the macroscopic stretch.

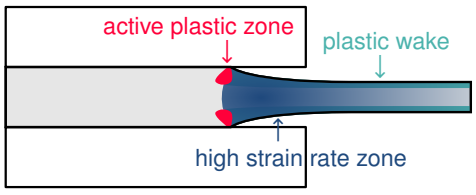

Figure V.11 Elasto-visco-plastic case: viscous dissipation in the high-strain rate zone over the entire thickness of the interlayer.

Take-home messages of chapter V

- The interface between glass and EVA had to be chemically modified to make delamination possible. Silanisation with methyltriethoxysilane (MTES) provided an adherence of 1.5 kJ·m^{-2} at 20°C, therefore allowing steady-state delamination in the Through Crack Tensile test.

- At room temperature, when EVA is elasto-plastic, neither interlayer thickness nor traction velocity affected the macroscopic work of fracture significantly. The value of G_{m} ranged between 4 and 6 kJ·m^{-2} while the thickness increased by a factor of 4, or the traction velocity by a factor of 100. Plastic dissipation occurs only around the delamination crack tip: the confined volume available for energy dissipation accounts for the low influence of the thickness. In the plastic EVA interlayer, the work of fracture arises principally from the debonding:

$$G_{\mathrm{m}} \approx 2\,\Gamma_{\mathrm{crack}}$$

- At the glass transition temperature, both thickness and velocity dependencies were recovered. In the end, the work of fracture with an EVA-laminate—with the adequate glass-surface chemistry—at the T_g of the polymer is greater compared to PVB tested in analogous conditions.

VI

Numerical modeling: a steady-state approach to crack propagation

Despite experimental data at the macroscopic level and hand-waving explanations, the underlying coupling between local processes, in the vicinity of the crack tip, and the fracture energy is still an ongoing question. In this chapter, we present a numerical method, based on finite-element analysis, to model the propagation of a steady-state adhesive crack at finite velocities, taking into account the dissipative properties of the polymer material.

As emphasized in the introduction (section I.5), the actual fracture energy Γ_{ss} required to propagate a crack is greater than the interfacial separation energy Γ_0, exactly because of energy dissipation in the material. The numerical scheme should provide us with a relationship between the fracture energy, the strength of the interface and the constitutive behavior of the interlayer:

$$\frac{\Gamma_{ss}}{\Gamma_0} = 1 + \mathfrak{F}\,(\text{interface, material})$$

Although implemented at the very beginning of finite-element codes in the early 1980s[2], the steady-state crack method has not made it to commercial softwares. Here, we propose an algorithm coupling a commercial FEA code (ABAQUS) and a numerical computing software (MATLAB) to implement this steady-state approach.

First of all, reported numerical models of the TCTT are shortly described in section VI.1, along with their shortcomings which motivate the development of the steady-state algorithm. Then, we present in section VI.2 the rate-dependent material behaviors considered here. In small strains, we make use of the additive decomposition of

the strain into elastic and inelastic contributions. We propose constitutive laws for the inelastic contribution, either with plastic or viscoelastic characteristics. In section VI.3, the basic equations underlying the steady-state crack scheme are presented, along with their practical implementation—in a short version. The technical details of the algorithm are described in the appendix A. We emphasize how the steady-state hypothesis makes the integration of the mechanical history straightforward—usually a cumbersome task when dealing with rate-dependent constitutive behaviors.

The steady-state crack method is validated on small-strain problems with a viscoplastic material law. First, an opening plane-strain crack is modeled in section VI.4. We consolidate the results from the method developed here, in comparison to the literature on steady-state cracks[3]. Eventually, the TCTT geometry is considered in section VI.5. The peculiar mode mixity is shown to affect drastically the evolution of the fracture energy, which increases sharply when plasticity is activated. We observe a transition from small-scale yielding—when plastic deformation occur only at the crack tip—to a fully-plastifying case—when plastic deformation develops over the entire thickness of the interlayer. Finally, we suggest further applications of the steady-state crack model developed here in section VI.6, and its extension to the case of finite strains in appendix B.

VI.1 Modeling the TCTT: dissipative interlayer and cohesive zone model?

2D plain-strain model with cohesive elements

Cohesive zone modeling has been applied to laminated glass problems by the "DuPont" team, *Bennison & Jagota* and their collaborators, in the 1990s–2000s[26,35,103]. Inspired by this literature, *Elzière* proposed a finite-strain numerical model of the TCTT[4]. In this model, the constitutive behavior of the interlayer is a combination of hyperelasticity—elasticity in large deformations—and viscoelasticity with one single characteristic timescale, as *Jagota et al.* proposed for another geometry[103]. Adhesion rupture is modeled using cohesive elements (*cf* section I.5).

From the prescription of a small fracture energy ($\Gamma_0 \approx 0.04\,\mathrm{kJ\cdot m^{-2}}$) in the cohesive zone model, *Elzière* estimated the macroscopic work of fracture G_m to reach several $\mathrm{kJ\cdot m^{-2}}$ (figure VI.1a) for the highly deformable viscoelastic material considered.

Furthermore, two dissipation zones were evidenced in the material (figure VI.1b). Observation of these two regions is consistent with the decomposition of G_m into interfacial and bulk contributions, according to equation I.1. The first zone was in the vicinity of the crack tip, where tensile stresses develop perpendicular to the interface, and favor mode 1 opening. Due to high strain gradients close to the crack tip, viscoelastic dissipation occur in this localized region and account for th Γ_crack term. The second zone extends behind the crack tip, in the stretched ligament where deformation goes from zero to a steady value. The strain increases over a length scale of the order of the interlayer thickness. Viscoelastic dissipation in this "fast stretching" zone, which develops over the entire thickness of the interlayer, accounts for the Π_bulk term.

However, this model presented two major drawbacks. First, a significant fraction of the computation time was spent in a transitory regime before reaching a steady-state regime—when it happened. The consequence of this transitory regime was a significant and unnecessary increase of the computation time. Moreover, as a few technical tricks were required to initiate crack propagation (*e.g.* a gradient of the cohesive properties), the physical significance of the transitory regime was dubious. For instance, the strain field far away from the crack tip was affected by a traction

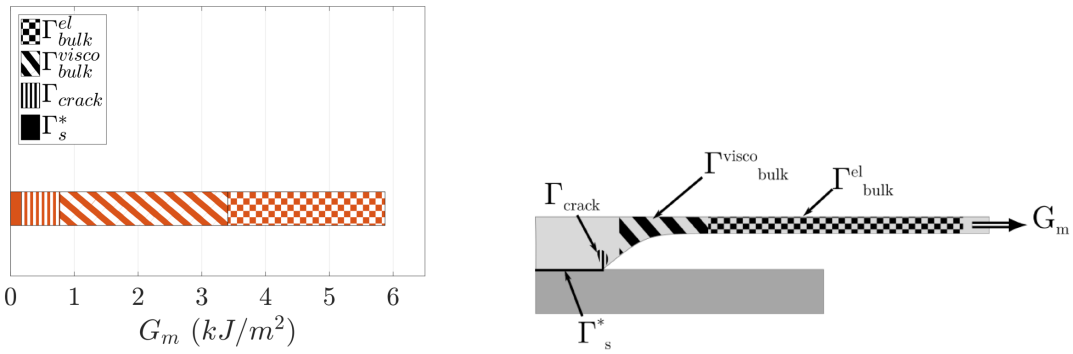

(a) Partition. **(b)** Location of dissipation zones.

Figure VI.1 Macroscopic work of fracture, from Elziere.

overshoot during the transitory regime in the case of a high adhesion. Another limitation arose at high velocities: despite a long model in terms of geometry, with several hundred thousand nodes, the length of the modeled ligament was still too short to reach a steady-state regime.

Another issue arose because of viscous regularization of the cohesive zone model: energy dissipation had to be added into the cohesive elements to ensure convergence. This additional energy affected the physical interpretation of the results: *Elzière*'s interfacial work of fracture Γ_s^* was actually higher than the prescribed Γ_0, whereas the objective of the numerical model was exactly to avoid the lumping of viscous dissipation, and to be able to interpret all energetic contributions.

3D model with cohesive surfaces

Blackman, Hooper, Dear and their collaborators[39,40] implemented the cohesive zone model with a surface-to-surface contact approach (*cf* ABAQUS Analysis User's Guide[6] §36). Glass was modeled as a linear elastic material and the PVB as a hyperelastic material with viscoelastic properties—a model similar to *Elzière*'s with more terms in the Prony series. The model of *Samieian*[40] contained between 1000 and 1500 elements: the goal was to model the macroscopic delamination behavior and reproduce the force profile observed in the TCTT, as in figure VI.2. However, the material dissipation near the crack tip is not calculated in this model because of the lax parameters of the cohesive zone model—low cohesive stress and large opening displacement leading to a large adhesion energy. This model addresses the stretched region and lumps out the details of the crack tip processes.

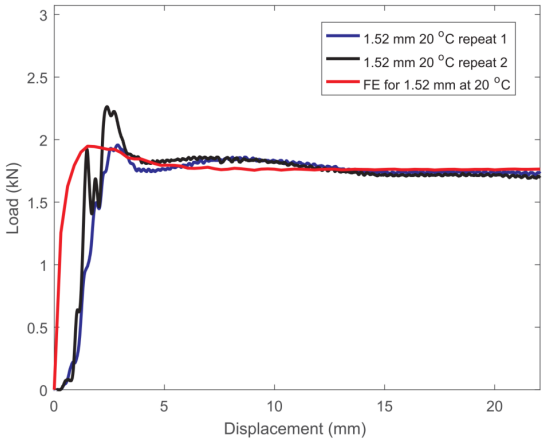

Figure VI.2 Force-displacement in the TCTT, fom Samieian.

Motivations for a steady-state crack propagation model

A change of paradigm leads to the current project: instead of trying to reach stable delamination in the simulation, the steady state regime is considered established *a priori*. An expected first advantage is the reduction of the computation time, simply because there is no transient regime to compute: we model directly the steady-state regime. Also, as explained further in section VI.3, the steady-state method allows to integrate rate-depend mechanical history directly from the spatial fields. Therefore, the inelastic behavior can be tailored at will in the steady-state crack model: plastic, viscoelastic, viscoplastic.

VI.2 Constitutive behaviors in small deformations

VI.2.1 Plasticity in the linear regime: additive decomposition of the strain

In the following, we consider an elasto-plastic material in the small-strain regime. In a small strain approach, the total deformation can be written as the sum of elastic and plastic deformations:

$$\varepsilon_{ij} = \varepsilon^{\mathrm{e}}_{ij} + \varepsilon^{\mathrm{p}}_{ij}$$

The stress is related to the elastic deformation only.. The elastic isotropic response obeys:

$$\sigma_{ij} = 2\,\mu\,\varepsilon'_{ij} + \kappa\,\varepsilon_{kk}\,\delta_{ij} \tag{VI.1}$$

In equation (VI.1), the deviatoric deformation tensor is defined by $\varepsilon'_{ij} = \varepsilon_{ij} - \delta_{ij}\varepsilon_{kk}/3$. The shear modulus μ and bulk modulus κ in equation (VI.1) are related to Young modulus E and Poisson ratio ν by the following elastic relations:

$$\mu = \frac{E}{2(1+\nu)} \qquad\qquad \kappa = \frac{E}{3\,(1-2\nu)}$$

Rate-independant plasticity

The additional deformation ε^{p} is due to plastic flow, a process active only in the region where the yield criterion is met. The simplest yield criterion is the equality between an equivalent stress $\overline{\sigma}$ and the yield stress σ_Y. We use Von Mises' equivalent stress measure:

$$\overline{\sigma} = \sqrt{\tfrac{3}{2}\sigma'_{ij}\sigma'_{ij}}$$

A common constitutive behavior for plasticity is a power-law model, which prescribes the total strain above the yield criterion. In an unidimensional model, the strain-stress response is given by:

$$\varepsilon = \frac{\sigma_Y}{E}\left(\frac{\sigma}{\sigma_Y}\right)^m \qquad \text{if} \quad \sigma \geq \sigma_Y$$

The elastic component of the deformation is $\varepsilon^{\mathrm{e}} = \sigma/E$, thus the plastic component is obtained from $\varepsilon^{\mathrm{p}} = \varepsilon - \varepsilon^{\mathrm{e}}$. Such rate-independent constitutive law was used by *Dean & Hutchinson*[2].

Viscoplastic material in the linear regime

Here, however, we use a viscoplastic model: the plastic strain rate $\dot{\boldsymbol{\varepsilon}}^{\mathbf{p}}$ is prescribed as a function of other mechanical values such as stress, stress rate, strain or strain rate. The practical advantage of the viscoplastic formulation resides in the direct integration of the inelastic strain rate, as presented in section VI.3.1.

In J_2-flow theory, the components of the plastic strain rate are then given by the flow rule:

$$\dot{\varepsilon}^p_{ij} = \dot{\overline{\varepsilon}}^{\,\mathrm{p}} \frac{3}{2} \frac{\sigma'_{ij}}{\overline{\sigma}} \tag{VI.2}$$

In equation (VI.2), σ' is the deviatoric Cauchy stress, $\overline{\sigma}$ the equivalent Von Mises' stress, and $\dot{\overline{\varepsilon}}^{\,\mathrm{p}}$ the "equivalent plastic strain rate".

The equivalent plastic strain rate $\dot{\overline{\varepsilon}}^{\,\mathrm{p}}$ is prescribed by a constitutive equation. Following the work of *Landis, Pardoen & Hutchinson*[3], we considered a power-law form for the flow rule:

$$\frac{\dot{\overline{\varepsilon}}^{\,\mathrm{p}}}{\dot{\varepsilon}_0} + 1 = \left(\frac{\overline{\sigma}}{\sigma_Y} \right)^m$$

In this model, the plastic behavior is dictated by the exponent m and the initial plastic strain rate $\dot{\varepsilon}_0$.

Uniaxial tensile response of the viscoplastic model

Uniaxial traction has been calculated at various strain rates for a better understanding of this viscoplastic constitutive model. The tensile response was computed assuming an imposed stress rate $\dot{\sigma}_0$. The only non-zero stress was $\sigma_{11}(t) = \dot{\sigma}_0 t = \overline{\sigma}$. The strain rate was decomposed into elastic and plastic parts. The uniaxial deformation was computed as:

$$\dot{\varepsilon}^{\mathrm{e}}_{11} = \frac{\dot{\sigma}_0}{E} \qquad \dot{\varepsilon}^{\mathrm{p}}_{11} = \dot{\overline{\varepsilon}}^{\,\mathrm{p}}(t) \qquad \varepsilon_{11}(t) = \int_0^t \left[\dot{\varepsilon}^{\mathrm{e}}_{11}(\zeta) + \dot{\varepsilon}^{\mathrm{p}}_{11}(\zeta) \right] \mathrm{d}\zeta$$

Plasticity was active when $\sigma_{11}/\sigma_Y \geq 1$ and $\dot{\sigma}_0 > 0$: we enforce zero plastic contribution upon unloading (dashed lines in the stress-strain curves, figure VI.3). The tensile strain was normalized by the yield strain $\varepsilon_Y = \sigma_Y / E$.

The stress-strain curves were plotted at given $\dot{\varepsilon}_0$ and increasing exponent m (figure VI.3a): the behavior evolved from elastic at $m = 0$ to almost perfect plasticity at $m = 100$. The exponent m can be considered as the inverse of a hardening exponent. Conversely, for a given hardening exponent $m = 10$, an increased value of $\dot{\varepsilon}_0$ (figure VI.3b) also enhanced the plastic deformation for a given stress. The behavior tends towards perfect rate-independent plasticity for $\dot{\varepsilon}_0 \gg 1$.

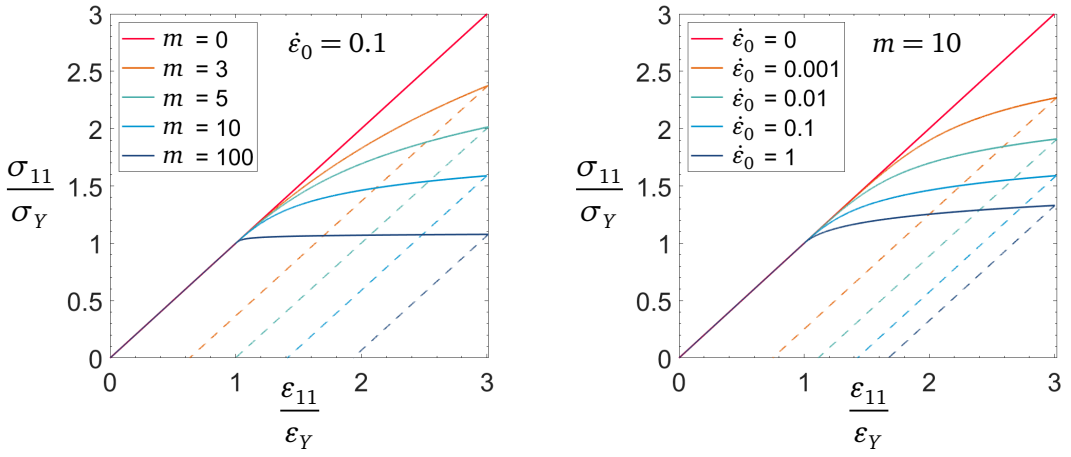

(a) Stress-strain curve: effect of the hardening exponent m.

(b) Stress-strain curve: effect of the initial plastic strain rate $\dot{\varepsilon}_0$.

Figure VI.3 Uniaxial extension response of the viscoplastic material, at imposed stress rate.

VI.2.2 Non-linear viscoelasticity in small strains: creep formulation

The actual viscoelastic behavior or interlayer materials, such as PVB, is not accurately described by simple linear viscoelasticity. A non-linear viscoelastic model was recently explored to account for the pseudo-yield behavior of PVB around its glass transition[63]. The viscous contribution was described by creep deformation in the same framework as plasticity:

$$\dot{\varepsilon} = \dot{\varepsilon}^{\mathrm{e}} + \dot{\varepsilon}^{\mathrm{cr}}$$

The creep was prescribed with a flow rule analogous to the plastic case (see ABAQUS User's Guide[6] §22.8.1).

$$\dot{\boldsymbol{\varepsilon}}^{\mathbf{cr}} = \bar{\dot{\varepsilon}}^{\mathrm{cr}} \frac{3}{2} \frac{\boldsymbol{\sigma}'}{\overline{\sigma'}} \qquad \bar{\dot{\varepsilon}}^{\mathrm{cr}} = \frac{\overline{\sigma'}}{\eta_\infty \, g(\varepsilon)} \qquad \eta_\infty = \tau \, \mu_\infty$$

The long-time viscosity η_∞ was weighted by the function $g(\varepsilon)$ to introduce a dependency of the creep on the strain, hence the non-linearity of the model. A stretched exponential form, inspired from the description of PVB in finite strains[63], was adapted to the case of small deformations as follows:

$$g(\varepsilon) = \exp\left(\sqrt{\frac{\bar{\varepsilon}^{\mathrm{cr}}}{\varepsilon_m^{\mathrm{cr}}}} \right)$$

The increase in viscosity was related to the first invariant of creep strain, *i.e.* $\overline{\varepsilon}^{\mathrm{cr}} = \sqrt{\frac{3}{2}\varepsilon_{ij}^{\mathrm{cr}}\varepsilon_{ij}^{\mathrm{cr}}}$. The characteristic creep deformation $\varepsilon_m^{\mathrm{cr}}$ defines a characteristic extensibility above which strain hardening occurs.

$$\dot{\varepsilon}_{ij}^{\mathrm{cr}}(t) = \frac{\sigma'_{ij}(t)}{\eta_\infty\, g\left(\overline{\varepsilon}^{\mathrm{cr}}(t)\right)}$$

Integration of the creep strain rate is detailed in the appendix (section A.4.4).

However, this model remains a small-strain approach. The enhancement of the steady-state method to finite-strain non-linear behaviors is discussed in appendix B.

VI.3 Steady-state scheme

In the steady-state configuration, the TCTT presents two symmetry axes, both in horizontal and vertical directions. Therefore, as depicted in figure VI.4, we need to model only one quarter of the geometry. A symmetry condition is enforced in the mid-plane of the interlayer through the thickness (X_2-symmetry). A displacement boundary condition δ, parallel to the X_1 direction, is applied on the right side of the ligament , while we impose zero displacement on the left side (*cf* figure VI.4).

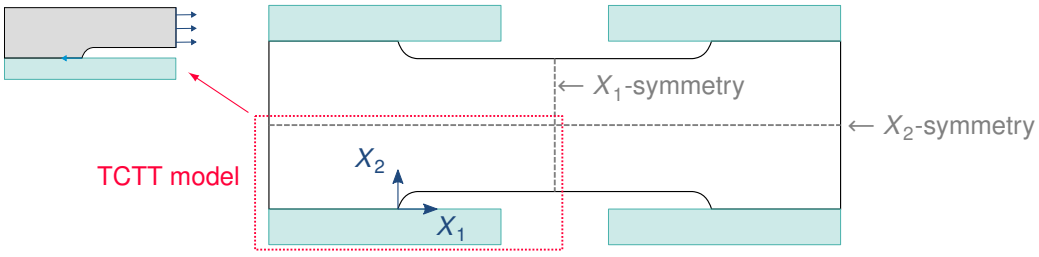

Figure VI.4 Steady-state model of the TCTT: the X_1-axis and X_2-axis symmetries allow to model only one quarter of the model.

VI.3.1 Principle of the method: “integrate along streamlines”

In a steady-state regime, the adhesive crack is propagating at a constant velocity $\dot{a}$. Therefore, instead of observing the crack advance in a fixed referential—the Lagrangian point of view illustrated in figure VI.5a—we can follow the crack at the same velocity $\dot{a}$—the Eulerian point of view illustrated in figure VI.5b.

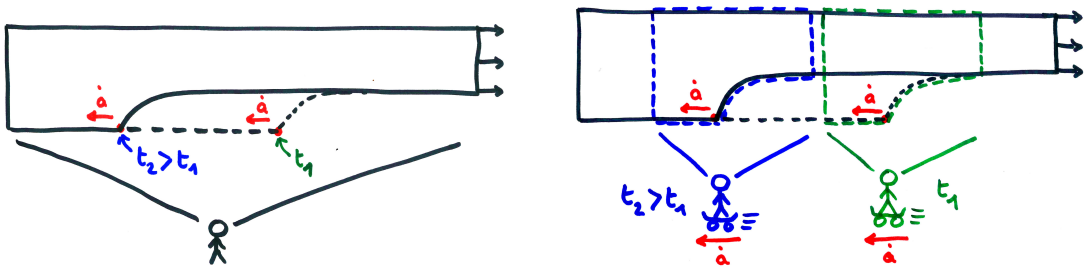

(a) Immobile Lagrangian observer, looking at the crack tip advancing with the velocity $\dot{a}$. From t_1 to t_2, the observer sees changing geometry and mechanical fields.

(b) Eulerian observer, moving at the same velocity $\dot{a}$ than the crack tip. From t_1 to t_2, the observer sees the same geometry and mechanical fields due to time invariance.

Figure VI.5 Illustration of the Lagrangian *vs.* Eulerian frameworks in a steady-state regime.

We illustrate the equivalence between time and space in figure VI.6. In the moving reference frame, the crack tip velocity is zero, and all the material points flow through the frame with the horizontal velocity $-\dot{a}$. Let us consider an element in its initial undeformed state, at the begining t_0 of its journey along the streamline: the red square in $X(t_0)$. After some time at t_1, it will pass by the crack tip and be deformed: it corresponds to the orange parallelogram in $X(t_1)$. At the end of its trip, it is stretched along the pulling direction in the deformed ligament, and corresponds to the blue rectangle in $X(t_2)$. Now, let us consider that we are observing the system at time t_2: if we want to get the past mechanical history of the blue rectangle, we just have to gather the information from the red element, then from the orange and finally the blue one. At any instant in the steady-state regime, the mechanical history lies directly under the eyes of the observer.

Properly speaking, the equivalence between space and time is ensured by the crack velocity $\dot{a}$:

$$\frac{\partial x_1}{\partial t} = -\dot{a}$$

From time derivative to spatial gradient

Considering a tensor field A_{ij} encountered in mechanics problems. The time derivative can be turned into a space derivative with the steady-state assumption by the chain rule:

$$\frac{\partial A_{ij}}{\partial t} = \frac{\partial x_1}{\partial t}\frac{\partial A_{ij}}{\partial x_1} = -\dot{a}\frac{\partial A_{ij}}{\partial x_1}$$

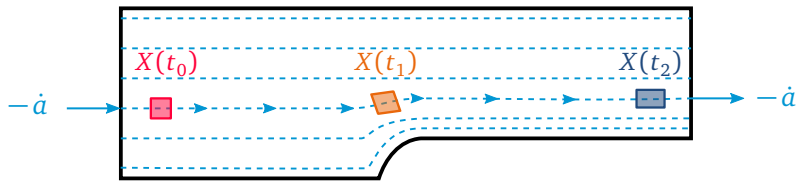

Figure VI.6 Time and space equivalence in steady-state Eulerian framework: the material element is translated along a material trajectory or streamline. Mechanical history, from t_0 to $t_2 > t_1 > t_0$, is retrieved from the elements along the streamline.

In steady-state regime, "time does not exist anymore": time rates are directly obtained from spatial gradients along the flow direction.

Integration along streamlines

The other consequence of the steady-state assumption is the transformation of time integrals into space integrals along the streamlines, through a change of variable justified by time invariance:

$$\int_0^t A(X,\zeta)\,\mathrm{d}\zeta = \int_0^t A(X+\dot{a}\zeta,0)\,\mathrm{d}\zeta \underset{x_1=-\dot{a}\zeta}{=} \frac{1}{-\dot{a}}\int_0^X A(X-x_1)\,\mathrm{d}x_1$$

Application: integration of rate-dependent constitutive behaviors

As described in section VI.2, small-strain rate-dependent constitutive behaviors define an inelastic strain rate, either "plastic" or "creep" rate, which depends on the stress. In the case of viscoplasticity, implemented in the following sections, the plastic strain field $\varepsilon_{ij}^{\mathrm{p}}$ is obtained by integration of the plastic strain rate $\dot{\varepsilon}_{ij}^{\mathrm{p}}$ along streamlines:

$$\varepsilon_{ij}^{\mathrm{p}}(X) = \frac{1}{-\dot{a}}\int_0^X \dot{\varepsilon}_{ij}^{\mathrm{p}}(X-x)\,\mathrm{d}x$$

VI.3.2 Technical implementation: post-processing of elastic solutions

Practically, modeling a steady-state crack is not implemented straightforwardly in the commercial finite-element-analysis software ABAQUS—or any other, for that matter.

Some Eulerian techniques are available, but they are not suitable when cohesive stresses need to be prescribed to model adhesion and de-adhesion problems.

Our methodology is based on the decomposition of the material behavior into elastic and inelastic parts, presented in section VI.2. Then, we take advantage of the cohesive zone modeling capacities of the FEA software to obtain the elastic response. Then, the history-dependent inelastic behavior is integrated in a post-processing step outside of ABAQUS. Typically, we obtain inelastic strains—plastic strains in the following—which are added to the elastic strains. With this new strain field, the stress distribution is no longer at equilibrium. Therefore, the inelastic contribution is re-injected into the finite-element calculation to compute the new stress equilibrium. The process is repeated until converges.

Technical details of the numerical scheme can be found in appendix A. In a few words, each iteration of the simulation proceeds as follow:

1. Stress and strain fields are computed with ABAQUS considering an elastic constitutive behavior.
2. The results are retrieved from the results file, and imported into MATLAB—the post-processing software.
3. Deformation due to the inelastic contribution—viscoplasticity in the following—is computed from the elastic solution, using the steady-state assumption to integrate the inelastic strain rate.
4. Unfortunately, the inelastic deformation cannot be passed on *talis qualis* to ABAQUS, which only accepts "residual stresses" as a general initial state. Thus, we need to "translate" strain into stress with equation (VI.1) .
5. The "residual stress" field is injected into ABAQUS with the `SIGINI` subroutine, which attributes a stress value to each integration point of the model.
6. The elastic calculation is performed again with the initial stress state dictated by the inelastic behavior: we go back to step 1.

In the calculation, the crack velocity $\dot{a}$ is fixed, and we take the value $\dot{a} = -1$ in the following. The displacement boundary condition δ is adjusted, if necessary, to enforce the crack-propagation condition $\sigma = \hat{\sigma}$ at the crack tip. Thus, we obtain strain an stress solutions corresponding to crack propagation at the velocity $\dot{a}$.

This scheme—accompanied with a few tweaks and tricks detailed in appendix A—is repeated until the inelastic solution do not vary anymore from one iteration

to another, according to a convergence criterion. We follow the relative distance—in the sens of matrix norm—between each iteration of the residual stress field: once this distance is below a given threshold, convergence is declared.

VI.3.3 Energy release rate and total work of fracture

In a steady-state model, the crack does not move for the observer. Therefore, we cannot directly compute the energy release rate by comparing the mechanical fields after crack advance—or it would require an additional calculation. Instead, we use the method of "fictitious crack advance", following the old arguments of *Rivlin & Thomas*[104] for crack propagation in rubber materials.

Elastic case

The strain energy release rate is defined by:

$$G = -\frac{\partial (U_{\text{el}} - W_{\text{ext}})}{\partial a}$$

G can be evaluated by considering a fictitious crack advancement Δa and computing the corresponding internal energy variation. For a small crack advance Δa, the change of work of external forces is distributed into a stored part—stored elastic strain energy ΔU_{el}—and a dissipated part represented by G:

$$\Delta W_{\text{ext}} = \Delta U_{\text{el}} + G\Delta a \tag{VI.3}$$

The change in internal energy ΔU, in the plain strain problem, is the difference in stored elastic energy between a strip of length Δa ahead of the crack tip and a similar strip behind the crack tip, as pictured in figure VI.7.

Mode I The seminal approach of *Rivlin & Thomas*[104] applies to a mode I crack, *i.e.* an opening crack (figure VI.7a). At fixed displacement δ, the work of external forces is constant: $\Delta W_{\text{ext}} = 0$. Upon crack propagation, the strain energy W_0 in the stretched region of initial volume $h_0 \Delta a$ is lost as it is transferred to the unstretched region. Equation (VI.3) leads to:

$$\Delta U_{\text{el}} = -W_0 h_0 \, \Delta a \Rightarrow G_I = W_0 h_0$$

TCTT mode A similar argument was applied to the TCTT configuration (figure VI.7b) following the same arguments of *Rivlin & Thomas* for the "simple extension tear"[104]. Steady-state propagation in the TCTT ensures that the crack advancement and the displacement are related through the far-field deformation: $\delta = a\,\varepsilon$. Starting again from equation (VI.3):

$$\Delta U_{\text{el}} = -G\,\Delta a + F\,\varepsilon\,\Delta a$$

The calculation of the left-hand term is analogous to the mode I case: at fixed force F, the variation of elastic energy upon crack propagation is $\Delta U_{\text{el}} = +W_0\,h_0\,\Delta a$.

$$G_{\text{TCTT}} = F\varepsilon - W_0 h_0$$

In small strains:

$$W_0 = \frac{1}{2}\sigma\varepsilon = \frac{1}{2}\frac{F}{h_0}\varepsilon \Rightarrow G = \frac{1}{2}F\varepsilon$$

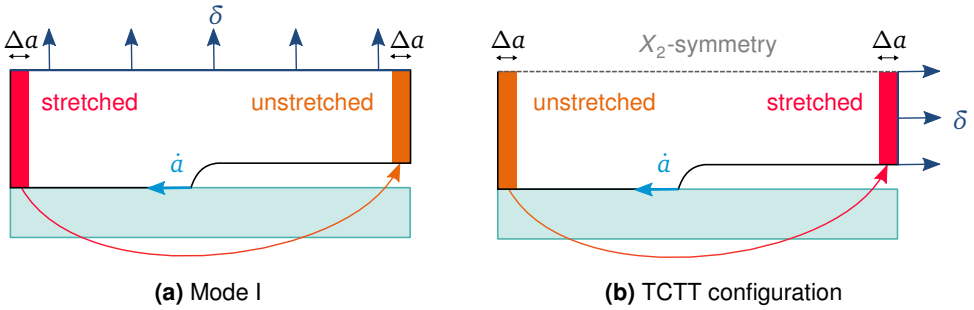

(a) Mode I **(b)** TCTT configuration

Figure VI.7 Energy release rate calculation in steady-state configuration. The energy required to propagate the crack by a length Δa is equal to the difference in stored energy ΔU between the unstretched and stretched strips.

Dissipative case

When dissipation occurs in the material, the energy balance contains an additional term corresponding to the dissipated energy

$$\Delta W_{\text{ext}} = \Delta U_{\text{el}} + \Delta U_{\text{diss}} + G_0\Delta a = \Delta U_{\text{el}} + G\Delta a$$

Here G_0 is the release rate due to interfacial debonding only, as in the elastic case. The actual energy release rate G is the sum of G_0 and the dissipative contribution.

In the case of a viscoplastic material, ΔU_{diss} corresponds to the work of plastic strains over the fictitious crack advance. The rate of plastic work per unit volume is:

$$\dot{w}^{\text{p}} = \sigma_{ij}\dot{\varepsilon}^{\text{p}}_{ij}$$

The variation of dissipated energy over the fictitious crack advance Δa is computed by integrating the rate of plastic work with the steady-state assumption. In our energy balance method, plastic work is null in the left strip ($x_1 \to -\infty$ in figure VI.7). After going through the crack tip, the strip has accumulated plastic work ($x_1 \to +\infty$ in figure VI.7), which corresponds to the additional dissipated energy:

$$\Delta U_{\text{diss}} = \frac{\Delta a}{-\dot{a}} \int_0^{h/2} \dot{w}^{\text{p}}(x_2)\, \mathrm{d}x_2 \qquad \text{at } x_1 \to +\infty$$

VI.4 Validation of the model: plane-strain opening crack in a rate-dependent plastic material

The numerical procedure was applied to an opening crack in plane strain, the same geometry as in *Landis, Pardoen & Hutchinson*[3], in order to validate the numerical method.

VI.4.1 Material properties and plastic zone size

Stress were normalized to $E = 1$, and the Poisson ratio was fixed at $\nu = 0.45$. The yield stress was $\sigma_Y = 0.02$, which corresponded to $E/\sigma_Y = 50$. In our calculations, the cohesive stress $\hat{\sigma}$ was changed while the yield stress σ_Y was kept constant. The ratio $\hat{\sigma}/\sigma_Y$ was varied between 1 and 6 at the maximum.

The work of separation*G_0 is estimated in the initial elastic calculation, from the energy balance presented in section VI.3.3.

*We designate the work of separation by G_0 and not Γ_0 since it is computed as an elastic energy release rate.

Plastic zone size

As stated in the introduction on fracture mechanics (section I.5.4), the plastic zone size scales with the fracture energy according to equation (I.2). In steady state, since $G_{ss} > G_0$, the size of the plastic zone increases due to the enhancement of the fracture energy:

$$R_{ss} \approx \frac{G_{ss}}{G_0} R_0$$

Crack velocity *vs.* plastic strain rate

According to *Landis et al.*, $\dot{\varepsilon}_0 R_0$ estimates the characteristic velocity of a material point going through the plastic zone. The crack velocity $\dot{a}$ should be compared to the value $\dot{\varepsilon}_0 R_0$ in order to make a distinction between "slow" and "fast" cracks. Thus, we consider the normalized velocity $v = \dot{a}/(\dot{\varepsilon}_0 R_0)$ in the calculations. As we impose the value of $\dot{a}$ to be 1, v was equal to $(\dot{\varepsilon}_0 R_0)^{-1}$. The "plastic strain rate amplitude" $\dot{\varepsilon}_0$ was adjusted to obtain a desired v value. "Slow cracks" correspond to $v \ll 1$ and fast cracks to $v \gg 1$.

The objective of the simulations was to establish the relationship between the steady-state fracture energy G_{ss} and the material parameters σ_Y, m, the rate v and the interface properties $\hat{\sigma}, G_0$:

$$\frac{G_{ss}}{G_0} = 1 + \mathscr{F}\left(\frac{\hat{\sigma}}{\sigma_Y}, v, m\right)$$

VI.4.2 Stress-based crack propagation criterion

Once our simulation has converged, we have to check whether the solution corresponds to a propagating crack. The condition for crack propagation was fixed based on the values of the stress at the crack tip (see appendix A for details). In this mode I model, we chose a criterion based on the normal stress only. Crack propagation occurs when the stress normal to the crack propagation direction, σ_{22}, reaches the cohesive stress. Our criterion is basically $\sigma_{22} = \hat{\sigma}$ at the crack tip.

VI.4.3 Effects of plasticity and loading rate

Varying the plastic behavior

In this opening-crack configuration, we now evaluate the influence of the dissipative properties of the material on fracture energy. We have first calculated G_{ss} for different values of the plastic exponent m, at fixed $\upsilon = 100$—*i.e.* for a fast crack. This value of υ corresponds to $\dot{\varepsilon}_0$ of the order of $0.01s^{-1}$ which favors fast convergence. Results are presented in figure VI.8a, for plastic exponent values of 3, 5 and 10. In all cases, the steady-state fracture energy starts to deviate from G_0 above $\hat{\sigma} = 2\sigma_Y$. The evolution in G_{ss} with $\hat{\sigma}$ is steeper at larger plastic exponents: with $m = 3$, G_{ss} behaves somehow linearly with $\hat{\sigma}$ and we do not obtain a strong exaltation in the explored range of cohesive stresses, while we observe a much faster increase of G_{ss} with $m = 10$.

Varying the loading rate: from small-scale yielding to fully-developed plasticity

Then, we have investigated the effect of loading rate with various values of υ at fixed plastic exponent $m = 10$, in figure VI.8b. When crack velocity increases, the onset of fracture energy exaltation is delayed towards higher values of the cohesive stress. This effect was attributed to an "increase in normal stresses along the crack plane"[3]: we discuss this feature in the following.

We now take a look at the mechanical fields in the converged steady state. The active plastic zone size is represented in the stress and plastic strain maps in figure VI.9. The equivalent stress is . In this case, the propagation criterion was $\hat{\sigma} = 2\sigma_Y$, which is satisfied at the crack tip. The active plastic zone, defined by $\overline{\sigma} \geq \sigma_Y$, extends in a lobe ahead of the crack, with a shape already seen in the literature (*cf* section I.5.4). In figure VI.9b, we have represented the plastic strain field in the tensile direction, *i.e.* along the X_2 direction. We observe a plastic wake (*cf* section I.5.4), a zone of constant plastic deformation, from the crack tip to the end of the free edge of the interlayer.

In fact, more plastic dissipation occurs at the crack tip when the crack velocity υ decreases, as it equivalent to boosting the value of $\dot{\varepsilon}_0$. Therefore, we need to pull more on the interlayer to satisfy the crack propagation criterion. The direct consequence is an enlargement of the active plastic zone. When the plastic zone size becomes comparable or greater than the thickness of the interlayer h_0, we attain a "fully plastifying" regime which accounts for the large exaltation of G_{ss} compared to

G_0. The typical shape of the plastic zone in the fully-plastic case is foreseen in figure VI.9a, as the pale green region extending between $X_1 = 0$ and $X_1 \approx -0.4$.

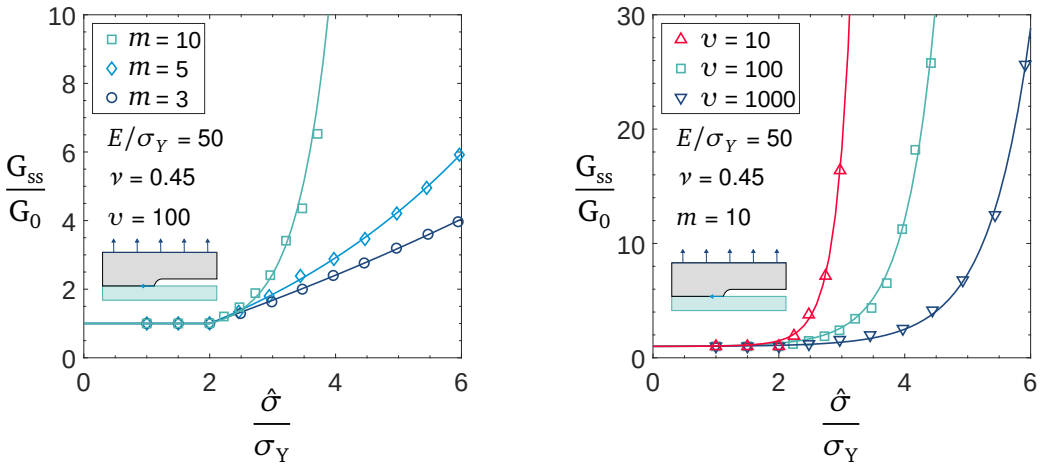

(a) Effect of the hardening exponent m.

(b) Effect of the normalized crack velocity υ.

Figure VI.8 Steady state fracture energy *vs.* cohesive stress for a mode I adhesive crack, with a viscoplastic material.

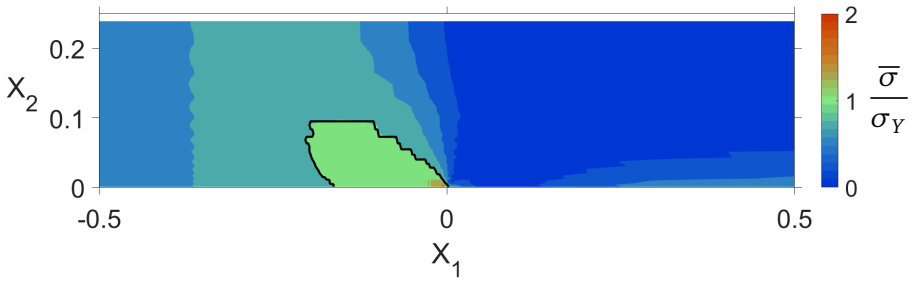

(a) Equivalent stress $\overline{\sigma}$. Black line: limit of the active plastic zone.

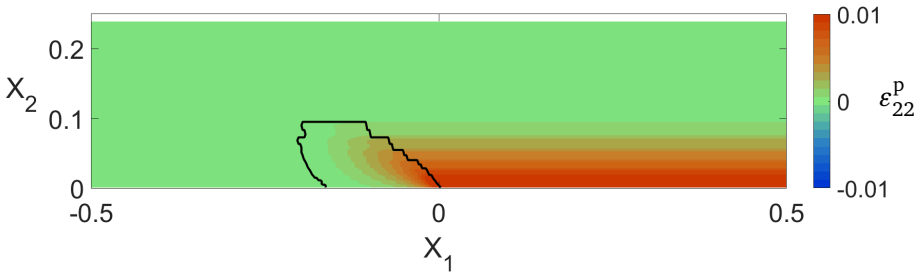

(b) Plastic strain ε_{22}^{p}. Black line: limit of the active plastic zone.

Figure VI.9 Equivalent stress and plastic strain field in steady-state for a mode I crack. Material parameters: $E/\sigma_y = 50$, $\nu = 0.45$, $m = 3$ and $\upsilon = 100$.

VI.5 Application to steady-state TCTT, with rate-dependent plasticity

The same steady-state scheme is here applied to the TCTT configuration. The upper edge of the interlayer is constrained by a symmetry boundary condition, and the displacement boundary condition is applied on the right edge (*cf* figure VI.4).

VI.5.1 Mixed-mode propagation criterion

In the case of an opening crack in mode I, the propagation criterion was fixed only on the normal stress σ_{22}. In the TCTT mode, the mode II contribution, related to the shear stress σ_{12}, is mixed with mode I and actually dominates. To take into account mode-mixity, we used a quadratic formulationof the criterion (*cf* ABAQUS Analysis User's guide[6] §32.5.6) :

$$\left(\frac{\sigma_{22}}{\hat{\sigma}_n}\right)^2 + \left(\frac{\sigma_{12}}{\hat{\sigma}_s}\right)^2 = 1$$

We chose equal values for the normal and shear cohesive stresses: $\hat{\sigma}_n = \hat{\sigma}_s = \hat{\sigma}$. Furthermore, the stiffnesses of normal and shear modes were also equal. The propagation criterion results in the equality between an "average" stress and the cohesive stress:

$$\langle\sigma\rangle = \hat{\sigma} \quad \text{with} \quad \langle\sigma\rangle = \sqrt{\sigma_{22}^2 + \sigma_{12}^2}$$

This choice is discussed in section VI.6.

VI.5.2 Steady-state fracture energy with a viscoplastic material

Parametric study: hardening exponent, strain rate effects

With this new configuration, we evaluate again the effect of the plastic exponent m, with the values 3 and 5. Results are presented in figure VI.10a: we observe first a slow linear increase of the fracture energy from $\hat{\sigma}/\sigma_Y = 0.5$ to a critical value which depends on m (*cf* table VI.1). Above this critical cohesive stress value, G_{ss} increases sharply even for a low value of m. We notice that the shape of G_{ss} is much steeper, once the critical value of $\hat{\sigma}/\sigma_Y$ is reached, compared to the mode I configuration (dashed lines in figure VI.10a).

m	υ	Critical $\hat{\sigma}/\sigma_Y$
3	10	1.5
3	100	2.2
3	1000	4.0
5	1000	2.7

Table VI.1 Critical cohesive stress value for fracture energy

The effect of the strain rate, via a variation of the normalized crack velocity υ, was investigated for $m = 3$. We remark that the plastic exponent value of 3 in the TCTT configuration (figure VI.10b) is lower than $m = 10$ in mode I simulations (figure VI.8b). Still, the shape of the fracture energy is, again, steeper in the TCTT configuration compared to mode I. At finite strain rates, the limit for crack propagation is shifted towards low values of the cohesive stress (*cf* table VI.1): for instance, it appears impossible to propagate a crack for $\hat{\sigma} \geq 2\,\sigma_Y$ in the case $\upsilon = 10$ and $m = 3$.

The fracture energy is presented against υ in figure VI.10c for a given interface strength $\hat{\sigma}$: the steady-state fracture increase at lower rates is clearly evidenced. Indeed, for high values of υ, the behavior is almost elastic—*cf* tensile curves in section VI.2.1—and $G_{ss} \to G_0$. At finite υ, G_{ss} departs from G_0, and is expected to increase even more for $\upsilon \to 0$, as the interlayer behavior tends towards perfect plasticity.

VI.5.3 From small-scale yielding to a fully-plastifying interlayer

In order to understand the "skyrocketing" behavior of the fracture energy above a certain cohesive stress, we take a closer look at the stress field in figure VI.11, and the plastic strain fields in figure VI.12. The plastic parameters in these stress and plastic strain maps are $m = 3$ and $\upsilon = 1000$.

Localized dissipation in small-scale yielding

Below the critical $\hat{\sigma}$ value, around 4 in this case, the active plastic zone extends only around the crack tip (figures VI.11a and VI.11b). The plastic-zone size R_{ss} (white half-circle in figure VI.11) scales consistently with the actual active plastic zone (thick black line) for the cases $\hat{\sigma}/\sigma_Y = 2$ and 3. In figure VI.12, the plastic wake—the region of constant plastic strain extending behind the crack tip—develops over a fraction of the thickness corresponding to R_{ss}/h_0.

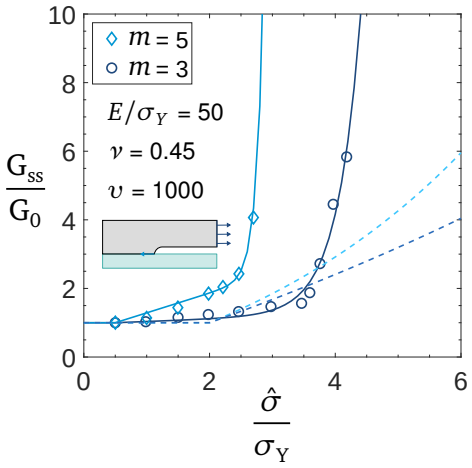

(a) Fracture energy *vs.* cohesive stress: effect of the plastic exponent m. Results in mode I are plotted in dashed lines.

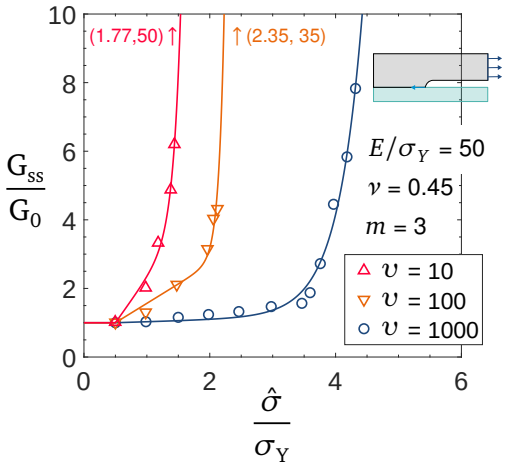

(b) Fracture energy *vs.* cohesive stress: effect of the normalized crack velocity υ.

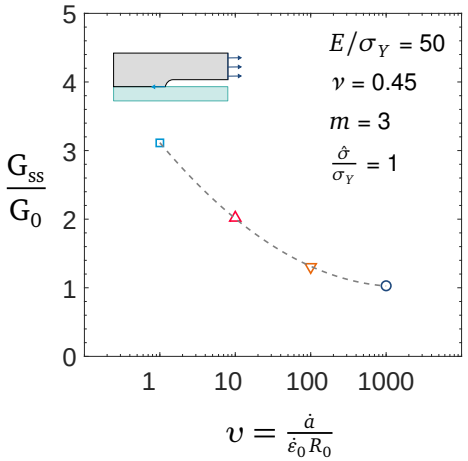

(c) Fracture energy *vs.* normalized crack velocity, in the case $\hat{\sigma} = \sigma_Y$.

Figure VI.10 Steady-state fracture energy G_{ss} in the TCTT configuration.

This situation corresponds to the "localized dissipation" hypothesis discussed in section V.2 (*cf* figure V.7a).

Transition to a fully-plastifying interlayer

At critical $\hat{\sigma} = 4$, however, the active plastic zone extends far beyond the crack tip region, over the entire thickness (figure VI.11c). This significant jump in the dissipative volume accounts for the fast and sharp increase of the macroscopic fracture energy.

When plasticity develops in the entire interlayer for $\hat{\sigma}/\sigma_Y = 4$, R_{ss} underestimates the size of the plastic zone (figure VI.11c): the small-scale yielding approach breaks, and we observe a fully-plastifying interlayer. This transition is also obseved in the plastic strain maps, in figure VI.12. For $\hat{\sigma}/\sigma_Y = 4$, we also observe a wake of constant plastic strain, over ∼20% of the thickness, right behind the crack tip at $X_1 \sim 0.25$ (figure VI.12e). In the wake, plasticity is not active due to softening induced by the pronounced plastic flow at the crack tip. Above the plastic wake, between $X_1 = 0$ and $X_1 = 1$, the plastic strain increases monotonically in the bulk of the interlayer.

In figure VI.12g, we notice that the interlayer becomes plastically active over the entire thickness far behind the crack tip, for $X_1 \geq 1$. In this far-field region, the wake is reloaded elastically, and we obtain an homogeneous plastic strain which goes on increasing along the length of the ligament.

VI.6 Conclusions and perspectives

VI.6.1 Successful implementation of a steady-state crack with a commercial FEA code

The first major conclusion of this chapter is that our steady-state crack model works. Indeed, we are able to provide the FEA simulation with an initial state of stress which represents the contribution of the inelastic behavior, evaluated from the steady-state fields. This inelastic contribution is proved to converge, and a fracture energy is computed by an energy balance presented in VI.3.3. In our calculations, the ratio G_{ss}/G_0 was typically between 1 and 10. That being said, higher values have been reached, up to 50, which the order of magnitude of high plastic effects[55]: our steady-state crack method is able to capture quite strong dissipative effects.

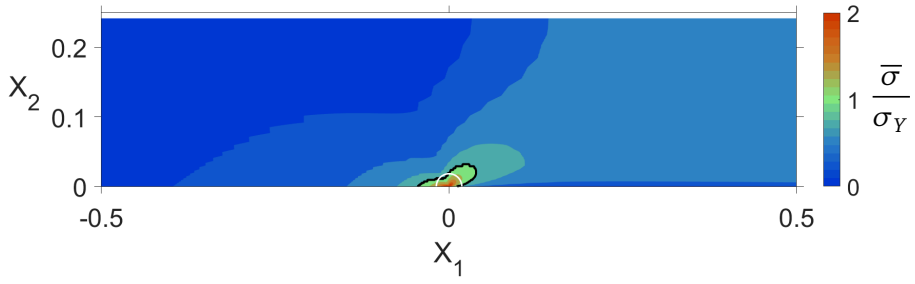

(a) $\hat{\sigma}/\sigma_Y = 2$

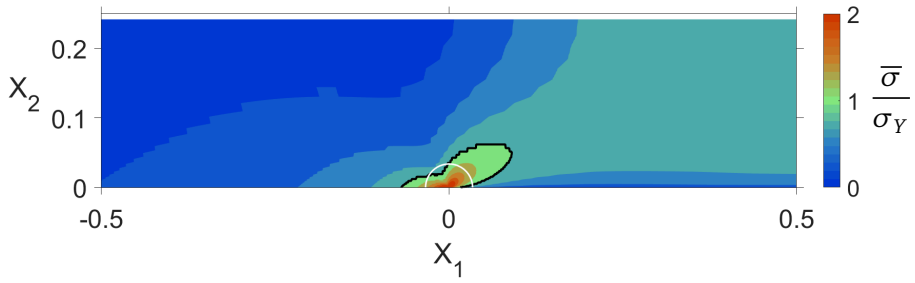

(b) $\hat{\sigma}/\sigma_Y = 3$

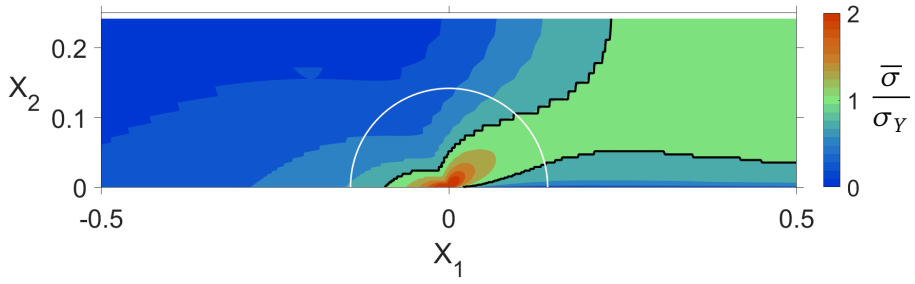

(c) $\hat{\sigma}/\sigma_Y = 4$

Figure VI.11 Equivalent stress $\overline{\sigma}$ in the converged step, with a viscoplastic material in the TCTT configuration. Material parameters: $E/\sigma_y = 50$, $\nu = 0.45$, $m = 3$ and $\upsilon = 1000$. The limit of the active plastic zone $\overline{\sigma} \geq \sigma_Y$ is indicated by the thick black line. The plastic zone size R_{ss} is indicated by the white half-circle.

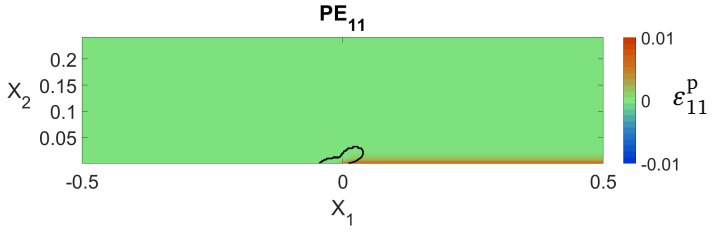

(a) $\hat{\sigma}/\sigma_Y = 2$

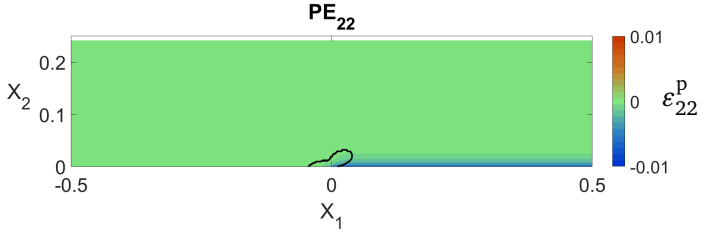

(b) $\hat{\sigma}/\sigma_Y = 2$

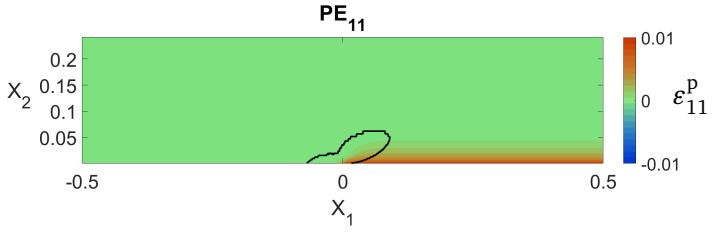

(c) $\hat{\sigma}/\sigma_Y = 3$

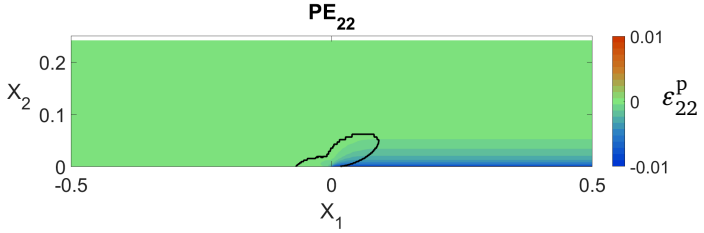

(d) $\hat{\sigma}/\sigma_Y = 3$

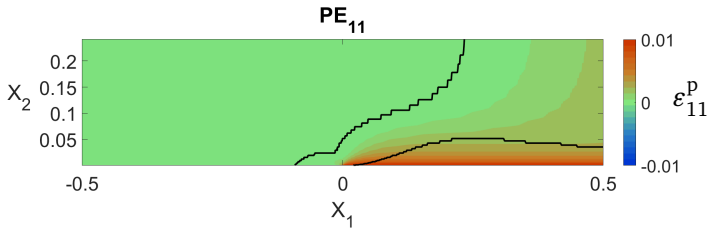

(e) $\hat{\sigma}/\sigma_Y = 4$

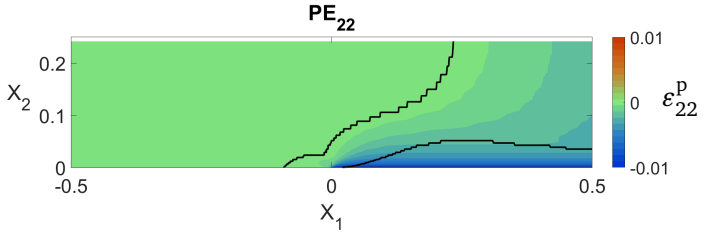

(f) $\hat{\sigma}/\sigma_Y = 4$

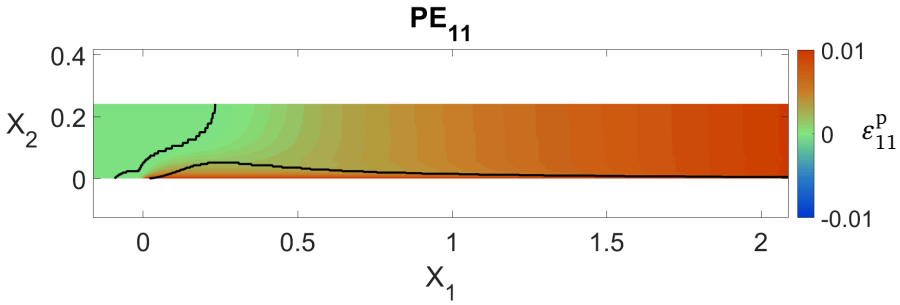

(g) $\hat{\sigma}/\sigma_Y = 4$

Figure VI.12 Plastic deformation in steady-state in converged step. Material parameters: $E/\sigma_y = 50$, $\nu = 0.45$, $m = 3$ and $\upsilon = 1000$. The thick black lines indicates the active plastic zone size $\overline{\sigma} = \sigma_Y$.

In the results presented here, we have investigated two effects: interfacial adhesion *via* the cohesive stress value $\hat{\sigma}$, and rate effects *via* the normalized crack velocity v. Up to this point, we have scratched the surface of the capacities of the numerical tool. The first results on the opening-crack configuration show consistency with the literature[3], comforting the relevance of the steady-state approach. Then, preliminary results on the TCTT demonstrate that the fracture energy increases much faster with the cohesive stress, due to the different mode mixity. A transition between small-scale yielding and a fully-plastifying interlayer is also evidenced.

These results—which are, after all, preliminary—pave the way to more thorough parametric studies. In particular, we suggest to investigate the role of interlayer thickness, wondering how it could affect the extent of the active plastic zone.

VI.6.2 Perspectives and improvements

Refinements of the cohesive-zone model: mode-mixity, rate-dependency

In our simulations, the choice of equal cohesive stresses in normal and shear modes surely affects the results, as evoked in section I.5.4 based on the simulation of *Tvergaard*[7]. The systematic study of mode-mixity effects within the cohesive zone would broaden the understanding of the coupling between interface processes and the macroscopic fracture energy.

Moreover, the interface model considered here is rate-independent: our cohesive zone is merely a layer of springs. Indeed, a rate-independent interfacial work of separation Γ_0 is an idealized vision of the de-adhesion process. For instance, it has been proved recently that molecular bond rupture in elastomers is actually rate-dependent[105]: the dissipative behavior also affects the fundamental debonding processes at the interface. Therefore, rate-dependency of the cohesive law, as implemented by *Landis et al.*[3], would be a further development of the method.

Different material constitutive behaviors

The foundations of the algorithm do not depend upon the choice of the material behavior, which makes the method versatile. We have implemented a viscoplastic model for the sake of simplicity in the integration procedure, and also for straightforward comparison with the literature. Nevertheless, a creep-based model for viscoelasticity

(*cf* section VI.2.2) is an almost immediate development of the method: we just need to write a different flow rule.

Towards a finite-strain algorithm

Finite-deformations are still beyond the scope of the small-strain method presented in this chapter. At this stage, the method cannot capture the effect of finite-strain at the crack tip. With highly deformable polymers, the crack opening displacement is large and tensile stresses develop at the crack tip. In such a situation, crack propagation is dictated by a mix between mode I and mode II processes—at least in a bidimensional problem. In addition, strain-hardening at the crack tip is suspected to affect stress triaxility locally, which also affects adhesion rupture.

Still, finite-deformations and "realistic" material behaviors—in the sense that polymers are stretchy and dissipative—are not so far from our grasp. Indeed, we propose a strategy to extend our current algorithm to the case of finite strains in appendix B, based on the multiplicative split of the deformation gradient.

Take-home messages of chapter VI

- The principle of the steady-state crack method is the integration of the mechanical history over streamlines. The method has been implemented by coupling the FEA software ABAQUS and a numerical computing software.
- The algorithm is based on the decomposition of the strain into elastic and inelastic parts. The dissipative strain contribution is computed outside of the FEA simulation, using the steady-state assumption. This additional strain is re-injected in the FEA calculation as an initial stress state.
- Simulation results are presented in a mode I crack and in the TCTT configuration, with a viscoplastic material law. The simulations establish a relationship between an interface property, namely the cohesive stress, and the macroscopic fracture energy. In the TCTT, a critical cohesive stress value was evidenced: it separates small-scale yielding for low interface toughness from a fully-plastifying regime at high interface toughness.

VII
Conclusion(s) & perspectives

In this work, we have used the Through Crack Tensile Test to investigate dissipative mechanisms originating in deadhesion and deformation of the interlayer in laminated glass. In particular, we have focused on the steady-state delamination regime, characterized by a constant force F_{ss} and a constant macroscopic stretch of the interlayer λ_{ss}. In steady-state, the amount of energy dissipated by the system is given by the macroscopic work of fracture $G_{\mathrm{m}} = F_{ss}(\lambda_{ss} - 1)/b_0$.

In steady-state, the work of fracture increases linearly with interlayer thickness (*cf* section I.4.2). This has been interpreted as the signature of two dissipative mechanisms: deadhesion of viscoelastic PVB, which involves significant dissipation at the crack tip represented by Γ_{crack}, and stretching of the interlayer characterized by a dissipated energy density Π_{bulk}, so that $G_{\mathrm{m}} = \Gamma_{\mathrm{crack}} + h_0 \cdot \Pi_{\mathrm{bulk}}$.

In the following, we summarize the evolution of G_{m} with adhesion, in the case of PVB laminates(*cf* chapter III), and with the change of rheology with the EVA interlayer (*cf* chapters IV & V). We also try and rationalize the "rupture" and "unstable" limits of the TCTT (*cf* section I.4.2).

Finally, we suggest further leads to follow, in particular for the numerical simulations.

VII.1 Adjusting adhesion for optimal energy dissipation

VII.1.1 Surface chemistry: a toolbox for a quantitative approach to adhesion modification

Adhesion modification with PVB: exploration of the steady-state regime

In chapter III, we have used silane chemistry to modify the surface of float glass, and control the adhesion between interlayer and glass. We have demonstrated that increasing the adherence of the PVB interlayer resulted in a higher macroscopic work of fracture (figure VII.1), however limited by the cohesive rupture of the interlayer at high adhesion. We have attributed this constant bulk dissipation term to the compensating effects of strain rate and stretch.

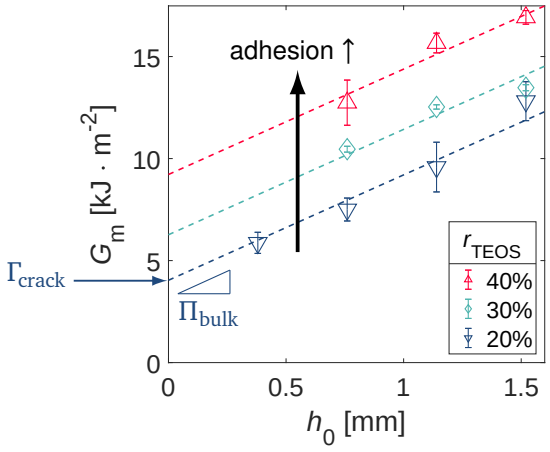

Figure VII.1 TCTT with PVB-laminated glass at various adhesion: macroscopic work of fracture vs. interlayer thickness.

Adhesion modification with EVA: from rupture to steady-state

In chapter V, TCTT results in EVA laminates remind us that steady-state delamination should not necessarily be expected *a priori*. In fact, the industrial PVB system results from decades of optimization: this is why we observe stable delamination and high energy dissipation in the TCTT. For EVA laminates however, some effort has been required to obtain deadhesion. With the same approach of surface chemistry mod-

ification, we have proved that delamination can be recovered with EVA laminated against a methylated surface.

VII.1.2 Interlayer strength as the limit to delamination

In the experiments, we have been confronted to a rupture of the interlayer at high loading rates. In previous work, an empirical limit between steady-state and "rupture" regimes has been estimated from the TCTT "phase diagram" (figure I.9).

Here, we derive a simplistic model to try and explain this "rupture" limit. We assume that tearing of the interlayer—*i.e.* the propagation of a cohesive crack within the polymer foil—is the limiting phenomenon, and designate by Γ_{PVB} the intrinsic fracture toughness of the PVB interlayer. A transversal crack is assumed to propagated at the velocity c, with the speed of sound $c_{\max} \sim \sqrt{E/\rho}$ as upper limit.

Now, we write an energy balance between the energy for interlayer delamination and the energy required to propagate a cohesive crack within the interlayer, over an increment of time $\mathrm{d}t$:

$$\mathrm{d}E_{delam} \sim G_{\mathrm{m}}\, b_0\, \dot{a}\, \mathrm{d}t \qquad\qquad \mathrm{d}E_{tear} \sim \Gamma_{PVB}\, h_0\, c\, \mathrm{d}t$$

The limit between delamination and tear regimes arises when it is more favorable to propagate a crack within PVB. The limit between the two occurs when the two increments are equal, which leads to a critical value for the work of fracture:

$$G_{\mathrm{m,c}} \sim \Gamma_{PVB}\, \frac{h_0}{b_0}\, \frac{c}{\dot{a}} \tag{VII.1}$$

Equation (VII.1) gives a rule of thumb for the evolution of the maximum work of fracture attainable. $G_{\mathrm{m,c}}$ scales with the intrinsic tear resistance of the interlayer: with a tougher material, we can expect higher values for the work of fracture. The geometric ratio h_0/b_0 is usually small compared to 1—of the order of $10^{-}2$ in our TCTT specimens. The velocity ratio $c/\dot{a}$ is usually large: from TCTT experiments, we know that $\dot{a} \sim 1-10\,\mathrm{mm\cdot s^{-1}}$ while $c \sim 10^3 - 10^4\,\mathrm{mm\cdot s^{-1}}$ when rupture of the interlayer occurs.

Limit of the work of fracture in thin interlayers

First, $G_{m,c}$ increases at higher interlayer thickness h_0: this is consistent with our experimental observations in section III.3. Conversely, all other parameters kept constant, tearing of the interlayer occurs more easily for thin interlayers. With our rule of thumb, we predict a "tear" limit depending on interlayer thickness (figure VII.2).

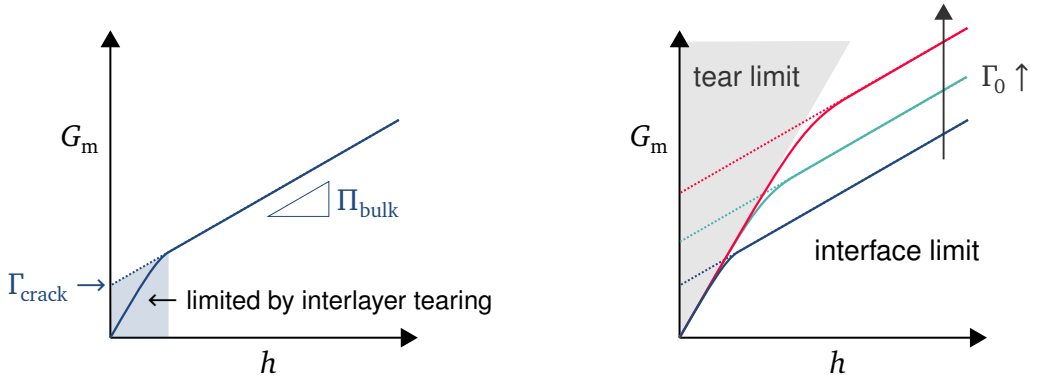

(a) Lower limit for the macroscopic work of fracture: cohesive tearing in thin interlayers.

(b) Effect of a the glass/polymer adhesion on the macroscopic work of fracture, and tear limit for low interlayer thickness.

Figure VII.2 "Rupture" limit in the TCTT for thin interlayers

The adhesion-modification method with silane chemistry seems to be an appropriate tool to explore more finely this "rupture" limit, relevant for impact performance. For instance, assuming we could get PVB interlayers with fine differences in thickness, we could determinate a minimal thickness of PVB required for steady-state delamination and the evolution of this critical thickness with adhesion.

Limit of the work of fracture at high velocities

Moreover, our scaling tells us that $G_{m,c}$ decreases at higher crack velocities, *i.e.* at higher loading rate, which is also consistent with our observations (*cf* section V.3). Under the crude approximation that all other values are fixed, this gives the velocity limit for the work of fracture: $G_{m,c} \sim \dot{a}^{-1}$. This relationship was schematically plotted in figure VII.3. Below the tear limit, we recover steady-state crack propagation—in a region we designate as "interface limited"—and the increase of G_m with crack velocity.

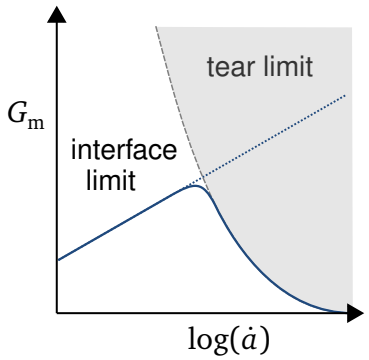

Figure VII.3 Velocity limit for the macroscopic work of fracture

VII.2 A large dissipating volume is needed for optimal performance

In previous work with PVB, the mechanisms for energy dissipation were pictured to occur in two spatially distinct zones (figure VII.5a), at the vicinity of the crack tip and in the volume of the interlayer. With such a large solicited volume, the work of fracture could reach between 5 and 15 $\mathrm{kJ \cdot m^{-2}}$.

VII.2.1 Elasto-plastic interlayer above the glass transition: localized dissipation?

As stressed out in chapter IV, the behavior of EVA is drastically different from PVB: at ambien temperature, EVA exhibits rate-independent plastic features originating in a crystalline content. Through Crack Tensile Tests with EVA have shown that the work of fracture evolved very little with interlayer thickness (figure VII.4) and loading rate with this elasto-plastic interlayer. For the loading rate, this observation is consistent with the rate-independency of the mechanical behavior at ambient temperature.

In this elasto-plastic material, dissipation at the crack tip has been shown to be dominant compared to bulk effects: the work of fracture is merely the contribution of each adhesive crack (figure VII.5b). The volume available for energy dissipation corresponds to the plastic zone size, which we estimated to be roughly the thickness of the interlayer.

VII.2.2 Dissipation dominated by viscoelasticity at the glass transition

Nonetheless, the work of fracture in TCTT is much higher at the glass transition of the polymer, and thickness and strain rate dependencies are recovered when EVA is tested at −20°C (figure VII.4). Viscoelasticity takes over plasticity as the dominant energy dissipation process at T_g. In EVA at lower temperatures, the effects of plasticity and viscoelasticity are combined (figure VII.5c) and the work of fracture reaches values up to $25\,\mathrm{kJ}\cdot\mathrm{m}^{-2}$.

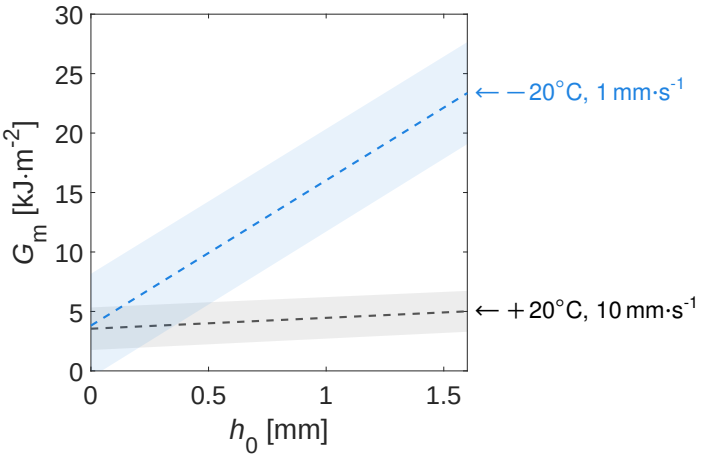

Figure VII.4 TCTT with EVA laminates: macroscopic work of fracture *vs.* interlayer thickness, at ambient temperature and close to the glass transition.

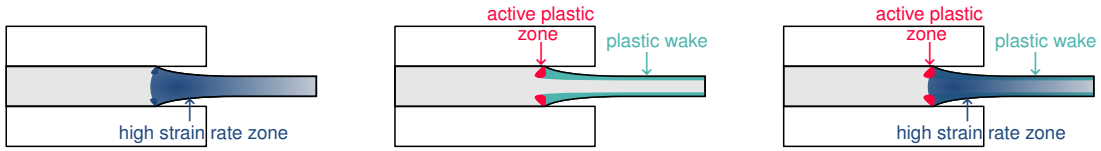

(a) Viscoelastic interlayer: PVB at ambient temperature.

(b) Elasto-plastic interlayer: EVA at ambient temperature.

(c) Elasto-visco-plastic interlayer: EVA at lower temperatures.

Figure VII.5 Schematic of the mechanisms for energy dissipation upon delamination and stretching of interlayers.

Compared at their respective glass transition temperatures, EVA even performs better than PVB in the TCTT: EVA would have been a material of choice to make windshields during the last ice age, 10,000 years ago. Actual impact tests—such as the ball-drop tests decribed in section I.2—on the EVA–methylated-glass system at low temperatures would be an immediate and thrilling confrontation of the TCTT

results. Unfortunately, we are not able to present such results here due to the heavy glass preparation protocol, despite their relevancy for industrial transposition of the TCTT.

Energy dissipation and molecular architecture

The elasto-plastic behavior of EVA is peculiar, as it is both stretchy and dissipative. Polymer materials in their glassy state, well below T_g, also exhibit plastic deformation but are less stretchable and more brittle. An example of such material could be SentryGlas® at ambient temperature[106]. Furthermore, a common feature between all interlayer materials is the manifestation of a secondary structure: hard and soft domains for PVB, crystalline domains for EVA, ionic clusters in SentryGlas®. Experimental investigation of structured polymers in laminate glass applications, such as thermo-plastic elastomers (TPE), would surely provide another insight on dissipation mechanisms.

VII.3 Numerical modeling of a steady-state crack

VII.3.1 Steady-state modeling, long story short

In chapter VI, we have developped a numerical scheme to implement the steady-state crack method with the commercial FEA software ABAQUS. The principle of the method has been presented in section VI.3, the practical implementation in appendix A.

This numerical tool has been validated with a viscoplastic material behavior: the dissipative behavior was prescribed through a plastic strain rate—the flow rule—which allows direct integration *via* the steady-state assumption. Then, we have implemented steady-state crack propagation in the TCTT configuration in section VI.5, still with a viscoplastic material model. The effect of the interface and of the strain rate have been numerically investigated. At higher adhesion, the exaltation of the steady-state work of fracture have been related to the development of an active plastic zone size at the crack tip. We have evidenced a dramatic steepening in the evolution of the fracture energy above a cohesive stress threshold, related to the development of the active plastic zone over the entire interlayer.

VII.3.2 Lower limit in the TCTT phase diagram: bridging viscoelasticity and plasticity

Viscoelastic fracture mechanics tells us that the fracture energy increases when the velocity increases, as observed in the TCTT "phase diagram" of *Elzière* (*cf* section I.4.2). However, viscoelastic theories alone do not explain the "unstable" regime, and why the PVB interlayer is able to stop from propagating until rupture whereas the loading rate is lower. Here, we invoke arguments from crack propagation in plastic media to explain this unstable limit at low velocities.

In the traction response of PVB, a pseudo-yield stress arises at high rate and low temperatures, due to the slowing down of polymer chain dynamics close to the glass transition. According to fracture mechanics in plastic media, a higher yield stress makes the fracture energy diminish. The actual physical process in PVB would be viscoelastic creep, not truly plastic flow. Still, both processes can be described with a rate-dependent inelastic strain, as described in section VI.2. For this similarity, we estimate relevant to interpret the low-rate limit with PVB in light of plastic crack propagation.

At lower loading rates, the pseudo-yield stress of PVB decreases: (visco)plastic fracture mechanics tells us that the fracture energy should increase at low crack velocity (figure VII.6).

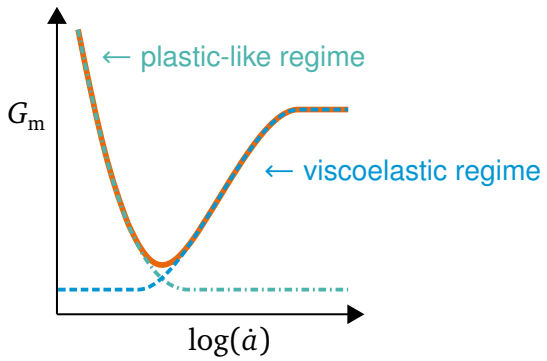

Figure VII.6 Combination of viscoelastic and plastic contribution to the work of fracture with PVB. The low-rate limit in the TCTT arises from plastic-like processes.

All in all, viscoelasticty and plasticity have counteracting effects on fracture energy:

- at higher loading rate and crack velocity, viscoelasticity makes the work of fracture increase while plastic effects fade out;
- at lower loading rates and crack velocity, plastic-like processes at the crack tip make the work of fracture increase while viscoelastic enhancement fades out.

Eventually, the variation of the work of fracture with crack velocity (or loading rate) is sketched in figure VII.6. We expect numerical simulations to consolidate this hand-waving model and provide more insight, considering a more realistic material behavior such as non-linear viscoelasticity.

VII.3.3 Perspectives: finite deformations and rate-dependent materials

An immediate step forward in the numerical simulations would be the implementation of a finite-strain method, as described in appendix B. A finite-strain model would allow the investigation of two major features, the first being mode mixity. Indeed, large deformations induce a large curvature at the crack tip, and the strong mode II turns into mode I+II at the crack tip. Moreover, the large-strain behavior of these polymers exhibits strain-hardening. Strain-hardening modifies the stress field, specifically the stress triaxiality, at the crack tip: such hydrostatic effects are known to affect significantly the fracture behavior of polymers.

Taking into account these non-linear features can only be achieved with a non-linear model, which we hope to develop in a near future.

APPENDICES

A

Steady-state scheme implementation with ABAQUS

The ABAQUS software (3DS Simulia®, version 2016) was used to build the numerical model. However, modeling a steady-state crack is not a built-in feature of a commercial FEA software like ABAQUS. The choice was made to use ABAQUS only as an "elastic solver" and to evaluate additional contributions to strains and stresses with post-processing*.

A.1 Using residual stresses to input additional deformation

The principle of virual work stated in a quasi-static assumption, without actual body forces, reduces to a balance between internal stresses and surface tractions (or boundary conditions):

$$\int_V \delta\varepsilon_{ij}\sigma_{ij}\,\mathrm{d}V - \int_S \delta u_i T_i\,\mathrm{d}S = 0$$

Considering that $\sigma_{ij} = \mathfrak{C}_{ijkl}\varepsilon^{\mathrm{e}}_{kl} = \mathfrak{C}_{ijkl}\left(\varepsilon_{kl} - \varepsilon^{\mathrm{p}}_{kl}\right)$, we can re-write the principle of virtual work considering that plastic strains engender an additional term in the

*Another way could have been to write a user material (*UMAT*) to integrate the dissipative behavior within ABAQUS itself. It would have required the storage of all strain history between adjacent elements, surely through Fortran *COMMON blocks*. Such an approach seemed to lie beyond our expertise.

equilibrium equation[59]:

$$\int_V \delta\varepsilon_{ij}\mathfrak{C}_{ijkl}\varepsilon_{kl}\,\mathrm{d}V - \int_S \delta u_i T_i\,\mathrm{d}S + \int_V \delta\varepsilon_{ij}\left(-\mathfrak{C}_{ijkl}\varepsilon^{\mathrm{p}}_{kl}\right)\mathrm{d}V = 0 \tag{A.1}$$

The third term in equation (A.1) could be considered either as a pseudo body force or a residual stress contribution. For the implementation in ABAQUS, we chose to treat this additional contribution as a residual stress. Indeed, one of the the most general method to provide ABAQUS with a non-zero mechanical history is the use of residual stresses through the subroutine `SIGINI`. This subroutine is called for every integration point in each element: it allows the input of any initial stress state.

For the FE solver, the initial stress field is therefore (in index notation):

$$\sigma^{\mathrm{R}}_{ij} = -\mathfrak{C}_{ijkl}\varepsilon^{\mathrm{p}}_{kl} = -\left(2\,\mu\,\varepsilon^{\mathrm{p}\prime}_{ij} + \kappa\,\varepsilon^{\mathrm{p}}_{kk}\,\delta_{ij}\right)$$

As the material behavior was tweaked outside of the FEA solver, convergence also had to be checked after each iteration (see figure A.2).

A.2 Data post-processing

The dissipative contributions to the mechanical behavior were computed with MATLAB (Mathworks®, r2017b). The results of ABAQUS' calculation were retrieved from the results file, and converted to matrices suitable for further calculations, detailed below.

Practically, only the non-zero values of residual stresses were written to a text file. Each line of this array was composed of the element number, the integration point, and the four values (in 2D) of residual stress to be read by Abaqus. The array is read only once in the `UEXTERNALDB` subroutine and passed on to the `SIGINI` subroutine via a *COMMON* block.

A.3 Definition of the model: geometry and boundary conditions

The model is developped in a 2D plain strain approach, which means that $\varepsilon_{33} = \varepsilon_{13} = \varepsilon_{23} = 0$ and $\sigma_{13} = \sigma_{23} = 0$. Lengths are taken to be millimeters, therefore the stresses are in MPa. The geometry was segmented into two sections (figure A.1):

- The interlayer section, a rectangle with length $L = 20$ ($X_1 = [-10, 10]$) and a thickness $h = 0.25 - 0.5$.
- The cohesive layer section, made of square elements of thickness $h_{coh} = 0.005$.

A.3.1 Mesh

The advancing front algorithm with quadrilateral elements was used to create the mesh. The edges of the geometry were seeded with smaller elements close to the crack tip. The size of the elements at the crack tip is typically 10 times smaller than elements in the far field region. The interlayer section was meshed with linear isoparametric elements *CPE4*, the cohesive layer with linear *COH2D4* elements. The node at $(0, 0)$ is common between the cohesive and the interlayer sections, it defines the crack tip.

The final mesh is composed of rectangular elements only, which allows a convenient post-processing of the data as this mesh resembles a matrix. Indeed, integration along the streamlines in the initial configuration is merely a sum along iso-X_2 lines. Physical values are retrieved and computed at integration points, *i.e.* suitable for integration following a quadrature scheme

A.4 Numerical integration

A full integration is performed by ABAQUS with the CPE4 linear plain strain elements. As a result, the physical values are obtained at 4 integration points.

The coordinates – and all other quantities – are retrieved in matrix form. The number of elements in the model is $N = n_l \times n_c$, the number of integration points is $4N = 2\,n_l \times 2\,n_c$. The coordinate x_1 along the first base vector, at the i-th integration point in the n-th element, is noted $x_1^{i(n)}$. Assuming a column-wise numbering of the

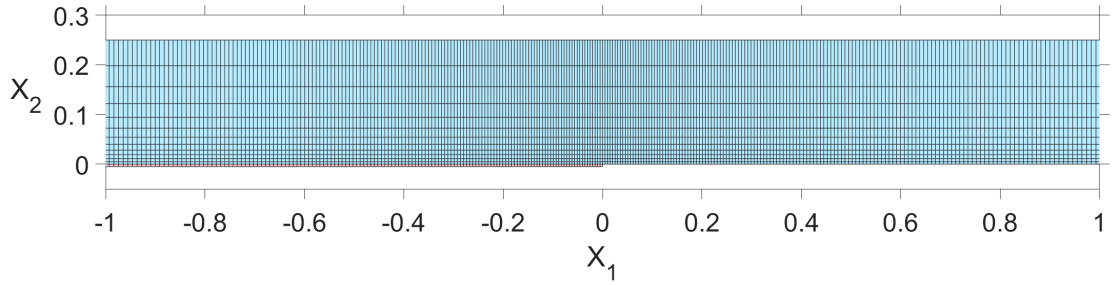

(a) Coarse view of the mesh.

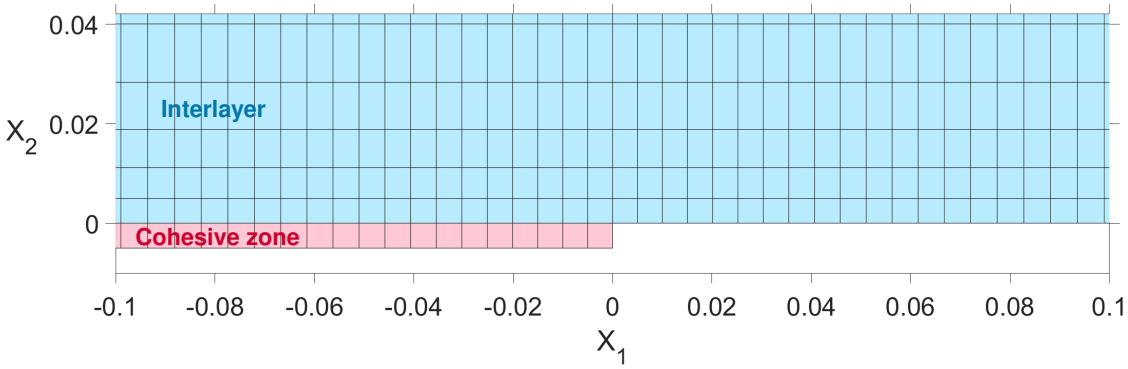

(b) Zoom on the crack tip, located in (0,0), where the layer of cohesive elements end.

Figure A.1 Finite element mesh obtained with graded edge seeding and the advancing front algorithm in ABAQUS.

elements[†], the coordinate matrix can be written in the following form:

$$[X_1] = \begin{bmatrix} x_1^{1(1)} & x_1^{2(1)} & \dots & x_1^{1(k)} & x_1^{2(k)} \\ x_1^{3(1)} & x_1^{4(1)} & \dots & x_1^{3(k)} & x_1^{4(k)} \\ x_1^{1(2)} & x_1^{2(2)} & \dots & \vdots & \vdots \\ x_1^{3(2)} & x_1^{4(2)} & \dots & \vdots & \vdots \\ \vdots & \vdots & \ddots & \vdots & \vdots \\ x_1^{1(n_l)} & x_1^{2(n_l)} & \dots & x_1^{1(N)} & x_1^{2(N)} \\ x_1^{3(n_l)} & x_1^{4(n_l)} & \dots & x_1^{3(N)} & x_1^{4(N)} \end{bmatrix}$$

[†]which is absolutely not what ABAQUS does, but nothing prevents us from re-ordering the elements as long as we do not lose track of the element numbers.

With $k = n_l(n_c - 1) + 1$ for the sake of readability. In the undeformed configuration, each column vector contains the same x_1 values.

Similarly, the 2nd-coordinate matrix $[X_2]$ contains equal values along its rows in the undeformed configuration.

For the integration, we need two matrices operations:

- The regular matrix product:
  $[C] = [A] \cdot [B] \leftrightarrow C_{ij} = \sum_k A_{ik} B_{kj}$
- The Hadamard product, or element-wise product, or "array" product:
  $[C] = [A] \circ [B] \leftrightarrow C_{ij} = A_{ij} B_{ij}$ (no sum)

A.4.1 Quadrature scheme in matrix form

A.4.2 1D integration

$$\int_{-\frac{a}{2}}^{+\frac{a}{2}} f(x)\,\mathrm{d}x = \int_{-1}^{+1} f\left(x\left(\xi\right)\right) \frac{\partial x}{\partial \xi}\,\mathrm{d}\xi$$

The $\frac{\partial x}{\partial \xi}$ term is the Jacobian associated to the mapping from current to normalized coordinates.

We define the two Jacobians along the first coordinate J_X and along the second coordinate J_Y. In the case of isoparaetric linear elements, with a rectangular shape of length a and height b, we obtain:

$$J_X = \frac{\partial x_1}{\partial \xi_1} = \frac{a}{2}$$
$$J_Y = \frac{\partial x_2}{\partial \xi_2} = \frac{b}{2}$$

The Jacobian is calculated for every rectangular element thanks to the position of the integration points. We know that the reduced distance between integration points is $\Delta\xi_1 = 2/\sqrt{3}$ in a rectangular element:

$$\Delta x_1 = \frac{2}{\sqrt{3}} J_X \Rightarrow J_X = \frac{\sqrt{3}}{2} \Delta x_1$$

As a consequence, integration along iso-X_2 lines reduces to a simple sum over matrix rows.

The Jacobian values for each element were obtained from the coordinate matrices, via a matrix product using the following square block matrix $[\Delta_{2n}]$:

$$[\Delta_{2n}] = \begin{bmatrix} -1 & -1 & 0 & 0 & \dots & 0 & 0 \\ 1 & 1 & 0 & 0 & \dots & 0 & 0 \\ 0 & 0 & -1 & -1 & \dots & 0 & 0 \\ 0 & 0 & 1 & 1 & \dots & 0 & 0 \\ \vdots & \vdots & \vdots & \vdots & \ddots & \vdots & \vdots \\ 0 & 0 & 0 & 0 & \dots & -1 & -1 \\ 0 & 0 & 0 & 0 & \dots & 1 & 1 \end{bmatrix}$$

Therefore :

$$[J_X] = \frac{\sqrt{3}}{2}[X_1] \cdot [\Delta_{2n_c}]$$
$$[J_Y] = \frac{\sqrt{3}}{2}[\Delta_{2n_l}]^T \cdot [X_2]$$

The quadrature formula then allows an approximate evaluation of the integral, as a weighted sum of the values at the integration points:

$$\int_{-1}^{1} f(\xi)\,\mathrm{d}\xi = \sum_i w_i f\left(\xi^{(i)}\right)$$

A.4.3 Special case of line integration: steady-state

Integration over a streamline was performed by row-wise cumulative sum. Indeed, the integration range could be segmented into the sum of the integral over each element. Then, the quadrature scheme was applied within each element.

$$F(X) = \int_0^X f(x)\,\mathrm{d}x = \sum_n \int_{X_n}^{X_{n+1}} f(x)\,\mathrm{d}x = \sum_n \sum_i w_i J_{X(n)} f_n\left(\xi^{(i)}\right)$$

The quadrature scheme was applied as a matrix operation: the values of the function are multiplied with J_X by an element-wise product, and then the sum is performed by a matrix product with a triangular-like matrix $[T]$:

$$[F] = ([f] \circ [J_X]) \cdot [T]$$

The sparse square matrix $[T]$ was built to perform the row-wise cumulative sum with a single matrix operation: $[T]$ is composed of a 2×2 matrix of 1's repeated along and above the diagonal n_c-times, and zeroes on the lower part.

$$[T] = \begin{bmatrix} 1 & 1 & 1 & 1 & \dots & 1 & 1 \\ 1 & 1 & 1 & 1 & \dots & 1 & 1 \\ 0 & 0 & 1 & 1 & \dots & 1 & 1 \\ 0 & 0 & 1 & 1 & \dots & 1 & 1 \\ \vdots & \vdots & \vdots & \vdots & \ddots & \vdots & \vdots \\ 0 & 0 & 0 & 0 & \dots & 1 & 1 \\ 0 & 0 & 0 & 0 & \dots & 1 & 1 \end{bmatrix}$$

A.4.4 Integration of non-linear viscoelastic behavior

Numerical integration of the ODE system cannot be performed directly (with a Runge-Kutta algorithm for example) as we lack a functional expression for the deviatoric stress. Once again, we used the steady-state assumption and quadrature scheme to perform the integration.

$$\begin{cases} \dot{\varepsilon}^{\mathrm{cr}}_{ij\,(n)} = \dfrac{g\left(\overline{\varepsilon}^{\mathrm{cr}}_{(n)}\right)}{\eta_\infty}\,\sigma'_{ij\,(n)} \\ \varepsilon^{\mathrm{cr}}_{ij\,(n)} = \displaystyle\sum_{k=0}^{n} J_k w_I \dot{\varepsilon}^{\mathrm{cr}}_{ij\,(k)} = \varepsilon^{\mathrm{cr}}_{ij\,(n-1)} + J_n w_I \dot{\varepsilon}^{\mathrm{cr}}_{ij\,(n)} \end{cases}$$

At the n-th integration point, we solve the non-linear system for $\left(\varepsilon^{\mathrm{cr}}_{11}, \varepsilon^{\mathrm{cr}}_{22}\right)$:

$$\frac{1}{J_n w_I}\left(\varepsilon^{\mathrm{cr}}_{ij\,(n)} - \varepsilon^{\mathrm{cr}}_{ij\,(n-1)}\right) - \frac{\sigma'_{ij}}{\eta_\infty}\, g\left(\overline{\varepsilon}^{\mathrm{cr}}_{(n)}\right) = 0$$

A.5 Fracture energy computation

The flow of energy towards the crack tip was computed following the energy balance presented in section VI.3.3. The strips of material considered to make the energy balance was taken in $X_1^+ = 8$ and $X_1^- = -8$. The extremal positions at $X_1 = \pm 10$ were avoided to circumvent edge effects. Indeed, the strain and stress fields could

behave badly at the far-right side of the model, where the residual stress field was constrained by the constant-displacement boundary condition.

The fictitious crack advance Δa was taken equal to the element length.

A.5.1 Elastic energy release

The elastic strain energy density was computed as $W_0 = \frac{1}{2}\,\sigma_{ij}\,\varepsilon_{ij}$, and integrated over the surface of the strip. The released elastic energy is the difference between the strain energy initially stored on the left side at X_1^- and the remaining strain energy on the right side at X_1^+. As the interlayer is traction-free behind the crack front, the strain energy in the right strip $W_0(X_1^+)$ could be neglected:

$$\Delta U^{\mathrm{e}} = \Delta a \int_0^{\frac{h}{2}} \left(W_0(X_1^+) - W_0(X_1^-)\right)\,\mathrm{d}x_2 \approx -\Delta a \int_0^{\frac{h}{2}} W_0(X_1^-)\,\mathrm{d}x_2$$

The reference work of separation G_0 was computed as the elastic energy release rate in the very first iteration of the procedure, before any dissipative contribution was incorporated in the model.

A.5.2 Plastic contribution

The dissipated energy per unit volume is obtained by integration with the steady-state relationship:

$$w^{\mathrm{p}}(X) = \int_0^t \dot{w}^{\mathrm{p}}(X,\zeta)\,\mathrm{d}\zeta = \frac{1}{-\dot{a}} \int_0^X \sigma_{ij}(X-x)\dot{\varepsilon}_{ij}^{\mathrm{p}}(X-x)\,\mathrm{d}x$$

The additional dissipated energy arises when the material is transferred from left to right through the active plastic zone. The plastic work accumulated by the initial strip was calculated by integrating the density of plastic work in the right strip. Energy dissipation due to plastic deformation was computed as:

$$\Delta W^{\mathrm{p}} = -\Delta a \int_0^{\frac{h}{2}} w^{\mathrm{p}}(X_1^+)\,\mathrm{d}x_2$$

A.5.3 Steady-state work of fracture for the elasto-plastic model

The steady-state work of fracture was eventually computed as:

$$G_{ss} = \frac{1}{\Delta a}(-\Delta U^{\mathrm{e}} - \Delta W^{\mathrm{p}}) = \int_0^{\frac{h}{2}} \left[W_0(X_1^-) - W_0(X_1^+) + w^{\mathrm{p}}(X_1^+) \right] \mathrm{d}x_2 \qquad \text{(A.2)}$$

Equation (A.2) takes into account the increase in elastic energy in the case of increased traction to satisfy the crack propagation criterion $\sigma_{\mathrm{tip}} = \hat{\sigma}$.

A.6 Summary of the steady-state numerical scheme

A.6.1 Determination of the additional strain and stress fields

The numerical scheme is summarized in figure A.2. The "elastic calculation" and "residual stress injection" steps are performed with ABAQUS (with the help of subroutines). Evaluation of the yield criterion, prescription plastic flow, integration to plastic strains and computation of residual stresses are performed in MATLAB. One iteration lasts about 1.5 minutes for a model with 10 000 elements.

A.6.2 Slowing down convergence

The initial guesses for the plastic strain field may be too far away from the actual solution, and the calculation diverges quickly in a few iterations. Such diverging behavior occurs when the yield stress is low – *i.e.* a large part of the ligament undergoes plastic deformation, and when the plastic strain rate $\dot{\varepsilon}_0$ is high.

A reduced-stepping procedure was implemented to favor convergence. At each iteration, the residual stress field σ^R_{n+1} was updated by adding a fraction of the current guess σ^R_* and a complementary fraction of the previous iteration:

$$\sigma^R_{(n+1)} = \eta\sigma^R_* + (1-\eta)\sigma^R_{(n)} \qquad 0 < \eta \leq 1$$

Note that the original algorithm is recovered for $\eta = 1$. As we are taking smaller steps, *i.e.* smaller values of the convergence parameter η, the actual solution is less likely to be missed but it would also take a longer time to reach it (figure A.3). The convergence parameter was divided by 2 when divergence occurred (*i.e.* relative

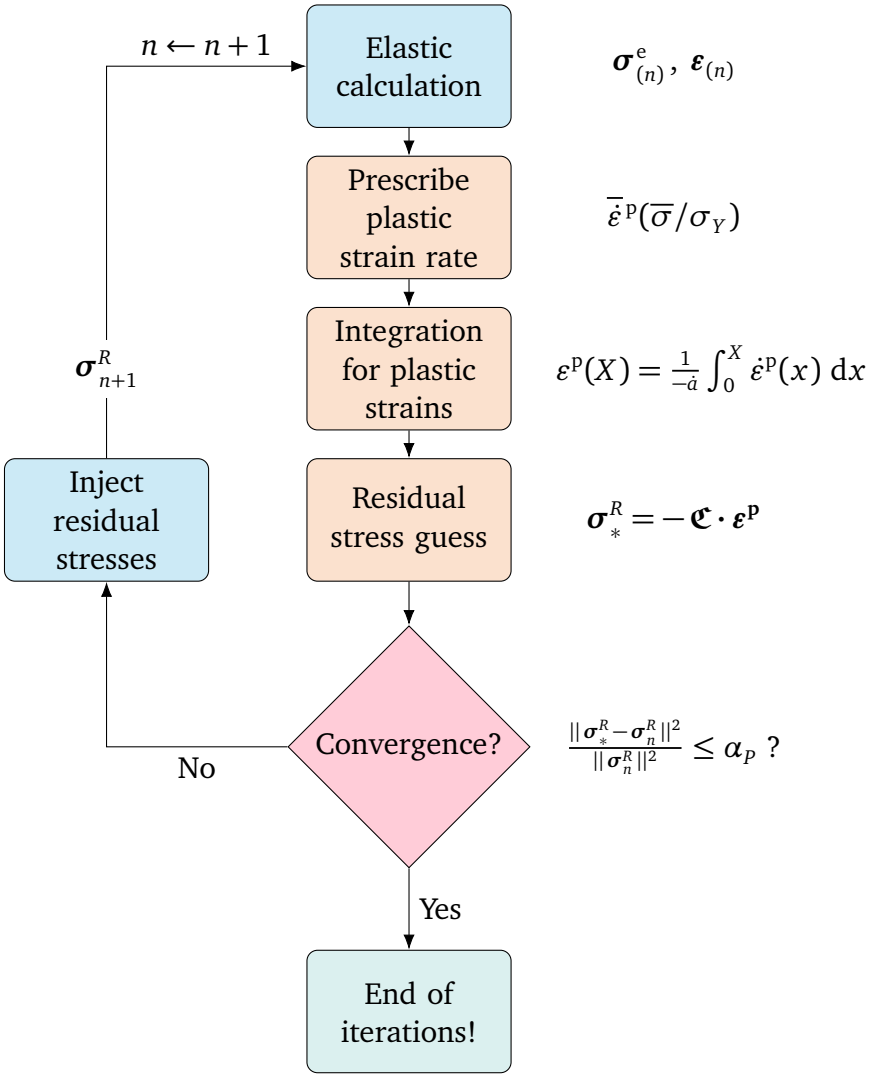

Figure A.2 Algorithm for plastic strain field computation

error $\geq 10^4$), and the computations were restarted from the initial plasticity-free case. The value of η could be increased when convergence seemed likely – *i.e.* a steadily decreasing relative error between iterations – but slow.

A.6.3 Global convergence iterations for delamination

An additional initial loop was added to adjust the displacement boundary condition so that the cohesive stress is attained in the cohesive zone at the crack tip at the first increment. A threshold α_D was fixed on the degradation parameter D: we assumed that delamination was occurring when $0 < D \leq \alpha_D$. In practice, the value

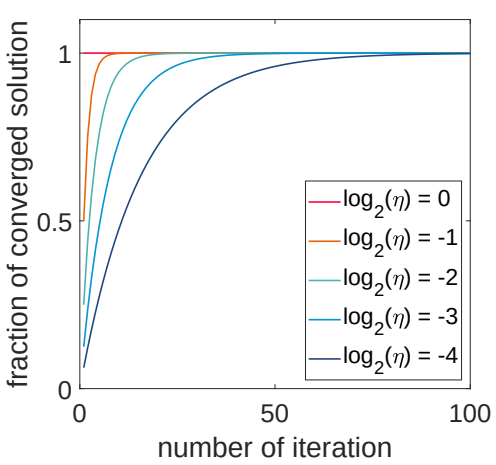

(a) Fraction of converged solution: series $a_n = 1-(1-\eta)^n$

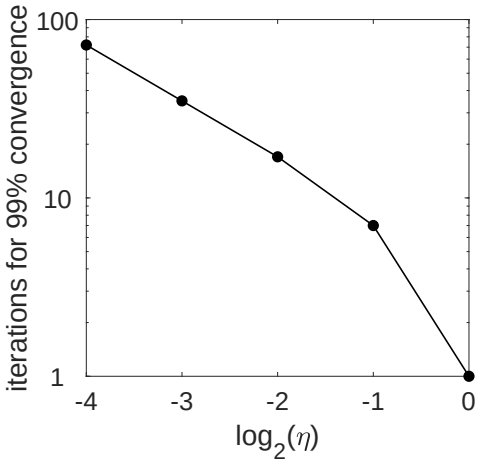

(b) Number of iterations required to achieve 99% of the actual solution

Figure A.3 Reduced-stepping scheme

of prescribed displacement was found by a bisection method, with the threshold $\alpha_D = 0.01$.

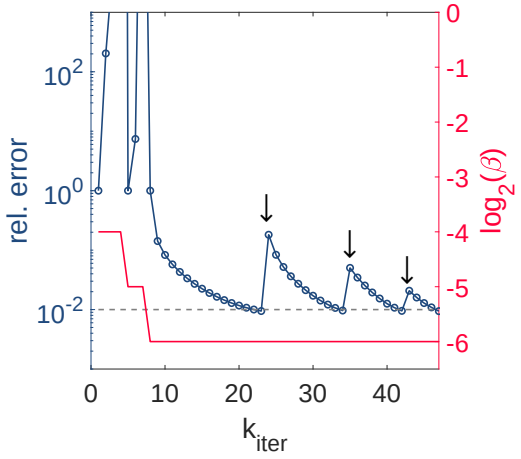

Figure A.4 Convergence plot: relative error *vs.* iteration number.

The two previous loops – for boundary condition check and residual stress field calculation – were embedded in a third one, designed to check if the cohesive stress is still reached at the crack tip at the end of the plastic strain field evaluation.

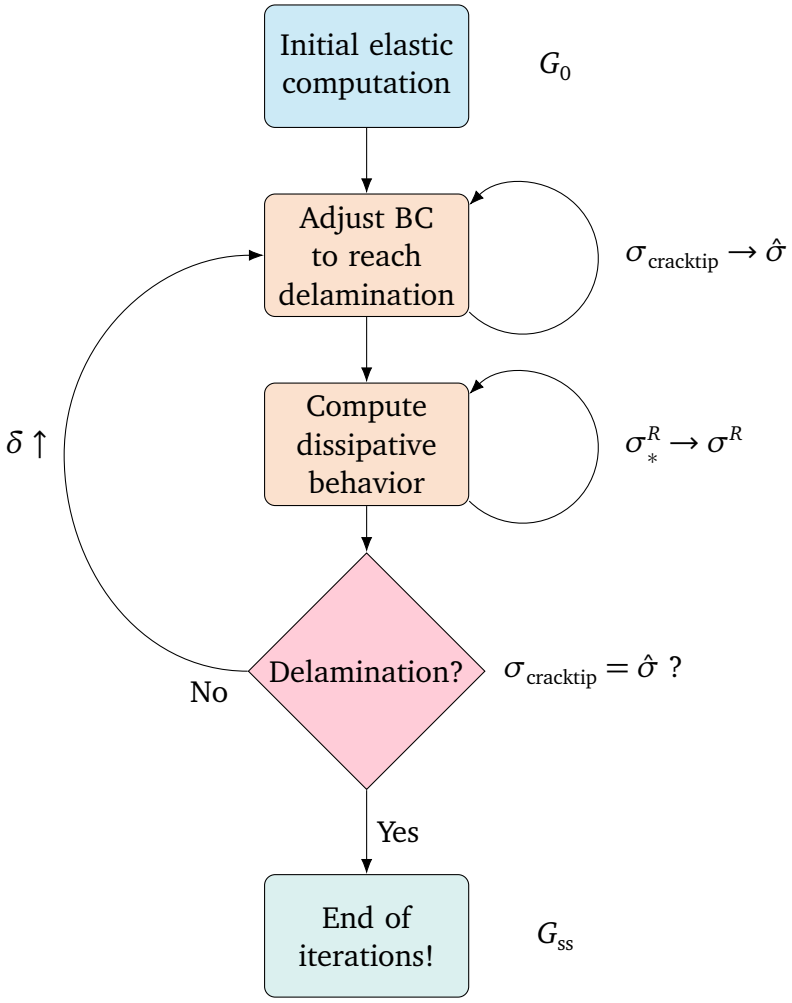

Figure A.5 Global iteration scheme for the steady-state model

A.7 Perspective: towards complete "integration" in ABAQUS

At the time this manuscript was written, several improvements to the technical implementation were already identified.

First, the use a numerical computing software for post-processing implies to read and write a large amount of data in text files. In particular, the "residual stress input" step took 30 minutes for each iteration in the very first versions of the algorithm, and only a few seconds in the latest using FORTRAN *COMMON* blocks. The limiting step was the input of data from ABAQUS' results file to the post-processing software: this required reading between 10^4 and 10^6 lines of a text file, which takes 1 to 2 minutes on a 16-thread CPU. As the calculations could require a few hundred iterations, several

hours were lost in the read/write process.

Actually, input/output of data arrays between softwares could be avoided by the use of ABAQUS' subroutines—coded in FORTRAN—to perform the evaluation of the inelastic term. Using a matrix-manipulation program such as MATLAB has shown efficiency in performing integration of the mechanical history: we suggest the transposition of this matrix-based method within a FORTRAN subroutine, called after the elastic computation. The result of this "inelastic" subroutine could then be passed on as residual stresses without leaving the memory of ABAQUS.

At last, performance should increase even more if one writes a user-material code, or `UMAT`, which would circumvent the use of "residual stresses" and the `SIGINI` subroutine. This `UMAT` could implement the steady-state integration directly in the core of the FEA code: however, as said in ABAQUS' User's Guide, "the use of this subroutine generally requires considerable expertise" which we did not have at the time of this work.

B

Perspectives on numerical modeling: finite deformations

Still, solving the crack propagation problem in the case of finite-strains is yet to be achieved.

Difficulties arise when the mechanical behavior of the material needs to be modeled with accuracy. Indeed, the interesting polymers for laminated-glass applications are highly deformable and highly inelastic at the same time—viscoelastic for PVB and plastic for EVA.

The case of elastic finite-deformations was addressed in the literature, for instance by *Long & Hui*[62]. However, combining finite-deformations and inelastic constitutive behaviors represents a significant step forward. In this chapter, we suggest a method to adapt our steady-state scheme of chapter VI to large deformation problems, based on two ideas.

First, the deformed configuration can be mapped back to the original geometry. Thus, the strategy of integration along streamlines remains relevant and simple in the initial configuration, given that we consider the adequate stress and strain measures.

Then, the constitutive behavior can be decomposed into elastic and inelastic parts, though not as simply as in the linear case. We make use of the multiplicative split of the deformation gradient.

B.1 Multiplicative decomposition of the deformation gradient

B.1.1 The deformation gradient

Definitions

In finite strain elasticity, the stress is derived from the deformation gradient $\boldsymbol{F}$. The deformation gradient is a tensor defining infinitesimal shape changes within the solid between the initial and deformed configurations:

$$\boldsymbol{F} = \frac{\partial \boldsymbol{x}}{\partial \boldsymbol{X}}$$

Considering any hyperelastic potential Ψ, the true (Cauchy) stress is:

$$\boldsymbol{\sigma} = \frac{1}{J}\frac{\partial \Psi}{\partial \boldsymbol{F}} \cdot \boldsymbol{F}^T \qquad \text{in the general case}$$

$$\boldsymbol{\sigma} = \frac{2}{J}\frac{\partial \Psi}{\partial \boldsymbol{B}} \cdot \boldsymbol{B} \qquad \text{for an isotropic material}$$

Example: Neo-Hookean potential The simplest hyperelastic model is the Neo-Hookean model:

$$\Psi = \frac{\mu}{2}(I_1 - 3) + \frac{\kappa}{2}(J-1)^2$$

B.1.2 Decomposition into elastic and inelastic deformation gradients

Additional strain arising from plastic or viscous deformation must be accounted for directly into the deformation gradient, leading to the well-reported "elastic-plastic split":

$$\boldsymbol{F} = \boldsymbol{F}^{\mathbf{e}} \cdot \boldsymbol{F}^{\mathbf{p}}$$

Such decomposition is also applicable for finite-strain viscoelastic formulation considering a creep contribution $\boldsymbol{F}^{\mathbf{cr}}$. The Parallel Rheological Network model available in ABAQUS is based on the same decomposition: what is derived with $\boldsymbol{F}^{\mathbf{p}}$ is applicable with $\boldsymbol{F}^{\mathbf{cr}}$.

The elastic-plastic split means that the loading path goes through a stress-free intermediate confguration, where deformations are only due to irreversible flow.

B.2 Constitutive equation for plastic flow

The flow rule is prescribed in terms of the plastic velocity gradient $\boldsymbol{L}^p = \dot{\boldsymbol{F}}^{\mathrm{p}} \cdot (\boldsymbol{F}^{\mathrm{p}})^{-1}$:

$$\boldsymbol{D}^p = \tfrac{1}{2}\left[\boldsymbol{L}^p + (\boldsymbol{L}^p)^T\right] = \bar{\dot{\varepsilon}}^{\mathrm{p}} \frac{3}{2} \frac{\boldsymbol{\sigma}'}{\bar{\sigma}}$$

The equivalent plastic strain rate $\bar{\dot{\varepsilon}}^{\mathrm{p}}$ can be defined by the same equations presented in the linear elasticity section.

Integration

Weber& Anand[107] for the finite-strain formulation: formulation $\boldsymbol{F} = \boldsymbol{F}^{\mathbf{e}} \cdot \boldsymbol{F}^{\mathbf{p}}$ and numerical scheme for time-integration. Integration in finite strain is not straightforward: the plastic deformation gradient is iteratively determined in a usual finite-element procedure following a push-forward - radial-return algorithm [107,108]. The numerical scheme presented by *Weber & Anand* [107] uses an exponential factor for the trial value of the plastic deformation gradient:

$$\boldsymbol{F}^{\mathbf{p}}_{n+1} = \exp\left(\Delta t \boldsymbol{D}^{\mathbf{p}}_{n+1}\right) \boldsymbol{F}^{\mathbf{p}}_{n} \tag{B.1}$$

The exponential is an adequate solution for the plastic velocity gradient. The equation $\dot{\boldsymbol{F}}^{\mathrm{p}} = \boldsymbol{L}^{\mathbf{p}} \cdot \boldsymbol{F}^{\mathbf{p}}$ is a differential equation of the form $\dot{y} = A(y)y$, for which a solution is $y(t) = \exp(At)$. The value after a time increment is then $y(t + \Delta t) = \exp(A\Delta t)y(t)$: this is equation (B.1). As underlined by Weber & Anand[107], this approximation is accurate to the first order in Δt.

The iteration index n in the formalism of Weber & Anand can be translated into the n-th element of a streamline in the steady-state calculation. The analogous to the time increment is the distance increment between two adjacent element $\Delta X = X_{n+1} - X_n$. Mesh size is a sensitive parameter here: refinement around the crack tip is mandatory to reduce the size of the increments in the region of strong gradients. The elastic deformation gradient is updated:

$$\boldsymbol{F}^{\mathbf{e}}_{n+1} = \boldsymbol{F}_{n+1} \cdot \left(\boldsymbol{F}^{\mathbf{p}}_{n+1}\right)^{-1} = \boldsymbol{F}_{n+1} \cdot \left(\boldsymbol{F}^{\mathbf{p}}_{n}\right)^{-1} \exp\left(-\Delta t \boldsymbol{D}^{\mathbf{p}}_{n+1}\right)$$

The elastic deformation gradient is known everywhere, therefore we can compute the updated stress from the hyperelastic potential:

$$\boldsymbol{\sigma}^*_{n+1} = \frac{2}{J}\frac{\partial \Psi}{\partial \boldsymbol{B}^{\mathbf{e}}_{n+1}} \cdot \boldsymbol{B}^{\mathbf{e}}_{n+1} \tag{B.2}$$

Example with a Neo-Hookean material

The calculation of the stress with an I_1-based hyperelastic potential reduces to:

$$\begin{aligned}\boldsymbol{\sigma}^*_{n+1} &= \frac{2}{J}\left[J^{-2/3}\frac{\partial \Psi}{\partial I_1}\boldsymbol{B}^{\mathbf{e}}_{n+1} + \left(-\frac{1}{3J}I_1\frac{\partial \Psi}{\partial I_1} + \frac{\partial \Psi}{\partial J}\right)\mathbf{1}\right] \\ &= \frac{2}{J}\left[J^{-2/3}\frac{\mu}{2}\boldsymbol{B}^{\mathbf{e}}_{n+1} + \left(-\frac{\mu}{6J}I_1 + \lambda(J-1)\right)\mathbf{1}\right]\end{aligned}$$

If this new stress distribution does not match the previous one, the residual stress is the difference between the updated stress, computed by equation (B.2), and the stress computed by the FE solver.

$$\boldsymbol{\sigma}^R_{n+1} = \boldsymbol{\sigma}^*_{n+1} - \boldsymbol{\sigma}_n$$

N.B: in small strains, this difference was exactly $-\mathfrak{C}_{ijkl}\varepsilon^{\mathrm{p}}_{kl}$ due to the additive decomposition. We cannot do such simplistic decomposition with finite-strains, but the definition of the residual stress – the stress difference induced by the additional deformation – is still meaningful.

B.3 Mapping back to the initial configuration

The residual stresses are prescribed in the undeformed configuration. Therefore, we need to map the residual stress field to the undeformed configuration, *via* a "pull-back" operation. Physically, the Cauchy stress σ is the stress acting on a deformed surface in the deformed configuration. The second Piola-Kirchoff stress correponds to the stress acting on an undeformed surface in the undeformed configuration:

$$\boldsymbol{\Sigma} = J\boldsymbol{F}^{-1} \cdot \boldsymbol{\sigma} \cdot \boldsymbol{F}^{-T}$$

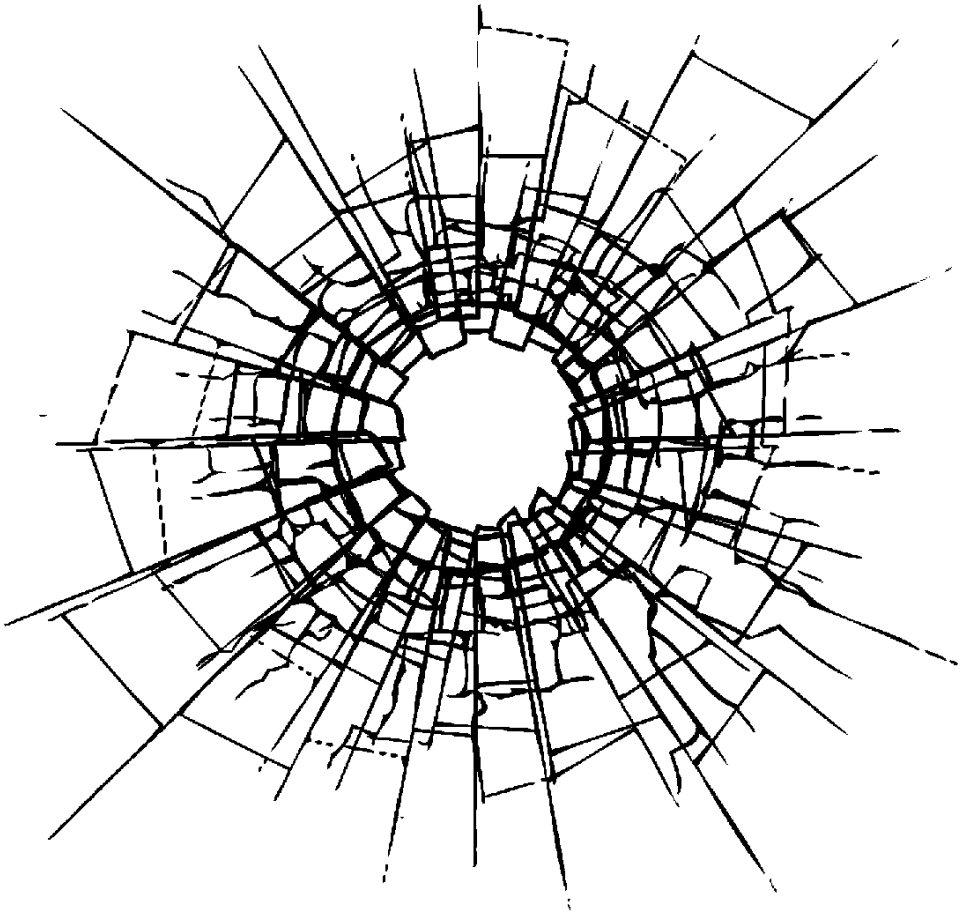

Bibliography

[1] J. A. GREENWOOD; "The Theory of Viscoelastic Crack Propagation and Healing"; Journal of Physics D: Applied Physics **37**, p. 2557 (2004). *cited p. viii*

[2] R. H. DEAN & J. W. HUTCHINSON; "Quasi-Static Steady Crack Growth in Small-Scale Yielding"; Fracture Mechanics (1980). *cited pp. viii, 25, 107 & 112*

[3] C. M. LANDIS, T. PARDOEN & J. W. HUTCHINSON; "Crack Velocity Dependent Toughness in Rate Dependent Materials"; Mechanics of Materials **32**, pp. 663–678 (2000). *cited pp. viii, xvi, 26, 27, 108, 113, 121, 123 & 132*

[4] P. ELZIÈRE; *Verre Feuilleté : Rupture Dynamique d'adhésion*; Ph.D. thesis; Paris 6 (2013). *cited pp. viii, 8, 18, 31, 33, 37, 45, 51, 68 & 109*

[5] P. ELZIÈRE, C. DALLE-FERRIER, C. CRETON, É. BARTHEL & M. CICCOTTI; "Large Strain Viscoelastic Dissipation during Interfacial Rupture in Laminated Glass"; Soft matter **13**, pp. 1624–1633 (2017). *cited pp. viii, 18, 19, 20, 62 & 105*

[6] 3DS SIMULIA; *Abaqus 2016 Documentation* (\copyright Dassault Systemes) (2015). *cited pp. xv, 110, 114 & 126*

[7] V. TVERGAARD; "Effect of Pure Mode I, II or III Loading or Mode Mixity on Crack Growth in a Homogeneous Solid"; International Journal of Solids and Structures **47**, pp. 1611–1617 (2010). *cited pp. xvi, 28 & 132*

[8] J.-M. MICHEL; "Le Verre Renforcé Triplex"; in "Contribution à l'histoire Industrielle Des Polymères En France," (Société Chimique de France). *cited p. 6*

[9] E. NOURRY; *Laminated Glass Behaviour under Perforating Impact*; Ph.D. thesis; Arts et Métiers ParisTech (2005). *cited p. 11*

[10] E. NOURRY & J.-C. NUGUE; "Impact on Laminated Glass: Post-Breakage Behaviour Assessment"; Proceedings of the 8th International Glass Conference; 2003 Jun 15-18; Tampere (Finland) (2003). *cited p. 11*

[11] R. DECOURCELLE; *Comportement Mécanique Des Vitrages Feuilletés Sous Chargements Statiques et Dynamiques*; Ph.D. thesis (2011). *cited p. 11*

[12] M. NOVOTNY & B. POOT; "Influence of Temperature on Laminated Glass Performances Assembled with Various Interlayers"; Challenging Glass Conference Proceedings **5**, pp. 219–232 (2016). *cited p. 12*

[13] A. VEDRTNAM & S. PAWAR; "Laminated Plate Theories and Fracture of Laminated Glass Plate – A Review"; Engineering Fracture Mechanics **186**, pp. 316–330 (2017). *cited p. 13*

[14] N. VANDENBERGHE, R. VERMOREL & E. VILLERMAUX; "Star-Shaped Crack Pattern of Broken Windows"; Physical Review Letters **110** (2013). *cited p. 13*

[15] N. VANDENBERGHE & E. VILLERMAUX; "Geometry and Fragmentation of Soft Brittle Impacted Bodies"; Soft Matter **9**, p. 8162 (2013). *cited p. 13*

[16] J. CHEN, J. XU, X. YAO, B. LIU, X. XU, Y. ZHANG & Y. LI; "Experimental Investigation on the Radial and Circular Crack Propagation of PVB Laminated Glass Subject to Dynamic Out-of-Plane Loading"; Engineering Fracture Mechanics **112-113**, pp. 26–40 (2013). *cited p. 13*

[17] J. CHEN, J. XU, X. YAO, X. XU, B. LIU & Y. LI; "Different Driving Mechanisms of In-Plane Cracking on Two Brittle Layers of Laminated Glass"; International Journal of Impact Engineering **69**, pp. 80–85 (2014). *cited p. 13*

[18] S. CHEN, M. ZANG, D. WANG, Z. ZHENG & C. ZHAO; "Finite Element Modelling of Impact Damage in Polyvinyl Butyral Laminated Glass"; Composite Structures **138**, pp. 1–11 (2016). *cited p. 13*

[19] S. J. BENNISON, A. JAGOTA & C. A. SMITH; "Fracture of Glass/Poly(Vinyl Butyral) (Butacite®) Laminates in Biaxial Flexure"; Journal of the American Ceramic Society **82**, pp. 1761–1770 (1999). *cited pp. 13, 14 & 17*

[20] F. W. FLOCKER & L. R. DHARANI; "Stresses in Laminated Glass Subject to Low Velocity Impact"; Engineering Structures **19**, pp. 851–856 (1997). *cited p. 14*

[21] F. W. FLOCKER & L. R. DHARANI; "Modelling Fracture in Laminated Architectural Glass Subject to Low Velocity Impact"; Journal of Materials Science **32**, pp. 2587–2594 (1997). *cited p. 14*

[22] L. GALUPPI & G. ROYER-CARFAGNI; "Laminated Beams with Viscoelastic Interlayer"; International Journal of Solids and Structures **49**, pp. 2637–2645 (2012). *cited p. 14*

[23] L. GALUPPI & G. ROYER-CARFAGNI; "Enhanced Effective Thickness of Multi-Layered Laminated Glass"; Composites Part B: Engineering **64**, pp. 202–213 (2014). *cited p. 14*

[24] L. GALUPPI & G. ROYER-CARFAGNI; "A Homogenized Model for the Post-Breakage Tensile Behavior of Laminated Glass"; Composite Structures **154**, pp. 600–615 (2016). *cited p. 14*

[25] L. GALUPPI & G. ROYER-CARFAGNI; "A Homogenized Analysis à La Hashin for Cracked Laminates under Equi-Biaxial Stress. Applications to Laminated Glass"; Composites Part B: Engineering **111**, pp. 332–347 (2017). *cited p. 14*

[26] M. SESHADRI, S. BENNISON, A. JAGOTA & S. SAIGAL; "Mechanical Response of Cracked Laminated Plates"; Acta Materialia **50**, pp. 4477–4490 (2002). *cited pp. 14, 15, 17 & 109*

[27] R. VILLEY, C. CRETON, P.-P. CORTET, M.-J. DALBE, T. JET, B. SAINTYVES, S. SANTUCCI, L. VANEL, D. J. YARUSSO & M. CICCOTTI; "Rate-Dependent Elastic Hysteresis during the Peeling of Pressure Sensitive Adhesives"; Soft Matter **11**, pp. 3480–3491 (2015). *cited p. 15*

[28] K. KENDALL; "Thin-Film Peeling-the Elastic Term"; Journal of Physics D: Applied Physics **8**, pp. 1449–1452 (1975). *cited pp. 15 & 43*

[29] D. KLOCK; *Contribution à l'étude Des Verres Feuilletés Verre-Polymère – Synthèse et Structure Du Poly(Vinyl Butyral) En Relation Avec Ses Propriétés Mécaniques et Adhésives*; Ph.D. thesis; Université de Haute Alsace (1989). *cited pp. 16, 21, 33 & 54*

[30] J. R. HUNTSBERGER; "Adhesion of Plasticized Polyvinyl Butyral) to Glass"; The Journal of Adhesion **13**, pp. 107–129 (1981). *cited pp. 16 & 17*

[31] C. BUTCHART & M. OVEREND; "Influence of Moisture on the Post-Fracture Performance of Laminated Glass"; p. 3 (2013). *cited p. 16*

[32] J. PELFRENE, S. VAN DAM & W. VAN PAEPEGEM; "Numerical Analysis of the Peel Test for Characterisation of Interfacial Debonding in Laminated Glass"; International Journal of Adhesion and Adhesives **62**, pp. 146–153 (2015). *cited p. 16*

[33] S. PONCE, J. BICO & B. ROMAN; "Effect of Friction on the Peeling Test at Zero-Degrees"; Soft Matter **11**, pp. 9281–9290 (2015). *cited p. 17*

[34] C.-Y. HUI, Z. LIU, H. MINSKY, C. CRETON & M. CICCOTTI; "Mechanics of an Adhesive Tape in a Zero Degree Peel Test: Effect of Large Deformation and Material Nonlinearity"; Soft Matter **14**, pp. 9681–9692 (2018). *cited p. 17*

[35] Y. SHA, C. HUI, E. KRAMER, P. GARRETT & J. KNAPCZYK; "Analysis of Adhesion and Interface Debonding in Laminated Safety Glass"; Journal of Adhesion Science and Technology **11**, pp. 49–63 (1997). *cited pp. 17, 21 & 109*

[36] S. MURALIDHAR, A. JAGOTA, S. BENNISON & S. SAIGAL; "Mechanical Behaviour in Tension of Cracked Glass Bridged by an Elastomeric Ligament"; Acta Materialia **48**, pp. 4577–4588 (2000). *cited p. 17*

[37] M. A. SAMIEIAN, D. CORMIE, D. SMITH, W. WHOLEY, B. R. BLACKMAN, J. P. DEAR & P. A. HOOPER; "Temperature Effects on Laminated Glass at High Rate"; International Journal of Impact Engineering **111**, pp. 177–186 (2018). *cited pp. 18, 19, 20, 48 & 105*

[38] P. HOOPER, R. SUKHRAM, B. BLACKMAN & J. DEAR; "On the Blast Resistance of Laminated Glass"; International Journal of Solids and Structures **49**, pp. 899–918 (2012). *cited p. 19*

[39] P. DEL LINZ, P. A. HOOPER, H. ARORA, Y. WANG, D. SMITH, B. R. BLACKMAN & J. P. DEAR; "Delamination Properties of Laminated Glass Windows Subject to Blast Loading"; International Journal of Impact Engineering **105**, pp. 39–53 (2017). *cited pp. 19, 48 & 110*

[40] M. A. SAMIEIAN, D. CORMIE, D. SMITH, W. WHOLEY, B. R. BLACKMAN, J. P. DEAR & P. A. HOOPER; "On the Bonding between Glass and PVB in Laminated Glass"; Engineering Fracture Mechanics **214**, pp. 504–519 (2019). *cited pp. 20 & 110*

[41] GRIFFITH ALAN ARNOLD & TAYLOR GEOFFREY INGRAM; "The Phenomena of Rupture and Flow in Solids"; Philosophical Transactions of the Royal Society of London. Series A, Containing Papers of a Mathematical or Physical Character **221**, pp. 163–198 (1921). *cited p. 22*

[42] A. NEEDLEMAN; "A Continuum Model for Void Nucleation by Inclusion Debonding"; Journal of Applied Mechanics **54**, p. 525 (1987). *cited p. 22*

[43] A. NEEDLEMAN; "An Analysis of Tensile Decohesion along an Interface"; Journal of the Mechanics and Physics of Solids **38**, pp. 289–324 (1990). *cited p. 22*

[44] R. S. RIVLIN & D. W. SAUNDERS; "Large Elastic Deformations of Isotropic Materials. VII. Experiments on the Deformation of Rubber"; Philosophical Transactions of the Royal Society A: Mathematical, Physical and Engineering Sciences **243**, pp. 251–288 (1951). *cited p. 23*

[45] GENT A. N., PETRICH R. P. & TABOR DAVID; "Adhesion of Viscoelastic Materials to Rigid Substrates"; Proceedings of the Royal Society of London. A. Mathematical and Physical Sciences **310**, pp. 433–448 (1969). *cited p. 23*

[46] A. N. GENT, S.-M. LAI, C. NAH & C. WANG; "Viscoelastic Effects in Cutting and Tearing Rubber"; Rubber Chemistry and Technology **67**, pp. 610–618 (1994). *cited p. 23*

[47] P.-G. DE GENNES; "Fracture d'un adhésif faiblement réticulé"; Comptes rendus de l'Académie des sciences. **307**, pp. 1949–1953 (1988). *cited p. 24*

[48] DE GENNES, PIERRE-GILLES; "Soft Adhesives"; Langmuir **12**, pp. 4497–4500 (1996). *cited p. 24*

[49] W. BRADLEY, W. CANTWELL & H. KAUSCH; "Viscoelastic Creep Crack Growth: A Review of Fracture Mechanical Analyses"; Mechanics of Time-Dependent Materials **1**, pp. 241–268 (1997). *cited p. 24*

[50] B. N. J. PERSSON, O. ALBOHR, G. HEINRICH & H. UEBA; "Crack Propagation in Rubber-like Materials"; Journal of Physics: Condensed Matter **17**, pp. R1071–R1142 (2005). *cited p. 24*

[51] F. SAULNIER, T. ONDARÇUHU, A. ARADIAN & E. RAPHAËL; "Adhesion between a Viscoelastic Material and a Solid Surface"; Macromolecules **37**, pp. 1067–1075 (2004). *cited p. 24*

[52] E. BARTHEL & C. FRÉTIGNY; "Adhesive Contact of Elastomers: Effective Adhesion Energy and Creep Function"; Journal of Physics D: Applied Physics **42**, p. 195302 (2009). *cited p. 24*

[53] C. CRETON & M. CICCOTTI; "Fracture and Adhesion of Soft Materials: A Review"; Reports on Progress in Physics **79**, p. 046601 (2016). *cited p. 25*

[54] V. TVERGAARD & J. W. HUTCHINSON; "The Influence of Plasticity on Mixed Mode Interface Toughness"; Journal of the Mechanics and Physics of Solids **41**, pp. 1119–1135 (1993). *cited pp. 25 & 28*

[55] Y. WEI & J. W. HUTCHINSON; "Models of Interface Separation Accompanied by Plastic Dissipation at Multiple Scales"; in "Fracture Scaling," , edited by Z. P. BAŽANT & Y. D. S. RAJAPAKSE; pp. 1–17 (Springer Netherlands, Dordrecht) (1999). *cited pp. 25, 26, 27 & 129*

[56] V. TVERGAARD & J. W. HUTCHINSON; "The Relation between Crack Growth Resistance and Fracture Process Parameters in Elastic-Plastic Solids"; Journal of the Mechanics and Physics of Solids **40**, pp. 1377–1397 (1992). *cited pp. 25 & 28*

[57] Z. SUO, C. SHIH & A. VARIAS; "A Theory for Cleavage Cracking in the Presence of Plastic Flow"; Acta Metallurgica et Materialia **41**, pp. 1551–1557 (1993). *cited p. 25*

[58] T. PARDOEN, T. FERRACIN, C. LANDIS & F. DELANNAY; "Constraint Effects in Adhesive Joint Fracture"; Journal of the Mechanics and Physics of Solids **53**, pp. 1951–1983 (2005). *cited p. 26*

[59] P. MARTINY, F. LANI, A. KINLOCH & T. PARDOEN; "Numerical Analysis of the Energy Contributions in Peel Tests: A Steady-State Multilevel Finite Element Approach"; International Journal of Adhesion and Adhesives **28**, pp. 222–236 (2008). *cited pp. 26 & 148*

[60] J. W. HUTCHINSON & Z. SUO; "Mixed Mode Cracking in Layered Materials"; in "Advances in Applied Mechanics," , volume 29pp. 64–191 (Academic Press Inc.) (1992). *cited p. 27*

[61] V. TVERGAARD & J. HUTCHINSON; "Mode III Effects on Interface Delamination"; Journal of the Mechanics and Physics of Solids **56**, pp. 215–229 (2008). *cited p. 28*

[62] R. LONG & C.-Y. HUI; "Crack Tip Fields in Soft Elastic Solids Subjected to Large Quasi-Static Deformation — A Review"; Extreme Mechanics Letters **4**, pp. 131–155 (2015). *cited pp. 29 & 161*

[63] P. ELZIERE, P. FOURTON, Q. DEMASSIEUX, A. CHENNEVIERE, C. DALLE-FERRIER, C. CRETON & M. CICCOTTI; "Macromolecular Structure, Large Strain and Dissipation for Impact Resistance – Why Poly(Vinylbutyral)?" Macromolecules p. 31 (in press). *cited pp. 31, 34 & 114*

[64] CHRISTIAN CARROT, AMINE BENDAOUD & CAROLINE PILLON; "Polyvinyl Butyral"; in "Handbook of Thermoplastics," (CRC Press) (2015). *cited pp. 32 & 33*

[65] M. TUPÝ, D. MĚŘÍNSKÁ, P. SVOBODA, A. KALENDOVÁ, A. KLÁSEK & J. ZVONÍČEK; "Effect of Water and Acid–Base Reactants on Adhesive Properties of Various Plasticized Poly(Vinyl Butyral) Sheets"; Journal of Applied Polymer Science **127**, pp. 3474–3484 (2013). *cited p. 33*

[66] F. MERTZ; *Etude de La Synthèse et de La Caractérisation Du Poly(Vinyl Butyral) – Influence Des Caractéristiques Du Polymère Sur La Structure Des Films – Répartition de l'eau Au Sein Des Films Plastifiés*; Ph.D. thesis; Université de Haute Alsace; Mulhouse (1992). *cited p. 33*

[67] C.-Y. HUI, J. A., S. J. BENNISON & J. D. LONDONO; "Crack Blunting and the Strength of Soft Elastic Solids"; Proceedings of the Royal Society A: Mathematical, Physical and Engineering Sciences **459**, pp. 1489–1516 (2003). *cited p. 33*

[68] X. ZHANG, H. HAO, Y. SHI & J. CUI; "The Mechanical Properties of Polyvinyl Butyral (PVB) at High Strain Rates"; Construction and Building Materials **93**, pp. 404–415 (2015). *cited p. 34*

[69] I. O. SALYER & A. S. KENYON; "Structure and Property Relationships in Ethylene–Vinyl Acetate Copolymers"; Journal of Polymer Science Part A-1: Polymer Chemistry **9**, pp. 3083–3103 (1971). *cited p. 34*

[70] J. M. COGEN, L. H. GROSS, M. J. KEOGH & J. A. OBAL; "Polyethylene Crosslinkable Composition"; (2001); cIB: C08K5/14; C08K5/3492; C08L23/04; H01B3/44; (IPC1-7): C08K5/34. *cited pp. 35 & 79*

[71] V. CHAPUIS, S. PÉLISSET, M. RAEIS-BARNÉOUD, H.-Y. LI, C. BALLIF & L.-E. PERRET-AEBI; "Compressive-Shear Adhesion Characterization of Polyvinyl-Butyral and Ethylene-Vinyl Acetate at Different Curing Times before and after Exposure to Damp-Heat Conditions: Compressive-Shear Adhesion Characterization of PVB and EVA"; Progress in Photovoltaics: Research and Applications **22**, pp. 405–414 (2014). *cited pp. 35 & 91*

[72] H. YAN, W. YUANHAO & Y. HONGXING; "TEOS/Silane Coupling Agent Composed Double Layers Structure: A Novel Super-Hydrophilic Coating with Controllable Water Contact Angle Value"; Applied Energy **185**, pp. 2209–2216 (2017). *cited pp. 36 & 37*

[73] V. PURCAR, O. CINTEZA, M. GHIUREA, A. BALAN, S. CAPRARESCU & D. DONESCU; "Influence of Hydrophobic Characteristic of Organo-Modified Precursor on Wettability of Silica Film"; Bulletin of Materials Science **37**, pp. 107–115 (2014). *cited p. 36*

[74] T. C. HUANG, H. TORAYA, T. N. BLANTON & Y. WU; "X-Ray Powder Diffraction Analysis of Silver Behenate, a Possible Low-Angle Diffraction Standard"; Journal of Applied Crystallography **26**, pp. 180–184 (1993). *cited p. 40*

[75] J. E. SCHAWE; "Measurement of the Thermal Glass Transition of Polystyrene in a Cooling Rate Range of More than Six Decades"; Thermochimica Acta **603**, pp. 128–134 (2015). *cited p. 42*

[76] P. INNOCENZI, M. O. ABDIRASHID & M. GUGLIELMI; "Structure and Properties of Sol-Gel Coatings from Methyltriethoxysilane and Tetraethoxysilane"; Journal of Sol-Gel Science and Technology **3**, pp. 47–55 (1994). *cited p. 52*

[77] A. MATSUDA, Y. MATSUNO, M. TATSUMISAGO & T. MINAMI; "Fine Patterning and Characterization of Gel Films Derived from Methyltriethoxysilane and Tetraethoxysilane"; Journal of the American Ceramic Society **81**, pp. 2849–2852 (1998). *cited pp. 52 & 53*

[78] M. VAN BOMMEL, T. BERNARDS & A. BOONSTRA; "The Influence of the Addition of Alkyl-Substituted Ethoxysilane on the Hydrolysis—Condensation Process of TEOS"; Journal of Non-Crystalline Solids **128**, pp. 231–242 (1991). *cited p. 52*

[79] C. A. FYFE & P. P. AROCA; "A Kinetic Analysis of the Initial Stages of the Sol-Gel Reactions of Methyltriethoxysilane (MTES) and a Mixed MTES/Tetraethoxysilane System by High-Resolution ^{29} Si NMR Spectroscopy"; The Journal of Physical Chemistry B **101**, pp. 9504–9509 (1997). *cited p. 52*

[80] S. PRABAKAR & R. ASSINK; "Hydrolysis and Condensation Kinetics of Two Component Organically Modified Silica Sols"; Journal of Non-Crystalline Solids **211**, pp. 39–48 (1997). *cited p. 52*

[81] M. DESLOIR, C. BENOIT, A. BENDAOUD, P. ALCOUFFE & C. CARROT; "Plasticization of Poly(Vinyl Butyral) by Water: Glass Transition Temperature and Mechanical Properties"; Journal of Applied Polymer Science **136**, p. 47230 (2019). *cited p. 67*

[82] M. BROGLY, M. NARDIN & J. SCHULTZ; "Effect of Vinylacetate Content on Crystallinity and Second-Order Transitions in Ethylene?Vinylacetate Copolymers"; Journal of Applied Polymer Science **64**, pp. 1903–1912 (1997). *cited p. 74*

[83] H. ZHOU & G. WILKES; "Comparison of Lamellar Thickness and Its Distribution Determined from d.s.c., SAXS, TEM and AFM for High-Density Polyethylene Films Having a Stacked Lamellar Morphology"; Polymer **38**, pp. 5735–5747 (1997). *cited p. 74*

[84] X.-M. SHI, J. ZHANG, D.-R. LI & S.-J. CHEN; "Effect of Damp-Heat Aging on the Structures and Properties of Ethylene-Vinyl Acetate Copolymers with Different Vinyl Acetate Contents"; Journal of Applied Polymer Science **112**, pp. 2358–2365 (2009). *cited p. 74*

[85] A. J. RYAN, W. BRAS, G. R. MANT & G. E. DERBYSHIRE; "A Direct Method to Determine the Degree of Crystallinity and Lamellar Thickness of Polymers: Application to Polyethylene"; Polymer **35**, pp. 4537–4544 (1994). *cited p. 75*

[86] F. ADDIEGO, A. DAHOUN, C. G'SELL & J.-M. HIVER; "Characterization of Volume Strain at Large Deformation under Uniaxial Tension in High-Density Polyethylene"; Polymer **47**, pp. 4387–4399 (2006). *cited pp. 75 & 76*

[87] M. F. BUTLER, A. M. DONALD & A. J. RYAN; "Time Resolved Simultaneous Small- and Wide-Angle X-Ray Scattering during Polyethylene Deformation—II.

Cold Drawing of Linear Polyethylene"; Polymer **39**, pp. 39–52 (1998). *cited pp. 75 & 76*

[88] Z. JIANG, Y. TANG, J. RIEGER, H.-F. ENDERLE, D. LILGE, S. V. ROTH, R. GEHRKE, Z. WU, Z. LI & Y. MEN; "Structural Evolution of Tensile Deformed High-Density Polyethylene at Elevated Temperatures: Scanning Synchrotron Small- and Wide-Angle X-Ray Scattering Studies"; Polymer **50**, pp. 4101–4111 (2009). *cited p. 76*

[89] K. THAWORN, P. BUAHOM & S. AREERAT; "Effects of Organic Peroxides on the Curing Behavior of EVA Encapsulant Resin"; Open Journal of Polymer Chemistry **02**, pp. 77–85 (2012). *cited pp. 77 & 80*

[90] H.-J. TAI & J. WANG; "A Study of the Reaction Kinetics Involved in a Crosslinked LDPE Foam"; Journal of Cellular Plastics **33** (1997). *cited p. 78*

[91] ARKEMA INC.; "DiCup(R) Dicumyl Peroxide Techical Information"; . *cited p. 80*

[92] ARKEMA INC.; "Luperox (R) TBEC Technical Information"; . *cited p. 80*

[93] H.-Y. XUE, W.-H. RUAN, M.-Q. ZHANG & M.-Z. RONG; "Fast Curing Ethylene Vinyl Acetate Films with Dual Curing Agent towards Application as Encapsulation Materials for Photovoltaic Modules"; Express Polymer Letters **8**, pp. 116–122 (2014). *cited p. 80*

[94] K. CHO, D. KIM & S. YOON; "Effect of Substrate Surface Energy on Transcrystalline Growth and Its Effect on Interfacial Adhesion of Semicrystalline Polymers"; Macromolecules **36**, pp. 7652–7660 (2003). *cited p. 90*

[95] T. P. FLANAGAN & I. KAYE; "Hot Melt Adhesives Containing Silane Compounds"; (1972); cIB: C08K5/54; C09J123/02; C09J201/00; (IPC1-7): C08F21/04. *cited p. 91*

[96] Y.-R. LUO; *Comprehensive Handbook of Chemical Bond Energies* (CRC Press) (2007). *cited p. 91*

[97] G. J. LAKE & A. G. THOMAS; "The Strength of Highly Elastic Materials"; Proceedings of the Royal Society A: Mathematical, Physical and Engineering Sciences **300**, pp. 108–119 (1967). *cited p. 91*

[98] S. WANG, S. PANYUKOV, M. RUBINSTEIN & S. L. CRAIG; "Quantitative Adjustment to the Molecular Energy Parameter in the Lake–Thomas Theory of Polymer Fracture Energy"; Macromolecules **52**, pp. 2772–2777 (2019). *cited p. 91*

[99] X. M. Liu, J. L. Thomason, F. R. Jones, J. L. Thomason & F. R. Jones; "The Concentration of Hydroxyl Groups on Glass Surfaces and Their Effect on the Structure of Silane Deposits"; https://www.taylorfrancis.com/ (2009). *cited p. 91*

[100] C. Jeenjitkaew & F. Guild; "The Analysis of Kissing Bonds in Adhesive Joints"; International Journal of Adhesion and Adhesives **75**, pp. 101–107 (2017). *cited p. 94*

[101] B. Z. Newby & M. K. Chaudhury; "Friction in Adhesion"; Langmuir **14**, pp. 4865–4872 (1998). *cited p. 100*

[102] N. Amouroux, J. Petit & L. Léger; "Role of Interfacial Resistance to Shear Stress on Adhesive Peel Strength"; Langmuir **17**, pp. 6510–6517 (2001). *cited p. 100*

[103] A. Jagota, S. Bennison & C. Smith; "Analysis of a Compressive Shear Test for Adhesion between Elastomeric Polymers and Rigid Substrates"; International Journal of Fracture **104**, pp. 105–130 (2000). *cited p. 109*

[104] R. S. Rivlin & A. G. Thomas; "Rupture of Rubber. I. Characteristic Energy for Tearing"; Journal of Polymer Science Part A: Polymer Chemistry **10**, pp. 291–318 (1953). *cited pp. 119 & 120*

[105] J. Slootman; *Détection Quantitative de l'endommagement Moléculaire, Par Mécano-Fluorescence, Dans Les Matériaux Mous.*; Ph.D. thesis (2019). *cited p. 132*

[106] D. Delincé; *Experimental Approaches for Assessing Time and Temperature Dependent Performances of Fractured Laminated Safety Glass*; Dissertation; Ghent University (2014). *cited p. 141*

[107] G. Weber & L. Anand; "Finite Deformation Constitutive Equations and a Time Integration Procedure for Isotropic, Hyperelastic-Viscoplastic Solids"; Computer Methods in Applied Mechanics and Engineering **79**, pp. 173–202 (1990). *cited p. 163*

[108] G. G. Weber, A. M. Lush, A. Zavaliangos & L. Anand; "An Objective Time-Integration Procedure for Isotropic Rate-Independent and Rate-Dependent Elastic-Plastic Constitutive Equations"; International Journal of Plasticity **6**, pp. 701–744 (1990). *cited p. 163*

RÉSUMÉ

Le verre feuilleté est un produit industriel centenaire dédié aux applications de sécurité. Un feuillet de polymère, d'épaisseur millimétrique, est intercalé entre deux panneaux de verre afin d'apporter résistance à l'impact et à la perforation, ainsi qu'une fonction de rétention d'éclats. Malgré les décennies de développement industriel, la compréhension du couplage entre les interfaces verre/polymère, le comportement mécanique du polymère, la propagation de rupture adhésive et la dissipation d'énergie totale.

Nous avons étudié l'effet d'une modification de chimie de surface du verre, par un dépôt sol-gel, sur les mécanismes de dissipation d'énergie. Une plus grand adhésion aux interfaces engendre une plus grande dissipation d'énergie dans le système, par l'augmentation de la déformation de l'intercalaire et de l'énergie dissipée en tête de fissure adhésive.

Nous avons caractérisé les propriétés mécaniques et structurales d'un autre intercalaire utilisé dans le verre feuilleté, à base de poly(ethylène vinyl-acetate). Cet intercalaire EVA présente un comportement élasto-plastique à température ambiante, dû à sa structure semi-cristalline. L'observation d'un régime de délamination nécessite un ajustement de l'adhésion entre l'intercalaire et le verre, également réalisée grâce a la chimie des silanes.

Les tests mécaniques et d'adhésion montrent qu'un regime de délamination stable peut être obtenu avec l'intercalaire EVA à condition de modifier les interfaces. En particulier, avec des surfaces de verres méthylées, nous avons pu montrer que la dissipation d'énergie par l'intercalaire élasto-plastique est plus faible car concentrée uniquement aux fronts de délamination. En revanche, en combinant les effets de plasticité et viscoélasticité dans la région de transition vitreuse, une forte dissipation d'énergie est retrouvée.

Enfin, une nouvelle méthode de simulations numériques par éléments finis a été développée, afin d'implémenter une approche en régime stationnaire. L'hypothèse de régime stationnaire permet de transformer les intégrales temporelles, c'est-à-dire l'histoire mécanique du matériau, en intégrales spatiales. Cette approche a été implémentée en interfaçant un logiciel commercial éléments finis et un logiciel d'analyse numérqiue, puis appliquée à un modèle linéaire pour validation, en vue d'une extension à des lois de comportement en grandes déformations adaptées aux matériaux polymères.

MOTS CLÉS

Verre feuilleté, Adhésion, Mécanique de la fracture, EVA, Chimie des silanes, Éléments Finis

ABSTRACT

Laminated glass is an industrial product designed for safety applications. A polymer interlayer is inserted between two glass plies to provide impact resistance properties to the glazing. Upon impact, this polymer interlayer debonds and deforms between glass fragments: these two coupled mechanisms provide the impact resistance properties.

On the "interface" side, we propose an original method to finely tune the adhesion between glass and interlayer in chapter III. The surface of the glass is modified with sol-gel chemistry using two silane species. Despite a non-standard deposition method and coatings thicker than a perfect molecular layer, we demonstrate that adhesion of the polymer interlayer can be tuned *via* surface chemistry.

On the "polymer" side, we decided to change completely the nature of the interlayer, from a viscoelastic to a plastic material. With this plastic interlayer, we have evidenced the necessity to modify the interfaces to retrieve a stable delamination behavior. Moreover, concomitant debonding and stretching of this plastic interlayer dissipates less energy due to the localization of energy dissipation close to the delamination fronts. Still, when viscoelastic processes are activated at the glass transition, we recover dissipation in the entire volume of the interlayer and high potency for impact applications.

Last but not least, to try and make a connection between interfaces, polymer rheology and delamination properties in laminated glass, we present a numerical simulation of the crack propagation problem with a steady-state approach. Since the steady-state crack scheme is not implemented in commercial finite-element codes, we propose a strategy coupling FEA and numerical computing softwares. First results in small strains validate the method, which is expected to be extended to rate-dependent non-linear material behaviors in the future.

KEYWORDS

Laminated glass, adhesion, fracture mechanics, EVA, silane chemistry, finite element method, steady-state crack